Communications Research Centre Canada
An Agency of Industry Canada

Centre de recherches sur les communications Canada
Un organisme d'Industrie Canada

Finite-Volume Time-Domain Modelling of Complex Geometries and Lumped Elements in Generalised Coordinate Systems

By Riaz Siushansian
Advanced Antenna Technology

July 2000

CRC Report No. CRC-RP-2000-07

Finite-Volume Time-Domain Modelling of Complex Geometries and Lumped Elements in Generalised Coordinate Systems

By Riaz Siushansian

Advanced Antenna Technology

CRC Report No. CRC-RP-2000-07
July 2000

Abstract

A time domain general purpose electromagnetic (EM) solver is developed using the Finite-Volume Time-Domain method (FVTD). The general formulation of the EM simulator is based on the mathematical formulation of a generalised coordinate system that is capable of modelling a broad range of EM problems defined via rectangular and/or non rectangular geometries in any given simulation environment. In addition, new models for lossy media, lumped elements, and lumped sources are derived and developed in order to improve and complement the original formulation of the FVTD. The performance of the developed FVTD engine is then evaluated and compared to other time domain methods (where possible) for a number of benchmark EM problems involving various types of geometries. The strengths and weaknesses of the developed EM simulator are further identified through its application to several practical EM problems. It is concluded that the current FVM based EM solver is capable of modelling and solving reasonably complex EM problems but requires further improvements and revisions for more geometrically complex structures.

Keywords: finite-volume time-domain, Maxwell's equations, Lax-Wendroff scheme, flux splitting, upwind scheme, generalised coordinate systems, lumped elements

Table of Contents

List of Tables

List of Figures

Abbreviations

1D, 2D, 3D	one-, two-, three-dimension
ABC	Absorbing Boundary Condition
BC	Boundary Condition
CEM	Computational Electromagnetics
CFD	Computational Fluid Dynamics
CP-FDTD	Contour-Path FDTD
DE	Differential Equation
DFT	Discrete Fourier Transform
DSI-FDTD	Discrete Surface Integral FDTD
EM	Electromagnetics
EMC	Electromagnetic Compatibility
EMI	Electromagnetic Immunity
FD	Frequency Domain
FDM	Finite Difference Method

FDTD	Finite-Difference Time-Domain
FEM	Finite-Element Method
FIT	Finite-Integration Technique
FVM	Finite Volume Method
FVTD	Finite-Volume Time-Domain
GTEM	Giga-hertz Transverse Electromagnetic
GUI	Graphical User Interface
IC	Initial Condition
IE	Integral Equation
LW	Lax-Wendroff
MOM	Method of Moments
MSDRA	Multi-Segment Dielectric Resonator Antennas
NCW	Number of Cells per Wavelength
N-FDTD	Non-orthogonal coordinates FDTD
OATS	Open Area Test Sites
PC	Personal Computers
PDE	Partial Differential Equation
PEC	Perfect Electric Conductor
PMC	Perfect Magnetic Conductor
PM-TD-FEM	Point-Matched TD-FEM
RK	Runge Kutta

RL	Return Loss
SCN-TLM	Symmetrical Condensed Node TLM
TD	Time Domain
TD-FEM	Time-Domain FEM
TE	Transverse Electric
TEM	Transverse Electromagnetic
TLM	Transmission-Line Matrix
TM	Transverse Magnetic
TSE	Taylor Series Expansion

Chapter 1

Introduction

1.1 Computational Electromagnetics (CEM): Past and Present

"Keep in mind that most of the problems that can be solved formally (analytically) have already been solved!" (Paris and Hurd, 1969)* When this statement was made, a little more than one hundred years had passed since the reading of Maxwell's now-famous work entitled, "A Dynamical Theory of Electromagnetic Field," to the British Royal Society in 1864 [2] and the publication of his treaties in which he "founded the science of electromagnetics [3]." His theories were initially met with skepticism, and an additional 15 years (a decade after Maxwell's death) were needed before they were accepted following the ground-breaking experiments by Heinrich Hertz.

The Paris and Hurd statement portrays a state of frustration that existed in the 1960s in the electromagnetics (EM) community. Practical problems were becoming ever more complex in nature and structure, and no amount of innovation and experience in classical

* See [1] page 166.

methods (namely the separation of variables and integral equations) was adequate in finding the solutions to these problems [4]. Even partial resolution of such problems would have restored the faith of the masses and would have restored the science of EM to its past glory. EM was at a new cusp when pioneers with new and revolutionary ideas were desperately and urgently needed.*

In the 1960s, a new tool was slowly moving from warehouse-sized government laboratories (where it was originally conceived and constructed) into the scientific community; computers were becoming increasingly more advanced, more affordable, and easier to operate. Although the operation and utilization of computers were still very tedious and time consuming, many researchers foresaw the potential and the future applications of this new technology and began developing applications for it. The EM community was no exception. The publication of the now classic papers of K. S. Yee [5] and R. F. Harrington [6] in the mid-1960s launched a new era of "computerated solution of EM problems" [7 page 1].

The response of the electromagnetic community to the use of computers to solve EM problems was initially lukewarm at best. This lack of enthusiasm was partly due to the limited computational power available to researchers in the early 1970s. In the 1980s, the advent of Personal Computers (PC) and work-stations alleviated past fears of computational costs, and interest in numerical methods for solving EM problems soared.† The field of Computational Electromagnetics (CEM) began to grow at an exponential rate.

* This might sound very melodramatic, but not all engineers are cold, calculating individuals!

† This was despite the efforts of those who advocated the use of massive and expensive super-computers in order to monopolize the newly emerging field and to keep other scholars at bay.

In the 1990s, computational costs fell much lower than had been predicted. The supercomputers of a decade earlier were now obsolete and were being replaced by low-cost, massively parallel systems, such as Beowulf Linux clusters. The future of CEM had never seemed brighter.

1.2 Numerical Methods and CEM

Until the 1940s, EM field problems were solved using experimental or analytical methods. Experiments are often expensive, time consuming, difficult to design, hard to control, and lack flexibility [4]. On the other hand, there is practically a mountain of solutions to classical EM problems. However, many assumptions that accompany these solutions reduce their applicability to practical cases. It is very laborious, and often impossible, to analytically solve field problems involving mixed boundary conditions, non-homogeneous regions, and/or involving complex geometries. Although many researchers have either developed new and innovative analytical methods or have extended classical ones to obtain solutions to more realistic problems [4], increasingly, many new practical problems simply defy such efforts!

Traditionally, the analytical expressions defining a problem were manipulated into forms that required minimal computational effort in order to avoid repetitive and tedious hand calculations [6]. Computers operate under a different philosophy. They are capable of performing very basic algebraic operations with remarkable speed and accuracy. Thus, in numerical methods (as opposed to the analytical methods), field equations must be simplified for computers to comprehend! The general expressions of a problem are approximated by simpler algebraic equations. The new expressions are not the exact

solution to the proposed problem; however, errors are manageable, and the desired level of accuracy dictates the complexity of the numerical algorithm. The obtained solutions from these methods are often sufficiently accurate for most engineering applications [4, 8].

1.3 A Critical Look at CEM

Prior to the introduction of the science of CEM, the EM community consisted of only a handful of brilliant members. A good EM scientist or engineer possessed either a vast knowledge of mathematics and analytical methods in EM or many hours of experience in laboratories; often a combination of both was required. These stringent requirements often intimidated potential recruits to the EM community, and subsequently, only the best minds and most devoted enrolled in this field. EM research became the domain of a few scientists with an extraordinary capacity to comprehend complex mathematical and EM concepts that eluded almost all novices.* The science of EM was labelled difficult, incomprehensible, and inaccessible by many engineers, a reputation and stigma that remain intact to present day.

The debut of PCs and the subsequent fall of computational costs were the major factors contributing to the introduction and growth of the CEM commercial industry in the late 1980s and early 1990s. A prolific surge of interest in this area, which was originally ignited by the military and scientific applications of a decade earlier, was now one of the major driving forces of research in the CEM community. The main attraction of the new generation of CEM software packages was their relative ease of use. Although the user still required basic knowledge of the operation of the software package and some

* Unfortunately, this fact is often accentuated by scholars and teachers of the science of EM!

knowledge of EM theory pertaining to the problems at hand, the user required little knowledge of the analytic solution of the resultant expressions and/or the inner working of the CEM software package. This clearly favoured novices to the EM community and made EM-based design and analysis more accessible to the engineering community.

1.3.1 Arguments For and Against CEM Use

Opponents of CEM often criticize researchers and students alike for relying heavily on numerical methods rather than on learning, understanding, and analysing the true phenomenon in EM field problems. Historically, most new tools have promoted a lax attitude among some users, and such tools have been misused as a substitute for basic knowledge.* However, if the tools were used as originally intended, they would facilitate education and precipitate research activities. Critics also cite the wide-spread utilization of CEM in the scientific and engineering community as the cause of the erosion of the quality of conducted and published research in the area. However, one must consider that the nature of CEM research often dictates an emphasis on the verification and accuracy of the numerical method rather than on a particular physical phenomenon. Yet, in some cases, the ease of data generation using CEM tools and a preoccupation with numerical methods often cause researchers to lose sight of the real goal (studying the physical phenomenon); thus, they report poorly analysed and ill-considered results. The onus is on the individual researcher to not lose sight of the research goals.

Proponents for the advancement of CEM point to the wide-spread use of CEM packages in education and industry. CEM packages often provide a visual representation

* For example, the use of calculators for multiplication tables, *etc.*

of complex concepts (such as wave propagation and reflection on various surfaces) that students and engineers find easier to grasp and study. After all, a picture is worth a thousand words!

Industry, and the soaring demand for wireless products in particular, have been calling for more versatile and reliable products that have a minimal effect on the surrounding environment and equipment. CEM packages have revolutionized many areas, such as antenna design, health risk assessment, and Electromagnetic Compatibility (EMC), to name a few [8]. In most cases, the application of CEM along with other numerical techniques (for example Genetic Algorithms [9]) have led to the solution of problems and/ or to the design of products that would have been impossible a few decades ago [4, 8].

1.4 About This Thesis

As discussed earlier, in the past 30-plus years, CEM has firmly established itself as the third tool (along with experimental observations and mathematical analysis) for solving EM problems. Although the contribution of numerical techniques to the modelling and solving of many problems involving non-homogenous and/or complex structures has been invaluable, it appears that the efforts of the CEM community are disjointed and fragmented. Scientific journals in the area of CEM are filled with countless variations of a few numerical methods, where each is designed and developed to solve a specific type of problem or structure. In addition, most of these techniques require the user to have an advanced knowledge of the proposed method of solution. Overall, it seems that the CEM community has lost sight of the original goals of developing CEM packages; these goals were the generality and simplicity of CEM tools.

1.4.1 Research Objectives

The purpose of this research is to investigate a versatile numerical method that is capable of providing accurate solutions to general EM field problems without placing restrictions on the composition or geometric configuration of the simulation space. The first step on the road to obtaining an accurate solution is to precisely model the significant features of the simulation space. That is, all bends, curves, and material boundaries (and boundary conditions) associated with the problem must be meticulously defined (and enforced). To achieve this task, the numerical technique that is implemented must be highly flexible in order to accurately model problems involving objects of both rectangular and non-rectangular geometries in various simulation environments. A class of time domain CEM techniques, namely the Finite Volume Method (FVM), possesses the afore-mentioned properties and is the subject of the investigation of this thesis. Based on the performance of a finite volume-based EM simulator, several conclusions and recommendations are made towards the development of a general purpose EM simulation tool.

1.4.2 Scope of Research

As part of this thesis, a time-domain general purpose EM solver was developed using the FVM. The general formulation of the EM simulator is based on the mathematical formulation of a generalised coordinate system that is capable of modelling a broad range of EM problems defined via rectangular and/or non rectangular geometries in any given simulation environment. In addition, new models for lossy media, lumped elements, and lumped sources were derived and developed in order to improve and complement the original formulation of the FVM. The performance of the FVM was then evaluated and compared to other time domain CEM methods (where possible) for a number of

benchmark EM problems involving various types of geometries. This process was necessary to validate the developed EM engine, as well as to identify the strengths and weaknesses of the developed CEM method. Furthermore, the pre-processing (defining the problem) associated with an EM simulation was considered. The developed EM simulator was evaluated for its simplicity and ease of use for the purposes of modelling and solving EM problems.

Since much of theory of the generalized coordinate system formulation of the FVM is scattered across a broad area of the available literature (dating back almost three decades), a conscious effort was made to collect and present the general theory of the FVM in a comprehensive and methodical manner. It is hoped that this presentation will instill the interested reader with a thorough understanding of the FVM and will facilitate any future modifications and extension of the technique. However, a formal and rigorous mathematical examination of numerical algorithms leading to a discussion of concepts, such as stability and convergence, is avoided since the numerical analysis of the original (rectangular) formulation of the FVM has been included in may excellent references, such as [10, 11]. Furthermore, while very little research has been conducted in the area of the numerical properties of a generalised coordinate system or the newly developed source term formulation of the FVM, this type of analysis is also beyond the scope of this thesis. Although the numerical properties of the FVM have not been fully explored, in most cases, a comparison of the numerical results with analytical or experimental data has confirmed the accuracy of the method. The main focus of this thesis is thus the engineering applications of CEM tools and the development of general purpose EM simulation tools for accurately modelling and solving complex EM field problems.

1.4.3 Organization

Since the main objective of this thesis is the development, investigation, and application of numerical techniques for solving general purpose EM problems, it is important to outline the fundamental concepts of numerical solutions used in CEM. Such a summary is included in **Chapter 2**. This chapter also contains a review of some of the more popular time domain techniques currently used in CEM. These methods are briefly explained and are compared for their capabilities and versatility in modelling geometrically complex EM problems. The governing equations, namely Maxwell's equations, and their formulation in general coordinate systems are discussed in **Chapter 3**. This chapter also includes a generalised solution of Maxwell's equations via the flux vector splitting technique. **Chapter 4** is truly the heart of this thesis where the finite volume time domain scheme is assembled one section at a time. This chapter begins by deriving a fully windward Lax-Wendroff algorithm and is followed by an explanation and the derivation of numerical fluxes used in the FVTD method and the boundary conditions associated with it. In addition to the validation of the newly derived FVTD method, **Chapter 5** also includes test cases for the general coordinate system formulation and the evaluation of characteristic absorbing boundary conditions. The development of the formulation for the inclusion of lumped elements in general coordinate systems is one of the main contributions of this thesis; the theory and procedure, as well as the validation of the outlined theory, is given in **Chapter 6**. Finally, the strengths and weaknesses of the Lax-Wendroff version of the FVTD method are highlighted in **Chapter 7** using several case studies. **Chapter 8** summarizes the research conducted in this thesis and provides recommendations for future research.

Chapter 2

A Review of Fundamental Concepts and Various Techniques in CEM

The mathematical study of an EM problem begins by formulating it via Maxwell's equations. Fundamentally, the solution of the EM formulation of any problem may be defined as a "*quantitative relationship between a cause (forcing function or input) and its effect (the response or output)*" [13]. This relationship, generally represented as a transfer function, is often referred to as a ***field propagator*** in the context of EM problems. Thus, the science of electromagnetics, and by default, CEM, is simply the study of field propagators [13]. Since an EM problem, and hence, the field propagators, can be formulated using various types of solution techniques, the classification of these techniques is the first step in selecting a method of solution. In this chapter, various types of field propagators are outlined and briefly discussed, and the rational for selecting a differential equation class of field propagators is given. Next, the basic principles of the finite difference method, which is utilized for numerically solving the differential equation form of field propagators, are outlined. Finally, some of the more popular differential equation-based numerical methods are briefly reviewed.

2.1 Formulation of Field Propagators in Electromagnetics

The first step in solving an EM problem is selecting the form of the field propagator. The four classes of field propagators are as follows: (1) the Integral Equation (IE) model, derived from Green's function for an infinite medium; (2) the Differential Equation (DE) model, which is based on Maxwell's curl equations; (3) the modal expansion method, which models fields as a sum of all possible modes; and (4) optical description, which uses high frequency asymptotic techniques, such as the geometrical theory of diffraction [13].

Due to the nature and solution requirements of the EM problems considered in this thesis, the modal expansion and optical description methods are not suitable. The optical description model assumes that the objects in the problem space are electrically large (that is, the dimensions of the object are large compared to the wavelength) [14], an assumption that does not hold for most of the problems to be studied later in the thesis. The modal expansion model, although a mathematically complete solution [15], is not practical as a full wave solver of Maxwell's equations. Thus, only the full wave solution of field propagators, namely integral and differential equation models, are considered.

2.1.1 Integral Equation (IE) Model

For EM problems, the IE model is developed by first selecting an appropriate Green's function for the problem.The original formulation of the problem is manipulated and simplified into the integral operator of an unknown source or field distribution [13], hence the term IE model. The unknown of the IE model is often solved using the Method of Moments (MOM) [6]. The computational domain of IE methods is limited to the source

region of interest which for scattering problems is typically the surface of the scatterer. IE-based methods have been successfully used to solve many scattering and radiation problems. However, for electrically large structures (larger than ten wavelengths), the system of linear equations, and its resulting matrix, become too large to store and solve [16]. In addition, the IE formulation is often not suited for modelling highly inhomogeneous and layered media [13, 16]. Even if such problems are formulated using IE methods, the computational resources required for solving them are greater than they would be using a differential equation model.

2.1.2 Differential Equation (DE) Model

In contrast to the global operators (Green's functions) of IE models, the differential operators of Maxwell's curl equations are local operators. Thus, inhomogeneous and layered media are easier and more computationally efficient to model. In order to solve the field propagator, either the differential or the integral form of Maxwell's equations is approximated by a Taylor's series from which the differential operators are replaced by finite differences (finite sums are substituted for integral operators) [13]. Despite the fact that DE models require a large computational space for electrically large problems (*i.e.* the problem may contain many unknowns), in general, they are more efficient and more practical than are IE models [17]. Therefore, the DE form of a field propagator is considered in this thesis.

2.1.3 Solution Domain: Frequency Versus Time Domain

A DE-based field propagator can be formulated and solved either in the time or frequency domain. The Frequency Domain (FD) formulation assumes an harmonic time

variation, $e^{j\omega t}$, and the generic operator, $L(\omega)$, is a function of a single frequency, ω. On the other hand, the Time Domain (TD) formulation regards time as an independent variable; thus, its generic operator is given by $L(t)$ [13]. The choice of the solution domain is often determined by the specific application and the required details of the final solution. For example, in antenna and radar cross-section analysis, where the solution to a single or a narrow band of frequencies is desired, an FD method is sufficient. However, in Electromagnetic Immunity (EMI) and EMC problems, where the transient response to a wide band pulse (a sharp Gaussian or a step pulse) is of interest, only a TD solution is acceptable. Generally, an FD solution of EM problems is suitable for studying the steady-state response to an excitation of a given frequency, whereas a TD solution provides transient and broad-band responses.

An added advantage of using TD methods is that the response of the structure at a specific frequency can be easily obtained via Fourier Transform; that is, only one TD simulation is required for a wide band of frequencies.* In contrast, FD methods require separate runs for each frequency of interest.† Also, TD methods provide a transient response that can be used as a powerful visualization tool that can supply designers with additional information that otherwise would not be available.‡ In light of these advantages, in this thesis, the DE model of field propagators is solved in time domain.

---

* Provided that the original excitation pulse has components in the desired frequency.

† However, most FD methods demand a fraction of the computation time required by TD methods.

‡ The visualization of EM problems has long been used as an educational, promotional, and even entertainment tool!

2.1.4 Definition of Hyperbolic Systems of PDEs

Maxwell's curl equations are represented by a system of Partial Differential Equations (PDEs) which contain an independent variable, t, or time, and a position variable (vector), $\boldsymbol{x}(x^1, x^2, x^3)$, defined in the (x^1, x^2, x^3) general coordinate system. In this thesis, a system of PDEs in a general coordinate system is written in the form [18]:

$$\frac{\partial \boldsymbol{Q}}{\partial t} + \frac{\partial \boldsymbol{E}}{\partial x^1} + \frac{\partial \boldsymbol{F}}{\partial x^2} + \frac{\partial \boldsymbol{G}}{\partial x^3} = \boldsymbol{S}, \tag{2.1}$$

where $\boldsymbol{Q}, \boldsymbol{E}, \boldsymbol{F}, \boldsymbol{G}$, and $\boldsymbol{S}$ are N-component vectors.* In general, $\boldsymbol{Q}$ is the unknown vector, $\boldsymbol{E}, \boldsymbol{F}$, and $\boldsymbol{G}$ are often referred to as flux vectors, and $\boldsymbol{S}$ is the source (forcing function) term [19]. In a ***linear*** system of PDEs, the flux vectors are functions of the independent variables $(\boldsymbol{x}, t)$, whereas in this case, the system of PDEs is ***quasi-linear***; that is, the flux vectors are functions of both the dependent and independent variables [10], *i.e.*

$$\frac{\partial \boldsymbol{Q}(\boldsymbol{x}, t)}{\partial t} + \frac{\partial \boldsymbol{E}(\boldsymbol{Q}, \boldsymbol{x}, t)}{\partial x^1} + \frac{\partial \boldsymbol{F}(\boldsymbol{Q}, \boldsymbol{x}, t)}{\partial x^2} + \frac{\partial \boldsymbol{G}(\boldsymbol{Q}, \boldsymbol{x}, t)}{\partial x^3} = \boldsymbol{S}(\boldsymbol{Q}, \boldsymbol{x}, t). \tag{2.2}$$

This system of ***first order*** PDEs† can be written as:

$$\frac{\partial \boldsymbol{Q}}{\partial t} + [\boldsymbol{A}]\frac{\partial \boldsymbol{Q}}{\partial x^1} + [\boldsymbol{B}]\frac{\partial \boldsymbol{Q}}{\partial x^2} + [\boldsymbol{C}]\frac{\partial \boldsymbol{Q}}{\partial x^3} = \boldsymbol{S} \tag{2.3}$$

where $[\boldsymbol{A}], [\boldsymbol{B}]$, and $[\boldsymbol{C}]$ are $N \times N$ matrices, which are commonly known as ***flux Jacobian matrices***; they are computed via [21]:

$$A_{ij} = \frac{\partial E_i}{\partial Q_j}, \quad B_{ij} = \frac{\partial F_i}{\partial Q_j}, \text{ and } \quad C_{ij} = \frac{\partial G_i}{\partial Q_j}. \tag{2.4}$$

---

* In the case of Maxwell's equations, $N = 6$.

† The *order* of a PDE is defined by the highest order of the derivative in the equation [10].

The flux matrices play an important role in the classification of PDEs and determine if the system is of ***elliptic***, ***parabolic***, or ***hyperbolic*** type [22]. This can be achieved by evaluating the eigenvalues of the flux matrices. For example, in a quasi-linear first order system of PDEs with two independent variables, t and x,

$$\frac{\partial \boldsymbol{u}}{\partial t} + [\boldsymbol{A}]\frac{\partial \boldsymbol{u}}{\partial x} = \boldsymbol{k}, \text{ where } u = \begin{bmatrix} v \\ w \end{bmatrix} \text{ and } [\boldsymbol{A}] = \begin{bmatrix} 0 & -c \\ -c & 0 \end{bmatrix}, \tag{2.5}$$

the eigenvalues, λ, of the flux matrix $[\boldsymbol{A}]$ are easily computed by solving the following expression [23]:

$$\begin{aligned} det|[\boldsymbol{A}] - \lambda[\boldsymbol{I}]| &= 0, \\ \lambda^2 - c^2 &= 0. \end{aligned} \tag{2.6}$$

A system of PDEs is hyperbolic if all eigenvalues are real; the system of equations is identified as elliptic or parabolic if the eigenvalues are complex or zero. A *mixed* system will have both real and complex eigenvalues [24].

Elliptic equations are often associated with potential problems (such as Poisson's equation); they have no time dependence and, thus, only require boundary values to determine the solution of a steady-state or an equilibrium problem [20]. Parabolic equations represent mechanisms, such as diffusion, convection, and dissipation; they require both Initial Conditions (ICs) and Boundary Conditions* (BCs). The propagation of waves is governed by hyperbolic equations that also require both ICs and BCs. Hyperbolic equations may be linear or nonlinear and may or may not contain dissipation mechanisms. A mixed system is known to exhibit both hyperbolic and parabolic properties [25].

* ***Boundary conditions*** are defined as the behaviour of the solution (vector) at the surfaces of discontinuity in the media. These surfaces usually mark abrupt changes in the medium's properties and often correspond to the interface between different material media.

In this thesis, a class of hyperbolic PDEs, *i.e.* Maxwell's equations, is considered and numerical methods based on ***method of characteristics*** are constructed. The mathematical formulation and derivation of the method of characteristics, along with other pertinent details, are discussed in the next chapter.

2.2 Theory of Differential Equation-Based Numerical Techniques

Thus far, the hyperbolic differential form of field propagators (*i.e.* Maxwell's curl equations) has been selected to be solved in time domain. Long before the age of digital computers, researchers believed that numerical methods might offer an alternative method of arriving at the solution of a complex system of PDEs [8]. The basic function of any numerical method is to transform a system of PDEs (that govern a physical phenomenon) into an algebraic system of equations that are easily solved with the aid of computers. This process of approximating PDEs (and some of the BCs) introduces errors in the final solution; hence, computational techniques can only provide an approximate solution to the governing equations [18]. What is required is that these approximate solutions converge to the exact solution (and they generally do for sufficiently small time and space discretisations) [10]. This section examines some of the theories and concepts associated with numerical methods and briefly reviews some of the more popular numerical techniques used in solving systems of PDEs.

2.2.1 Background and Terminology

The computational solution of a system of PDEs is obtained through a two stage process (see **Figure 2.1**). The first step, commonly known as ***discretisation***, involves the transformation of the governing PDEs, BCs, and ICs into a discrete system of algebraic

equations [24]. The second step (***solver***) is solving the system of algebraic equations. The majority of errors associated with numerical solutions is introduced at the discretisation step; whereas, in most cases, the solver introduces little or no errors [24]. Thus, it is important to consider and understand the discretisation process. The discretisation process is performed on both space and time variables; both types of discretisation are considered next.

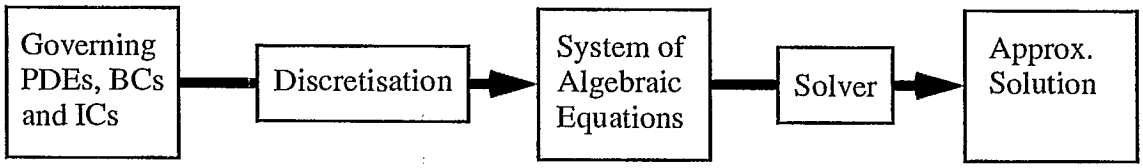

Figure 2.1. Computational solution procedure [24]

2.2.1.1 Discretisation

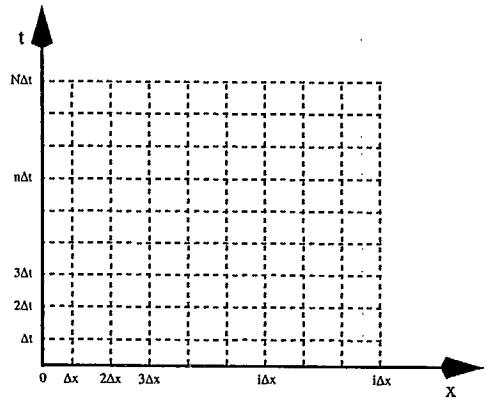

Figure 2.2. A discrete grid

In the discretisation process, a continuous function, $\bar{u}(t, x)$, is replaced by a discrete function, $u(n\Delta t, i\Delta x)$ or u_i^n, where the value of the discrete function is only known on the *i-th* ***grid*** (***mesh***) point and at the *n-th* ***time step*** [25]. Similarly, differential operators are replaced by algebraic expressions that represent the differentiated term of the PDEs in terms of discrete function values at discrete spatial ***nodes*** (or ***cells*** when dealing with 2D or 3D problems) and time steps.

For example, in the following first order differential equation:

$$\frac{\partial \bar{u}}{\partial t} + c\frac{\partial \bar{u}}{\partial x} = 0, \tag{2.7}$$

the definition of a derivative at a given point, $x = i\Delta x$ [27],

$$\frac{\partial \bar{u}}{\partial x} = \lim_{\Delta x \to 0} \frac{u(n\Delta t, i\Delta x + \Delta x) - u(n\Delta t, i\Delta x)}{\Delta x} = \lim_{\Delta x \to 0} \frac{u_{i+1}^n - u_i^n}{\Delta x}, \tag{2.8}$$

is substituted in the PDE of (2.7) without the limit procedures giving:

$$\frac{u_i^{n+1} - u_i^n}{\Delta t} + c\frac{u_{i+1}^n - u_i^n}{\Delta x} = 0. \tag{2.9}$$

This completes the discretisation step. The above algebraic equation is then solved for the future time step of the discrete function. Therefore, the following update equation is derived where the future discrete value of the discrete function is calculated in terms of the present value of the discrete function at various grid points [28]; that is,

$$u_i^{n+1} = \left(u_i^n - c\frac{u_{i+1}^n - u_i^n}{\Delta x} \right)(\Delta t). \tag{2.10}$$

Hence, for given ICs, $\bar{u}(0, x) = \bar{U}_0(x) \approx u_i^0$ for $0 \le i \le I$, and time independent BCs, $\bar{u}(0) \approx u_0^n = a$ and $\bar{u}(X) \approx u_I^n = b$, the time-marching formulation of (2.10) provides solutions to all grid points at any time step.

In the above example, one of the simplest finite difference algorithms was utilized to solve a first order PDE. It takes little imagination to realize that a large number of schemes can be devised to represent the differential terms using countless combinations of discrete function values evaluated at various spatial nodes and time steps. In general, time derivatives are estimated by the finite difference method, whereas either ***finite difference***, ***finite element***, or ***finite volume*** methods can be used to discretise the spatial derivatives. These spatial discretisation methods are briefly discussed in **Section 2.3**.

2.2.1.2 Time Discretisation

In general, time derivatives are estimated by finite differences where the estimating expression of the time derivatives is evaluated in terms of a current, u^n, and next, u^{n+1}, time-step. An algorithm is said to be ***explicit*** if only one spatial term is evaluated at the future time step, say u_i^{n+1}; that is, there is only one unknown per equation per grid point. An ***implicit*** algorithm has several spatial terms evaluated at the future time step, and thus, has more than one unknown per equation per grid point. The solution matrix formed by the discretisation of a system of PDEs using an explicit algorithm is a diagonal matrix; it is often solved using direct methods (solving for the unknown variables) and requires minimal computational effort in the equation solver stage for each time step. The solution matrix formed by the application of an implicit method is not diagonal and often requires the application of (sometimes computationally expensive) iterative methods for matrix inversion.

In general, explicit methods have more stringent stability and convergence criteria than have the implicit methods. That is, the size of the time step required for an explicit method may be several orders of magnitude smaller than its counterpart for an implicit method. This discrepancy in the size of the time step between the two types of algorithms can sometimes balance the computational time requirements of the two types of schemes. On one hand, implicit methods are memory and computation-time intensive but require fewer time steps, whereas, explicit methods are computationally efficient, but require many thousands of time steps! Often, explicit schemes are preferred over implicit schemes due to their low memory requirement and ease of implementation.

2.2.2 Numerical Versus Exact Solutions

One of the most frequently asked questions by those new to (or skeptical of) CEM is, "How do we know that the computational solution coincides with the exact solution?" The answer to this question is rather complex and consists of two parts. First, it is often difficult to establish that the numerical solution ***converges*** to the exact solution using direct methods; however, it is possible to establish convergence using other properties of numerical methods (such as consistency and stability) [21]. The second issue involves the introduction of numerical errors as a result of the method of discretisation applied to the PDEs. These issues have been the subject of numerous papers in the field of CEM, including [10, 18, 21, 29, 31], and will be briefly considered here.

2.2.2.1 Convergence

If a system of PDEs is approximated by a set of algebraic equations, the solution of the algebraic equations is ***convergent*** if it approaches the exact solution of the PDEs when infinitely fine time and space grids are used (*i.e.* $\Delta t \to 0$ and $\Delta x \to 0$) [21]. With the exception of a few simple algorithms [30], a rigorous proof of convergence is very difficult (and in most cases, impossible) to develop. Thus, convergence is often proved via an indirect route; one such method is to use the Lax equivalence theorem [31] along with the stability and consistency properties of an algorithm. A ***consistent*** system of algebraic equations (resulting from the discretisation of PDEs) yields the original PDEs if the limit of grid spacing approaches zero [29]. A similar system is said to be ***stable*** if the cumulative effect of truncation errors (resulting from the discretisation process) and round-off errors (produced in the computation stage) does not amplify without bound as the time-stepping is performed [31]. The important Lax equivalence theorem links these

two concepts and states [32 page 45]:

> *"Given a properly posed linear initial value problem and finite difference approximation to it that satisfies the* ***consistency*** *condition,* ***stability*** *is the necessary and sufficient condition for* ***convergence****".*

Certainly, consistency is necessary for achieving convergence. After all, the discretised equations must resemble what they are approximating! However, some schemes are, by nature, numerically unstable, and they diverge rapidly. Hence, a stability criterion is required to root out unstable algorithms. Three of the most common methods of stability analysis are: the matrix method, the Von Neumann method, and Fourier series analysis [11]. A detailed stability analysis of many algorithms has been performed and compiled in many text books, such as [10, 18, 21, 29, 33], and hence, will not be discussed here.

Many implicit methods are unconditionally stable; *i.e.* for a given spatial grid size, there is no restriction on the size of the time step; only accuracy limits the step size. In contrast, all explicit methods are conditionally stable, which means that for a given grid spacing, the size of the time step must satisfy a specific ratio, often know as the stability condition [31]. One of the most famous stability conditions for finite difference methods is referred to as the ***CFL condition*** (named after R. Courant, K. O. Friedrichs, and H. Lewy, the authors of the landmark paper published in 1928). However, the CFL condition derived for a given scheme often does not include BCs, and a separate stability analysis is required for the BCs.

Finally, although the Lax equivalence theorem appears only to include finite difference methods, it has been shown that this theorem also applies to any discretisation procedure that is equivalent to finite difference methods, such as finite element and finite volume methods [10]. However, one must exercise caution when applying the Lax equivalence theorem to problems that include BCs; it has been shown that the addition of BCs may result in a non-convergent algorithm that satisfies the Lax equivalence theorem [24]. Thus, the theorem should only be used as an elimination tool for non-convergent schemes rather than as an absolute proof of convergence.

2.2.2.2 Errors Due to Dissipation and Dispersion

Heretofore, the solutions of the PDEs of interest have been assumed to be "smooth" and continuous for most physical problems; often, this is not the case. Most situations feature some type of discontinuity, in either the simulated space or in the initial or boundary conditions, which results in highly discontinuous solution profiles. The effects of discontinuities are most pronounced in the numerical solution of hyperbolic systems where they propagate through the entire computational domain and cause inaccurate (and sometimes non-convergent) solutions [10]. Hence, most numerical methods are designed to manage discontinuities.

Most finite difference methods exhibit either numerical ***dispersion*** (phase change) or numerical ***dissipation*** (damping) or both. The Fourier series expansion method is often used to analyse and derive expressions of ***numerical amplification factors*** (damping) or ***phase errors*** per time step [10]. An in depth review of dispersion and dissipation is beyond the scope of the current discussion and can be found in [10, 31]. Ideally, both

dissipation and dispersion must be minimal, but practically, in the majority of cases, one is minimized at the expense of the other. To date, no algorithm has been found to be the "best" method in a general sense.

2.2.2.3 Truncation, Modelling, and Round-Off Errors

Previously, it was established that the discretisation process that converts PDEs into discrete algebraic equations introduces errors in the numerical solution. These errors, which arise from approximating a partial derivative with a truncated Taylor series, are referred to as ***truncation errors*** [4]. Theoretically, a function (or differential) can be exactly represented via an infinite Taylor series expansion; however, due to the limitation of computation resources, a Taylor expansion has to be truncated after a few terms. Truncation errors are inversely related to both the number of series terms and to the grid size. Thus, truncation errors may be reduced by using a higher order of approximation (*i.e.* more Taylor series terms) or by using finer space and time discretisation [4]. **Appendix A** includes a more detailed discussion of this topic.

Along with truncation errors, **modelling errors** are the most significant class of errors in numerical methods. These errors may either be due to the improper modelling of a physical phenomenon (such as the conductivity or the dispersive property of a material [34]) or to the inaccurate modelling of the size or shape of an object due to inaccurate meshing and/or the improper application of BCs. The former can be remedied by using more rigorous models for the phenomenon of interest, while the latter determines the complexity of the formulation of the discretisation process [35]. As was indicated earlier, it is apparent that the density of the grid (coarse vs. fine grids) plays an important role in

the accuracy of the numerical solution. The coarseness of the grid determines the number of sampling points per wavelength and thus the accuracy of the numerical solution; for example, to obtain an accurate solution using the finite difference time domain method, a minimum of ten cells per wavelength of the largest frequency of interest is required [8]. In addition, the shape of the computational cells may also significantly affect the accuracy of the numerical solution. A conformal grid ensures the accurate representation of curved surfaces and the proper enforcement of BCs [26]; it also avoids a stair-stepping representation of a curved surface by rectangular cells. It has been shown that when representing curved surfaces, a coarse but conformal grid yields more accurate results than does a finer mesh that stair-steps a curved surface [37]. A more accurate modelling of curved surfaces and the enforcement of BCs are the primary purposes of using algorithms that are based on curvilinear coordinate systems. The characteristics and some of the advantages of these schemes are explored in subsequent chapters.

Unlike truncation and modelling errors, ***round-off errors*** appear at the computation stage where, due to limited computational resources, finite precision arithmetic is performed. These errors can be reduced (at the expense of memory and computation speed) by using higher order precision for the storage of (and the arithmetic operation on) a variable. For example, a single precision (32 bit) float number that can accurately represent nine significant figures can be replaced by a double-precision (64 bit) float number that can support operations with up to 17 significant figures of accuracy [36]. Round-off errors are often of little concern since in most applications, truncation and modelling errors are significantly larger than are round-off errors.

2.3 A Review of Differential Equation-Based Numerical Techniques

Although time discretisation is typically achieved via the finite difference method, either the finite difference, finite element, or finite volume method may be used to estimate the spatial derivatives of a system of PDEs. A brief review of these methods follows.

2.3.1 The Finite Difference Method

In the past few decades, the Finite Difference Method (FDM) has become one of the most preferred methods of solving PDEs. It owes its popularity to its simplicity as well as to its generic format. Although one of the earliest applications of this method dates back to Euler in 1768 [22], it was formally developed by A. Thom in 1920 [38]. As in the case of the discretisation process, the FDM subdivides the solution domain into a domain consisting of discrete mesh points both in space and time. Then, using the properties of the Taylor series expansion around a given point, the FDM approximates a differential operator by an algebraic expression. The details of this process, some of its properties, and some of the issues that arise from the application of the Taylor series expansion are discussed in **Appendix A**. Suffice it to say that this simple idea has given rise to many popular CEM methods; two of these methods are considered next.

2.3.1.1 The Finite-Difference Time-Domain Method

Yee's version of the finite difference method is simply known as the Finite-Difference Time-Domain (FDTD) method [5] in CEM and is arguably the simplest and the most popular time domain method of solving Maxwell's curl equations. Although numerous features (and enhancements) have been added to its formulation since its conception in 1966, surprisingly, the originally proposed time and space discretisation has endured over

the years. The original FDTD algorithm discretises the governing equations via a centre difference approximation that is second order accurate in both space and time [42]. The FDTD scheme is mapped on a staggered grid system, where in most formulations, the electric field components are placed on the grid lines, while the magnetic field components are located on the "half cell" points* [43] (see **Figure 2.3**). The electric (E) and magnetic (H) field components throughout the computation domain are updated (computed) in space and time via fully explicit expressions [44].

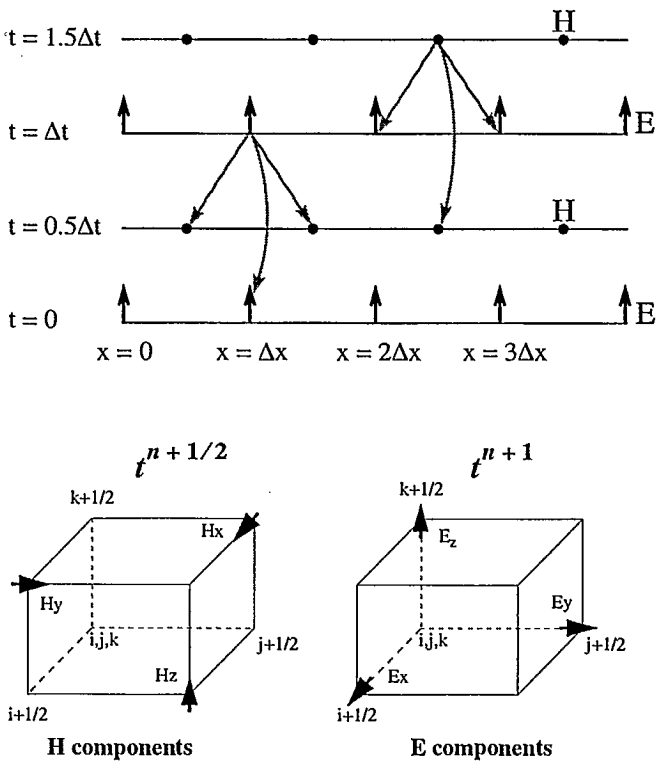

Figure 2.3. Yee's staggered grid and updating scheme for a 1D electromagnetic field (Top) and its corresponding 3D computational molecules (Bottom) [45]

---

* In most physical problems, objects (such as good conductors) are defined in terms of their electrical boundary conditions; placing the electric field components on the grid lines will allow the boundary conditions to be readily identified and imposed.

The details of the formulation of the FDTD method and its applications are beyond the scope of this section. The reader is encouraged to consult references [42, 44-46] for a comprehensive review of the formulation, implementation, and numerous applications of the FDTD method. However, it is important to note some of the properties, advantages, and disadvantages of the FDTD method as they relate to the thesis topic.

One of the most noted advantages of the FDTD technique is the simplicity and elegance in which it models and solves Maxwell's equations using minimal computational resources (as compared to other numerical methods solving a similar class of problems). However, the main disadvantage of FDTD is its reliance on orthogonal grids. Traditionally, FDTD has approximated curved surfaces and geometrically complex objects using stair-stepped rectangular meshes, which, in the majority of cases, degrade the accuracy of the results [8, 42, 46]. One of the first attempts at formulating the FDTD method for generalized Nonorthogonal coordinates (N-FDTD) was made by Holland in 1983 [47]. Others followed his work by proposing to model curved surfaces either through globally deformed meshes [48, 49] or through locally deformed grids (Contour-Path FDTD, CP-FDTD) [50, 51]. Another class of proposed methods is the Discrete Surface Integral method (DSI-FDTD) which utilizes a fully conformal but unstructured grid [52, 53]. With the possible exception of the DSI-FDTD, most of the aforementioned conformal FDTD methods, in addition to being computationally inefficient, require extensive preprocessing of the mesh [53], and often have restrictions placed on the type of material they are capable of modelling (either dielectrics or perfectly conducting surfaces, but not both) [54].

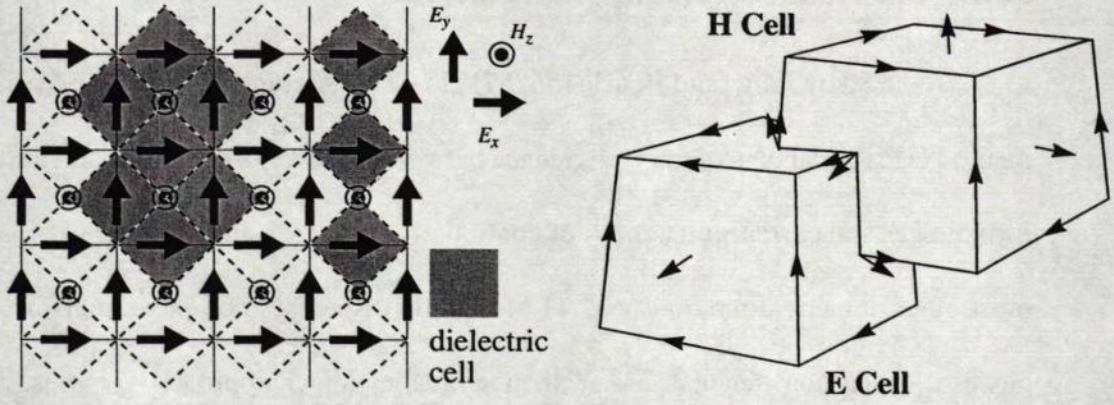

Figure 2.4. Object definition and location of field components in Yee's FDTD grid (Left) and computational cells in an irregular dual lattice (Right) [53]

As in Yee's original FDTD grid, all of the aforementioned schemes are based on staggered grids of E and H fields in space and time. This indicates that all of the field components are located on the edges of the computational cell, and thus, the exact location of the boundaries of modelled objects are "fuzzy" at best! **Figure 2.4** depicts the location of the material boundaries in both standard and conformal FDTD methods where permeability and permittivity cells are interlaced [44]. In general, objects are defined in terms of the location of their tangential E field components; therefore, only Perfect Electric Conductors (PECs) are accurately modelled.* All other material boundaries are diamond (saw-tooth) shaped, and for any given cell, the object's properties (such as permeability, permittivity, and conductivity) are computed as a weighted average (in the best case scenario) [46]. It appears that a more stringent method of defining material boundaries could be achieved through the use of a single grid that collects all E and H field components at the centre of the computational cell.

---

* This is not exactly correct! Since all field components are staggered, an unequal number of E and H field components fall within the PEC object.

2.3.1.2 The Transmission-Line Matrix Method

Introduced by Johns and Beurle [56, 57] in 1971, the Transmission-Line Matrix (TLM) method takes advantage of the equivalence between Maxwell's equations and the equations for voltages and currents on a mesh of continuous two-wire transmission lines [55]. Unlike most other numerical methods, the TLM method discretises computational space using a physical discretion scheme rather than a mathematical approach. That is, the TLM technique models field equations often using an orthogonal grid of transmission lines with possibly some lumped elements [58]. The E and H fields are represented in terms of voltage pulses where the TLM algorithm simulates the propagation of these fields in terms of the evolution of voltage pulses along the aforementioned network of transmission lines in all directions [59]. The boundary conditions at the computational cells' interfaces are represented in terms of scattering and transfer events of voltage pulses at all transmission line boundaries [58]. The voltage variables are computed via a second order accurate (in both space and time) explicit algorithm. Finally, the solution to the original field problem is obtained by a mapping from the voltage variables to the field components. The details of this process and the theory of the TLM method and its various formulations have been extensively studied; some excellent references on this topic include [55-60].

It has been shown that TLM models of EM field problems are equivalent to FDMs [61]. In particular, Johns was successful in deriving Yee's original FDTD field update equations using a TLM model [62], while other efforts have been made to derive TLM formulations from time-domain finite-element algorithms [63]. Similar to Yee's original formulation, the standard TLM method utilizes orthogonal meshes in the space discretisation which forces the modelling of curved surfaces via stair-stepping [60]. Recently, there has been

some progress in the area of conformal TLM formulation; several researchers have taken advantage of the latest advances of nonorthogonal FDTD algorithms to derive similar TLM models [64], while others have derived TLM algorithms on conformal arbitrary grids using a finite element template [63]. However, the research in this field is ongoing and appears to be lagging behind similar work in the area of conformal FDTD.

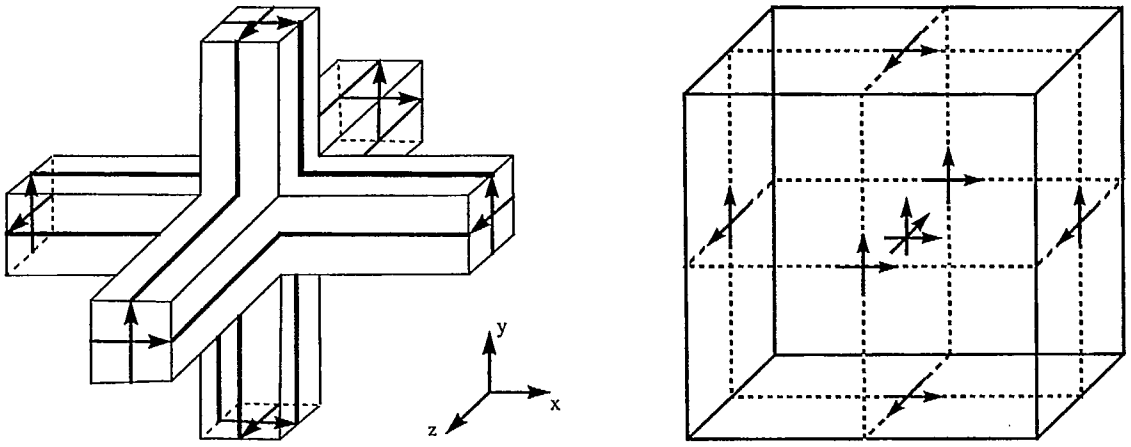

Figure 2.5. Schematic of SCN-TLM [58] (Left) and its corresponding 3D computational molecule [65] (Right)

Among the various formulations of TLM models, one of the most popular techniques for spatial discretisation is the Symmetrical Condensed Node TLM (SCN-TLM)* model [60] (see **Figure 2.5**). The clear advantage of using an SCN-TLM discretisation over Yee's version of FDTD is that (in SCN-TLM method) all of the E and H field components are located at the same point in space (at the centre of the cell), and all are solved in the same physical time [65].† Another positive consequence of utilizing an SCN-TLM model is the clear location of boundary conditions. Unlike Yee's FDTD model, in SCN-TLM models,

* It must be noted that unlike the traditional TLM algorithms, the newer TLM models, such as SCN-TLM, do not have a direct analogue with a physically-realizable circuit. The circuit analogy is a convenient manner of understanding TLM models but is not sufficient for the development of new schemes.

† Recall that FDTD uses a staggered grid in space and time.

all field components are placed at the centre of the computational cells, while the boundaries of these cells are located along their interfaces at known locations [59]. Since only tangential field components exist at cell boundaries, the continuity of these components can be enforced effortlessly, thus defining clear boundaries for objects with different properties [60].

2.3.2 The Time-Domain Finite-Element Method

As mentioned in previous sections, the main disadvantage of the standard FDTD and TLM methods is their reliance on orthogonal grids for spatial discretisation. Therefore, it is natural to look beyond the conventional methods of discretisation and consider other alternatives. One such alternative is to discretise the problem space using elements (or sub-domains), hence the term Finite-Element Method (FEM) [4]. In contrast to finite difference schemes where the fields are represented in terms of discrete functions at each mesh point, FEMs model fields within each element using an interpolating polynomial of the respective field values at the element's nodes [60]. This general formulation allows the use of arbitrary conformal elements (of various shapes, sizes, configurations, and order of approximation) which are required to accurately model complex geometries and spatially varying resolutions [66]. The details of various FEMs and their formulations are clearly beyond the scope of this brief review; references [4, 66] provide additional information for interested readers.

Traditionally, FEMs have been formulated in the frequency domain, where a matrix inversion is required for each frequency point of the solution [66]. Although a frequency domain formulation of FEMs is convenient, it is not necessary. Both Lynch and Paulsen

[67] and Gedney and Navsariwala [68] have shown that Time-Domain FEM (TD-FEM) can be derived to solve a vector wave form of Maxwell's equations using either explicit (in case of the former) or implicit (in case of the latter) algorithms. There have been many adaptations of the TD-FEM, in order to take advantage of the conformal grids utilized in FEMs. While some, such as the point-matched TD-FEM, use a fully unstructured conformal mesh [69], others have derived a hybrid FDTD-TD-FEM engine [70]. The latter was developed in order to reduce the computational load in the areas of the problem space where a uniform orthogonal (FDTD) grid is sufficient [70]. The hybrid methods often exhibit late time instability [71]; they are also very sensitive to the type of mesh used to provide a transition between FDTD and TD-FEM regions [72]. Research in both areas is ongoing. The main focus of research involving Point-Matched TD-FEM (PM-TD-FEM) is the formulation of ABCs and material boundary conditions [73-75] (Ironically, the use of dual irregular lattices seems to have eliminated some of the advantages of using an FEM formulation.). Despite the clear advantages of using TD-FEM, due to their complex formulation and the significant effort required for mesh preparation (as compared to the FDTD and TLM methods), these methods have received little attention and are thus lacking in maturity and diversity of applications.

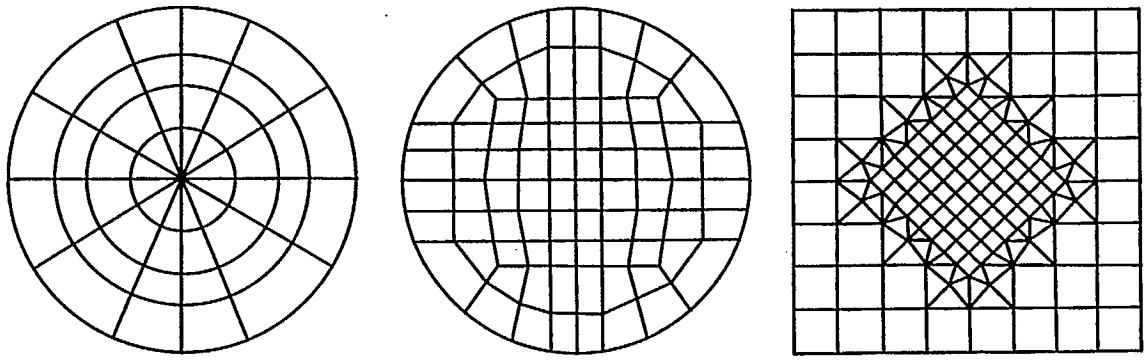

Figure 2.6. Various conformal mesh configurations: (Left) structured mesh (Centre) unstructured mesh [18] (Right) and hybrid mesh [71]

2.3.3 The Finite-Volume Time-Domain Method

The Finite-Volume Time-Domain (FVTD) method* was originally developed by the Computational Fluid Dynamics (CFD) community. In this method, the governing PDEs (*i.e.* Maxwell's curl equations) are cast in conservative form [18]. All E and H field components are collected at the centre of the computational cell, while the tangential field components are projected on the respective cell walls [35]. A "jump" condition is used to enforce the continuity of tangential field components at cell interfaces [17]. Finally, a Lax-Wendroff windward explicit scheme is used to solve field values at cell centres [19]. The FVTD method is often formulated using a local curvilinear coordinate system that allows for conformal meshing. Due to the aforementioned properties, the FVTD method was selected as the method of choice for investigating EM problems containing complex geometries. The remainder of this thesis will focus on the formulation, enhancements, and several applications of the FVTD technique.

2.4 Summary and Conclusions

This chapter attempted to define and specify the scope of the CEM problems that will be considered in this thesis; that is, Maxwell's curl equations (a set of hyperbolic PDEs which form the field propagator) are solved in the time domain using the method of characteristics. The solution to this problem is provided via numerical methods. The theory of differential equations based on numerical techniques, as well as some fundamental concepts, such as discretisation, convergence, and sources of errors were also

* It must be noted that a conformal version of the FDTD method, based on the integral form of Maxwell's equations and the volume integral of a DSI-FDTD type dual lattice, is also referred to as an FVTD method [49]. These two methods are fundamentally different and must not be confused with each other.

briefly reviewed. A review of some of the more popular differential equation-based numerical methods, such as various types of FDTD, TLM, TD-FEM, and FVTD, was completed where each technique was evaluated for its ability to model complex and curved geometries. A summary of this survey is given in **Table 2.1**. It was concluded that currently, both TD-FEM and FVTD methods are the most promising methods; however, (as will be explained in future chapters) the maturity of research involving the FVTD method was the deciding factor in selecting FVTD as the method for solving the type of EM problems that are considered in this thesis.

Table 2.1. Classification of various differential equation-based numerical methods

Algorithm	Mesh Type[a]	Grid Type[b]	Object Boundaries[c]	
Yee's FDTD	orthogonal	staggered	stair-stepped	fuzzy
N-FDTD	semi-conformal	staggered	exact	averaged
CP-FDTD	semi-conformal	staggered	exact	averaged
DSI-FDTD	conformal	staggered	exact	averaged
Standard TLM	orthogonal	staggered	stair-stepped	fuzzy
SCN-TLM	orthogonal	centred	stair-stepped	exact
Conformal SCN-TLM	semi-conformal	centred	exact	averaged
Lynch's TD-FEM	conformal	centred	exact	exact
Gedney's TD-FEM	conformal	centred	exact	exact
PM-TD-FEM	conformal	staggered	exact	averaged
Hybrid TD-FEM	semi-conformal	staggered	exact	averaged
FVTD	conformal	centred	exact	exact

a. Defines the general shape of computational cells; *orthogonal* (cuboid), *semi-conformal* (mostly cuboid with some irregular shaped cells), and *conformal* (all irregular shaped cells).

b. Indicates the type of mesh with respect to the location of the electric and magnetic field components.

c. Indicates both the type of approximation of the physical boundary (*stair-stepped* or *exact*) and the quality of the method of enforcing tangential components on cell interfaces; *fuzzy* (very poor enforcement), *averaged* (weak enforcement or averaging of neighbouring cell properties), and *exact* enforcement of the boundaries.

Chapter 3

Formulation and Solution of Governing Equations

The initial formulation of an EM field problem often affects the efficiency of the solution method and can further affect the accuracy of the obtained solution. In the FVTD method, the conservative form of Maxwell's equations is formulated in a general (curvilinear) coordinate system. The equations are then often solved on a conformal grid using the method of characteristics. This chapter aims to explain this process.

3.1 Basic Formulation of Governing Equations

3.1.1 Conservative Form of PDEs

If $Q(x, t)$ represents the density of a substance, and its flux is denoted by $F(Q)$, then the conservation law states that the time rate of change of the total amount of the substance contained in a fixed domain, G, is equal to the flux of that substance across the boundary of G (assuming that F has continuous first partial derivatives within G) [29]; that is,

$$\frac{d}{dt}\int_G Q(x,t)dx = -\int_{\partial G} F(Q)\cdot \boldsymbol{n}\, dS, \tag{3.1}$$

where $\boldsymbol{n}$ and dS are the outward normal* to G and the surface element of the boundary, ∂G, respectively. Following the application of the divergence theorem, then evaluating the resultant volume integral, and after some mathematical manipulations (assuming that $G \to 0$), the conservation law is given in differential form as:

$$\frac{\partial Q}{\partial t} + \frac{\partial F(Q)}{\partial x} = 0. \tag{3.2}$$

In most practical applications, the above formulation is quasi-linear in nature and will take the form of (2.1). This form is required for the FVTD formulation (and the solution) of Maxwell's governing equations.

3.1.2 The Generalised-Vector Form of Maxwell's Equations

Consider the differential form of Maxwell's equations:

$$\nabla\times\mathcal{E} = -\frac{\partial \boldsymbol{B}}{\partial t}, \tag{3.3}$$

$$\nabla\times\mathcal{H} = \frac{\partial \boldsymbol{D}}{\partial t} + \boldsymbol{J}, \tag{3.4}$$

$$\nabla\cdot\boldsymbol{D} = \rho, \tag{3.5}$$

$$\nabla\cdot\boldsymbol{B} = 0, \tag{3.6}$$

and the constitutive relations given by:

$$\boldsymbol{B} = \mu\mathcal{H}, \tag{3.7}$$

$$\boldsymbol{D} = \varepsilon\mathcal{E}, \tag{3.8}$$

$$\boldsymbol{J} = \sigma\mathcal{E}, \tag{3.9}$$

where $\mathcal{E}$ is the electric field intensity in V/m, $\boldsymbol{D}$ is the electric flux density in C/m^2,

* The right-hand-side of (3.1) measures flux outflow, hence the negative sign.

$\mathcal{H}$ is the magnetic field intensity in A/m, $\boldsymbol{B}$ is the magnetic flux density in Wb/m^2, $\boldsymbol{J}$ is the electric current density in A/m^2, and ρ is the electric charge density in C/m^3 [15].* Also, the constitutive parameters of the medium are: μ, the permeability (H/m), ε, the permittivity (F/m), and σ, the conductivity $(1/\Omega m)$. In general, some assumptions are required to simplify the discussions surrounding the solution of Maxwell's equations in a given solution space. In this thesis, the solution space is assumed to be *isotropic* (the material's properties are independent of direction) and *linear* ($\boldsymbol{D}$ is a linear function of $\mathcal{E}$).

Following the substitution of the constitutive relations (3.7) to (3.9) in (3.3) and (3.4) (and after some algebraic manipulations where the field components are rearranged in terms of the differential variables), Maxwell's equations are written using generalised vectors in a Cartesian frame as:

$$\frac{\partial \overline{\boldsymbol{Q}}}{\partial t} + \frac{\partial \overline{\boldsymbol{E}}}{\partial x} + \frac{\partial \overline{\boldsymbol{F}}}{\partial y} + \frac{\partial \overline{\boldsymbol{G}}}{\partial z} = \overline{\boldsymbol{S}}, \tag{3.10}$$

where the solution vector, $\overline{\boldsymbol{Q}}$, flux vectors, $\overline{\boldsymbol{E}}$, $\overline{\boldsymbol{F}}$, $\overline{\boldsymbol{G}}$, and the source term, $\overline{\boldsymbol{S}}$, are given by:

$$\overline{\boldsymbol{Q}} = \begin{bmatrix} B_x \\ B_y \\ B_z \\ D_x \\ D_y \\ D_z \end{bmatrix}, \overline{\boldsymbol{E}} = \begin{bmatrix} 0 \\ -D_z/\varepsilon \\ D_y/\varepsilon \\ 0 \\ B_z/\mu \\ -B_y/\mu \end{bmatrix}, \overline{\boldsymbol{F}} = \begin{bmatrix} D_z/\varepsilon \\ 0 \\ -D_x/\varepsilon \\ -B_z/\mu \\ 0 \\ B_x/\mu \end{bmatrix}, \overline{\boldsymbol{G}} = \begin{bmatrix} -D_y/\varepsilon \\ D_x/\varepsilon \\ 0 \\ B_y/\mu \\ -B_x/\mu \\ 0 \end{bmatrix}, \overline{\boldsymbol{S}} = \begin{bmatrix} 0 \\ 0 \\ 0 \\ -\sigma D_x/\varepsilon \\ -\sigma D_y/\varepsilon \\ -\sigma D_z/\varepsilon \end{bmatrix}. \tag{3.11}$$

Upon closer examination of the above expressions, and after comparing them with ***Faraday's induction law***, (3.3), and the generalised ***Ampere's circuit law,*** (3.4), the conservative form of Maxwell's equations can be formulated in terms of vector products

* Note that *coulomb*, $C = As$ and *weber*, $Wb = Vs$.

of electric and magnetic fields; that is,

$$\begin{pmatrix} \boldsymbol{B} \\ \boldsymbol{D} \end{pmatrix}_t + \begin{pmatrix} \boldsymbol{a}_x \times \mathcal{E} \\ -\boldsymbol{a}_x \times \mathcal{H} \end{pmatrix}_x + \begin{pmatrix} \boldsymbol{a}_y \times \mathcal{E} \\ -\boldsymbol{a}_y \times \mathcal{H} \end{pmatrix}_y + \begin{pmatrix} \boldsymbol{a}_z \times \mathcal{E} \\ -\boldsymbol{a}_z \times \mathcal{H} \end{pmatrix}_z = \begin{pmatrix} 0 \\ -\sigma \mathcal{E} \end{pmatrix}, \tag{3.12}$$

where subscripts denote partial derivatives of the argument with respect to the subscript's variable, and $\boldsymbol{a}_x$, $\boldsymbol{a}_y$, $\boldsymbol{a}_z$ are unit vectors* of the Cartesian coordinate system. This indicates that the flux vectors, $\overline{\boldsymbol{E}}$, $\overline{\boldsymbol{F}}$, and $\overline{\boldsymbol{G}}$, contain electric and magnetic field components that are tangential to the respective constant x-, y-, or z- surfaces [16]. These flux vectors are an integral part of most FVTD algorithms since they are often used to represent physical phenomena (such as dielectric objects in the computation space or conducting objects' boundary conditions) through the enforcement of the appropriate boundary conditions of tangential components at a given surface.

In conclusion, a brief clarification of the terminology used thus far seems in order; the above formulation of the governing equations, (3.10), is frequently (but erroneously) referred to as the conservative form of Maxwell's equations [16, 26]. However, with the exception of the electric charge-current density conservation law,

$$\frac{\partial \rho}{\partial t} + \nabla \cdot \boldsymbol{J} = 0, \tag{3.13}$$

Maxwell's equations do not describe explicitly a conservative law [76]. Thus, a strong conservative formulation of the governing equations is not essential. The only real benefit of a conservative type of formulation is its convenient and manageable format that represents all field components as either vectors or flux vectors. Consequently, it is more appropriate to refer to equation (3.10) as the ***generalised vector form*** of Maxwell's equations [77].

---

* Note that in the Cartesian coordinate system, unitary and unit vectors are identical.

3.2 Maxwell's Equations in General Coordinate Systems

Traditionally, the curved surfaces of geometrically complex objects are represented (approximated) by an orthogonal grid of stair-stepped lines that often degrade the accuracy of the results. This has prompted many researchers to use methods that are capable of utilizing a body-fitted coordinate representation of geometrically complex objects, thereby increasing the accuracy of the representation of curved surfaces, as well as reducing the ambiguity of the location of material boundaries often encountered in simulations using non-conformal grids [25]. The main motivation for the research and development of the FVTD method is its versatility for modelling complex geometries via conformal (body-fitted) grids. Thus, it is important to review the theory of coordinate systems and explore some of the issues that are associated with it.

3.2.1 Conformal Grids: Background

Following the review of FDMs in **Chapter 2**, it is evident that they were originally designed for (and work best on) uniform orthogonal grids. Although it is possible to design (derive) schemes that are not restricted to uniform orthogonal meshes (such as N-FDTD, CP-FDTD, TD-FEM, *etc.*), the additional complexity of the formulation of such algorithms often compels CEM code developers to make certain assumptions that may erode the generality of applications, the accuracy of results, or both (see **Section 2.3.1**). A better alternative is presented by the CFD community via the use of localized coordinate systems. In this method, the problem space is meshed using a non-uniform conformal (often non-orthogonal) grid, called a ***physical space***, where the coordinate of each mesh point is specified by its Cartesian coordinates, (x, y, z). The physical mesh and the corresponding

governing equations are then ***transformed*** into a uniform rectangular grid, (ξ, η, ζ), generally referred to as the ***computational space*** [23], where the system of discretised PDEs is formulated and solved via a finite volume algorithm. Finally, the obtained solution in the computational space is transformed back into its corresponding locations and values in the physical space (see **Figure 3.1**).

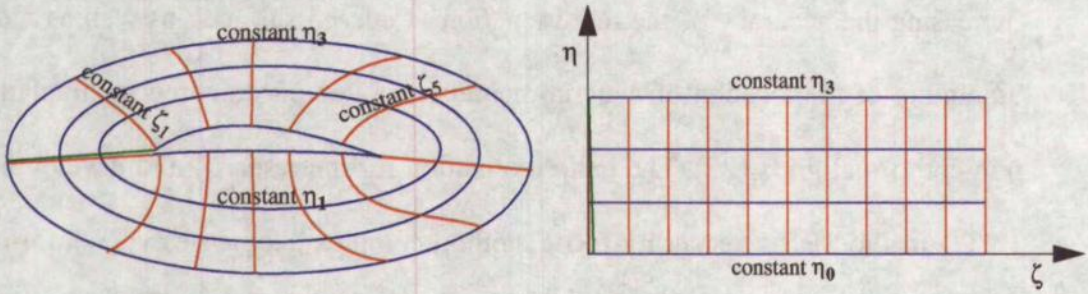

(a) Physical Space **(b) Computational Space**

Figure 3.1. Conformal coordinate systems and the FVTD method [25]

There are several advantages to using body-fitted grids. The most obvious is the proper representation of the physical space and accurately enforcing and satisfying the (objects') boundary conditions [78]. Other advantages, to name a few, include: facilitating the formulation of governing equations that are better suited for windward characteristic-based algorithms (which have a more favourable stability property than do central differences schemes) and facilitating the application of simpler and more effective ABCs [79]. The advantages of using a general coordinate system formulation of the governing equations will be discussed in due course.

3.2.2 Theory of Coordinate Transformation

The theory of coordinate transformation is studied in a branch of mathematics known as ***differential geometry*** that uses differential and integral calculus to study geometric

properties of point sets (*i.e.* curves, surfaces, *etc.*) [80]. Although the present discussion requires only a basic knowledge of the general theory of coordinate systems, an overview of this theory is given in **Appendix B** in the interest of completeness. However, since it is necessary to develop a method of transforming Maxwell's equations in any type of physical grid into ones with a computational grid, the following is a summary of the coordinate transformation method as discussed in [23].

A ***general* (*curvilinear*) *coordinate system***, defined in **Appendix B**, is denoted by:

$$\begin{aligned} \xi &= \xi(x, y, z, t), \\ \eta &= \eta(x, y, z, t), \\ \zeta &= \zeta(x, y, z, t), \\ \tau &= \tau(t), \end{aligned} \tag{3.14}$$

where x, y, and z represent the Cartesian coordinate system. Based on the chain rule of partial differentiation and the results of (B.39), the following linear relations between the differentials of the rectangular coordinate system and the differentials of the general coordinates are given as:

$$\begin{aligned} d\xi &= \frac{\partial \xi}{\partial x}dx + \frac{\partial \xi}{\partial y}dy + \frac{\partial \xi}{\partial z}dz \\ d\eta &= \frac{\partial \eta}{\partial x}dx + \frac{\partial \eta}{\partial y}dy + \frac{\partial \eta}{\partial z}dz \\ d\zeta &= \frac{\partial \zeta}{\partial x}dx + \frac{\partial \zeta}{\partial y}dy + \frac{\partial \zeta}{\partial z}dz \end{aligned} \tag{3.15}$$

where partial derivatives $\frac{\partial \xi}{\partial x}, \frac{\partial \xi}{\partial y}, \frac{\partial \xi}{\partial z}, \frac{\partial \eta}{\partial x}, \frac{\partial \eta}{\partial y}, \frac{\partial \eta}{\partial z}, \frac{\partial \zeta}{\partial x}, \frac{\partial \zeta}{\partial y}$, and $\frac{\partial \zeta}{\partial z}$, are denoted by ξ_x, ξ_y, ξ_z, η_x, η_y, η_z, ζ_x, ζ_y, and ζ_z respectively. Thus (3.15) is written in matrix form as:

* In this document, $\tau = t$. Although this appears to be trivial, it should be included in the transformation process to preserve the generality of the derivations. However, in the current discussion, it does not affect the final expressions and may be dropped in the interest of simplicity.

$$\begin{bmatrix} d\xi \\ d\eta \\ d\zeta \end{bmatrix} = \begin{bmatrix} \xi_x & \xi_y & \xi_z \\ \eta_x & \eta_y & \eta_z \\ \zeta_x & \zeta_y & \zeta_z \end{bmatrix} \begin{bmatrix} dx \\ dy \\ dz \end{bmatrix}. \tag{3.16}$$

Similarly, the following is also true:

$$\begin{bmatrix} dx \\ dy \\ dz \end{bmatrix} = \begin{bmatrix} x_\xi & x_\eta & x_\zeta \\ y_\xi & y_\eta & y_\zeta \\ z_\xi & z_\eta & z_\zeta \end{bmatrix} \begin{bmatrix} d\xi \\ d\eta \\ d\zeta \end{bmatrix}. \tag{3.17}$$

Further examination of (3.16) and (3.17) results in:

$$\begin{bmatrix} \xi_x & \xi_y & \xi_z \\ \eta_x & \eta_y & \eta_z \\ \zeta_x & \zeta_y & \zeta_z \end{bmatrix} = \begin{bmatrix} x_\xi & x_\eta & x_\zeta \\ y_\xi & y_\eta & y_\zeta \\ z_\xi & z_\eta & z_\zeta \end{bmatrix}^{-1}. \tag{3.18}$$

A simple matrix inversion operation is performed on the right hand side of (3.18). Thus, the mathematical expressions of the partial derivatives of the general coordinate system are obtained.

$$\begin{aligned} \xi_x &= J(y_\eta z_\zeta - y_\zeta z_\eta) \\ \xi_y &= J(x_\zeta z_\eta - x_\eta z_\zeta) \\ \xi_z &= J(x_\eta y_\zeta - x_\zeta y_\eta) \\ \eta_x &= J(y_\zeta z_\xi - y_\xi z_\zeta) \\ \eta_y &= J(x_\xi z_\zeta - x_\zeta z_\xi) \\ \eta_z &= J(x_\zeta y_\xi - x_\xi y_\zeta) \\ \zeta_x &= J(y_\xi z_\eta - y_\eta z_\xi) \\ \zeta_y &= J(x_\eta z_\xi - x_\xi z_\eta) \\ \zeta_z &= J(x_\xi y_\eta - x_\eta y_\xi) \end{aligned} \tag{3.19}$$

where the Jacobian of transformation, J, is defined by:

$$J = \frac{\partial(\xi, \eta, \zeta)}{\partial(x, y, z)} = \begin{vmatrix} \xi_x & \xi_y & \xi_z \\ \eta_x & \eta_y & \eta_z \\ \zeta_x & \zeta_y & \zeta_z \end{vmatrix} = 1 \Big/ \left(\begin{vmatrix} x_\xi & x_\eta & x_\zeta \\ y_\xi & y_\eta & y_\zeta \\ z_\xi & z_\eta & z_\zeta \end{vmatrix} \right), \tag{3.20}$$

Next, the generalised vector form of a set of PDEs is considered,

$$\bar{Q}_t + \bar{E}_x + \bar{F}_y + \bar{G}_z = \bar{S} \tag{3.21}$$

where $\bar{E}$, $\bar{F}$, and $\bar{G}$ are flux vectors, $\bar{S}$ is the source term, and $\bar{Q}$ is the solution vector. The spatial derivatives of the above vector equation are evaluated by the chain rule as:

$$\begin{aligned} \frac{\partial}{\partial x} &= \frac{\partial \xi}{\partial x}\frac{\partial}{\partial \xi} + \frac{\partial \eta}{\partial x}\frac{\partial}{\partial \eta} + \frac{\partial \zeta}{\partial x}\frac{\partial}{\partial \zeta} = \xi_x \frac{\partial}{\partial \xi} + \eta_x \frac{\partial}{\partial \eta} + \zeta_x \frac{\partial}{\partial \zeta}, \\ \frac{\partial}{\partial y} &= \frac{\partial \xi}{\partial y}\frac{\partial}{\partial \xi} + \frac{\partial \eta}{\partial y}\frac{\partial}{\partial \eta} + \frac{\partial \zeta}{\partial y}\frac{\partial}{\partial \zeta} = \xi_y \frac{\partial}{\partial \xi} + \eta_y \frac{\partial}{\partial \eta} + \zeta_y \frac{\partial}{\partial \zeta}, \\ \frac{\partial}{\partial z} &= \frac{\partial \xi}{\partial z}\frac{\partial}{\partial \xi} + \frac{\partial \eta}{\partial z}\frac{\partial}{\partial \eta} + \frac{\partial \zeta}{\partial z}\frac{\partial}{\partial \zeta} = \xi_z \frac{\partial}{\partial \xi} + \eta_z \frac{\partial}{\partial \eta} + \zeta_z \frac{\partial}{\partial \zeta}, \end{aligned} \tag{3.22}$$

and is substituted in (3.21); that is:

$$\bar{Q}_t + \xi_x \bar{E}_\xi + \eta_x \bar{E}_\eta + \zeta_x \bar{E}_\zeta + \xi_y \bar{F}_\xi + \eta_y \bar{F}_\eta + \zeta_y \bar{F}_\zeta + \xi_z \bar{G}_\xi + \eta_z \bar{G}_\eta + \zeta_z \bar{G}_\zeta = \bar{S}. \tag{3.23}$$

After dividing both sides of the above equation by the Jacobian of the transformation, it is reformulated in vector form.*

$$\begin{aligned} &\left(\frac{\bar{Q}}{J}\right)_t + \left(\frac{\xi_x \bar{E} + \xi_y \bar{F} + \xi_z \bar{G}}{J}\right)_\xi + \left(\frac{\eta_x \bar{E} + \eta_y \bar{F} + \eta_z \bar{G}}{J}\right)_\eta + \left(\frac{\zeta_x \bar{E} + \zeta_y \bar{F} + \zeta_z \bar{G}}{J}\right)_\zeta \\ &\quad - \bar{E}\left\{\left(\frac{\xi_x}{J}\right)_\xi + \left(\frac{\eta_x}{J}\right)_\eta + \left(\frac{\zeta_x}{J}\right)_\zeta\right\} - \bar{F}\left\{\left(\frac{\xi_y}{J}\right)_\xi + \left(\frac{\eta_y}{J}\right)_\eta + \left(\frac{\zeta_y}{J}\right)_\zeta\right\} \\ &\quad - \bar{G}\left\{\left(\frac{\xi_z}{J}\right)_\xi + \left(\frac{\eta_z}{J}\right)_\eta + \left(\frac{\zeta_z}{J}\right)_\zeta\right\} = \left(\frac{\bar{S}}{J}\right) \end{aligned} \tag{3.24}$$

The last three bracketed terms of the above equation vanish following the substitution of the expressions derived in (3.19). Therefore, the vector form of (3.21) on Cartesian

* Recall that $u\frac{dv}{dx} = \frac{d}{dx}(uv) - v\frac{du}{dx}$.

coordinates is transformed into one cast on a general coordinate system; it is written as:

$$Q_t + E_\xi + F_\eta + G_\zeta = S \tag{3.25}$$

where

$$Q = \frac{\overline{Q}}{J} \tag{3.26}$$

$$E = \frac{1}{J}(\xi_x \overline{E} + \xi_y \overline{F} + \xi_z \overline{G}) \tag{3.27}$$

$$F = \frac{1}{J}(\eta_x \overline{E} + \eta_y \overline{F} + \eta_z \overline{G}) \tag{3.28}$$

$$G = \frac{1}{J}(\zeta_x \overline{E} + \zeta_y \overline{F} + \zeta_z \overline{G}) \tag{3.29}$$

$$S = \frac{\overline{S}}{J} \tag{3.30}$$

It must be noted that the above flux and field vectors are not transformed in the traditional sense; rather, they are formulated (and calculated) in terms of vector fields in the Cartesian coordinate system. However, if one desires to obtain field components in the transformed coordinate system in terms of their counter-parts in Cartesian coordinates, **Section B.4** of **Appendix B** derives such a procedure.

3.2.3 Transformed Maxwell's Equations

The vector form of Maxwell's equations is transformed into a curvilinear coordinate system via (3.25); that is:

$$Q_t + E_\xi + F_\eta + G_\zeta = S \tag{3.31}$$

where the solution vector and the source term are given by:

$$Q = \frac{\bar{Q}}{J} = \frac{1}{J}\left[B_x\ B_y\ B_z\ D_x\ D_y\ D_z\right]^T,\ S = \frac{\bar{S}}{J} = \frac{1}{J}\left[0\ 0\ 0\ -\sigma\frac{D_x}{\varepsilon}\ -\sigma\frac{D_y}{\varepsilon}\ -\sigma\frac{D_z}{\varepsilon}\right]^T, \quad (3.32)$$

respectively, and the flux vectors are written as:

$$E = \frac{1}{J}\begin{bmatrix} \frac{D_z}{\varepsilon}\xi_y - \frac{D_y}{\varepsilon}\xi_z \\ \frac{D_x}{\varepsilon}\xi_z - \frac{D_z}{\varepsilon}\xi_x \\ \frac{D_y}{\varepsilon}\xi_x - \frac{D_x}{\varepsilon}\xi_y \\ \frac{B_y}{\mu}\xi_z - \frac{B_z}{\mu}\xi_y \\ \frac{B_z}{\mu}\xi_x - \frac{B_x}{\mu}\xi_z \\ \frac{B_x}{\mu}\xi_y - \frac{B_y}{\mu}\xi_x \end{bmatrix}, \quad F = \frac{1}{J}\begin{bmatrix} \frac{D_z}{\varepsilon}\eta_y - \frac{D_y}{\varepsilon}\eta_z \\ \frac{D_x}{\varepsilon}\eta_z - \frac{D_z}{\varepsilon}\eta_x \\ \frac{D_y}{\varepsilon}\eta_x - \frac{D_x}{\varepsilon}\eta_y \\ \frac{B_y}{\mu}\eta_z - \frac{B_z}{\mu}\eta_y \\ \frac{B_z}{\mu}\eta_x - \frac{B_x}{\mu}\eta_z \\ \frac{B_x}{\mu}\eta_y - \frac{B_y}{\mu}\eta_x \end{bmatrix}, \quad G = \frac{1}{J}\begin{bmatrix} \frac{D_z}{\varepsilon}\zeta_y - \frac{D_y}{\varepsilon}\zeta_z \\ \frac{D_x}{\varepsilon}\zeta_z - \frac{D_z}{\varepsilon}\zeta_x \\ \frac{D_y}{\varepsilon}\zeta_x - \frac{D_x}{\varepsilon}\zeta_y \\ \frac{B_y}{\mu}\zeta_z - \frac{B_z}{\mu}\zeta_y \\ \frac{B_z}{\mu}\zeta_x - \frac{B_x}{\mu}\zeta_z \\ \frac{B_x}{\mu}\zeta_y - \frac{B_y}{\mu}\zeta_x \end{bmatrix}. \quad (3.33)$$

In [24], it is shown that coordinate transformation does not change the type or the properties of a system of PDEs. Since Maxwell's equations form a quasi-linear hyperbolic system of PDEs [26], (3.31) can be rewritten in the form of (2.3),

$$Q_t + [A]Q_\xi + [B]Q_\eta + [C]Q_\zeta = [K]Q \quad (3.34)$$

where the flux matrices in the transformed coordinate system are defined as:

$$[\boldsymbol{A}] = \begin{bmatrix} 0 & 0 & 0 & 0 & -\frac{\xi_z}{J\varepsilon} & \frac{\xi_y}{J\varepsilon} \\ 0 & 0 & 0 & \frac{\xi_z}{J\varepsilon} & 0 & -\frac{\xi_x}{J\varepsilon} \\ 0 & 0 & 0 & -\frac{\xi_y}{J\varepsilon} & \frac{\xi_x}{J\varepsilon} & 0 \\ 0 & \frac{\xi_z}{J\mu} & -\frac{\xi_y}{J\mu} & 0 & 0 & 0 \\ -\frac{\xi_z}{J\mu} & 0 & \frac{\xi_x}{J\mu} & 0 & 0 & 0 \\ \frac{\xi_y}{J\mu} & -\frac{\xi_x}{J\mu} & 0 & 0 & 0 & 0 \end{bmatrix}, \quad [\boldsymbol{B}] = \begin{bmatrix} 0 & 0 & 0 & 0 & -\frac{\eta_z}{J\varepsilon} & \frac{\eta_y}{J\varepsilon} \\ 0 & 0 & 0 & \frac{\eta_z}{J\varepsilon} & 0 & -\frac{\eta_x}{J\varepsilon} \\ 0 & 0 & 0 & -\frac{\eta_y}{J\varepsilon} & \frac{\eta_x}{J\varepsilon} & 0 \\ 0 & \frac{\eta_z}{J\mu} & -\frac{\eta_y}{J\mu} & 0 & 0 & 0 \\ -\frac{\eta_z}{J\mu} & 0 & \frac{\eta_x}{J\mu} & 0 & 0 & 0 \\ \frac{\eta_y}{J\mu} & -\frac{\eta_x}{J\mu} & 0 & 0 & 0 & 0 \end{bmatrix}, \tag{3.35}$$

$$[\boldsymbol{C}] = \begin{bmatrix} 0 & 0 & 0 & 0 & -\frac{\zeta_z}{J\varepsilon} & \frac{\zeta_y}{J\varepsilon} \\ 0 & 0 & 0 & \frac{\zeta_z}{J\varepsilon} & 0 & -\frac{\zeta_x}{J\varepsilon} \\ 0 & 0 & 0 & -\frac{\zeta_y}{J\varepsilon} & \frac{\zeta_x}{J\varepsilon} & 0 \\ 0 & \frac{\zeta_z}{J\mu} & -\frac{\zeta_y}{J\mu} & 0 & 0 & 0 \\ -\frac{\zeta_z}{J\mu} & 0 & \frac{\zeta_x}{J\mu} & 0 & 0 & 0 \\ \frac{\zeta_y}{J\mu} & -\frac{\zeta_x}{J\mu} & 0 & 0 & 0 & 0 \end{bmatrix}, \quad [\boldsymbol{K}] = \begin{bmatrix} 0 & 0 & 0 & 0 & 0 & 0 \\ 0 & 0 & 0 & 0 & 0 & 0 \\ 0 & 0 & 0 & 0 & 0 & 0 \\ 0 & 0 & 0 & \frac{-\sigma}{J\varepsilon} & 0 & 0 \\ 0 & 0 & 0 & 0 & \frac{-\sigma}{J\varepsilon} & 0 \\ 0 & 0 & 0 & 0 & 0 & \frac{-\sigma}{J\varepsilon} \end{bmatrix}. \tag{3.36}$$

In the transformed Maxwell's equations, the transformed flux vectors, $\boldsymbol{E}, \boldsymbol{F}$, and $\boldsymbol{G}$, contain electric and magnetic field components that are tangential to the ξ-, η-, and ζ-constant surfaces of the new coordinate system. Thus, an alternative generalised vector form of Maxwell's equations in the curvilinear coordinate system is written as:

$$\frac{1}{J}\begin{pmatrix}\boldsymbol{B}\\ \boldsymbol{D}\end{pmatrix}_t + \frac{1}{J}\begin{pmatrix}\boldsymbol{a}_\xi \times \mathcal{E}\\ -\boldsymbol{a}_\xi \times \mathcal{H}\end{pmatrix}_\xi + \frac{1}{J}\begin{pmatrix}\boldsymbol{a}_\eta \times \mathcal{E}\\ -\boldsymbol{a}_\eta \times \mathcal{H}\end{pmatrix}_\eta + \frac{1}{J}\begin{pmatrix}\boldsymbol{a}_\zeta \times \mathcal{E}\\ -\boldsymbol{a}_\zeta \times \mathcal{H}\end{pmatrix}_\zeta = \frac{1}{J}\begin{pmatrix}0\\ -\sigma\mathcal{E}\end{pmatrix}. \tag{3.37}$$

The above flux vectors (the second, third, and fourth terms of the left-hand-side) are

determined via the expressions of the vector transformation in **Section B.4** of **Appendix B**. For example, in the case of $\boldsymbol{E}$,

$$\boldsymbol{E} = \frac{1}{J}\begin{bmatrix} \boldsymbol{a}_\xi \times \mathcal{E} \\ -\boldsymbol{a}_\xi \times \mathcal{H} \end{bmatrix}, \tag{3.38}$$

the vector product of a unitary vector of the general coordinate system, $\boldsymbol{a}_\xi$, and either the electric or magnetic field are evaluated in terms of Cartesian coordinate field components as shown in (B.47); that is:

$$\boldsymbol{a}_\xi \times \mathcal{E} = \begin{vmatrix} \boldsymbol{a}_x & \boldsymbol{a}_y & \boldsymbol{a}_z \\ \xi_x & \xi_y & \xi_z \\ \frac{D_x}{\varepsilon} & \frac{D_y}{\varepsilon} & \frac{D_z}{\varepsilon} \end{vmatrix}, \quad \boldsymbol{a}_\xi \times \mathcal{H} = \begin{vmatrix} \boldsymbol{a}_x & \boldsymbol{a}_y & \boldsymbol{a}_z \\ \xi_x & \xi_y & \xi_z \\ \frac{B_x}{\mu} & \frac{B_y}{\mu} & \frac{B_z}{\mu} \end{vmatrix}. \tag{3.39}$$

Similar expressions can be derived for transformed flux vectors, $\boldsymbol{F}$ and $\boldsymbol{G}$.

3.3 Solution of Governing Equations

In the previous section, the governing equations of an EM field problem were written as coupled quasi-linear hyperbolic systems of PDEs cast in generalised vector form on a curvilinear frame. Generally, this class of PDEs lends itself to be solved via characteristic-based methods. The theory of the method of characteristics and its solution of the vector form of Maxwell's equations are discussed next.

3.3.1 Generalised Solution: Theory and Background

A quasi-linear PDE in conservative form, say:

$$\frac{\partial Q}{\partial t} + \frac{\partial F}{\partial x} = \frac{\partial Q}{\partial t} + [A]\frac{\partial Q}{\partial x} = 0, \tag{3.40}$$

is said to be hyperbolic if the eigenvalue of the flux matrix, λ, is real. An ***initial value problem*** is defined as the solution of (3.40), *i.e.* $Q(x, t)$, given an initial condition [82],

$$Q(x, 0) = Q_0(x). \tag{3.41}$$

A geometric solution to the above initial value problem can be obtained via the method of characteristics. One of the consequences of (3.40) is that its solution, Q, is constant along trajectories (***characteristics lines***) $x = x(t)$ in the x-t plane (see **Figure 3.2**). The waves described by the conservation form of Maxwell's equations propagate along these characteristic lines with speed [83]:

$$\lambda = \frac{dx}{dt}, \tag{3.42}$$

where λ is an eigenvalue of the flux matrix, $[A]$. This geometric solution of (3.40) is based on the original assumption of the integral form of the conservation law, (3.1), where $Q(x, t)$ is assumed to be continuous within the solution domain. Often, these solutions are continuous everywhere in the domain except across a given boundary where they are discontinuous [84]. A special relation must be satisfied at these boundaries; the derivation of this relation is considered next.

If a solution to an initial value problem, $Q(x, t)$, is continuous everywhere in the solution space but is discontinuous across a boundary specified by $x = x(t)$, then one half of the conservation law (over an interval $a \le x \le b$ at time t) is written as [83]:

---

* It has been shown that for continuous functions, it makes no difference whether the flux matrix $[A]$ is inside or outside of the derivative term [22]; that is

$$([A]Q)_x = [A]Q_x.$$

However, from a numerical point of view, the right and left hand sides of the above equation yield dissimilar discretised expressions, unless it is assumed that

$$([A])_x Q = 0.$$

$$\frac{d}{dt}\int_a^b Q(x,t)dx = \frac{d}{dt}\int_a^k Q(x,t)dx + \frac{d}{dt}\int_k^b Q(x,t)dx. \tag{3.43}$$

It is split into two regions where Q is continuous. The above expression is then solved using the values of Q immediately to the left and right of the discontinuity, denoted by Q_L and Q_R respectively (see **Figure 3.2**); that is:

$$\frac{d}{dt}\int_a^b Q(x,t)dx = \int_a^k Q_t dx + Q_L\frac{dx}{dt} + \int_k^b Q_t dx - Q_R\frac{dx}{dt}. \tag{3.44}$$

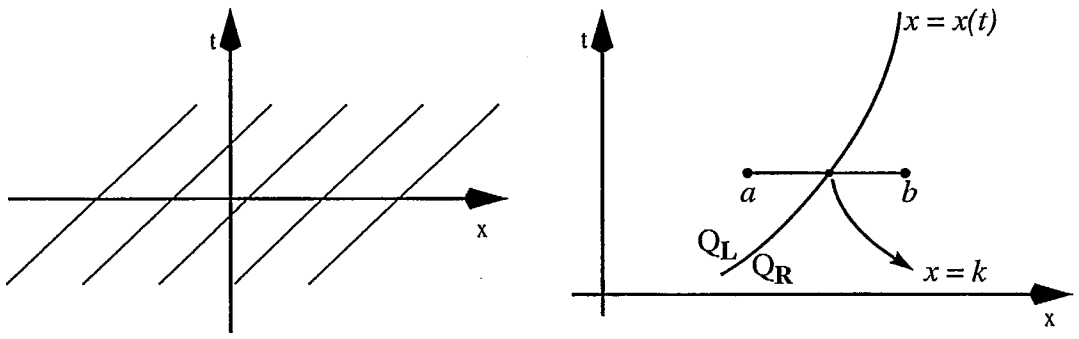

Figure 3.2. Characteristic lines of a PDE (Left) and characteristic lines in the presence of a discontinuity (Right) [83]

After substituting for Q_t from the conservation law of (3.2), replacing the expression of speed of propagation along the characteristic line from (3.42), and evaluating the integral terms, (3.44) becomes:

$$\frac{d}{dt}\int_a^b Q(x,t)dx = -F(Q_L) + F(Q(a)) + \lambda Q_L - F(Q(b)) + F(Q_R) - \lambda Q_R. \tag{3.45}$$

However, the conservation law requires that:

$$\frac{d}{dt}\int_a^b Q(x,t)dx = F(Q(a)) - F(Q(b)). \tag{3.46}$$

Equating the right-hand-side of (3.45) and (3.46), and after some algebraic manipulations:

$$\lambda(Q_R - Q_L) = F(Q_R) - F(Q_L). \tag{3.47}$$

This relation is often called the ***Rankine-Hugoniot jump condition*** or simply the ***jump condition***; it is denoted by the *jump operator*, $\| \ \|$, [83]; that is:

$$\lambda \| Q \| = \| F \| . \tag{3.48}$$

Thus far, a class of ***generalised solutions*** to an initial value problem is found via geometric solutions and the Rankine-Hugoniot jump condition (in regions that may contain non-differentiable and even discontinuous functions). However, generalised solutions often provide more than one solution for any given initial data with only one having physical significance (*i.e.* the solution is unique). In order to eliminate non-physical solutions, thereby achieving a unique solution, Lax [83] proposed that at discontinuities, an ***entropy condition*** must also be satisfied in addition to a jump condition. The entropy condition ensures that the characteristics continue to follow in the direction of the increasing dependent variable after intersecting with the discontinuity [83]. The entropy condition is written as an inequality:

$$\lambda(Q_L) > \lambda(k) > \lambda(Q_R) . \tag{3.49}$$

For systems of N-PDEs, the entropy condition is generalised for cases of both increasing and decreasing characteristic speeds on either side of the discontinuity; hence [85],

$$\lambda_i(Q_L) > \lambda(k) > \lambda_i(Q_R) , \tag{3.50}$$

$$\lambda_{i-1}(Q_L) < \lambda(k) < \lambda_{i+1}(Q_R) , \tag{3.51}$$

where $i = 1 \ldots\ldots N$. A ***k-shock*** is defined as a discontinuity that satisfies both the jump relation and the entropy condition. In [83], Lax has shown that for ***linearly degenerate k-shocks*** (see [83] for definition), the speed of propagation at the discontinuity is given by the eigenvalue of the flux matrix at the discontinuity; that is:

$$\lambda(k) = \lambda_i(Q). \tag{3.52}$$

Hence, the modified Rankine-Hugoniot jump condition is rewritten as:

$$\lambda_i \|Q\|_i = \|F\|_i. \tag{3.53}$$

where it defines the relationships between the flux variables on both sides of the discontinuity surface (*i.e.* F_L and F_R) and the solution variables at the cells neighbouring the discontinuity (*i.e.* Q_L and Q_R) in terms of the eigenvalues of the flux matrix, $[A]$.

3.3.2 Diagonalization and Flux Vector Splitting

Thus far, it has been shown that every initial value problem of (3.40) has a unique generalised solution for $t \geq 0$ via either the characteristic lines or the modified Rankine-Hugoniot jump condition at the discontinuities [83]. However, in the majority of cases, there exists more than one dependent variable in each equation of the governing system of PDEs (*i.e.* the system is ***coupled***) [20]. Thus, the first step in obtaining the solution is to uncouple the system of equations.

Consider the solution of the following quasi-linear hyperbolic coupled system of PDEs in two independent variables, t and x:

$$Q_t + F_x = Q_t + [A]Q_x = 0, \text{ where } Q = \begin{bmatrix} q_1 \\ q_2 \end{bmatrix} \text{ and } [A] = \begin{bmatrix} 0 & -c \\ -c & 0 \end{bmatrix}. \tag{3.54}$$

This coupled system of PDEs, *i.e.*

$$\begin{aligned} (q_1)_t - c(q_2)_x &= 0 \\ (q_2)_t - c(q_1)_x &= 0 \end{aligned} \tag{3.55}$$

can be uncoupled and solved for a given characteristic variable, say $\Theta = \begin{bmatrix} \Theta_1 & \Theta_2 \end{bmatrix}^T$; that is

$$(\Theta_1)_t - c(\Theta_1)_x = 0$$
$$(\Theta_2)_t + c(\Theta_2)_x = 0 \qquad (3.56)$$

where c and $-c$ are the eigenvalues of the flux matrix $[A]$ and $\Theta = [T]^{-1}Q$ [86]. In this case, matrix $[T]$ and its corresponding inverse, $[T]^{-1}$, are non-singular matrices which form the similarity transformation:*

$$[T]^{-1}[A][T] = [\Lambda] = diag(\lambda_i) = \begin{bmatrix} \lambda_1 & 0 \\ 0 & \lambda_2 \end{bmatrix}, \qquad (3.57)$$

where

$$[T] = \frac{1}{2c}\begin{bmatrix} 1 & 1 \\ 1 & -1 \end{bmatrix}, \; [T]^{-1} = \begin{bmatrix} c & c \\ c & -c \end{bmatrix}, \text{ and } [\Lambda] = \begin{bmatrix} -c & 0 \\ 0 & c \end{bmatrix}. \qquad (3.58)$$

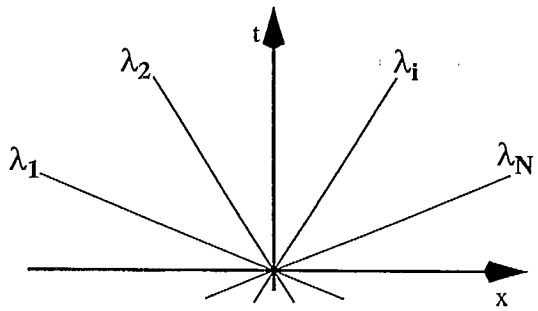

Figure 3.3. Characteristic line solutions of a system of PDEs

In general, a coupled system of N- PDEs written in the conservative form of (3.40) can be transformed to an uncoupled system [87],

$$(\Theta_i)_t + \lambda_i(\Theta_i)_x = 0$$
$$i = 1, 2, \ldots, N, \qquad (3.59)$$

where $[T]^{-1}Q = \Theta = \left[\Theta_1 \; \Theta_2 \; \ldots \; \Theta_N\right]^T$ and $[T]^{-1}[A][T] = [\Lambda] = diag(\lambda_i)$. Thus, a coupled system of PDEs is converted (diagonalized) into a set of scalar PDEs and is represented in terms of the characteristic variable, Θ, and the corresponding eigenvalues of the flux matrix, $[A]$. For each equation of the uncoupled system of PDEs, (3.59), the generalised solution of an initial value

* A matrix, $[A]$, is ***similar*** to a matrix, $[B]$, if there exists a non-singular matrix, $[T]$, such that

$$[B] = [T][A][T]^{-1}$$

and matrix $[B]$ is referred to as the ***similarity transformation*** of $[A]$ [29 page 78].

problem is given along characteristics lines with slopes given by their respective eigenvalues [87].

Next, consider a diagonal matrix of eigenvalues of $[A]$,

$$[\Lambda] = [\Lambda^+] + [\Lambda^-] \tag{3.60}$$

where $[\Lambda^+]$ and $[\Lambda^-]$ have diagonal elements, λ_i^+ and λ_i^-, respectively. The above expression is pre- and post-multiplied by similarity matrices, $[T]$ and $[T]^{-1}$, respectively.

$$[T][\Lambda][T]^{-1} = [T]([\Lambda^+] + [\Lambda^-])[T]^{-1} \tag{3.61}$$

Then it is expanded and simplified to (noting that $[A] = [T][\Lambda][T]^{-1}$):

$$\begin{aligned} [A] &= [T][\Lambda^+][T]^{-1} + [T][\Lambda^-][T]^{-1} \\ [A] &= [A^+] + [A^-] \end{aligned} \tag{3.62}$$

where the initial flux matrix, $[A]$, is now represented in terms of two matrices, one with non-negative eigenvalues, $[A^+]$, and one that has only non-positive eigenvalues, $[A^-]$, [87]. Following the substitution of the above in the original quasi-linear system of PDEs,

$$\frac{\partial Q}{\partial t} + ([A^+] + [A^-])\frac{\partial Q}{\partial x} = 0 \tag{3.63}$$

the split flux matrices are taken inside the derivative term; that is:

$$\frac{\partial Q}{\partial t} + \frac{\partial F^+}{\partial x} + \frac{\partial F^-}{\partial x} = 0. \tag{3.64}$$

The above expression indicates that the flux vector can be split into two sub-vectors (thus the term ***flux vector splitting*** [86]) each corresponding to positive, in the case of F^+, and negative, for F^-, eigenvalues of $[A]$. The main advantage of using a flux-vector splitting representation of the governing equations is its ability to formulate the problem via directional signal propagation. This means that the original initial value problem is

represented as a sum of simpler problems where the direction of wave propagation is known and specified by the sign of the eigenvalues [89], thus allowing the use of directional-biased numerical procedures. The properties of directional biased numerical solution techniques of PDEs and their advantage over more traditional central differencing methods are discussed in the next chapter.

3.3.3 Riemann Problems and Governing Equations

The superposition principle states that for a given set of ("complex") linear differential equations with "complex" initial or boundary conditions, the solution to this set of equations can be obtained via the sum of solutions of sets of "easier" linear differential equations [20]. Accordingly, the solution to the initial value problem of (3.40) can also be obtained by solving a succession of simpler initial value problems with

$$Q(x<0,0) = Q_L \quad \text{and} \quad Q(x>0,0) = Q_R; \tag{3.65}$$

these simpler initial value problems are called ***Riemann problems*** [90].

It has been shown that the solution to a multi-dimensional spatial problem can be constructed via solving a succession of 1D Riemann problems [90]. Hence, an initial value problem of a quasi-linear system of PDEs can be solved via successive Riemann problems formulated using the flux-vector splitting method. In the case of the generalised vector form of Maxwell's equations,

$$\boldsymbol{Q}_t + ([\boldsymbol{A}]\boldsymbol{Q})_\xi + ([\boldsymbol{B}]\boldsymbol{Q})_\eta + ([\boldsymbol{C}]\boldsymbol{Q})_\zeta = 0, \tag{3.66}$$

the system of PDEs is represented as three one-dimensional systems:

$$\begin{aligned} \boldsymbol{Q}_t + ([\boldsymbol{A}]\boldsymbol{Q})_\xi &= 0, \\ \boldsymbol{Q}_t + ([\boldsymbol{B}]\boldsymbol{Q})_\eta &= 0, \\ \boldsymbol{Q}_t + ([\boldsymbol{C}]\boldsymbol{Q})_\zeta &= 0. \end{aligned} \tag{3.67}$$

where $\boldsymbol{Q}$ is the transformed solution vector given by (3.32). These equations are then solved in sequence using one of many available numerical techniques.

The eigenvalues of the original flux matrices of (3.67), *i.e.* $[\boldsymbol{A}]$, $[\boldsymbol{B}]$, and $[\boldsymbol{C}]$ given in (3.35) and (3.36), are found via the solution of the characteristic equation for each of the coefficient matrices (each being a polynomial of degree six). The resulting eigenvalues are:

$$[\Lambda_\xi] = diag\left[\frac{-\alpha}{J\sqrt{\mu\varepsilon}} \frac{-\alpha}{J\sqrt{\mu\varepsilon}} \frac{\alpha}{J\sqrt{\mu\varepsilon}} \frac{\alpha}{J\sqrt{\mu\varepsilon}} \quad 0 \quad 0\right] \text{ for } \alpha = \sqrt{\xi_x^2 + \xi_y^2 + \xi_z^2}, \quad (3.68)$$

$$[\Lambda_\eta] = diag\left[\frac{-\beta}{J\sqrt{\mu\varepsilon}} \frac{-\beta}{J\sqrt{\mu\varepsilon}} \frac{\beta}{J\sqrt{\mu\varepsilon}} \frac{\beta}{J\sqrt{\mu\varepsilon}} \quad 0 \quad 0\right] \text{ for } \beta = \sqrt{\eta_x^2 + \eta_y^2 + \eta_z^2}, \quad (3.69)$$

$$[\Lambda_\zeta] = diag\left[\frac{-\gamma}{J\sqrt{\mu\varepsilon}} \frac{-\gamma}{J\sqrt{\mu\varepsilon}} \frac{\gamma}{J\sqrt{\mu\varepsilon}} \frac{\gamma}{J\sqrt{\mu\varepsilon}} \quad 0 \quad 0\right] \text{ for } \gamma = \sqrt{\zeta_x^2 + \zeta_y^2 + \zeta_z^2}. \quad (3.70)$$

Although the eigenvalues of each flux matrix contain multiplicities, they correspond to linearly independent (unique to a multiplicative constant) eigenvectors in each time-space plane. These eigenvectors are then used to compute similarity matrices required for diagonalization:*

$$\begin{aligned}
&([\boldsymbol{T}_\xi]^{-1}\boldsymbol{Q})_t + [\boldsymbol{T}_\xi]^{-1}([\boldsymbol{T}_\xi][\Lambda_\xi^+][\boldsymbol{T}_\xi]^{-1} + [\boldsymbol{T}_\xi][\Lambda_\xi^-][\boldsymbol{T}_\xi]^{-1}\boldsymbol{Q})_\xi = 0,\\
&([\boldsymbol{T}_\eta]^{-1}\boldsymbol{Q})_t + [\boldsymbol{T}_\eta]^{-1}([\boldsymbol{T}_\eta][\Lambda_\eta^+][\boldsymbol{T}_\eta]^{-1} + [\boldsymbol{T}_\eta][\Lambda_\eta^-][\boldsymbol{T}_\eta]^{-1}\boldsymbol{Q})_\eta = 0,\\
&([\boldsymbol{T}_\zeta]^{-1}\boldsymbol{Q})_t + [\boldsymbol{T}_\zeta]^{-1}([\boldsymbol{T}_\zeta][\Lambda_\zeta^+][\boldsymbol{T}_\zeta]^{-1} + [\boldsymbol{T}_\zeta][\Lambda_\zeta^-][\boldsymbol{T}_\zeta]^{-1}\boldsymbol{Q})_\zeta = 0.
\end{aligned} \quad (3.71)$$

After some algebraic manipulations, and after using the flux splitting procedure of the previous section, the following flux-split Riemann problems emerge as:

---

* In the interest of brevity, the details of the computation of the eigenvalues of (3.68)-(3.70), the eigenvectors, and similar matrices of (3.71) are not included but are found in [77, 90].

$$Q_t + ([A^+]Q)_\xi = 0, \quad Q_t + ([A^-]Q)_\xi = 0,$$
$$Q_t + ([B^+]Q)_\eta = 0, \quad Q_t + ([B^-]Q)_\eta = 0,$$
$$Q_t + ([C^+]Q)_\zeta = 0, \quad Q_t + ([C^-]Q)_\zeta = 0, \tag{3.72}$$

where the flux split coefficient matrices are given by:

$$[A^+] = \begin{bmatrix}
\frac{\xi_y^2+\xi_z^2}{2J\alpha\sqrt{\mu\varepsilon}} & \frac{-\xi_x\xi_y}{2J\alpha\sqrt{\mu\varepsilon}} & \frac{-\xi_x\xi_z}{2J\alpha\sqrt{\mu\varepsilon}} & 0 & \frac{-\xi_z}{2J\varepsilon} & \frac{\xi_y}{2J\varepsilon} \\
\frac{-\xi_x\xi_y}{2J\alpha\sqrt{\mu\varepsilon}} & \frac{\xi_x^2+\xi_z^2}{2J\alpha\sqrt{\mu\varepsilon}} & \frac{-\xi_y\xi_z}{2J\alpha\sqrt{\mu\varepsilon}} & \frac{\xi_z}{2J\varepsilon} & 0 & \frac{-\xi_x}{2J\varepsilon} \\
\frac{-\xi_x\xi_z}{2J\alpha\sqrt{\mu\varepsilon}} & \frac{-\xi_y\xi_z}{2J\alpha\sqrt{\mu\varepsilon}} & \frac{\xi_x^2+\xi_y^2}{2J\alpha\sqrt{\mu\varepsilon}} & \frac{-\xi_y}{2J\varepsilon} & \frac{\xi_x}{2J\varepsilon} & 0 \\
0 & \frac{\xi_z}{2J\mu} & \frac{-\xi_y}{2J\mu} & \frac{\xi_y^2+\xi_z^2}{2J\alpha\sqrt{\mu\varepsilon}} & \frac{-\xi_x\xi_y}{2J\alpha\sqrt{\mu\varepsilon}} & \frac{-\xi_x\xi_z}{2J\alpha\sqrt{\mu\varepsilon}} \\
\frac{-\xi_z}{2J\mu} & 0 & \frac{\xi_x}{2J\mu} & \frac{-\xi_x\xi_y}{2J\alpha\sqrt{\mu\varepsilon}} & \frac{\xi_x^2+\xi_z^2}{2J\alpha\sqrt{\mu\varepsilon}} & \frac{-\xi_y\xi_z}{2J\alpha\sqrt{\mu\varepsilon}} \\
\frac{\xi_y}{2J\mu} & \frac{-\xi_x}{2J\mu} & 0 & \frac{-\xi_x\xi_z}{2J\alpha\sqrt{\mu\varepsilon}} & \frac{-\xi_y\xi_z}{2J\alpha\sqrt{\mu\varepsilon}} & \frac{\xi_x^2+\xi_y^2}{2J\alpha\sqrt{\mu\varepsilon}}
\end{bmatrix}, \tag{3.73}$$

$$[A^-] = \begin{bmatrix}
\frac{-(\xi_y^2+\xi_z^2)}{2J\alpha\sqrt{\mu\varepsilon}} & \frac{\xi_x\xi_y}{2J\alpha\sqrt{\mu\varepsilon}} & \frac{\xi_x\xi_z}{2J\alpha\sqrt{\mu\varepsilon}} & 0 & \frac{-\xi_z}{2J\varepsilon} & \frac{\xi_y}{2J\varepsilon} \\
\frac{\xi_x\xi_y}{2J\alpha\sqrt{\mu\varepsilon}} & \frac{-(\xi_x^2+\xi_z^2)}{2J\alpha\sqrt{\mu\varepsilon}} & \frac{\xi_y\xi_z}{2J\alpha\sqrt{\mu\varepsilon}} & \frac{\xi_z}{2J\varepsilon} & 0 & \frac{-\xi_x}{2J\varepsilon} \\
\frac{\xi_x\xi_z}{2J\alpha\sqrt{\mu\varepsilon}} & \frac{\xi_y\xi_z}{2J\alpha\sqrt{\mu\varepsilon}} & \frac{-(\xi_x^2+\xi_y^2)}{2J\alpha\sqrt{\mu\varepsilon}} & \frac{-\xi_y}{2J\varepsilon} & \frac{\xi_x}{2J\varepsilon} & 0 \\
0 & \frac{\xi_z}{2J\mu} & \frac{-\xi_y}{2J\mu} & \frac{-(\xi_y^2+\xi_z^2)}{2J\alpha\sqrt{\mu\varepsilon}} & \frac{\xi_x\xi_y}{2J\alpha\sqrt{\mu\varepsilon}} & \frac{\xi_x\xi_z}{2J\alpha\sqrt{\mu\varepsilon}} \\
\frac{-\xi_z}{2J\mu} & 0 & \frac{\xi_x}{2J\mu} & \frac{\xi_x\xi_y}{2J\alpha\sqrt{\mu\varepsilon}} & \frac{-(\xi_x^2+\xi_z^2)}{2J\alpha\sqrt{\mu\varepsilon}} & \frac{\xi_y\xi_z}{2J\alpha\sqrt{\mu\varepsilon}} \\
\frac{\xi_y}{2J\mu} & \frac{-\xi_x}{2J\mu} & 0 & \frac{\xi_x\xi_z}{2J\alpha\sqrt{\mu\varepsilon}} & \frac{\xi_y\xi_z}{2J\alpha\sqrt{\mu\varepsilon}} & \frac{-(\xi_x^2+\xi_y^2)}{2J\alpha\sqrt{\mu\varepsilon}}
\end{bmatrix}. \tag{3.74}$$

The expression of the other flux split matrices is obtained by: (1) replacing ξ with η (in the case of $[\boldsymbol{B}^+]$ and $[\boldsymbol{B}^-]$) or ζ (in the case of $[\boldsymbol{C}^+]$ and $[\boldsymbol{C}^-]$) for partial derivatives; and (2) replacing variable α with β (in the case of $[\boldsymbol{B}^+]$ and $[\boldsymbol{B}^-]$) or γ (in the case of $[\boldsymbol{C}^+]$ and $[\boldsymbol{C}^-]$).

3.4 Summary

In this chapter, the governing equations of an EM field problem were expressed in terms of Maxwell's equations in vector form on a curvilinear frame using a general coordinate system transformation. It was shown that the solution to this multi-dimensional system of PDEs can be obtained through solving a succession of flux-split one-dimensional Riemann problems. The generalised solution to each equation of this set of scalar PDEs is given via the method of characteristics along with the modified Rankine-Hugoniot jump condition. Since the direction of wave propagation in each one-dimensional time-space flux-split Riemann problem is dictated by its corresponding eigenvalue, directional biased numerical techniques can be used to solve each Riemann problem. The next chapter is devoted to these types of Riemann solvers.

Chapter 4

The Finite-Volume Time-Domain Method

The traditional FVTD method is based on the ***subdomain method***, a subclass of the ***method of weighted residuals*** [24]. In the subdomain method, the computational space is divided into discrete domains where the conservation law is enforced via the governing equations. In the original FVTD method, the integral form of the governing equations is discretised; thus, the update equations require the computation of cell volumes and cell surface areas (where fluxes flow) [24]. In contrast, the FVTD method (in the context of this document) operates on the semi-discrete differential form of Maxwell's equations in the time domain. The three-dimensional Maxwell's equations are cast on a general curvilinear coordinate system and are expressed in the form of a system of PDEs given in (3.31) to (3.36). The field and flux vectors in the general coordinate system are expressed in terms of their Cartesian counterparts via a coordinate transformation and its respective Jacobian, J, of transformation, (3.26) to (3.30). Since the Jacobian of transformation is associated with the volume of a discretised cell, V, (where $V = 1/J$), this method is

(erroneously) known as the ***finite volume*** method [17].

In **Chapter 3**, it was proposed that the solution to the aforementioned system of PDEs can be obtained by incorporating solutions of one-dimensional flux-split Riemann problems. This class of Riemann problems is well suited to be solved using directional biased numerical techniques, such as the family of ***windward*** (***upwind***) schemes. In this chapter, one such characteristic-based windward Riemann solver (known as the ***Lax-Wendroff (LW) upwind scheme***) is considered, and the appropriate expressions for solving three-dimensional Maxwell's equations are derived.

4.1 Characteristic-Based Windward Riemann Solvers

The flux-vector splitting procedure, which was originally developed by Steger and Warming for the conservation form of inviscid gas dynamic equations [87], is easily adaptable for solving the time domain Maxwell's equations. The direction of wave propagation in a flux split Riemann problem is given by the sign of the eigenvalues of the flux matrix where positive eigenvalues are associated with forward (right) travelling waves and negative eigenvalues represent backward (left) travelling waves [26]. The solution to these types of Riemann problems is best obtained by windward schemes.

In the windward class of algorithms, the unknown variable is computed using only variables downwind to the direction of the signal (wave) propagation. This is in direct contrast to traditional central differencing schemes where a symmetric computational molecule is used (see **Figure 4.1**). Some of the advantages of using windward schemes over traditional central differencing schemes include: (1) superior dispersion and stability properties, (2) a simpler and more accurate representation of fixed external boundaries,

and (3) a more accurate representation of discontinuities [92]. The only disadvantage of using windward schemes is that the propagating waves must remain upwind with respect to the computational stencil. This can be easily achieved in most EM field problems since the original wave is split into two sets of components (via a flux splitting procedure where one set is travelling forward and the other set is travelling backward). By using forward differencing on the backward travelling waves, and by performing backward differencing on the forward travelling signals, the scheme remains upwind and stable regardless of the direction of the signals' propagation within the simulation space (see **Appendix A** for the definition and notation of differencing operators).

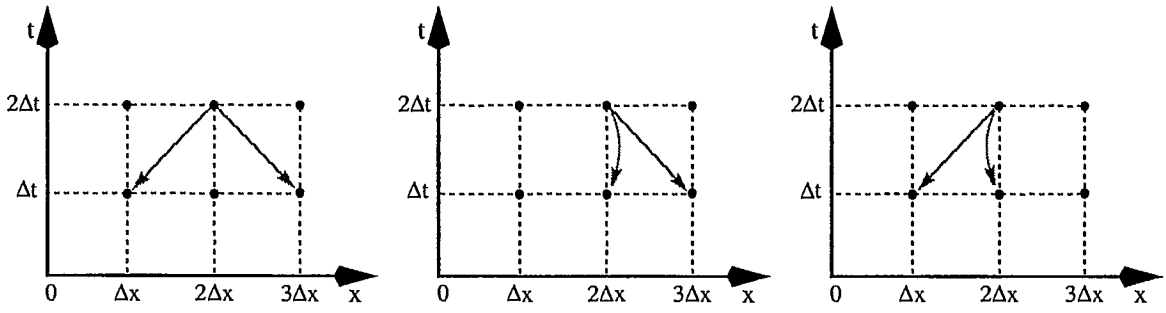

Figure 4.1. Various stencils for spatial differencing: (left) central differencing, (centre) forward differencing, and (right) backward differencing

The aforementioned flux split Riemann problems can be transformed into discrete algebraic equations through one of several *explicit* windward finite difference discretisation procedures, such as ***fractional-step*** algorithms, single-step or the multi-stage ***Runge-Kutta*** family of procedures, and LW upwind schemes [91]. All of these explicit schemes are (at least) second-order accurate in space and time. In this thesis, the explicit LW upwind scheme was the method of choice for discretising and solving

Riemann problems. This method was chosen primarily due to it ease of formulation and its proven track record in the field of CEM [93, 94].

In the following sections, two second-order accurate upwind schemes are derived. First, a symmetric (MacCormack's) windward algorithm [95] is considered, and some of its disadvantages are discussed. These discussions will pave the road for the derivation of a fully windward scheme (*i.e.* the LW scheme) [92]. Although the presence of source terms or losses (the S vector in (3.31)) in the governing equations has been mentioned in most FVTD related work [16, 26], the formulation of these terms has not been explicitly discussed. Only recently has an attempt been made to formulate non-homogenous Euler equations using the LW technique [96-98]. Unfortunately, all of the previous LW formulations of source terms are simplistic in their approach; that is, the source term is simply added to an already available LW update expression. In the following discussions, the source term is included at the beginning of the formulation of the LW algorithm; hence, the non-homogenous PDEs are rigorously treated and their solution is derived.

4.1.1 MacCormak's Scheme

Consider the non-homogenous one-dimensional flux split Riemann problem:

$$Q_t + F^-_x = S, \tag{4.1}$$

where F^- and S are linear functions of the solution vector, Q; see (2.4); hence,

$$F^- = [A^-]Q, \text{ and } S = [K]Q.^* \tag{4.2}$$

A second order accurate time-derivative (using forward differencing),

---

* From this point on, the square bracket, [ ], of the matrices and the superscript " $^-$" of the split flux vectors and matrices are dropped in the interest of conciseness.

$$(Q_t)_i^n = \frac{Q_i^{n+1} - Q_i^n}{\Delta t} - \frac{\Delta t}{2}(Q_{tt})_i^n, \tag{4.3}$$

and space-derivative (using a centred differencing stencil),

$$(Q_x)_i^n = \frac{Q_{i+1}^n - Q_{i-1}^n}{2\Delta x}, \tag{4.4}$$

Taylor series expansion is utilized to approximate equation (4.1); *i.e.*

$$\frac{Q_i^{n+1} - Q_i^n}{\Delta t} - \frac{\Delta t}{2}(Q_{tt})_i^n + \frac{F_{i+1}^n - F_{i-1}^n}{2\Delta x} = KQ_i^n. \tag{4.5}$$

Next, the Riemann problem of (4.1) is differentiated with respect to time and space; that is:

$$Q_{tt} + F_{xt} = S_t, \tag{4.6}$$

$$Q_{tx} + F_{xx} = S_x. \tag{4.7}$$

The definitions of flux and the source term in (4.2) are substituted in the above equations, and after some algebraic manipulations, Q_{tt} is determined as:

$$Q_{tt} = A^2 Q_{xx} + KQ_t - AKQ_x, \tag{4.8}$$

which is then substituted in (4.5),

$$\frac{Q_i^{n+1} - Q_i^n}{\Delta t} - \frac{\Delta t}{2}A^2(Q_{xx})_i^n - \frac{\Delta t}{2}K(Q_t)_i^n + \frac{\Delta t}{2}AK(Q_x)_i^n + \frac{F_{i+1}^n - F_{i-1}^n}{2\Delta x} - KQ_i^n = 0. \tag{4.9}$$

The time derivative of (4.9) is approximated by a first order accurate forward differencing scheme, whereas the spatial derivatives are estimated using a second order accurate centred differencing formula; thus:

$$\frac{Q_i^{n+1}-Q_i^n}{\Delta t}-\frac{\Delta t}{2}A^2\left(\frac{Q_{i+1}^n-2Q_i^n+Q_{i-1}^n}{\Delta x^2}\right)+\left(\frac{F_{i+1}^n-F_{i-1}^n}{2\Delta x}\right)$$
$$+\frac{\Delta t}{2}AK\left(\frac{Q_{i+1}^n-Q_{i-1}^n}{2\Delta x}\right)-\frac{\Delta t}{2}K\left(\frac{Q_i^{n+1}-Q_i^n}{\Delta t}\right)-KQ_i^n=0. \tag{4.10}$$

Grouping all of the error terms and solving for Q_i^{n+1} yield:

$$Q_i^{n+1}=Q_i^n+\frac{\Delta t^2}{2\Delta x^2}A^2(Q_{i+1}^n-2Q_i^n+Q_{i-1}^n)-\frac{\Delta t}{2\Delta x}(F_{i+1}^n-F_{i-1}^n)$$
$$-\frac{\Delta t^2}{4\Delta x}AK(Q_{i+1}^n-Q_{i-1}^n)+\frac{\Delta t}{2}K(Q_i^{n+1}+Q_i^n)=0. \tag{4.11}$$

From the relation $F=AQ$ and the addition of a *zero term*, $Q_i^n-Q_i^n$, to (4.11), it becomes:

$$(2I-\Delta tK)Q_i^{n+1}=(2+\Delta tK)Q_i^n+\frac{\Delta t^2}{\Delta x^2}A(F_{i+1}^n-2F_i^n+F_{i-1}^n)$$
$$-\frac{\Delta t}{\Delta x}A(Q_{i+1}^n-Q_{i-1}^n)-(2+\Delta tK)\frac{\Delta t}{2\Delta x}A(Q_{i+1}^n-Q_{i-1}^n+Q_i^n-Q_i^n). \tag{4.12}$$

The next stage of the development of the scheme requires the reorganization of (4.12) into easily recognizable patterns; *i.e.*

$$(2-\Delta tK)Q_i^{n+1}=(2+\Delta tK)Q_i^n-(2+\Delta tK)\frac{\Delta t}{2\Delta x}A(Q_i^n-Q_{i-1}^n)$$
$$-\frac{\Delta t}{\Delta x}A\left\{\left(\frac{2+\Delta tK}{2}\right)Q_{i+1}^n-\frac{\Delta t}{\Delta x}(F_{i+1}^n-F_i^n)-\left(\frac{2+\Delta tK}{2}\right)Q_i^n-\frac{\Delta t}{\Delta x}(F_i^n-F_{i-1}^n)\right\}. \tag{4.13}$$

Now the ***predictor*** term can be defined as (see **Appendix A** for definition of backward difference operator, ∇):

$$\overline{Q_i^{n+1}}=\left(\frac{2+\Delta tK}{2}\right)Q_i^n-\frac{\Delta t}{\Delta x}(F_i^n-F_{i-1}^n)$$
$$=\left(\frac{2+\Delta tK}{2}\right)Q_i^n-\frac{\Delta t}{\Delta x}\nabla F_i^n. \tag{4.14}$$

Then equation (4.13) is rewritten in terms of the predictor:

$$(2-\Delta tK)Q_i^{n+1} = (2+\Delta tK)Q_i^n - (2+\Delta tK)\frac{\Delta t}{2\Delta x}A(Q_i^n - Q_{i-1}^n) - \frac{\Delta t}{\Delta x}A(\overline{Q_{i+1}^{n+1}} - \overline{Q_i^{n+1}}), \tag{4.15}$$

where it is reorganized once more in order to outline yet another familiar pattern, *i.e.*

$$(2-\Delta tK)Q_i^{n+1} =$$

$$\left(\frac{2+\Delta tK}{2}\right)\left\{(2-\Delta tK)Q_i^n + \left(\frac{2+\Delta tK}{2}\right)Q_i^n - \frac{\Delta t}{\Delta x}A(Q_i^n - Q_{i-1}^n)\right\} - \frac{\Delta t}{\Delta x}(\overline{F_{i+1}^{n+1}} - \overline{F_i^{n+1}}). \tag{4.16}$$

After using the definition of the predictor, the ***corrector*** is given by:

$$(2-\Delta tK)Q_i^{n+1} = \left(\frac{2+\Delta tK}{2}\right)\left\{(2-\Delta tK)Q_i^n + \overline{Q_i^{n+1}}\right\} - \frac{\Delta t}{\Delta x}\Delta\overline{F_i^{n+1}}. \tag{4.17}$$

This scheme is referred to as ***MacCormak's scheme***; the complete update of the field components consists of the evaluation of both the predictor and corrector terms:

$$\overline{Q_i^{n+1}} = \left(\frac{2+\Delta tK}{2}\right)Q_i^n - \frac{\Delta t}{\Delta x}\nabla(F^-)_i^n$$

$$Q_i^{n+1} = \left(\frac{2+\Delta tK}{2-\Delta tK}\right)\left\{\frac{(2-\Delta tK)Q_i^n + \overline{Q_i^{n+1}}}{2}\right\} - \left(\frac{\Delta t}{\Delta x}\right)\frac{\Delta\overline{(F^-)_i^{n+1}}}{2-\Delta tK}. \tag{4.18}$$

It must be noted that the above formulation of MacCormak's scheme is only stable for negative eigenvalues of $[A]$ (backward travelling waves). However, this scheme is only a quasi-upwind algorithm; although, the predictor is based on a one-sided (upwind) stencil, the corrector still requires points to both the left and right side of

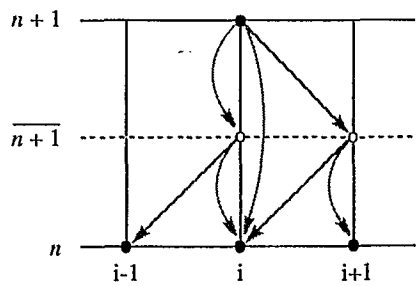

Figure 4.2. Numerical stencil for MacCormak's scheme

the wave front (*i.e.* the update point), thus rendering the overall technique essentially a centred-difference scheme (see **Figure 4.2**). Since in most applications a fully one-sided scheme is desired, the LW algorithm is considered next.

4.1.2 Derivation of a Fully Backward Lax-Wendroff Scheme

Consider a generic one-sided update equation for the flux split Riemann problem, $Q_t + [A^+]Q_x = \mathbf{S}$, which is supported by fields at $(i, i-1, i-2)$,

$$Q_i^{n+1} = a_i Q_i^n + a_{i-1} Q_{i-1}^n + a_{i-2} Q_{i-2}^n \tag{4.19}$$

where a_i, a_{i-1}, and a_{i-2} are coefficients which contain both spatial and time steps, Δx and Δt, as well as matrices, $[K]$ and $[A^+]$.* The second order accurate Taylor series expansion of Q_i^{n+1}, Q_{i-1}^n, and Q_{i-2}^n; that is:

$$Q_i^{n+1} = Q_i^n + \Delta t (Q_t)_i^n + \frac{\Delta t^2}{2}(Q_{tt})_i^n + O(\Delta t^3), \tag{4.20}$$

$$Q_{i-1}^n = Q_i^n - \Delta x (Q_x)_i^n + \frac{\Delta x^2}{2}(Q_{xx})_i^n + O(\Delta x^3), \tag{4.21}$$

$$Q_{i-2}^n = Q_i^n - 2\Delta x (Q_x)_i^n + \frac{4\Delta x^2}{2}(Q_{xx})_i^n + O(\Delta x^3), \tag{4.22}$$

is substituted in (4.19),

$$\begin{aligned} Q_i^n + \Delta t (Q_t)_i^n - \frac{\Delta t^2}{2}(Q_{tt})_i^n + O(\Delta t^3) \\ = a_i Q_i^n + a_{i-1}\left\{ Q_i^n - \Delta x (Q_x)_i^n + \frac{\Delta x^2}{2}(Q_{xx})_i^n + O(\Delta x^3) \right\} \\ a_{i-2}\left\{ Q_i^n - 2\Delta x (Q_x)_i^n + \frac{4\Delta x^2}{2}(Q_{xx})_i^n + O(\Delta x^3) \right\} \end{aligned} \tag{4.23}$$

* Once more, the square brackets and the superscripts are dropped for brevity.

and after the expansion of the above expression,

$$Q_i^n + \Delta t(Q_t)_i^n - \frac{\Delta t^2}{2}(Q_{tt})_i^n + O(\Delta t^3) = (a_i + a_{i-1} + a_{i-2})Q_i^n$$
$$- \Delta x(a_{i-1} + 2a_{i-2})(Q_x)_i^n + \frac{\Delta x^2}{2}(a_{i-1} + 4a_{i-2})(Q_{xx})_i^n + O(\Delta x^3). \tag{4.24}$$

Next, the expressions for Q_{tt} and Q_t from (4.8) and (4.1) are substituted in (4.24); that is:

$$\begin{aligned} Q_{tt} &= A^2 Q_{xx} + KQ_t - AKQ_x \\ &= A^2 Q_{xx} + K(KQ - AQ_x) - AKQ_x \\ &= A^2 (Q_{xx})_i^n + K^2 Q_i^n - 2AK(Q_x)_i^n. \end{aligned} \tag{4.25}$$

Hence, it becomes:

$$Q_i^n + \Delta t(Q_t)_i^n - \frac{\Delta t^2}{2}\left\{A^2(Q_{xx})_i^n + K^2 Q_i^n - 2AK(Q_x)_i^n\right\} + O(\Delta t^3) =$$
$$(a_i + a_{i-1} + a_{i-2})Q_i^n - \Delta x(a_{i-1} + 2a_{i-2})(Q_x)_i^n + \frac{\Delta x^2}{2}(a_{i-1} + 4a_{i-2})(Q_{xx})_i^n + O(\Delta x^3) \tag{4.26}$$

which is rewritten as:

$$(Q_t)_i^n - \Delta tKA(Q_x)_i^n + \left\{\frac{1}{\Delta t} + \frac{\Delta t}{2}K^2\right\}Q_i^n + \frac{\Delta t}{2}A^2(Q_{xx})_i^n + O(\Delta t^2) =$$
$$\frac{a_i + a_{i-1} + a_{i-2}}{\Delta t}Q_i^n - \frac{\Delta x}{\Delta t}(a_{i-1} + 2a_{i-2})(Q_x)_i^n + \frac{\Delta x^2}{2\Delta t}(a_{i-1} + 4a_{i-2})(Q_{xx})_i^n + \frac{O(\Delta x^3)}{\Delta t}. \tag{4.27}$$

Next, (4.28) is reorganized and is compared to the original Riemann problem, $Q_t + AQ_x - KQ = 0$. It it apparent that the right-hand-side of (4.28), which approximates the original Riemann problem, is second order accurate both in space and time (assuming that $\Delta t = O(\Delta x)$).

$$
\begin{aligned}
&(Q_t)_i^n + A(Q_x)_i^n - KQ_i^n = \\
&(Q_t)_i^n + \left\{\frac{\Delta x}{\Delta t}(a_{i-1} + 2a_{i-2}) - \Delta t K A\right\}(Q_x)_i^n - \left\{\frac{a_i + a_{i-1} + a_{i-2}}{\Delta t} - \frac{1}{\Delta t} - \frac{\Delta t}{2}K^2\right\}Q_i^n \\
&\quad + \left\{\frac{\Delta t}{2}A^2 - \frac{\Delta x^2}{2\Delta t}(a_{i-1} + 4a_{i-2})\right\}(Q_{xx})_i^n + O(\Delta t^2) + \frac{O(\Delta x^3)}{\Delta t}.
\end{aligned}
\tag{4.28}
$$

The unknown coefficients of (4.19) can now be determined by equating the coefficients of the like terms on the left- and right-hand-side of (4.28); hence, the following system of equations is obtained:

$$
\begin{aligned}
\frac{a_i + a_{i-1} + a_{i-2}}{\Delta t} - \frac{1}{\Delta t} - \frac{\Delta t}{2}K^2 &= K, \\
\frac{\Delta x}{\Delta t}(a_{i-1} + 2a_{i-2}) - \Delta t K A &= A, \\
\frac{\Delta t}{2}A^2 - \frac{\Delta x^2}{2\Delta t}(a_{i-1} + 4a_{i-2}) &= 0.
\end{aligned}
\tag{4.29}
$$

A change of notation, defined by:

$$
\rho = \frac{\Delta t}{\Delta x},\ \alpha = \rho A\text{, and } \beta = \Delta t K,
\tag{4.30}
$$

is followed by further algebraic manipulation resulting in:

$$
\begin{aligned}
a_i + a_{i-1} + a_{i-2} &= 1 + \beta + \frac{\beta^2}{2}, \\
a_{i-1} + 2a_{i-2} &= \alpha + \alpha\beta, \\
a_{i-1} + 4a_{i-2} &= \alpha^2,
\end{aligned}
\tag{4.31}
$$

where the unknowns in this system are the coefficients of (4.19); that is;

$$
\begin{aligned}
a_i &= \frac{1}{2}(\alpha^2+\beta^2-3\alpha\beta-3\alpha+2\beta+2),\\
a_{i-1} &= 2\alpha+2\alpha\beta-\alpha^2,\\
a_{i-2} &= \frac{1}{2}(\alpha^2-\alpha\beta-\alpha).
\end{aligned}
\tag{4.32}
$$

As a result, the update equation of the Riemann problem of (4.19) is given by:

$$
2Q_i^{n+1} = (\alpha^2+\beta^2-3\alpha\beta+2\beta-3\alpha+2)Q_i^n + (4\alpha\beta+4\alpha-2\alpha^2)Q_{i-1}^n + (\alpha^2-\alpha-\alpha\beta)Q_{i-2}^n.
\tag{4.33}
$$

It is reorganized into:

$$
\begin{aligned}
Q_i^{n+1} = &-\frac{\alpha(1+\beta)}{2}Q_i^n + \frac{\alpha^2}{2}Q_i^n - \frac{\alpha(1+\beta)}{2}Q_i^n - \frac{\alpha(1+\beta)}{2}Q_i^n + \frac{(1+\beta)^2}{2}Q_i^n + \frac{1}{2}Q_i^n\\
&+\frac{2\alpha(1+\beta)}{2}Q_{i-1}^n - \frac{2\alpha^2}{2}Q_{i-1}^n + \frac{\alpha(1+\beta)}{2}Q_{i-1}^n + \frac{\alpha(1+\beta)}{2}Q_{i-1}^n\\
&-\frac{\alpha(1+\beta)}{2}Q_{i-2}^n + \frac{\alpha^2}{2}Q_{i-2}^n
\end{aligned}
\tag{4.34}
$$

and then is put into recognizable patterns, such as:

$$
\begin{aligned}
Q_i^{n+1} = &-\frac{\alpha(1+\beta)}{2}(Q_i^n - 2Q_{i-1}^n + Q_{i-2}^n)\\
&-\left\{\left[\frac{\alpha(1+\beta)}{2}Q_i^n - \frac{\alpha^2}{2}(Q_i^n - Q_{i-1}^n)\right] - \left[\frac{\alpha(1+\beta)}{2}Q_{i-1}^n - \frac{\alpha^2}{2}(Q_{i-1}^n - Q_{i-2}^n)\right]\right\}\\
&+\left[\frac{(1+\beta)^2}{2}Q_i^n - \frac{\alpha(1+\beta)}{2}(Q_i^n - Q_{i-1}^n)\right] + \frac{Q_i^n}{2}.
\end{aligned}
\tag{4.35}
$$

After substituting $\alpha = \rho A$ and after further simplification:

$$
\begin{aligned}
Q_i^{n+1} = &-\frac{\rho(1+\beta)}{2}A(Q_i^n - 2Q_{i-1}^n + Q_{i-2}^n)\\
&-\frac{\rho}{2}A\{[(1+\beta)Q_i^n - \rho A(Q_i^n - Q_{i-1}^n)] - [(1+\beta)Q_{i-1}^n - \rho A(Q_{i-1}^n - Q_{i-2}^n)]\}\\
&+\frac{(1+\beta)}{2}[(1+\beta)Q_i^n - \rho A(Q_i^n - Q_{i-1}^n)] + \frac{Q_i^n}{2}.
\end{aligned}
\tag{4.36}
$$

The predictor is then defined by:

$$\overline{Q_i^{n+1}} = (1+\beta)Q_i^n - \rho A(Q_i^n - Q_{i-1}^n) = (1+\beta)Q_i^n - \rho \nabla F_i^n \tag{4.37}$$

and the corrector becomes:

$$Q_i^{n+1} = -\frac{\rho(1+\beta)}{2} A \nabla^2 Q_i^n - \frac{\rho}{2} A \left\{ \overline{Q_i^{n+1}} - \overline{Q_{i-1}^{n+1}} \right\} + \frac{(1+\beta)}{2} \overline{Q_i^{n+1}} + \frac{Q_i^n}{2}. \tag{4.38}$$

Hence, a fully backward version of the LW scheme (which is stable only for positive eigenvalues of $[A]$) is given by:

$$\begin{aligned} \overline{Q_i^{n+1}} &= (I + \Delta t K_i) Q_i^n - \frac{\Delta t}{\Delta x} \nabla (F^+)_i^n \\ Q_i^{n+1} &= \frac{1}{2}(Q_i^n + (I + \Delta t K_i)\overline{Q_i^{n+1}}) - \frac{\Delta t}{2\Delta x} \nabla (F^+)_i^{\overline{n+1}} - (I + \Delta t K) \frac{\Delta t}{2\Delta x} \nabla^2 (F^+)_i^n. \end{aligned} \tag{4.39}$$

4.1.3 Derivation of a Fully Forward Lax-Wendroff Scheme

The derivation of a forward differencing version of the LW scheme begins by considering the flux split Riemann problem:

$$Q_t + F_x^- = Q_t + [A^-] Q_x = [K] Q, ^* \tag{4.40}$$

and its generic solution:

$$Q_i^{n+1} = b_i Q_i^n + b_{i+1} Q_{i+1}^n + b_{i+2} Q_{i+2}^n, \tag{4.41}$$

where b_i, b_{i+1}, and b_{i+2} are unknown. The second order accurate Taylor's expansion of the terms Q_i^{n+1}, Q_{i+1}^n, and Q_{i+2}^n is given by:

$$Q_i^{n+1} = Q_i^n + \Delta t (Q_t)_i^n + \frac{\Delta t^2}{2} (Q_{tt})_i^n + O(\Delta t^3), \tag{4.42}$$

---

* Once more, the square brackets and the superscripts are dropped for brevity.

$$Q_{i+1}^n = Q_i^n + \Delta x(Q_x)_i^n + \frac{\Delta x^2}{2}(Q_{xx})_i^n + O(\Delta x^3), \tag{4.43}$$

$$Q_{i+2}^n = Q_i^n + 2\Delta x(Q_x)_i^n + \frac{4\Delta x^2}{2}(Q_{xx})_i^n + O(\Delta x^3). \tag{4.44}$$

Thus, (4.41) becomes:

$$\begin{aligned} &Q_i^n + \Delta t(Q_t)_i^n - \frac{\Delta t^2}{2}(Q_{tt})_i^n + O(\Delta t^3) \\ &\quad = b_i Q_i^n + b_{i+1}\left\{Q_i^n + \Delta x(Q_x)_i^n + \frac{\Delta x^2}{2}(Q_{xx})_i^n + O(\Delta x^3)\right\} \\ &\qquad b_{i+2}\left\{Q_i^n + 2\Delta x(Q_x)_i^n + \frac{4\Delta x^2}{2}(Q_{xx})_i^n + O(\Delta x^3)\right\} \end{aligned} \tag{4.45}$$

and after substituting terms from (4.8) and (4.1) for Q_{tt} and Q_t:

$$(Q_t)_i^n - \Delta t K A(Q_x)_i^n + \left\{\frac{1}{\Delta t} + \frac{\Delta t}{2}K^2\right\}Q_i^n + \frac{\Delta t}{2}A^2(Q_{xx})_i^n + O(\Delta t^2) =$$

$$\frac{b_i + b_{i+1} + b_{i+2}}{\Delta t}Q_i^n + \frac{\Delta x}{\Delta t}(b_{i+1} + 2b_{i+2})(Q_x)_i^n + \frac{\Delta x^2}{2\Delta t}(b_{i+1} + 4b_{i+2})(Q_{xx})_i^n + \frac{O(\Delta x^3)}{\Delta t}. \tag{4.46}$$

Again, the truncation errors of (4.46) imply that the approximation of the Riemann problem of (4.40) is second order accurate in both space and time.

After equating the coefficients of the like terms of (4.46) and using the notation of (4.30), the following system of equations is obtained:

$$\begin{aligned} b_i + b_{i+1} + b_{i+2} &= 1 + \beta + \frac{\beta^2}{2} \\ b_{i+1} + 2b_{i+2} &= -\alpha - \alpha\beta \\ b_{i+1} + 4b_{i+2} &= \alpha^2 \end{aligned} \tag{4.47}$$

where its solution is given by:

$$b_i = \frac{1}{2}(\alpha^2+\beta^2+3\alpha\beta+3\alpha+2\beta+2),$$
$$b_{i+1} = \alpha^2-2\alpha-2\alpha\beta,$$
$$b_{i+2} = \frac{1}{2}(\alpha^2-\alpha\beta-\alpha). \tag{4.48}$$

The above coefficients are substituted back into the initial update equation of (4.41); that is,

$$2Q_i^{n+1} = (\alpha^2+\beta^2+3\alpha\beta+2\beta+3\alpha+2)Q_i^n + (2\alpha^2-4\alpha\beta-4\alpha)Q_{i-1}^n + (\alpha^2-\alpha-\alpha\beta)Q_{i-2}^n \tag{4.49}$$

which is reorganized into:

$$\begin{aligned} Q_i^{n+1} = {} & \frac{\alpha(1+\beta)}{2}Q_i^n + \frac{\alpha^2}{2}Q_i^n + \frac{\alpha(1+\beta)}{2}Q_i^n + \frac{\alpha(1+\beta)}{2}Q_i^n + \frac{(1+\beta)^2}{2}Q_i^n + \frac{1}{2}Q_i^n \\ & - \frac{2\alpha(1+\beta)}{2}Q_{i+1}^n - \frac{2\alpha^2}{2}Q_{i+1}^n - \frac{\alpha(1+\beta)}{2}Q_{i+1}^n - \frac{\alpha(1+\beta)}{2}Q_{i+1}^n \\ & + \frac{\alpha(1+\beta)}{2}Q_{i+2}^n + \frac{\alpha^2}{2}Q_{i+2}^n \end{aligned} \tag{4.50}$$

and then is put into recognizable patterns,

$$\begin{aligned} Q_i^{n+1} = {} & \frac{\rho(1+\beta)}{2}A(Q_{i+2}^n - 2Q_{i+1}^n + Q_i^n) \\ & - \frac{\rho}{2}A\{[(1+\beta)Q_{i+1}^n - \rho A(Q_{i+2}^n - Q_{i+1}^n)] - [(1+\beta)Q_i^n - \rho A(Q_{i+1}^n - Q_i^n)]\} \\ & + \frac{(1+\beta)}{2}[(1+\beta)Q_i^n - \rho A(Q_{i+1}^n - Q_i^n)] + \frac{Q_i^n}{2}. \end{aligned} \tag{4.51}$$

Thus, the predictor is defined as:

$$\overline{Q_i^{n+1}} = (1+\beta)Q_i^n - \rho A(Q_{i+1}^n - Q_i^n) = (1+\beta)Q_i^n - \rho\Delta F_i^n, \tag{4.52}$$

and the corrector becomes:

$$Q_i^{n+1} = \frac{\rho(1+\beta)}{2}A\Delta^2 Q_i^n - \frac{\rho}{2}A\left\{\overline{Q_{i+1}^{n+1}} - \overline{Q_i^{n+1}}\right\} + \frac{(1+\beta)}{2}\overline{Q_i^{n+1}} + \frac{Q_i^n}{2}. \tag{4.53}$$

Hence, a fully forward differencing version of the LW scheme (which is stable only for negative eigenvalues of $[A]$) is given by:

$$\overline{Q_i^{n+1}} = (1+\Delta t K_i)Q_i^n - \frac{\Delta t}{\Delta x}\Delta(F^-)_i^n,$$

$$Q_i^{n+1} = \frac{1}{2}(Q_i^n + (1+\Delta t K_i)\overline{Q_i^{n+1}}) - \frac{\Delta t}{2\Delta x}\Delta(F^-)_i^{\overline{n+1}} + (I+\Delta t K)\frac{\Delta t}{2\Delta x}\Delta^2(F^-)_i^n. \tag{4.54}$$

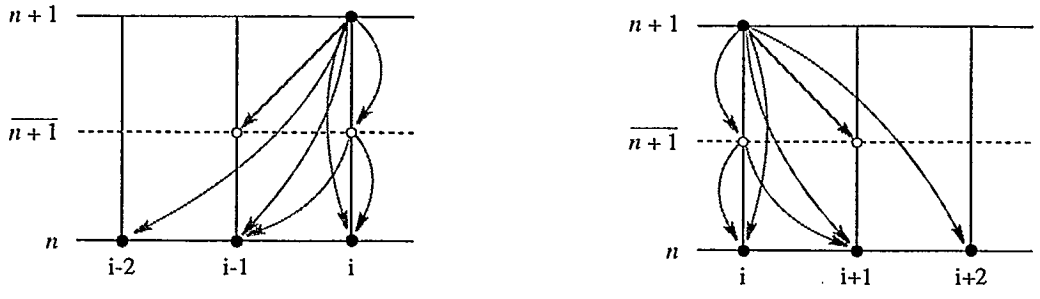

Figure 4.3. Numerical stencils for a Lax-Wendroff scheme: (Left) fully backward LW and (right) fully forward LW computational molecules

4.1.4 Derivation of a Fully Windward Lax-Wendroff Scheme

In the previous sections, two versions of the LW upwind algorithm were derived, each one suited for solving complementary flux split Riemann problems (see **Figure 4.3**). In contrast to **Section 3.3.3**, where the principle of superposition was utilized to split Riemann problems, the principle of superposition is now applied to devise a fully windward LW algorithm via combining the update equations of fully backward-forward LW schemes given by (4.39) and (4.54), respectively. These new update equations, which are capable of solving Riemann problems containing both negative and positive eigenvalues, are given by:

$$\overline{Q_i^{n+1}} = (I + \Delta t K_i) Q_i^n - \frac{\Delta t}{\Delta x} \nabla (F^+)_i^n - \frac{\Delta t}{\Delta x} \Delta (F^-)_i^n,$$

$$Q_i^{n+1} = \frac{1}{2}(Q_i^n + (I + \Delta t K_i)\overline{Q_i^{n+1}}) - \frac{\Delta t}{2\Delta x} \nabla (F^+)_i^{\overline{n+1}} - (I + \Delta t K_i) \frac{\Delta t}{2\Delta x} \nabla^2 (F^+)_i^n$$
$$- \frac{\Delta t}{2\Delta x} \Delta (F^-)_i^{\overline{n+1}} + (I + \Delta t K_i) \frac{\Delta t}{2\Delta x} \Delta^2 (F^-)_i^n. \quad (4.55)$$

4.2 Determination of Fluxes in the LW Scheme

In addition to the flux-vector splitting procedure (see **Section 3.3.2**), the ***flux-difference splitting*** technique [99] has also utilized for solving Euler equations via flux split Riemann solvers [24]. Both methods allow for shock waves to be captured at discontinuities using the modified Rankine-Hugoniot jump condition [100]. The main difference between these two methods is their approach to resolving fields at discontinuities. It has been shown that in the case of an inviscid flow simulation of CFD problems, the eigenvalues of the governing equations are functions of the dependent variables; thus, the generated *flux-vector split* expressions at best only approximate Riemann problems [26]. This class of problems is more accurately solved using the flux-difference splitting (with limiter) technique [101, 102]. However, in the case of CEM, the eigenvalues of the governing equations are independent of the EM fields; hence, the flux split Riemann problems more accurately model Maxwell's equations [26]. In addition, the discontinuities in a CEM problem are due to a change in material properties (with jump conditions located at cell interfaces), whereas in CFD, the discontinuities are often due to shocks encountered in supersonic flow, which are much more severe than in the case of a CEM simulation [89]. The difference in solution of time-dependent Maxwell's equations, formulated using either flux-difference splitting and flux-vector splitting schemes, has

been reported as insignificant [77]. Therefore, in this document, the flux-vector splitting procedure is preferred over the slightly more accurate but more complex and computationally less efficient flux-difference splitting technique.

4.2.1 Numerical Fluxes

The LW formulation given in (4.55) requires the calculation of split fluxes (and their respective coefficient matrices) at every point. It is more computationally efficient if these split fluxes are lumped together and then represented using a single variable. Previously, flux vectors were defined in terms of tangential field components on constant coordinate surfaces (see **Section 3.1.2**). In addition, these tangential components represent (and enforce) boundary conditions on computational cell surfaces. Since a ***cell-centred*** FVTD algorithm (where the field components are located in the centre of the computational cell) is of interest, the flux vectors have to be computed on the cell walls that are located at the half-grid points (*i.e.* $i+1/2$). On any given cell wall, a ***numerical flux***, $h^F_{i+1/2}$, is defined as the sum of total influx. Hence, the following numerical fluxes can be defined as (see **Figure 4.4**):

$$
\begin{aligned}
h^F_{i+1/2} &= (F^+)_i + (F^-)_{i+1}, \\
h^F_{i-1/2} &= (F^+)_{i-1} + (F^-)_i, \\
h^F_{i+3/2} &= (F^+)_{i+1} + (F^-)_{i+2}, \\
h^F_{i-3/2} &= (F^+)_{i-2} + (F^-)_{i-1}. \qquad (4.56)
\end{aligned}
$$

The flux split difference terms of the windward LW algorithm can be written in terms of the numerical fluxes defined in (4.56). In the case of the predictor

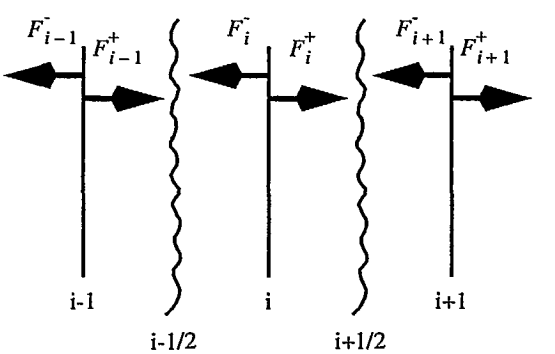

Figure 4.4. Numerical flux configuration in a windward scheme [22]

equation, the first order flux split difference terms are first expanded and then are reorganized into:

$$\begin{aligned}\nabla(F^+)_i^n + \Delta(F^-)_i^n &= (F^+)_i^n - (F^+)_{i-1}^n + (F^-)_{i+1}^n - (F^-)_i^n, \\ &= [(F^+)_i^n + (F^-)_{i+1}^n] - [(F^+)_{i-1}^n + (F^-)_i^n]. \end{aligned} \tag{4.57}$$

Subsequently, the above equation is compared to the expression of numerical fluxes given in (4.56). Thus, the first order flux split difference terms are given by:

$$\nabla(F^+)_i^n + \Delta(F^-)_i^n = (h_{i+1/2}^F)^n - (h_{i-1/2}^F)^n. \tag{4.58}$$

Similarly, the second order flux split difference terms of the corrector are written as:

$$\begin{aligned}&\nabla^2(F^+)_i^n - \Delta^2(F^-)_i^n = \\ &= (F^+)_i^n - (F^+)_{i-1}^n - (F^+)_{i-1}^n + (F^+)_{i-2}^n - (F^-)_{i+2}^n + (F^-)_{i+1}^n + (F^-)_{i+1}^n - (F^-)_i^n, \\ &= [(F^+)_i^n + (F^-)_{i+1}^n] - [(F^+)_{i-1}^n + (F^-)_i^n] + [(F^+)_{i-2}^n - (F^+)_{i-1}^n] - [-(F^-)_{i+1}^n + (F^-)_{i+2}^n] \\ &= (h_{i+1/2}^F)^n - (h_{i-1/2}^F)^n + [(F^+)_{i-2}^n - (F^+)_{i-1}^n] - [-(F^-)_{i+1}^n + (F^-)_{i+2}^n]. \end{aligned} \tag{4.59}$$

Using the definition of flux splitting, the split flux components can be rearranged to:

$$(F^+)_{i-1}^n = F_{i-1}^n - (F^-)_{i-1}^n \quad \text{and} \quad -(F^-)_{i+1}^n = -F_{i+1}^n + (F^+)_{i+1}^n. \tag{4.60}$$

After substituting (4.60) in (4.59), the expression for the second order flux split difference terms of the corrector becomes:

$$\begin{aligned}&\nabla^2(F^+)_i^n - \Delta^2(F^-)_i^n = \\ &= (h_{i+1/2}^F)^n - (h_{i-1/2}^F)^n + [(F^+)_{i-2}^n + (F^-)_{i-1}^n] - F_{i-1}^n - [(F^+)_{i+1}^n + (F^-)_{i+2}^n] + F_{i+1}^n \\ &= (h_{i+1/2}^F)^n - (h_{i-1/2}^F)^n + (h_{i-3/2}^F)^n - F_{i-1}^n - (h_{i+3/2}^F)^n + F_{i+1}^n. \end{aligned} \tag{4.61}$$

Thus, a fully upwind version of the LW algorithms can be written it terms of the numerical fluxes as:

$$\overline{\boldsymbol{Q}_i^{n+1}} = (\boldsymbol{I} + \Delta t \boldsymbol{K}_i)\boldsymbol{Q}_i^n - \frac{\Delta t}{\Delta x}[(\boldsymbol{h}_{i+1/2}^F)^n - (\boldsymbol{h}_{i-1/2}^F)^n]$$

$$\boldsymbol{Q}_i^{n+1} = \frac{1}{2}(\boldsymbol{Q}_i^n + (\boldsymbol{I} + \Delta t \boldsymbol{K}_i)\overline{\boldsymbol{Q}_i^{n+1}}) - \frac{\Delta t}{2\Delta x}\left[(\boldsymbol{h}_{i+1/2}^F)^{\overline{n+1}} - (\boldsymbol{h}_{i-1/2}^F)^{\overline{n+1}}\right]$$

$$- (\boldsymbol{I} + \Delta t \boldsymbol{K}_i)\frac{\Delta t}{2\Delta x}[(\boldsymbol{h}_{i-3/2}^F)^n - (\boldsymbol{h}_{i-1/2}^F)^n + (\boldsymbol{h}_{i+1/2}^F)^n - (\boldsymbol{h}_{i+3/2}^F)^n - \boldsymbol{F}_{i-1}^n + \boldsymbol{F}_{i+1}^n]. \tag{4.62}$$

4.2.2 Evaluation of Numerical Fluxes

The next step in developing the LW version of the FVTD algorithm is computing numerical fluxes located at cell boundaries (interfaces). However, in order to accurately model cell boundaries, the calculation of numerical fluxes at discontinuous regions (*i.e.* cell interfaces) must satisfy Maxwell's equations; that is, the variation of material properties (such as permittivity and permeability) on either side of the boundaries must be considered while allowing for the continuity of tangential electric and magnetic field components. In other words, the numerical fluxes have the same property as flux vectors but are located at $(i + 1/2, j, k)$; hence they are defined as:*

$$\boldsymbol{h}_{i+1/2,\,j,\,k}^E = \frac{1}{J}\begin{bmatrix} a_\xi \times \mathcal{E}_{i+1/2} \\ -a_\xi \times \mathcal{H}_{i+1/2} \end{bmatrix}_{j,\,k}. \quad \dagger \tag{4.63}$$

In **Section 3.3.1**, the unique solution to an initial value problem posed on a discontinuous region is given by the modified Rankine-Hugoniot jump relation,

$$\lambda_k \|\boldsymbol{Q}\| = \|\boldsymbol{E}\|, \tag{4.64}$$

where λ_k is the speed of propagation at the discontinuity given by the eigenvalues of the

* Although the current discussion revolves around the derivation of a 1D-FVTD algorithm, in the interest of completeness, 3D field components are operated on in order to facilitate future derivations.

† From this point onward, the superscript of the numerical flux vectors corresponds with the flux vectors that they are representing. For the definition and notation of flux vectors, see (3.27)-(3.29).

flux matrix, $[A]$ ($E = [A]Q$), and the *jump operator*, $\| \ \|$, is defined by the difference between the right and left quantities adjacent to the discontinuous surface (see **Section 3.3.1**). Therefore, at a constant surface, ξ, the jump condition for Maxwell's equations can be written by substituting (3.26) and (3.38) in (4.64);

$$\lambda_k \left\| \begin{matrix} \boldsymbol{B} \\ \boldsymbol{D} \end{matrix} \right\| = \left\| \begin{matrix} \boldsymbol{a}_\xi \times \mathcal{E} \\ -\boldsymbol{a}_\xi \times \mathcal{H} \end{matrix} \right\|. \tag{4.65}$$

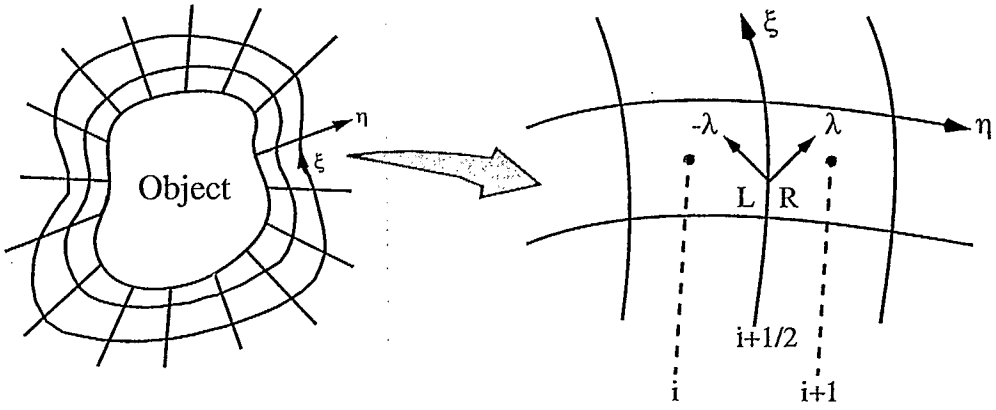

Figure 4.5. Visual representation of a jump condition at the interface between two cells [17]

The flux matrix, $[A]$, has at least three distinct eigenvalues given by (3.68) which indicate three distinct cases of jump conditions. These three cases can be represented in terms of the field and flux components of the cells using the jump operator (see **Figure 4.5**); that is:

(A) forward travelling waves ($\lambda > 0$)

$$\lambda \left\| \begin{matrix} \boldsymbol{B} \\ \boldsymbol{D} \end{matrix} \right\| = \left\| \begin{matrix} \boldsymbol{a}_\xi \times \mathcal{E} \\ -\boldsymbol{a}_\xi \times \mathcal{H} \end{matrix} \right\|$$

$$\lambda_{i+1,j,k} \begin{bmatrix} \boldsymbol{B}_{i+1} - \boldsymbol{B}^R \\ \boldsymbol{D}_{i+1} - \boldsymbol{D}^R \end{bmatrix}_{j,k} = \begin{bmatrix} \boldsymbol{a}_\xi \times (\mathcal{E}_{i+1} - \mathcal{E}^R) \\ -\boldsymbol{a}_\xi \times (\mathcal{H}_{i+1} - \mathcal{H}^R) \end{bmatrix}_{j,k} \tag{4.66}$$

(B) backward travelling waves ($\lambda < 0$)

$$-\lambda \begin{Vmatrix} \boldsymbol{B} \\ \boldsymbol{D} \end{Vmatrix} = \begin{Vmatrix} \boldsymbol{a}_\xi \times \mathcal{E} \\ -\boldsymbol{a}_\xi \times \mathcal{H} \end{Vmatrix}$$

$$\lambda_{i,j,k} \begin{bmatrix} \boldsymbol{B}^L - \boldsymbol{B}_i \\ \boldsymbol{D}^L - \boldsymbol{D}_i \end{bmatrix}_{j,k} = \begin{bmatrix} \boldsymbol{a}_\xi \times (\mathcal{E}^L - \mathcal{E}_i) \\ -\boldsymbol{a}_\xi \times (\mathcal{H}^L - \mathcal{H}_i) \end{bmatrix}_{j,k} \tag{4.67}$$

(C) waves (surface currents) at the interface ($\lambda = 0$)*

$$\begin{Vmatrix} \boldsymbol{a}_\xi \times \mathcal{E} \\ -\boldsymbol{a}_\xi \times \mathcal{H} \end{Vmatrix} = \begin{bmatrix} \boldsymbol{a}_\xi \times (\mathcal{E}^R - \mathcal{E}^L) \\ -\boldsymbol{a}_\xi \times (\mathcal{H}^R - \mathcal{H}^L) \end{bmatrix}_{j,k} = 0, \tag{4.68}$$

where $\boldsymbol{D}^L, \boldsymbol{B}^L, \boldsymbol{D}^R, \boldsymbol{B}^R$ are flux components and $\mathcal{E}^L, \mathcal{H}^L, \mathcal{E}^R, \mathcal{H}^R$ are field components on the cell boundaries located at $i + 1/2$. Since the tangential components of both the electric and magnetic field components are continuous across the boundary between two media (in absence of a current sheet at the boundary), (4.68) can be re-written as:

$$\begin{bmatrix} \boldsymbol{a}_\xi \times \mathcal{E}^R \\ -\boldsymbol{a}_\xi \times \mathcal{H}^R \end{bmatrix}_{j,k} = \begin{bmatrix} \boldsymbol{a}_\xi \times \mathcal{E}^L \\ -\boldsymbol{a}_\xi \times \mathcal{H}^L \end{bmatrix}_{j,k} = \begin{bmatrix} \boldsymbol{a}_\xi \times \mathcal{E}_{i+1/2} \\ -\boldsymbol{a}_\xi \times \mathcal{H}_{i+1/2} \end{bmatrix}_{j,k}, \tag{4.69}$$

where (4.69) represents the numerical flux terms defined in (4.62). These numerical fluxes must be represented (evaluated) in terms of field components located at the centre of the cells as well as the cells' properties. The derivation of these expressions is considered next.

The second rows of equations (4.66) and (4.67) are modified using the characteristic admittance ($Y = \mu\lambda = \sqrt{\varepsilon/\mu}$).

$$\begin{aligned} Y_{i+1,j,k}(\mathcal{E}_{i+1} - \mathcal{E}^R)_{j,k} &= -\boldsymbol{a}_\xi \times (\mathcal{H}_{i+1} - \mathcal{H}^R)_{j,k} \\ Y_{i,j,k}(\mathcal{E}^L - \mathcal{E}_i)_{j,k} &= \boldsymbol{a}_\xi \times (\mathcal{H}^L - \mathcal{H}_i)_{j,k} \end{aligned} \tag{4.70}$$

---

* Only valid for the case of no thin resistive sheet at the cells' interface.

First, the vector product of a unitary vector, a_ξ, and both of the above equations are obtained. Then $a_\xi \times \mathcal{E}^R$ is substituted from (4.69), and the system of equations of (4.70) is solved for $a_\xi \times \mathcal{E}_{i+1/2}$ terms.

$$(Y_{i+1} + Y_i)_{j,k}(a_\xi \times \mathcal{E}_{i+1/2})_{j,k} =$$
$$= Y_{i+1,j,k}(a_\xi \times \mathcal{E})_{i+1,j,k} + Y_{i,j,k}(a_\xi \times \mathcal{E})_{i,j,k} + a_\xi \times (a_\xi \times (\mathcal{H}_{i+1} - \mathcal{H}_i)_{j,k}) \quad (4.71)$$

The definition of characteristic impedance ($Z = \varepsilon\lambda = \sqrt{\mu/\varepsilon}$) is used to modify the first rows of equations (4.66) and (4.67):

$$Z_{i+1,j,k}(\mathcal{H}_{i+1} - \mathcal{H}^R)_{j,k} = a_\xi \times (\mathcal{E}_{i+1} - \mathcal{E}^R)_{j,k}$$
$$Z_{i,j,k}(\mathcal{H}^L - \mathcal{H}_i)_{j,k} = -a_\xi \times (\mathcal{E}^L - \mathcal{E}_i)_{j,k} \quad (4.72)$$

Using a similar procedure as before, the above system of equations is solved for $a_\xi \times \mathcal{H}_{i+1/2}$ terms.

$$(Z_{i+1} + Z_i)_{j,k}(a_\xi \times \mathcal{H}_{i+1/2})_{j,k} =$$
$$= Z_{i+1,j,k}(a_\xi \times \mathcal{H})_{i+1,j,k} + Z_{i,j,k}(a_\xi \times \mathcal{H})_{i,j,k} - a_\xi \times (a_\xi \times (\mathcal{E}_{i+1} - \mathcal{E}_i)_{j,k}) \quad (4.73)$$

Then, equations (4.71) and (4.73) are substituted in (4.63) where an expression for the numerical flux at the cell boundaries is given as:

$$h^E_{i+1/2,j,k} = \frac{1}{J}\begin{bmatrix} a_\xi \times \mathcal{E} \\ -a_\xi \times \mathcal{H} \end{bmatrix}_{i+1/2,j,k} =$$
$$\begin{bmatrix} \frac{Y_{i+1}(a_\xi \times \mathcal{E}_{i+1})}{(Y_{i+1} + Y_i)} \\ \frac{Z_{i+1}(a_\xi \times \mathcal{H}_{i+1})}{Z_{i+1} + Z_i} \end{bmatrix}_{j,k} + \begin{bmatrix} \frac{Y_i(a_\xi \times \mathcal{E}_i)}{Y_{i+1} + Y_i} \\ \frac{Z_i(a_\xi \times \mathcal{H}_i)}{Z_{i+1} + Z_i} \end{bmatrix}_{j,k} + \begin{bmatrix} \frac{a_\xi \times (a_\xi \times \mathcal{E}_{i+1})}{Y_{i+1} + Y_i} \\ \frac{a_\xi \times (a_\xi \times \mathcal{H}_{i+1})}{Z_{i+1} + Z_i} \end{bmatrix}_{j,k} - \begin{bmatrix} \frac{a_\xi \times (a_\xi \times \mathcal{E}_i)}{Y_{i+1} + Y_i} \\ \frac{a_\xi \times (a_\xi \times \mathcal{H}_i)}{Z_{i+1} + Z_i} \end{bmatrix}_{j,k}$$
(4.74)

The above expression is then evaluated in terms of Cartesian field components; that is:*

$$h^{E}_{i+1/2,\,j,\,k} = \frac{1}{J}\begin{bmatrix} a_\xi \times \mathcal{E} \\ -a_\xi \times \mathcal{H} \end{bmatrix}_{i+1/2,\,j,\,k}$$

$$= \begin{bmatrix} \dfrac{Y_{i+1}(\xi_y E_z - \xi_z E_y)_{i+1}}{Y_{i+1}+Y_i} \\ \dfrac{Y_{i+1}(\xi_z E_x - \xi_x E_z)_{i+1}}{Y_{i+1}+Y_i} \\ \dfrac{Y_{i+1}(\xi_x E_y - \xi_y E_x)_{i+1}}{Y_{i+1}+Y_i} \\ \dfrac{Z_{i+1}(\xi_z H_y - \xi_y H_z)_{i+1}}{Z_{i+1}+Z_i} \\ \dfrac{Z_{i+1}(\xi_x H_z - \xi_z H_x)_{i+1}}{Z_{i+1}+Z_i} \\ \dfrac{Z_{i+1}(\xi_y H_x - \xi_x H_y)_{i+1}}{Z_{i+1}+Z_i} \end{bmatrix}_{j,k} + \begin{bmatrix} \dfrac{Y_i(\xi_y E_z - \xi_z E_y)_i}{Y_{i+1}+Y_i} \\ \dfrac{Y_i(\xi_z E_x - \xi_x E_z)_i}{Y_{i+1}+Y_i} \\ \dfrac{Y_i(\xi_x E_y - \xi_y E_x)_i}{Y_{i+1}+Y_i} \\ \dfrac{Z_i(\xi_z H_y - \xi_y H_z)_i}{Z_{i+1}+Z_i} \\ \dfrac{Z_i(\xi_x H_z - \xi_z H_x)_i}{Z_{i+1}+Z_i} \\ \dfrac{Z_i(\xi_y H_x - \xi_x H_y)_i}{Z_{i+1}+Z_i} \end{bmatrix}_{j,k}$$

$$= \begin{bmatrix} \dfrac{(-(\xi_y^2+\xi_z^2)H_x + \xi_x\xi_y H_y + \xi_x\xi_z H_z)_{i+1}}{Y_{i+1}+Y_i} \\ \dfrac{(\xi_x\xi_y H_x - (\xi_x^2+\xi_z^2)H_y + \xi_y\xi_z H_z)_{i+1}}{Y_{i+1}+Y_i} \\ \dfrac{(\xi_x\xi_z H_x + \xi_y\xi_z H_y - (\xi_x^2+\xi_y^2)H_z)_{i+1}}{Y_{i+1}+Y_i} \\ \dfrac{(-(\xi_y^2+\xi_z^2)E_x + \xi_x\xi_y E_y + \xi_x\xi_z E_z)_{i+1}}{Z_{i+1}+Z_i} \\ \dfrac{(\xi_x\xi_z E_x + \xi_y\xi_z E_y - (\xi_x^2+\xi_y^2)E_z)_{i+1}}{Z_{i+1}+Z_i} \\ \dfrac{(\xi_x\xi_z E_x + \xi_y\xi_z E_y - (\xi_x^2+\xi_y^2)E_z)_{i+1}}{Z_{i+1}+Z_i} \end{bmatrix}_{j,k} - \begin{bmatrix} \dfrac{(-(\xi_y^2+\xi_z^2)H_x + \xi_x\xi_y H_y + \xi_x\xi_z H_z)_i}{Y_{i+1}+Y_i} \\ \dfrac{(\xi_x\xi_y H_x - (\xi_x^2+\xi_z^2)H_y + \xi_y\xi_z H_z)_i}{Y_{i+1}+Y_i} \\ \dfrac{(\xi_x\xi_z H_x + \xi_y\xi_z H_y - (\xi_x^2+\xi_y^2)H_z)_i}{Y_{i+1}+Y_i} \\ \dfrac{(-(\xi_y^2+\xi_z^2)E_x + \xi_x\xi_y E_y + \xi_x\xi_z E_z)_i}{Z_{i+1}+Z_i} \\ \dfrac{(\xi_x\xi_z E_x + \xi_y\xi_z E_y - (\xi_x^2+\xi_y^2)E_z)_i}{Z_{i+1}+Z_i} \\ \dfrac{(\xi_x\xi_z E_x + \xi_y\xi_z E_y - (\xi_x^2+\xi_y^2)E_z)_i}{Z_{i+1}+Z_i} \end{bmatrix}_{j,k} \tag{4.75}$$

Next, the impedance, $Z_{i,\,j,\,k}$, and admittance, $Y_{i,\,j,\,k}$, of each cell are defined as:

* One must note that the Jacobian of transformation has been dropped for brevity. Thus, each field component, say H_x, in fact represents H_x/J, *etc.*

$$Z_{i,j,k} = (\mu\bar{c})_{i,j,k} \text{ and } \quad Y_{i,j,k} = (\varepsilon\bar{c})_{i,j,k}, \tag{4.76}$$

where $\bar{c}_{i,j,k}$ is the speed of wave propagation within a cell centred at (i, j, k). The speed of propagation within a cell in the general coordinate system is given by the magnitude of the eigenvalues of the flux matrix. Therefore, for numerical fluxes which represent an $\boldsymbol{E}$ flux vector, the eigenvalues of $[\boldsymbol{A}]$ are given by (3.68); thus

$$\left|(\lambda_\xi)_{i,j,k}\right| = \bar{c}_{i,j,k} = \left(\frac{\sqrt{\xi_x^2+\xi_y^2+\xi_z^2}}{\sqrt{\varepsilon\mu}}\right)_{i,j,k}. \tag{4.77}$$

Finally, expressions for each component of the numerical flux, located on ξ-constant surfaces, are obtained by expanding and simplifying (4.75) and are given below. In the following expressions, $]_{\boldsymbol{m}}$ denotes the $\boldsymbol{m}\,\boldsymbol{th}$ component of the numerical flux vector at the specified cell boundary. Thus, flux vectors at $(i+1/2, j, k)$ are given by:

$$h^E_{i+\frac{1}{2},j,k}\Big]_1 = \left(\frac{\bar{c}_{i+1}(\xi_y D_z - \xi_z D_y)_{i+1} + \bar{c}_i(\xi_y D_z - \xi_z D_y)_i}{(\varepsilon\bar{c})_{i+1} + (\varepsilon\bar{c})_i}\right)_{j,k}$$
$$+\left(\frac{\left(\frac{-(\xi_y^2+\xi_z^2)B_x + \xi_x\xi_y B_y + \xi_x\xi_z B_z}{\mu}\right)_{i+1} + \left(\frac{(\xi_y^2+\xi_z^2)B_x - \xi_x\xi_y B_y - \xi_x\xi_z B_z}{\mu}\right)_i}{(\varepsilon\bar{c})_{i+1} + (\varepsilon\bar{c})_i}\right)_{j,k} \tag{4.78}$$

$$h^E_{i+\frac{1}{2},j,k}\Big]_2 = \left(\frac{\bar{c}_{i+1}(\xi_z D_x - \xi_x D_z)_{i+1} + \bar{c}_i(\xi_z D_x - \xi_x D_z)_i}{(\varepsilon\bar{c})_{i+1} + (\varepsilon\bar{c})_i}\right)_{j,k}$$
$$+\left(\frac{\left(\frac{\xi_x\xi_y B_x - (\xi_x^2+\xi_z^2)B_y + \xi_y\xi_z B_z}{\mu}\right)_{i+1} + \left(\frac{-\xi_x\xi_y B_x + (\xi_x^2+\xi_z^2)B_y - \xi_y\xi_z B_z}{\mu}\right)_i}{(\varepsilon\bar{c})_{i+1} + (\varepsilon\bar{c})_i}\right)_{j,k} \tag{4.79}$$

$$h^E_{i+\frac{1}{2},j,k}\Big]_3 = \left(\frac{\bar{c}_{i+1}(\xi_x D_y - \xi_y D_x)_{i+1} + \bar{c}_i(\xi_x D_y - \xi_y D_x)_i}{(\varepsilon\bar{c})_{i+1} + (\varepsilon\bar{c})_i}\right)_{j,k}$$

$$+ \left(\frac{\left(\frac{\xi_x\xi_z B_x + \xi_y\xi_z B_y - (\xi_x^2+\xi_y^2)B_z}{\mu}\right)_{i+1} + \left(\frac{-\xi_x\xi_z B_x - \xi_y\xi_z B_y + (\xi_x^2+\xi_y^2)B_z}{\mu}\right)_i}{(\varepsilon\bar{c})_{i+1} + (\varepsilon\bar{c})_i}\right)_{j,k} \tag{4.80}$$

$$h^E_{i+\frac{1}{2},j,k}\Big]_4 = \left(\frac{\bar{c}_{i+1}(\xi_z B_y - \xi_y B_z)_{i+1} + \bar{c}_i(\xi_z B_y - \xi_y B_z)_i}{(\mu\bar{c})_{i+1} + (\mu\bar{c})_i}\right)_{j,k}$$

$$+ \left(\frac{\left(\frac{-(\xi_y^2+\xi_z^2)D_x + \xi_x\xi_y D_y + \xi_x\xi_z D_z}{\varepsilon}\right)_{i+1} + \left(\frac{(\xi_y^2+\xi_z^2)D_x - \xi_x\xi_y D_y - \xi_x\xi_z D_z}{\varepsilon}\right)_i}{(\mu\bar{c})_{i+1} + (\mu\bar{c})_i}\right)_{j,k} \tag{4.81}$$

$$h^E_{i+\frac{1}{2},j,k}\Big]_5 = \left(\frac{\bar{c}_{i+1}(\xi_x B_z - \xi_z B_x)_{i+1} + \bar{c}_i(\xi_x B_z - \xi_z B_x)_i}{(\mu\bar{c})_{i+1} + (\mu\bar{c})_i}\right)_{j,k}$$

$$+ \left(\frac{\left(\frac{\xi_x\xi_y D_x - (\xi_x^2+\xi_z^2)D_y + \xi_y\xi_z D_z}{\varepsilon}\right)_{i+1} + \left(\frac{-\xi_x\xi_y D_x + (\xi_x^2+\xi_z^2)D_y - \xi_y\xi_z D_z}{\varepsilon}\right)_i}{(\mu\bar{c})_{i+1} + (\mu\bar{c})_i}\right)_{j,k} \tag{4.82}$$

$$h^E_{i+\frac{1}{2},j,k}\Big]_6 = \left(\frac{\bar{c}_{i+1}(\xi_y B_x - \xi_x B_y)_{i+1} + \bar{c}_i(\xi_y B_x - \xi_x B_y)_i}{(\mu\bar{c})_{i+1} + (\mu\bar{c})_i}\right)_{j,k}$$

$$+ \left(\frac{\left(\frac{\xi_x\xi_z D_x + \xi_y\xi_z D_y - (\xi_x^2+\xi_y^2)D_z}{\varepsilon}\right)_{i+1} + \left(\frac{-\xi_x\xi_z D_x - \xi_y\xi_z D_y + (\xi_x^2+\xi_y^2)D_z}{\varepsilon}\right)_i}{(\mu\bar{c})_{i+1} + (\mu\bar{c})_i}\right)_{j,k} \tag{4.83}$$

Likewise, numerical flux components located at $(i-1/2,\, j,\, k)$ are computed via:

$$h^E_{i-\frac{1}{2},j,k}\Big]_1 = \left(\frac{\bar{c}_i(\xi_y D_z - \xi_z D_y)_i + \bar{c}_{i-1}(\xi_y D_z - \xi_z D_y)_{i-1}}{(\varepsilon\bar{c})_i + (\varepsilon\bar{c})_{i-1}}\right)_{j,k}$$

$$+\left(\frac{\left(\frac{-(\xi_y^2+\xi_z^2)B_x + \xi_x\xi_y B_y + \xi_x\xi_z B_z}{\mu}\right)_i + \left(\frac{(\xi_y^2+\xi_z^2)B_x - \xi_x\xi_y B_y - \xi_x\xi_z B_z}{\mu}\right)_{i-1}}{(\varepsilon\bar{c})_i + (\varepsilon\bar{c})_{i-1}}\right)_{j,k} \tag{4.84}$$

$$h^E_{i-\frac{1}{2},j,k}\Big]_2 = \left(\frac{\bar{c}_i(\xi_z D_x - \xi_x D_z)_i + \bar{c}_{i-1}(\xi_z D_x - \xi_x D_z)_{i-1}}{(\varepsilon\bar{c})_i + (\varepsilon\bar{c})_{i-1}}\right)_{j,k}$$

$$+\left(\frac{\left(\frac{\xi_x\xi_y B_x - (\xi_x^2+\xi_z^2)B_y + \xi_y\xi_z B_z}{\mu}\right)_i + \left(\frac{-\xi_x\xi_y B_x + (\xi_x^2+\xi_z^2)B_y - \xi_y\xi_z B_z}{\mu}\right)_{i-1}}{(\varepsilon\bar{c})_i + (\varepsilon\bar{c})_{i-1}}\right)_{j,k} \tag{4.85}$$

$$h^E_{i-\frac{1}{2},j,k}\Big]_3 = \left(\frac{\bar{c}_i(\xi_x D_y - \xi_y D_x)_i + \bar{c}_{i-1}(\xi_x D_y - \xi_y D_x)_{i-1}}{(\varepsilon\bar{c})_i + (\varepsilon\bar{c})_{i-1}}\right)_{j,k}$$

$$+\left(\frac{\left(\frac{\xi_x\xi_z B_x + \xi_y\xi_z B_y - (\xi_x^2+\xi_y^2)B_z}{\mu}\right)_i + \left(\frac{-\xi_x\xi_z B_x - \xi_y\xi_z B_y + (\xi_x^2+\xi_y^2)B_z}{\mu}\right)_{i-1}}{(\varepsilon\bar{c})_i + (\varepsilon\bar{c})_{i-1}}\right)_{j,k} \tag{4.86}$$

$$h^E_{i-\frac{1}{2},j,k}\Big]_4 = \left(\frac{\bar{c}_i(\xi_z B_y - \xi_y B_z)_i + \bar{c}_{i-1}(\xi_z B_y - \xi_y B_z)_{i-1}}{(\mu\bar{c})_i + (\mu\bar{c})_{i-1}}\right)_{j,k}$$

$$+\left(\frac{\left(\frac{-(\xi_y^2+\xi_z^2)D_x + \xi_x\xi_y D_y + \xi_x\xi_z D_z}{\varepsilon}\right)_i + \left(\frac{(\xi_y^2+\xi_z^2)D_x - \xi_x\xi_y D_y - \xi_x\xi_z D_z}{\varepsilon}\right)_{i-1}}{(\mu\bar{c})_i + (\mu\bar{c})_{i-1}}\right)_{j,k} \tag{4.87}$$

$$h^E_{i-\frac{1}{2},j,k}\Big]_5 = \left(\frac{\bar{c}_i(\xi_x B_z - \xi_z B_x)_i + \bar{c}_{i-1}(\xi_x B_z - \xi_z B_x)_{i-1}}{(\mu\bar{c})_i + (\mu\bar{c})_{i-1}}\right)_{j,k}$$

$$+\left(\frac{\left(\frac{\xi_x\xi_y D_x - (\xi_x^2+\xi_z^2)D_y + \xi_y\xi_z D_z}{\varepsilon}\right)_i + \left(\frac{-\xi_x\xi_y D_x + (\xi_x^2+\xi_z^2)D_y - \xi_y\xi_z D_z}{\varepsilon}\right)_{i-1}}{(\mu\bar{c})_i + (\mu\bar{c})_{i-1}}\right)_{j,k} \tag{4.88}$$

$$h^E_{i-\frac{1}{2},j,k}\Big]_6 = \left(\frac{\bar{c}_i(\xi_y B_x - \xi_x B_y)_i + \bar{c}_{i-1}(\xi_y B_x - \xi_x B_y)_{i-1}}{(\mu\bar{c})_i + (\mu\bar{c})_{i-1}}\right)_{j,k}$$

$$+\left(\frac{\left(\frac{\xi_x\xi_z D_x + \xi_y\xi_z D_y - (\xi_x^2+\xi_y^2)D_z}{\varepsilon}\right)_i + \left(\frac{-\xi_x\xi_z D_x - \xi_y\xi_z D_y + (\xi_x^2+\xi_y^2)D_z}{\varepsilon}\right)_{i-1}}{(\mu\bar{c})_i + (\mu\bar{c})_{i-1}}\right)_{j,k} \tag{4.89}$$

Similarly, numerical flux components at $(i+3/2,\ j,\ k)$ are calculated by:

$$h^E_{i+\frac{3}{2},j,k}\Big]_1 = \left(\frac{\bar{c}_{i+2}(\xi_y D_z - \xi_z D_y)_{i+2} + \bar{c}_{i+1}(\xi_y D_z - \xi_z D_y)_{i+1}}{(\varepsilon\bar{c})_{i+2} + (\varepsilon\bar{c})_{i+1}}\right)_{j,k}$$

$$+\left(\frac{\left(\frac{-(\xi_y^2+\xi_z^2)B_x + \xi_x\xi_y B_y + \xi_x\xi_z B_z}{\mu}\right)_{i+2} + \left(\frac{(\xi_y^2+\xi_z^2)B_x - \xi_x\xi_y B_y - \xi_x\xi_z B_z}{\mu}\right)_{i+1}}{(\varepsilon\bar{c})_{i+2} + (\varepsilon\bar{c})_{i+1}}\right)_{j,k} \tag{4.90}$$

$$h^E_{i+\frac{3}{2},j,k}\Big]_2 = \left(\frac{\bar{c}_{i+2}(\xi_z D_x - \xi_x D_z)_{i+2} + \bar{c}_{i+1}(\xi_z D_x - \xi_x D_z)_{i+1}}{(\varepsilon\bar{c})_{i+2} + (\varepsilon\bar{c})_{i+1}}\right)_{j,k}$$

$$+\left(\frac{\left(\frac{\xi_x\xi_y B_x - (\xi_x^2+\xi_z^2)B_y + \xi_y\xi_z B_z}{\mu}\right)_{i+2} + \left(\frac{-\xi_x\xi_y B_x + (\xi_x^2+\xi_z^2)B_y - \xi_y\xi_z B_z}{\mu}\right)_{i+1}}{(\varepsilon\bar{c})_{i+2} + (\varepsilon\bar{c})_{i+1}}\right)_{j,k} \tag{4.91}$$

$$h^E_{i+\frac{3}{2},j,k}\Big]_3 = \left(\frac{\bar{c}_{i+2}(\xi_x D_y - \xi_y D_x)_{i+2} + \bar{c}_{i+1}(\xi_x D_y - \xi_y D_x)_{i+1}}{(\varepsilon\bar{c})_{i+2} + (\varepsilon\bar{c})_{i+1}}\right)_{j,k}$$

$$+ \left(\frac{\left(\frac{\xi_x\xi_z B_x + \xi_y\xi_z B_y - (\xi_x^2+\xi_y^2)B_z}{\mu}\right)_{i+2} + \left(\frac{-\xi_x\xi_z B_x - \xi_y\xi_z B_y + (\xi_x^2+\xi_y^2)B_z}{\mu}\right)_{i+1}}{(\varepsilon\bar{c})_{i+2} + (\varepsilon\bar{c})_{i+1}}\right)_{j,k} \tag{4.92}$$

$$h^E_{i+\frac{3}{2},j,k}\Big]_4 = \left(\frac{\bar{c}_{i+2}(\xi_z B_y - \xi_y B_z)_{i+2} + \bar{c}_{i+1}(\xi_z B_y - \xi_y B_z)_{i+1}}{(\mu\bar{c})_{i+2} + (\mu\bar{c})_{i+1}}\right)_{j,k}$$

$$+ \left(\frac{\left(\frac{-(\xi_y^2+\xi_z^2)D_x + \xi_x\xi_y D_y + \xi_x\xi_z D_z}{\varepsilon}\right)_{i+2} + \left(\frac{(\xi_y^2+\xi_z^2)D_x - \xi_x\xi_y D_y - \xi_x\xi_z D_z}{\varepsilon}\right)_{i+1}}{(\mu\bar{c})_{i+2} + (\mu\bar{c})_{i+1}}\right)_{j,k} \tag{4.93}$$

$$h^E_{i+\frac{3}{2},j,k}\Big]_5 = \left(\frac{\bar{c}_{i+2}(\xi_x B_z - \xi_z B_x)_{i+2} + \bar{c}_{i+1}(\xi_x B_z - \xi_z B_x)_{i+1}}{(\mu\bar{c})_{i+2} + (\mu\bar{c})_{i+1}}\right)_{j,k}$$

$$+ \left(\frac{\left(\frac{\xi_x\xi_y D_x - (\xi_x^2+\xi_z^2)D_y + \xi_y\xi_z D_z}{\varepsilon}\right)_{i+2} + \left(\frac{-\xi_x\xi_y D_x + (\xi_x^2+\xi_z^2)D_y - \xi_y\xi_z D_z}{\varepsilon}\right)_{i+1}}{(\mu\bar{c})_{i+2} + (\mu\bar{c})_{i+1}}\right)_{j,k} \tag{4.94}$$

$$h^E_{i+\frac{3}{2},j,k}\Big]_6 = \left(\frac{\bar{c}_{i+2}(\xi_y B_x - \xi_x B_y)_{i+2} + \bar{c}_{i+1}(\xi_y B_x - \xi_x B_y)_{i+1}}{(\mu\bar{c})_{i+2} + (\mu\bar{c})_{i+1}}\right)_{j,k}$$

$$+ \left(\frac{\left(\frac{\xi_x\xi_z D_x + \xi_y\xi_z D_y - (\xi_x^2+\xi_y^2)D_z}{\varepsilon}\right)_{i+2} + \left(\frac{-\xi_x\xi_z D_x - \xi_y\xi_z D_y + (\xi_x^2+\xi_y^2)D_z}{\varepsilon}\right)_{i+1}}{(\mu\bar{c})_{i+2} + (\mu\bar{c})_{i+1}}\right)_{j,k} \tag{4.95}$$

Finally, the components of the numerical flux of cell boundary $(i-3/2,\ j,\ k)$ are given by:

$$h^E_{i-\frac{3}{2},j,k}\Big]_1 = \left(\frac{\bar{c}_{i-1}(\xi_y D_z - \xi_z D_y)_{i-1} + \bar{c}_{i-2}(\xi_y D_z - \xi_z D_y)_{i-2}}{(\varepsilon\bar{c})_{i-1} + (\varepsilon\bar{c})_{i-2}}\right)_{j,k}$$

$$+\left(\frac{\left(\frac{-(\xi_y^2+\xi_z^2)B_x + \xi_x\xi_y B_y + \xi_x\xi_z B_z}{\mu}\right)_{i-1} + \left(\frac{(\xi_y^2+\xi_z^2)B_x - \xi_x\xi_y B_y - \xi_x\xi_z B_z}{\mu}\right)_{i-2}}{(\varepsilon\bar{c})_{i-1} + (\varepsilon\bar{c})_{i-2}}\right)_{j,k} \tag{4.96}$$

$$h^E_{i-\frac{3}{2},j,k}\Big]_2 = \left(\frac{\bar{c}_{i-1}(\xi_z D_x - \xi_x D_z)_{i-1} + \bar{c}_{i-2}(\xi_z D_x - \xi_x D_z)_{i-2}}{(\varepsilon\bar{c})_{i-1} + (\varepsilon\bar{c})_{i-2}}\right)_{j,k}$$

$$+\left(\frac{\left(\frac{\xi_x\xi_y B_x - (\xi_x^2+\xi_z^2)B_y + \xi_y\xi_z B_z}{\mu}\right)_{i-1} + \left(\frac{-\xi_x\xi_y B_x + (\xi_x^2+\xi_z^2)B_y - \xi_y\xi_z B_z}{\mu}\right)_{i-2}}{(\varepsilon\bar{c})_{i-1} + (\varepsilon\bar{c})_{i-2}}\right)_{j,k} \tag{4.97}$$

$$h^E_{i-\frac{3}{2},j,k}\Big]_3 = \left(\frac{\bar{c}_{i-1}(\xi_x D_y - \xi_y D_x)_{i-1} + \bar{c}_{i-2}(\xi_x D_y - \xi_y D_x)_{i-2}}{(\varepsilon\bar{c})_{i-1} + (\varepsilon\bar{c})_{i-2}}\right)_{j,k}$$

$$+\left(\frac{\left(\frac{\xi_x\xi_z B_x + \xi_y\xi_z B_y - (\xi_x^2+\xi_y^2)B_z}{\mu}\right)_{i-1} + \left(\frac{-\xi_x\xi_z B_x - \xi_y\xi_z B_y + (\xi_x^2+\xi_y^2)B_z}{\mu}\right)_{i-2}}{(\varepsilon\bar{c})_{i-1} + (\varepsilon\bar{c})_{i-2}}\right)_{j,k} \tag{4.98}$$

$$h^E_{i-\frac{3}{2},j,k}\Big]_4 = \left(\frac{\bar{c}_{i-1}(\xi_z B_y - \xi_y B_z)_{i-1} + \bar{c}_{i-2}(\xi_z B_y - \xi_y B_z)_{i-2}}{(\mu\bar{c})_{i-1} + (\mu\bar{c})_{i-2}}\right)_{j,k}$$

$$+\left(\frac{\left(\frac{-(\xi_y^2+\xi_z^2)D_x + \xi_x\xi_y D_y + \xi_x\xi_z D_z}{\varepsilon}\right)_{i-1} + \left(\frac{(\xi_y^2+\xi_z^2)D_x - \xi_x\xi_y D_y - \xi_x\xi_z D_z}{\varepsilon}\right)_{i-2}}{(\mu\bar{c})_{i-1} + (\mu\bar{c})_{i-2}}\right)_{j,k} \tag{4.99}$$

$$h^E_{i-\frac{3}{2},j,k}\Big]_5 = \left(\frac{\bar{c}_{i-1}(\xi_x B_z - \xi_z B_x)_{i-1} + \bar{c}_{i-2}(\xi_x B_z - \xi_z B_x)_{i-2}}{(\mu\bar{c})_{i-1} + (\mu\bar{c})_{i-2}}\right)_{j,k}$$

$$+ \left(\frac{\left(\frac{\xi_x\xi_y D_x - (\xi_x^2 + \xi_z^2)D_y + \xi_y\xi_z D_z}{\varepsilon}\right)_{i-1} + \left(\frac{-\xi_x\xi_y D_x + (\xi_x^2 + \xi_z^2)D_y - \xi_y\xi_z D_z}{\varepsilon}\right)_{i-2}}{(\mu\bar{c})_{i-1} + (\mu\bar{c})_{i-2}} \right)_{j,k} \tag{4.100}$$

$$h^E_{i-\frac{3}{2},j,k}\Big]_6 = \left(\frac{\bar{c}_{i-1}(\xi_y B_x - \xi_x B_y)_{i-1} + \bar{c}_{i-2}(\xi_y B_x - \xi_x B_y)_{i-2}}{(\mu\bar{c})_{i-1} + (\mu\bar{c})_{i-2}}\right)_{j,k}$$

$$+ \left(\frac{\left(\frac{\xi_x\xi_z D_x + \xi_y\xi_z D_y - (\xi_x^2 + \xi_y^2)D_z}{\varepsilon}\right)_{i-1} + \left(\frac{-\xi_x\xi_z D_x - \xi_y\xi_z D_y + (\xi_x^2 + \xi_y^2)D_z}{\varepsilon}\right)_{i-2}}{(\mu\bar{c})_{i-1} + (\mu\bar{c})_{i-2}} \right)_{j,k} \tag{4.101}$$

An identical procedure can be used to derive expressions for computing numerical fluxes on the η- and ζ- constant surfaces. These equations are similar to the ones previously discussed with the following two exceptions: (1) all ξ symbols denoting partial derivatives are replaced by η or ζ, respectively, and (2) i, j and k subscripts must be interchanged.

4.3 Summary of 3D-FVTD Algorithm

In **Section 4.1**, a fully windward LW algorithm for solving inhomogeneous Riemann problems of mixed eigenvalues was derived on a uniform rectangular grid; see (4.54). Since the computational space (ξ, η, ζ) is also a rectangular grid (see **Section 3.2.1**), the aforementioned Riemann solver can easily be applied to transformed Riemann problems where the flux and field components are the transformed vectors of the governing equations given by (3.26) to (3.30). Also, in order to better (and more efficiently) serve

CEM applications, the fully windward LW scheme of (4.54) has been further developed in terms of numerical fluxes and is given by equation (4.62); the general coordinate system components of the numerical fluxes are computed in terms of Cartesian coordinate field components which are defined in **Section 4.2.2.**

Since the original system of PDEs formulated by the generalised vector form of Maxwell's equations was split into three 1D Riemann problems of mixed eigenvalues (see **Section 3.3.3**), superposition can unite all three solutions under one update equation. Thus, the expressions for the predictor corrector of the 3D-FVTD algorithm are given by:

$$\overline{Q^{n+1}_{i,j,k}} = (I + \Delta t[K]_{i,j,k})Q^{n}_{i,j,k} - \frac{\Delta t}{\Delta\xi}[h^{E}_{i+1/2} - h^{E}_{i-1/2}]^{n}_{j,k} - \frac{\Delta t}{\Delta\eta}[h^{F}_{j+1/2} - h^{F}_{j-1/2}]^{n}_{i,k} - \frac{\Delta t}{\Delta\zeta}[h^{G}_{k+1/2} - h^{G}_{k-1/2}]^{n}_{i,j}$$

$$\begin{aligned} Q^{n+1}_{i,j,k} = {} & \frac{1}{2}[Q^{n}_{i,j,k} + (I + \Delta t[K]_{i,j,k})\overline{Q^{n+1}_{i,j,k}}] - \frac{\Delta t}{2\Delta\xi}[h^{E}_{i+1/2} - h^{E}_{i-1/2}]^{\overline{n+1}}_{j,k} \\ & - \frac{\Delta t}{2\Delta\eta}[h^{F}_{j+1/2} - h^{F}_{j-1/2}]^{\overline{n+1}}_{i,k} - \frac{\Delta t}{2\Delta\zeta}[h^{G}_{k+1/2} - h^{G}_{k-1/2}]^{\overline{n+1}}_{i,j} \\ & - (I + \Delta t[K]_{i,j,k})\frac{\Delta t}{2\Delta\xi}[-h^{E}_{i-1/2} + h^{E}_{i-3/2} - E_{i-1} + h^{E}_{i+1/2} - h^{E}_{i+3/2} + E_{i+1}]^{n}_{j,k} \\ & - (I + \Delta t[K]_{i,j,k})\frac{\Delta t}{2\Delta\eta}[-h^{F}_{j-1/2} + h^{F}_{j-3/2} - F_{j-1} + h^{F}_{j+1/2} - h^{F}_{j+3/2} + F_{j+1}]^{n}_{i,k} \\ & - (I + \Delta t[K]_{i,j,k})\frac{\Delta t}{2\Delta\zeta}[-h^{G}_{k-1/2} + h^{G}_{k-3/2} - G_{k-1} + h^{G}_{k+1/2} - h^{G}_{k+3/2} + G_{k+1}]^{n}_{i,j} \end{aligned} \tag{4.102}$$

where the numerical flux terms are computed by equations (4.87) to (4.101) (and their similar counterparts on constant η- and ζ- surfaces), the vector fluxes terms calculated at the centre of each cell are given by (4.103) to (4.104), and the source or loss term is in the form of (4.104).*

* The significance of this term will become apparent in the next section.

$$\boldsymbol{E}_{i\pm1,j,k}=\frac{1}{J_{i\pm1,j,k}}\begin{bmatrix}\frac{D_z}{\varepsilon}\xi_y-\frac{D_y}{\varepsilon}\xi_z\\ \frac{D_x}{\varepsilon}\xi_z-\frac{D_z}{\varepsilon}\xi_x\\ \frac{D_y}{\varepsilon}\xi_x-\frac{D_x}{\varepsilon}\xi_y\\ \frac{B_y}{\mu}\xi_z-\frac{B_z}{\mu}\xi_y\\ \frac{B_z}{\mu}\xi_x-\frac{B_x}{\mu}\xi_z\\ \frac{B_x}{\mu}\xi_y-\frac{B_y}{\mu}\xi_x\end{bmatrix}_{i\pm1,j,k},\quad \boldsymbol{F}_{i,j\pm1,k}=\frac{1}{J_{i,j\pm1,k}}\begin{bmatrix}\frac{D_z}{\varepsilon}\eta_y-\frac{D_y}{\varepsilon}\eta_z\\ \frac{D_x}{\varepsilon}\eta_z-\frac{D_z}{\varepsilon}\eta_x\\ \frac{D_y}{\varepsilon}\eta_x-\frac{D_x}{\varepsilon}\eta_y\\ \frac{B_y}{\mu}\eta_z-\frac{B_z}{\mu}\eta_y\\ \frac{B_z}{\mu}\eta_x-\frac{B_x}{\mu}\eta_z\\ \frac{B_x}{\mu}\eta_y-\frac{B_y}{\mu}\eta_x\end{bmatrix}_{i,j\pm1,k} \tag{4.103}$$

$$\boldsymbol{G}_{i,j,k\pm1}=\frac{1}{J_{i,j,k\pm1}}\begin{bmatrix}\frac{D_z}{\varepsilon}\zeta_y-\frac{D_y}{\varepsilon}\zeta_z\\ \frac{D_x}{\varepsilon}\zeta_z-\frac{D_z}{\varepsilon}\zeta_x\\ \frac{D_y}{\varepsilon}\zeta_x-\frac{D_x}{\varepsilon}\zeta_y\\ \frac{B_y}{\mu}\zeta_z-\frac{B_z}{\mu}\zeta_y\\ \frac{B_z}{\mu}\zeta_x-\frac{B_x}{\mu}\zeta_z\\ \frac{B_x}{\mu}\zeta_y-\frac{B_y}{\mu}\zeta_x\end{bmatrix}_{i,j,k\pm1},\quad [\boldsymbol{K}]_{i,j,k}=diag\left(\begin{bmatrix}0\\0\\0\\ \frac{\sigma}{J\varepsilon}\\ \frac{\sigma}{J\varepsilon}\\ \frac{\sigma}{J\varepsilon}\end{bmatrix}\right)_{i,j,k} \tag{4.104}$$

4.3.1 Stability of the Fully Windward LW Scheme

The stability analysis for the fully upwind LW algorithm can be performed by the standard ***von Neumann*** (***Fourier***) ***method*** [10]. Therefore, the stability criterion for the 3D-FVTD scheme of (4.102) is given by [16]:

$$\Delta t\le\frac{2}{\lambda_{max}\sqrt{\frac{1}{\Delta\xi^2}+\frac{1}{\Delta\eta^2}+\frac{1}{\Delta\zeta^2}}} \tag{4.105}$$

where λ_{max} is the maximum sum of eigenvalues in all directions and is computed by:

$$\lambda_{max} = \boldsymbol{max}(\left|(\lambda_\xi)_{i,j,k}\right| + \left|(\lambda_\eta)_{i,j,k}\right| + \left|(\lambda_\zeta)_{i,j,k}\right|). \tag{4.106}$$

However, the above stability analysis has only been successfully performed on the update equations of a homogeneous Riemann solver (*i.e.* $[\boldsymbol{K}] = \boldsymbol{0}$) [92]. A definitive von Neumann stability analysis of most algorithms used for solving Maxwell's equations with a source term has yet to be completed [104]. In most algorithms, the Fourier stability analysis of the update equations with a source term results in very complex mathematical expressions that often defy concrete conclusions.* Thus, the stability of non-homogenous Riemann solvers has often been verified empirically via the numerical simulation of actual problems. In the majority of cases, minor changes to the algorithm are required in order to achieve stability using the original CFL condition [46]. In the case of the FVTD method, a similar approach was followed.

Using the CFL condition as the stability criterion, first the predictor and then the predictor-corrector update equations of the newly derived FVTD algorithm of (4.102) were tested for numerical stability† via the simulation of wave propagation in a perfect dielectric ($[\boldsymbol{K}] = \boldsymbol{0}$). Both test cases were numerically stable as predicted by their stability analysis [10]. Next, the predictor of (4.102) was tested for lossy media ($[\boldsymbol{K}] \neq \boldsymbol{0}$); the scheme became numerically unstable after a few time steps. Borrowing a page from the treatment of source terms in the FDTD method [45], a semi-implicit technique was used in order to achieve a stable update equation; that is, the field components associated

* The author has first hand experience in the futility of performing a von Neumann stability analysis on the proposed windward LW algorithm of (4.55).

† Numerical stability is gauged by monitoring the total amount of energy in the computational space. In stable systems, the total amount of energy in the system (due to an initial condition) must not increase over time (steps).

with the source term of the predictor, ($[K]Q^n$), were averaged over the previous, n, and present, $\overline{n+1}$, time step, respectively; *i.e.*

$$[K]Q^n = [K]\vartheta Q(n, \overline{n+1}) = [K]\left(\frac{Q^{\overline{n+1}} + Q^n}{2}\right). \tag{4.107}$$

This technique is loosely referred to as ***time averaging***. The time-averaged predictor was tested and remained numerically stable for several thousand time steps. Next, the stability of the complete LW scheme was tested using the time-averaged predictor and various combinations of time-averaged correctors. Various configurations and their respective stability test results are given in **Table 4.1**. The lightly shaded rows indicate the progression and selection of different combinations of schemes that led to a stable algorithm (the last row).

Table 4.1. Numerical stability test results of various schemes proposed for the fully upwind LW algorithm with a source term

Predictor	**Corrector**		**Stability**[a]	
Field Terms (KQ^n)	Field Terms ($KQ^{\overline{n+1}}$)	Flux Terms ($K[E,h]^n$)	Pred.	Both
No Averaging	No Averaging	No Averaging	No	No
$\vartheta Q(n, \overline{n+1})$	Corrector equation was not used.		Yes	--
$\vartheta Q(n, \overline{n+1})$	$\vartheta Q(n, n+1)$	No Averaging	Yes	No
$\vartheta Q(n, \overline{n+1})$	$\vartheta Q(n, \overline{n+1})$	No Averaging	Yes	No
$\vartheta Q(n, \overline{n+1})$	$\vartheta Q(n+1, \overline{n+1})$	No Averaging	Yes	No
$\vartheta Q(n, \overline{n+1})$	$\vartheta Q(n, n+1)$	$\vartheta(E,h)(n, \overline{n+1})$	Yes	Slow
$\vartheta Q(n, \overline{n+1})$	$\vartheta Q(n, \overline{n+1})$	$\vartheta(E,h)(n, \overline{n+1})$	Yes	No
$\vartheta Q(n, \overline{n+1})$	$\vartheta Q(n+1, \overline{n+1})$	$\vartheta(E,h)(n, \overline{n+1})$	Yes	Slow
$\vartheta Q(n, \overline{n+1})$	$\vartheta Q(n+1, \vartheta Q(n+1, n))$	$\vartheta(E,h)(n, \overline{n+1})$	Yes	Yes

a. "No" indicates that the algorithm is numerically unstable, "Slow" means that the scheme is initially stable but becomes unstable after 50 or more time steps, and "Yes" denotes a stable algorithm.

Thus, the final format of the FVTD scheme (a fully windward LW algorithm) for solving 3D Maxwell's equations is given by:

$$\left(I-\frac{\Delta t[K]_{i,j,k}}{2}\right)\overline{Q}^{n+1}_{i,j,k}=\left(I+\frac{\Delta t[K]_{i,j,k}}{2}\right)Q^{n}_{i,j,k}-\frac{\Delta t}{\Delta\xi}[h^{E}_{i+1/2}-h^{E}_{i-1/2}]^{n}_{j,k}$$
$$-\frac{\Delta t}{\Delta\eta}[h^{F}_{j+1/2}-h^{F}_{j-1/2}]^{n}_{i,k}-\frac{\Delta t}{\Delta\zeta}[h^{G}_{k+1/2}-h^{G}_{k-1/2}]^{n}_{i,j}$$

$$\left(I-\frac{3\Delta t[K]_{i,j,k}}{4}\right)Q^{n+1}_{i,j,k}=\frac{1}{2}\left[\left(I-\frac{3\Delta t[K]_{i,j,k}}{4}\right)Q^{n}_{i,j,k}+\overline{Q^{n+1}_{i,j,k}}\right]$$

$$-\left(\frac{\Delta t}{2\Delta\xi}\right)\left(I+\frac{\Delta t[K]_{i,j,k}}{2}\right)[h^{E}_{i+1/2}-h^{E}_{i-1/2}]^{\overline{n+1}}_{j,k}$$

$$-\left(\frac{\Delta t}{2\Delta\xi}\right)\left(\frac{\Delta t[K]_{i,j,k}}{2}\right)[h^{E}_{i-3/2}-E_{i-1}+-h^{E}_{i+3/2}+E_{i+1}]^{\overline{n+1}}_{j,k}$$

$$-\left(\frac{\Delta t}{2\Delta\xi}\right)\left(I+\frac{\Delta t[K]_{i,j,k}}{2}\right)[-h^{E}_{i-1/2}+h^{E}_{i-3/2}-E_{i-1}+h^{E}_{i+1/2}-h^{E}_{i+3/2}+E_{i+1}]^{n}_{j,k}$$

$$-\left(\frac{\Delta t}{2\Delta\eta}\right)\left(I+\frac{\Delta t[K]_{i,j,k}}{2}\right)[h^{F}_{j+1/2}-h^{F}_{j-1/2}]^{\overline{n+1}}_{i,k}$$

$$-\left(\frac{\Delta t}{2\Delta\eta}\right)\left(\frac{\Delta t[K]_{i,j,k}}{2}\right)[h^{F}_{j-3/2}-F_{j-1}-h^{F}_{j+3/2}+F_{j+1}]^{\overline{n+1}}_{i,k}$$

$$-\left(\frac{\Delta t}{2\Delta\eta}\right)\left(I+\frac{\Delta t[K]_{i,j,k}}{2}\right)[-h^{F}_{j-1/2}+h^{F}_{j-3/2}-F_{j-1}+h^{F}_{j+1/2}-h^{F}_{j+3/2}+F_{j+1}]^{n}_{i,k}$$

$$-\left(\frac{\Delta t}{2\Delta\zeta}\right)\left(I+\frac{\Delta t[K]_{i,j,k}}{2}\right)[h^{G}_{k+1/2}-h^{G}_{k-1/2}]^{\overline{n+1}}_{i,j}$$

$$-\left(\frac{\Delta t}{2\Delta\zeta}\right)\left(\frac{\Delta t[K]_{i,j,k}}{2}\right)[h^{G}_{k-3/2}-G_{k-1}-h^{G}_{k+3/2}+G_{k+1}]^{\overline{n+1}}_{i,j}$$

$$-\left(\frac{\Delta t}{2\Delta\zeta}\right)\left(I+\frac{\Delta t[K]_{i,j,k}}{2}\right)[-h^{G}_{k-1/2}+h^{G}_{k-3/2}-G_{k-1}+h^{G}_{k+1/2}-h^{G}_{k+3/2}+G_{k+1}]^{n}_{i,j} \tag{4.108}$$

4.4 Numerical Fluxes and Boundary Conditions

Thus far, the discussion has focused on computing solutions of EM fields within a homogenous, infinitely large space containing materials that do not require special treatment. Obviously, this assumption is not realistic since the simulation space must be abruptly terminated by either physical BCs (such as a ground plane) or artificial/absorbing BCs (*i.e.* ABCs).* In either case, these boundary conditions are located at the outer walls of the first and/or the last cell of the computational mesh. Therefore, the numerical fluxes located at these walls require special treatment and are computed with expressions derived using their specific properties. In this section, five of the most common BCs are discussed, and their respective numerical flux expressions are derived.

4.4.1 Perfect Electric Conductor BCs

It can be shown from Maxwell's equations that "*at the interface between any two media, the tangential components of the electric and magnetic fields are continuous* [1 page 71];" that is:

$$\begin{aligned} \boldsymbol{n} \times (\mathcal{E}_2 - \mathcal{E}_1) &= 0, \\ \boldsymbol{n} \times (\mathcal{H}_2 - \mathcal{H}_1) &= \boldsymbol{J}_s, \end{aligned} \tag{4.109}$$

where $\boldsymbol{n}$ is the unit vector normal to the surface of the boundary and $\boldsymbol{J}_s$ is the surface current. Since all fields at any interior point of a Perfect Electric Conductor (PEC) ($\sigma_2 = \infty$) are zero, then the tangential electric field on the surface of the conductor is zero, while the tangential magnetic field is finite and is given by the conduction current term, *i.e.*

* Since the use of an infinitely large mesh would require an infinite amount of memory!

$$\mathcal{E}_{t_1} = 0,$$
$$\mathcal{H}_{t_1} = \boldsymbol{J}_s. \tag{4.110}$$

When modelling PEC objects, *i.e.* PEC BCs, the numerical fluxes located on the boundaries must be computed according to the conditions specified in (4.109) to (4.110). For example, if a PEC object is placed to the left of $(i-1/2,\, j,\, k)$ (see **Figure 4.6**), all the fields and numerical fluxes within the PEC region, as well as the numerical flux components associated with tangential electric field components on the PEC boundary, must be set to zero; that is:

$$\boldsymbol{Q}_{i-1,\,j,\,k} = \boldsymbol{E}_{i-1,\,j,\,k} = \boldsymbol{h}^{E}_{i-3/2,\,j,\,k} = \begin{bmatrix} 0 & 0 & 0 & 0 & 0 & 0 \end{bmatrix}^T \tag{4.111}$$

$$h^{E}_{i-1/2,\,j,\,k}]_1 = h^{E}_{i-1/2,\,j,\,k}]_2 = h^{E}_{i-1/2,\,j,\,k}]_3 = 0. \tag{4.112}$$

In contrast, the numerical fluxes associated with tangential magnetic field components are non-trivial and must be computed. Since all fields are vanishing within a PEC material, one can represent this phenomenon via a *zero* speed of propagation of these waves within the PEC media;* thus, setting $\bar{c}_{i-1} = 0$, the expressions of numerical fluxes given in (4.87) to (4.89) become:

$$h^{E}_{i-\frac{1}{2},\,j,\,k}\Big]_4 = \left(\frac{\xi_z B_y - \xi_y B_z}{\mu}\right)_{i,\,j,\,k} + \left(\frac{-(\xi_y^2+\xi_z^2)D_x + \xi_x\xi_y D_y + \xi_x\xi_z D_z}{\varepsilon\mu\bar{c}}\right)_{i,\,j,\,k} \tag{4.113}$$

$$h^{E}_{i-\frac{1}{2},\,j,\,k}\Big]_5 = \left(\frac{\xi_x B_z - \xi_z B_x}{\mu}\right)_{i,\,j,\,k} + \left(\frac{\xi_x\xi_y D_x - (\xi_x^2+\xi_z^2)D_y + \xi_y\xi_z D_z}{\varepsilon\mu\bar{c}}\right)_{i,\,j,\,k} \tag{4.114}$$

$$h^{E}_{i-\frac{1}{2},\,j,\,k}\Big]_6 = \left(\frac{\xi_y B_x - \xi_x B_y}{\mu}\right)_{i,\,j,\,k} + \left(\frac{\xi_x\xi_z D_x + \xi_y\xi_z D_y - (\xi_x^2+\xi_y^2)D_z}{\varepsilon\mu\bar{c}}\right)_{i,\,j,\,k} \tag{4.115}$$

* Note that this hypothesis cannot be applied to points within a PEC material.

a) Perfect Electric Conductor (PEC)

$$\boldsymbol{n} \times \mathcal{E}_p = 0$$

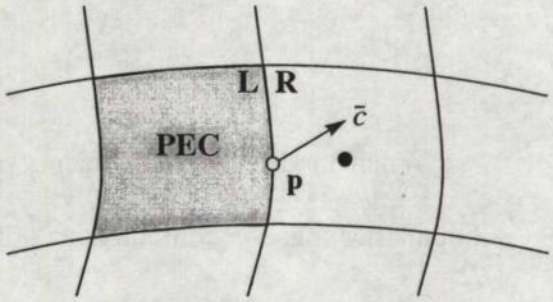

b) Perfect Magnetic Conductor (PMC)

$$\boldsymbol{n} \times \mathcal{H}_p = 0$$

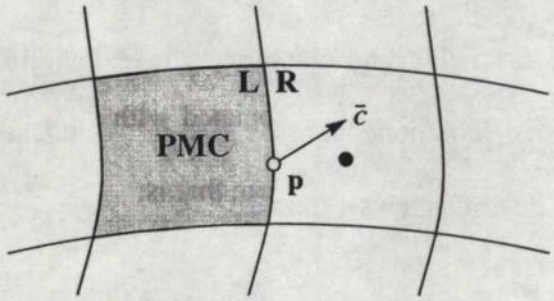

c) Absorbing Boundary Condition (ABC)

$$\mathcal{E}_L = 0$$

$$\mathcal{H}_L = 0$$

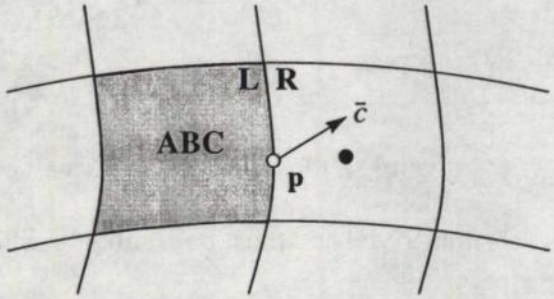

d) Periodic Boundary
links field components at

$k = K_{max}$ and $k = 1$

$k = K_{max} - 1$ and $k = 2$

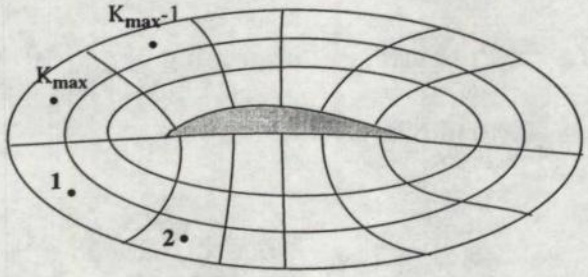

e) Zero-Flux Boundary

$$\boldsymbol{n} \times \mathcal{E}_p = 0$$

$$\boldsymbol{n} \times \mathcal{H}_p = 0$$

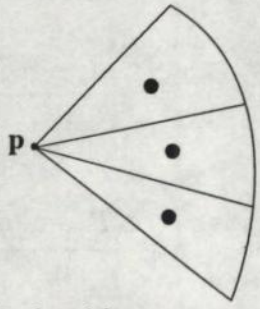

Figure 4.6. Boundary conditions required for the FVTD algorithm

4.4.2 Perfect Magnetic Conductor BCs

Two variables that occupy identical positions in two equations of the same mathematical form are known as ***dual quantities***. Naturally, the solution of these two equations, each describing the behaviour of a different variable, is the same. Thus, the solution of one variable can be derived from the solution of the other variable by a systematic interchange of the variables. This concept is commonly known as the ***duality theorem***. However, it must be remembered that duality is a mathematical concept which only serves to provide purely mathematical solutions that may not be physically realisable.

Since Maxwell's equations can be modified to describe the behaviour of dual variables, the duality theorem is applicable. Thus, a Perfect Magnetic Conductor (PMC), an evil twin to PEC, is born as a result of the unholy union of Maxwell's equations and the duality theorem. Similar to PECs, all field components within a PMC material are zero; in contrast to PECs, tangential magnetic field components vanish on the surface of a PMC, while its tangential magnetic field components are finite and are given in terms of the magnetic conduction current, M_s; *i.e.*

$$\begin{aligned} \mathcal{H}_{t_1} &= 0, \\ \mathcal{E}_{t_1} &= M_s. \end{aligned} \tag{4.116}$$

Although the concept of PMC materials is purely mathematical and has no physical significance, its mathematical properties are often exploited to simplify physical problems. Hence, it is important to derive expressions for enforcing PMC BCs. As in the case of PECs, a PMC BC is placed to the left of $(i-1/2,\, j,\, k)$ (see **Figure 4.6**). All the fields and numerical fluxes within the PMC region, as well as the numerical flux components associated with tangential magnetic field components on the PMC boundary,

must be set to zero; that is:

$$\boldsymbol{Q}_{i-1,j,k} = \boldsymbol{E}_{i-1,j,k} = \boldsymbol{h}^{E}_{i-3/2,j,k} = \left[0\ 0\ 0\ 0\ 0\ 0\right]^{T} \tag{4.117}$$

$$+h^{E}_{i-1/2,j,k}]_4 = h^{E}_{i-1/2,j,k}]_5 = h^{E}_{i-1/2,j,k}]_6 = 0. \tag{4.118}$$

Once again, numerical fluxes associated with the tangential electric field components are computed by assuming a *zero* speed of propagation of the wave within the PMC material. Hence, the expressions of numerical fluxes given in (4.84) to (4.86) become:

$$h^{E}_{i-\frac{1}{2},j,k}\Big]_1 = \left(\frac{\xi_y D_z - \xi_z D_y}{\varepsilon}\right)_{i,j,k} + \left(\frac{-(\xi_y^2+\xi_z^2)B_x + \xi_x\xi_y B_y + \xi_x\xi_z B_z}{\varepsilon\mu\bar{c}}\right)_{i,j,k} \tag{4.119}$$

$$h^{E}_{i-\frac{1}{2},j,k}\Big]_2 = \left(\frac{\xi_z D_x - \xi_x D_z}{\varepsilon}\right)_{i,j,k} + \left(\frac{\xi_x\xi_y B_x - (\xi_x^2+\xi_z^2)B_y + \xi_y\xi_z B_z}{\varepsilon\mu\bar{c}}\right)_{i,j,k} \tag{4.120}$$

$$h^{E}_{i-\frac{1}{2},j,k}\Big]_3 = \left(\frac{\xi_x D_y - \xi_y D_x}{\varepsilon}\right)_{i,j,k} + \left(\frac{\xi_x\xi_z B_x + \xi_y\xi_z B_y - (\xi_x^2+\xi_y^2)B_z}{\varepsilon\mu\bar{c}}\right)_{i,j,k} \tag{4.121}$$

4.4.3 Absorbing Boundary Conditions

One of the fundamental dilemmas of CEM is the scarcity of computational resources. The finite size of computer memory and the constant demand for faster computation time are the reasons for economizing the computation resources required for an EM simulation. This issue becomes very apparent in the case of "open-space" problems where the simulation space is surrounded by free-space in one (or more) direction(s). Since the numerical modelling of an infinitely large space is impossible, the problem space must be truncated using BCs that emulate the properties of an infinite space and that reflect very little of the incoming waves; this means that the proposed boundary must *absorb* the entire energy of the incoming EM wave over a wide frequency range without changing the

physics being modelled within the mesh. These BCs are called Absorbing Boundary Conditions (ABC).

Most ABCs are either: (1) derived from the differential form of the governing equations or (2) employ material absorbers [42]. The development of differential-equation-based ABCs is nearly as old as TD-numerical methods, and research in this area is ongoing [105-108]. Most of these ABCs are designed to absorb best outgoing waves normal to the ABC; thus waves propagating on angles of incidence other than normal to the ABC are partially reflected back into the simulation space causing inaccurate results [42]. Material-based ABCs have also been devised based on the same assumption until recently when Berenger, in a landmark paper in 1994 [109], used a "split-field" formulation of Maxwell's equations resulting in an artificial absorbing material which absorbs incoming waves over a wide band of frequencies for all angles of incidence. Since Berenger's Perfectly Matched Layer (PML) technique has proven to be more effective than most other ABCs and provides superior performance with a significant accuracy, differential-based ABCs have been partially side-lined in favour of PML ABCs. A large amount of research effort has been devoted to PMC-ABCs as is evident by the number of research papers published in the area [109-112].

Traditionally, the FVTD method has relied on differential-based ABCs since characteristic-based procedures provide a natural framework for this type of ABCs. Due to the fact that the incoming and outgoing components of waves are separated via the flux-vector splitting procedure, the ABC can easily be enforced by setting the incoming fluxes (defined as the waves reflected into the computational space from the ABC) to zero. Hence, if the ABC is defined at $(i-1/2, j, k)$ (*i.e.* the computation space is truncated to

the left of the ABC as shown in **Figure 4.6**), in the expression of numerical fluxes, $h^E_{i-1/2,\,j,\,k}$ of (4.56), the incoming waves are vanishing, *i.e.* $(\boldsymbol{E}^+)_{i-1} = 0$ (see **Figure 4.4**). This implies that all the field and flux components within the ABC region must be set to zero; that is:

$$\boldsymbol{Q}_{i-1,\,j,\,k} = \boldsymbol{E}_{i-1,\,j,\,k} = \boldsymbol{h}^E_{i-3/2,\,j,\,k} = \begin{bmatrix} 0 & 0 & 0 & 0 & 0 & 0 \end{bmatrix}^T \tag{4.122}$$

$$h^E_{i-\frac{1}{2},\,j,\,k}\Big]_1 = \left(\frac{\xi_y D_z - \xi_z D_y}{2\varepsilon}\right)_{i,\,j,\,k} + \left(\frac{-(\xi_y^2+\xi_z^2)B_x + \xi_x\xi_y B_y + \xi_x\xi_z B_z}{2\varepsilon\mu\bar{c}}\right)_{i,\,j,\,k} \tag{4.123}$$

$$h^E_{i-\frac{1}{2},\,j,\,k}\Big]_2 = \left(\frac{\xi_z D_x - \xi_x D_z}{2\varepsilon}\right)_{i,\,j,\,k} + \left(\frac{\xi_x\xi_y B_x - (\xi_x^2+\xi_z^2)B_y + \xi_y\xi_z B_z}{2\varepsilon\mu\bar{c}}\right)_{i,\,j,\,k} \tag{4.124}$$

$$h^E_{i-\frac{1}{2},\,j,\,k}\Big]_3 = \left(\frac{\xi_x D_y - \xi_y D_x}{2\varepsilon}\right)_{i,\,j,\,k} + \left(\frac{\xi_x\xi_z B_x + \xi_y\xi_z B_y - (\xi_x^2+\xi_y^2)B_z}{2\varepsilon\mu\bar{c}}\right)_{i,\,j,\,k} \tag{4.125}$$

$$h^E_{i-\frac{1}{2},\,j,\,k}\Big]_4 = \left(\frac{\xi_z B_y - \xi_y B_z}{2\mu}\right)_{i,\,j,\,k} + \left(\frac{-(\xi_y^2+\xi_z^2)D_x + \xi_x\xi_y D_y + \xi_x\xi_z D_z}{2\varepsilon\mu\bar{c}}\right)_{i,\,j,\,k} \tag{4.126}$$

$$h^E_{i-\frac{1}{2},\,j,\,k}\Big]_5 = \left(\frac{\xi_x B_z - \xi_z B_x}{2\mu}\right)_{i,\,j,\,k} + \left(\frac{-\xi_x\xi_y D_x + (\xi_x^2+\xi_z^2)D_y - \xi_y\xi_z D_z}{2\varepsilon\mu\bar{c}}\right)_{i,\,j,\,k} \tag{4.127}$$

$$h^E_{i-\frac{1}{2},\,j,\,k}\Big]_6 = \left(\frac{\xi_y B_x - \xi_x B_y}{2\mu}\right)_{i,\,j,\,k} + \left(\frac{\xi_x\xi_z D_x + \xi_y\xi_z D_y - (\xi_x^2+\xi_y^2)D_z}{2\varepsilon\mu\bar{c}}\right)_{i,\,j,\,k} \tag{4.128}$$

It must be noted that in order to match the material properties at the boundary conditions, the ABC region is assumed to have the same material properties as the neighbouring cells of the absorbing boundary.

Although the aforementioned ABCs for the FVTD technique can only effectively absorb the normal components of the incident wave due to the flexibility of the mesh generation process, it is possible to align one of the computational (transformed)

coordinates with the direction of wave propagation ($\mathcal{E} \times \mathcal{H}$) thus ensuring that the incident field is perpendicular to the absorbing boundary [26].* The PML-ABC technique has yet to be derived for the LW windward version of the FVTD scheme; however, the performance of PML-ABC using FDTD and FVTD-ABC will be compared in **Chapter 5**.

4.4.4 Periodic Boundary Conditions

When using a conformal-structured mesh to model a circularly symmetric problem space, the transformation into a uniform rectangular computational space requires that the transformed coordinates, aligned with the azimuth direction (for example, θ of a cylindrical coordinate system), exhibit the same properties; this means that the beginning and the end of the aforementioned transformed coordinate must map into the same points in the physical space (as shown in **Figure 3.1**). Hence, the periodic boundary conditions simply ensure that when computing field or flux components at the vicinity of these boundaries, the field components that lie beyond the periodic boundary are properly associated with their respective symmetric point at the other extreme (see **Figure 4.6**). In other words, the periodic boundaries maintain the *wrap-around* nature of the azimuth direction.

4.4.5 Zero-Flux Boundary Conditions

The zero-flux boundary condition is proposed for cases where all of the grid points collapse into a single point on a given boundary condition (for example, at $r = 0$ in a cylindrical or spherical coordinate system). Theoretically, numerical fluxes would not flow in or out of that point since there is no surface through which they may flow (see **Figure**

* This is often not the case, however, since in many scattering problems, the direction of the outgoing wave is unknown.

4.6). This means that all of the numerical flux components at that cell interface must be set to zero (*i.e.* $h_p = 0$) which implies that in addition to the tangential electric and magnetic fields at the zero flux boundary, all of the field and fluxes lying beyond the zero-flux boundary are also vanishing [93]. This formulation of a zero-flux BC was implemented in the 3D-FVTD scheme and was tested on both a pyramidal structure as well as on a circular waveguide. In both cases, the numerical solution became unstable at the zero-flux boundary. It appears that the method is theoretically flawed. As will be shown in future chapters, in the majority of cases, zero-flux boundaries can be replaced by PMC walls.

4.5 Summary

In this chapter, the 3D-FVTD scheme was methodically developed. A fully windward Riemann solver was derived from a directional-biased upwind LW flux split Riemann solver. Then, the flux split difference terms of the newly derived algorithm were defined with respect to the numerical fluxes at cell interfaces which resulted in 3D-FVTD update equations as well as expressions for computing numerical fluxes at any given cell boundary. Next, the newly derived algorithm was tested for lossy media, and, in order to maintain the numerical stability of the scheme for the given CFL criterion, a new semi-implicit version of FVTD was proposed. Since all simulation spaces have to be terminated by some type of boundary conditions, a discussion of several types of boundary conditions (PEC, PMC, ABC, periodic BCs, and zero-flux BCs) and their formulation was also included. The task of formulating the 3D-FVTD algorithm and its respective BCs has now been completed. The next chapter deals with its validation and some of the issues that arise while implementing and developing a 3D-FVTD engine.

Chapter 5

Validation of the Finite-Volume Time-Domain Method

Thus far, an explicit, fully windward, flux split version of the Lax-Wendroff algorithm has been described for solving the 3D Maxwell's equations with sources. The next logical step is to develop a 3D-FVTD computational engine using the implementation of the aforementioned algorithm. The 3D-FVTD engine must then be tested and validated using several benchmark problems. As is always the case, any numerical solution of analytical problems involves some numerical issues that are a consequence of the method of solution. These are often referred to as "computational issues." The windward LW technique is no exception. Hence, in the following sections, in addition to testing and validating the 3D-FVTD engine, some numerical issues that arise from the LW method of solving Maxwell's equations are also discussed. In this case, some computational issues surface before implementation can even begin! They are considered first.

5.1 Computational Issues: Pre-Processing

In most computational engines, the problem has to be "prepared" before it can be solved by the simulator. This means that in addition to defining the problem's geometry and structure, the simulator also requires the problem to be meshed (*i.e.* discretised) by the user. This preparation before processing is appropriately known as ***pre-processing***.

5.1.1 Mesh Generation

Although some EM simulators (especially FEM-based packages) have been partially successful in automating the mesh generation process, the pre-processing stage still requires a significant investment of time and effort by the user. This is largely in the form of drawing, defining, and meshing the problem structure using a Graphical User Interface (GUI) tool. Since the mesh generator is a separate entity from the EM solver, a discussion of the different types of mesh generators and various methods of mesh generation employed by them is beyond the scope of this thesis. It is sufficient to recognize that the computation space can be meshed using one of three types of (often non-uniform and conformal) meshes. These include: structured, unstructured, and hybrid meshes.

A ***structured mesh*** is defined as a grid in which the nodes follow a certain regular pattern, and the constant-coordinate lines do not cross. In these types of meshes, the nodal points are arranged in an structured manner where the next nodal point can be located by simply incrementing the indices of the current node. In contrast, an ***unstructured mesh*** follows no regular pattern and has no specific coordinate lines. At any given node, a look-up table must be used in order to locate the next nodal point. Finally, a ***hybrid mesh*** contains both structured and unstructured meshes. An example of both structured and

unstructured grids is shown in **Figure 5.1**.

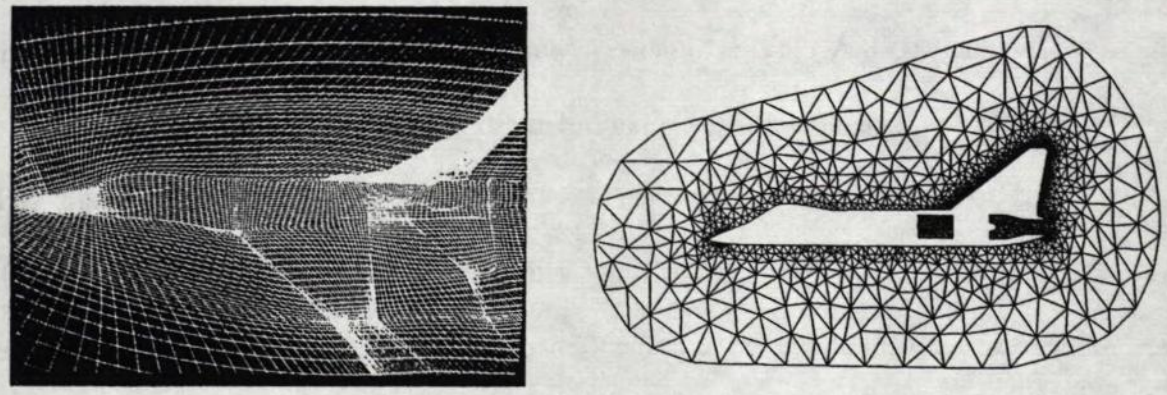

Figure 5.1. Examples of structured (left) [25] and unstructured meshes (right) [46]

Although unstructured meshes are more flexible when modelling very complex geometries, their irregular grid pattern requires a certain amount of computation effort for *bookkeeping*. On the other hand, structured meshes require no bookkeeping and, in many cases, can perform just as well as unstructured grids. However, since unstructured mesh generators have been developed and used for FEM-based solvers for several decades, they are more readily available, whereas structured meshes have just recently come to the attention of the CEM community; therefore, these types of mesh generators lack maturity and a diversity of tested applications. Thus, when seeking a structured grid mesh generator, one often faces a limited selection (especially for a modest budget). A list of public domain and commercial mesh generators (both structured and unstructured) is included in [113].

Due to the simplicity of its implementation and its computational efficiency, the 3D-FVTD engine was designed based on a 3D structured mesh; hence, the engine's initial requirement is an input data file that provides the coordinates of the meshed computational space. The search for a mesh generator capable of generating a 3D multi-block structured

mesh began by examining several public domain packages, namely **Chalmesh** (Chalmers University of Technology, Sweden) [114], **Genie**$^{++}$ [115], and **NGP** (Mississippi State University, U.S.A.) [116]. In general, public domain packages fall short of the minimum requirements of flexibility, diversity of meshing capabilities, and ease of use. Therefore, several commercial software packages were considered and tested. Both **Gridgen**® (Pointwise, *Inc.*) [117] and **TrueGrid**® (XYZ Scientific Applications, *Inc.*) [118] performed well above the aforementioned minimum requirements. However, **TrueGrid**® was more economically feasible and was selected as the pre-processor and mesh generator for the 3D-FVTD engine. A sample of the input file generated by **TrueGrid**® is given in **Figure 5.2.**

```
# COAXIAL WAVEGUIDE TEST PROBLEM
# Generated: Mon. Oct. 19 10:11:46 1998
#
# This file was created using TrueGrid by XYZ Scientific Applications, Inc.
# For further information, call (510) 373-0628 or write to:
#
#    XYZ Scientific Applications, Inc.
#    1324 Concannon Blvd.
#    Livermore, Ca. 94550
#
# size of computational mesh (Imin, Imax, Jmin, Jmax, Kmin, Kmax)
     1     31      1     61      1     251
# number of materials, material identification/tag numbers
  1  1
# output mesh
# computational coordinates (i,j,k) and physical coordinates (x, y, z),
# material tag/ID number, and Node number
#     i     j     k      x              y              z            ID    Node
      1     1     1  1.036000E-03  0.000000E+00  0.000000E+00     1     1
      2     1     1  1.121867E-03  0.000000E+00  0.000000E+00     1     2
      3     1     1  1.207733E-03  0.000000E+00  0.000000E+00     1     3
      4     1     1  1.293600E-03  0.000000E+00  0.000000E+00     1     4
      5     1     1  1.379467E-03  0.000000E+00  0.000000E+00     1     5
      6     1     1  1.465333E-03  0.000000E+00  0.000000E+00     1     6
      7     1     1  1.551200E-03  0.000000E+00  0.000000E+00     1     7
     .....
     .....
```

Figure 5.2. The mesh input file generated by **TrueGrid**® for the 3D-FVTD engine

5.1.2 Numerical Evaluation of Partial Derivatives

Although some structured grid generators (such as **Gridgen**®) use a family of elliptic partial differential equations (such as Laplace's equations) to define conformal grids [23, 119], in the majority of cases, simple geometrical techniques (such as the geometric

projection method that is used in **TrueGrid®** [120]) are utilized to construct a conformal mesh. Hence, in many instances, the transformation does not involve (closed-form) analytic expressions which means that the exact nature and value of the metrical coefficients of the transformation are unknown. The transformation of physical to computational coordinates is given by a mesh file which maps a set of computational coordinates to their corresponding points in the physical space. Thus, the coordinate transformation and its corresponding partial derivatives must be computed for each cell using conventional finite difference methods (see **Appendix A**).

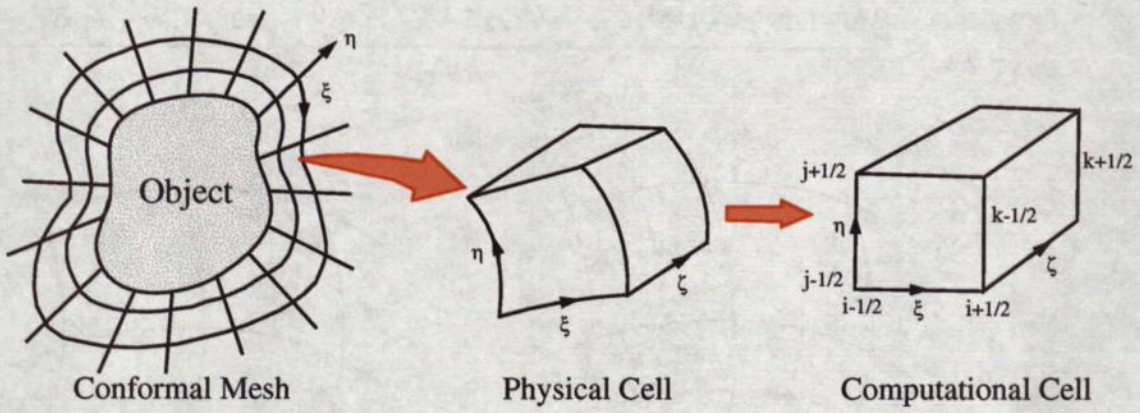

Figure 5.3. Schematic of cells in the 3D-FVTD engine

Since the FVTD algorithm proposed in **Chapter 4** is a cell-centred algorithm, the local coordinate transformation must also be computed with respect to the centre of each FVTD cell. However, most mesh generators (including **TrueGrid®**) define computational cells in terms of their corresponding nodes (see **Figure 5.3**). Therefore, in order to accurately compute and apply a coordinate transformation, it is essential to find the exact location of cell centres. The location of the cell centres can be found using: (1) a linear approximation (averaging) of the geometric centre of each cell or (2) via a double discretised mesh.

A linear approximation of the ***geometric centre*** of a cell can be found by computing the average of the computational cell's nodal coordinates. Then, the partial derivatives required for the local coordinate transformation of each cell are calculated at the cell's centre using one of the proposed centre differencing schemes in **Appendix A**. These partial derivatives are calculated at the approximated cell centre and are assumed constant over the whole computational cell. For example, a second order accurate centre difference approximation, equation **(A.8)**, of x_ξ located at (i, j, k), is given by:

$$(x_\xi)_{i,j,k} = \frac{\left[\begin{array}{l}(x_{i+1/2} - x_{i-1/2})_{j-1/2,\,k-1/2} + (x_{i+1/2} - x_{i-1/2})_{j+1/2,\,k-1/2} + \\ (x_{i+1/2} - x_{i-1/2})_{j-1/2,\,k+1/2} + (x_{i+1/2} - x_{i-1/2})_{j+1/2,\,k+1/2}\end{array}\right]}{4\Delta\xi}. \quad (5.1)$$

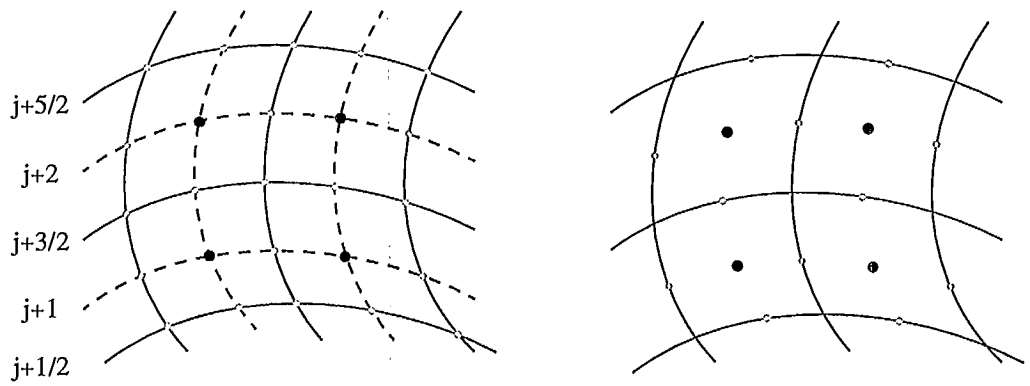

Figure 5.4. Double discretised mesh (left) and its respective single discretised grid (right)

The main disadvantage of the aforementioned method is the linear approximation of the geometric centre of a cell. This method becomes especially unreliable (*i.e.* inaccurate) for curved or stretched cells. In the ***double discretisation*** technique, the computational space is discretised using twice the number of nodal points required. Thus, it is clear that the exact geometric centre of each cell and their respective neighbours are located at the intersection of *even numbered* grid lines (*i.e.* the dashed lines in **Figure 5.4**). Therefore, it

is conceivable that more accurate partial derivatives (with respect to the centre of each cell) can be computed by applying the second order accurate centre differencing expression of **(A.8)** to the exact geometric centres of the lines forming each cell. The accuracy of the approximation of the metrical coefficients and the Jacobian of transformation can be further improved if the fourth order accurate central differencing scheme of **(A.10)** (spanning the mid-point of the sides of the cell and the centres of its neighbours) is applied to the double discretised mesh. The partial derivatives of the cells adjacent to the boundaries of the computational space are calculated via the second order accurate forward (for the cells on the lower boundary) or backward (for upper boundary cells) differencing scheme given in **Appendix A.**

In order to evaluate the accuracy of the aforementioned methods for computing partial derivatives, the Jacobian of transformation of a simple coaxial waveguide structure, with $r_{inner} = 1\ cm$ and $r_{outer} = 10\ cm$, was calculated analytically at all points and was compared with similar values obtained using numerical methods of various accuracies. One such comparison of the computed Jacobian of transformation is given in **Table 5.1**. As expected, the most accurate value of the Jacobian of transformation (and its respective partial derivatives and metrical coefficients) is obtained using a fourth order accurate central differencing scheme applied to a double discretised mesh. Finally, it must be noted that although the use of double discretised meshes increases the amount of memory required in the mesh generation stage by a factor of eight, it adds very little to the computational burden of the FVTD code. Thus, it is used as the default method of computing partial derivatives in the 3D-FVTD computational engine.

Table 5.1. A comparison of analytic and calculated Jacobians of transformation

Method	Analytic	$O(\Delta x)^2$, linear approx.	$O(\Delta x)^2$, double discrete.	$O(\Delta x)^4$, double discrete.
Jacobian	6.447	6.693	6.502	6.447
% difference[a]	---	3.820	0.850	0.000

a. As compared to the analytical value.

5.1.3 Ratio of Eigenvalues and the Accuracy of the Solution

Although one of the advantages of using conformal meshes is their capability of accurately modelling curved surfaces, some PDE solvers may not be able to take full advantage of this property. It has been shown that the majority of upwind schemes only achieve second order accuracy on uniform meshes [94]. In general, the accuracy of most upwind schemes (such as the Lax-Wendroff technique) begins to erode as the grid becomes more non-uniform. This degradation in accuracy of the numerical solution is in part due to the method of estimation of the fields on the cell faces. In most upwind schemes, the value of the fields (located on the cell centres) is extrapolated to the cell faces using a first order accurate model. However, the error terms of this estimation are proportional to the difference in neighbouring cell dimensions [46]. Thus, the larger the difference in cell dimensions, the lower is the (order of) accuracy of the solution. This deficiency of many upwind schemes can be partly avoided by using a *uniform conformal grid*. This implies that although each cell is shaped to fit various features present in the problem space, its volume and (in most cases) its respective dimensions remain uniform, thus avoiding the lower accuracy of the solution due to large differences in cell dimensions.

The eigenvalues of a computational space indicate the numerical speed of waves on

the computational grid. Eigenvalues are used to compensate for the difference between the physical and computational cells and play a critical role in maintaining a link between the two meshes. For example, a physical cell that is twice as long in the x-direction than it is in the y-direction will have a counterpart in the transformed space that has equal dimensions; hence the task of maintaining a physically accurate model of wave propagation will fall on the eigenvalues of each cell. That is, in the above computation cell, the magnitude of the cell's eigenvalue (hence its speed of wave propagation) aligned with the transformed x-axis must be twice as large as the magnitude of the eigenvalue of its counterpart aligned with the transformed y-axis in order to maintain the correct wave propagation model in the computational space. Therefore, the difference in the cells' dimensions can be tracked via the change in magnitude of the eigenvalues in any given direction. Consequently, when considering the entire computational space, the maximum, λ_{max}, and minimum, λ_{min}, eigenvalue in each transformed coordinate will correspond to the largest and smallest cell dimensions in that direction. **Table 5.2** includes the ratio of the maximum to minimum eigenvalues in any direction and the ratio of each eigenvalue with respect to the sum of the maximum eigenvalues in all directions, λ_{total}, given by (4.106). Thus, the most accurate solutions ($O(\Delta x)^2$) that are obtained using the 3D-FVTD method require an eigenvalue ratio of unity or near unity.

Table 5.2. The ratio of eigenvalues in a uniform waveguide

	$\left\|\frac{\lambda_{max}}{\lambda_{min}}\right\|$	$\left\|\frac{\lambda_{total}}{\lambda_{max}}\right\|$	$\left\|\frac{\lambda_{total}}{\lambda_{min}}\right\|$
ξ-direction	1.00	3.00	3.00
η-direction	1.00	3.00	3.00
ξ-direction	1.00	3.00	3.00

5.2 Testing and Verification of the 3D-FVTD Engine

5.2.1 Verification of the Source Term Formulation

The theoretical modelling and derivation of source terms in the FVTD technique and the time-averaged FVTD algorithm are tested for their accuracy of formulation using a simple benchmark problem of reflection from a lossy medium. The solution to the problem of reflection of normally incident plane waves from a lossy medium is well known. In general, the reflection coefficient of a uniform plane wave (launched in medium *one* with intrinsic impedance, Z_1) that is normally incident on (a single and sufficiently thick lossy)* medium *two* of intrinsic impedance, Z_2, is given by [3]:

$$\rho = \frac{Z_2 - Z_1}{Z_2 + Z_1} \tag{5.2}$$

which is defined as the reflection coefficient of medium *one* (referred to as the boundary of media *one* and *two*). The intrinsic impedance of a medium is determined by the medium's permittivity, permeability, conductivity, and the angular frequency/frequency-content of the incident wave, $\omega = 2\pi f$,

$$Z = \sqrt{\frac{j\omega\mu}{\sigma + j\omega\varepsilon}} \ [\Omega]. \tag{5.3}$$

If one of the media is free space,

$$Z_0 = \sqrt{\frac{\mu_0}{\varepsilon_0}} = 376.73 \ [\Omega] . \tag{5.4}$$

---

* This assumption assures that there are no reflected waves within medium *two*.

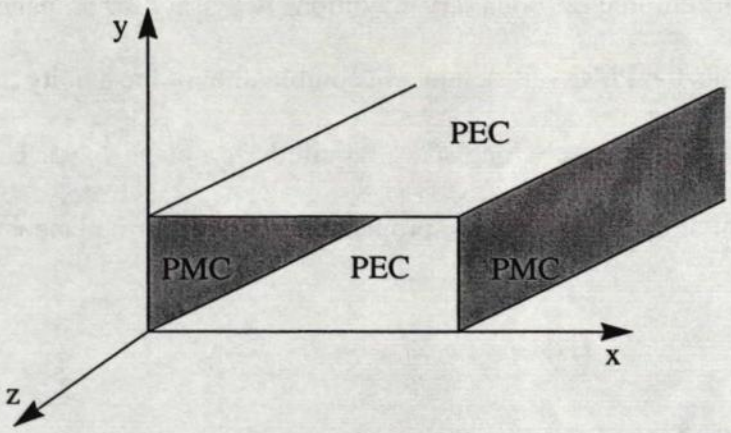

Figure 5.5. Boundary conditions required for the propagation of a uniform plane wave

5.2.1.1 Excitation of the Problem Space

Although the reflection of a plane wave from a single dielectric boundary is a 1D problem, it can be modelled and solved using a 3D simulator. In order to excite and propagate a uniform plane wave in a rectangular computational space, certain initial conditions must be imposed. For example, a uniform plane wave propagating in the z-direction of the problem space can be launched by imposing an E_y Gaussian pulse initial condition, given by:

$$E_y(x, y, z) = Ae^{-\frac{(z-z_0)^2}{b^2}} \tag{5.5}$$

where A is the pulse's maximum amplitude at the pulse centre, z_0, b is the width of the pulse, and z is the spatial position over the entire computational space. In addition, particular boundary conditions must also be enforced in order to maintain the propagation of a uniform plane wave; that is, in a problem space with a rectangular cross section, PEC boundary conditions are enforced on the lower and upper y-bound, and PMC boundary conditions are enforced on the lower and upper x-bound (as shown in **Figure 5.5**). The

PEC walls enforce the boundary conditions necessary for propagating a transverse electric wave while the PMC walls employ a combination of the duality theorem and image theory to simulate an infinitely long space required for a plane wave. These boundary conditions are essential for supporting the propagation of a uniform plane wave in the computational space.

5.2.1.2 Problem Configuration

In order to investigate the performance of the new time-averaged FVTD algorithm, the method's accuracy for computing reflection coefficients was compared to an analytical solution as well as to results obtained using other popular finite difference methods, such as FDTD and TLM. In a problem space 80 *cm* in length, the free space-medium boundary of a sufficiently thick slab of a lossy dielectric ($\varepsilon_r = 1.5$ and $\sigma = 0, 0.01, 0.10, 1, 10, 50$, and 100 [*S/m*]) was placed at $z = 7.5$ *cm*. For both the 1D-FDTD and TLM codes, the space was uniformly discretised using $\Delta l = 0.1$ *mm*; the mesh size for the 3D-FVTD space was $\Delta l = 0.25$ *mm*. The simulation space was terminated at both ends (lower and upper z-bound) using first order ABCs for the TLM simulation, Mur's first order ABCs in the case of FDTD, and characteristic-based ABCs in the FVTD simulation. Since these ABCs are all reported to have better than a -40 *dB* reflection coefficient for similar problems [45, 59, 121], the reflected waves from these artificial boundaries were negligible.

The problem space was excited by a uniform plane wave of Gaussian shape. This Gaussian pulse of spatial width of approximately 1.3 *cm* (with a frequency content of about 50 *GHz* at -40 *dB* level) was centred at $z = 2.5$ *cm*. It was launched in the free-

space region of the problem, and the wave impinged normally onto the dielectric-lossy medium. The value of the electric field component, transverse to the direction of propagation at $z = 4.5\ cm$, was recorded after each time step for a total time of 1.7 *ns* and is shown in **Figure 5.6**. However, for low conductivity cases ($\sigma = 0.01, 0.1\ [S/m]$), the sampling period of the transient response was increased to 5.8 *ns*. A longer transient response was required due to the diffusion behaviour exhibited by the reflected signal where the reflection from the lossy medium required a much longer interval to reach zero.*

5.2.1.3 Calculation of Reflection Coefficients

The reflection coefficient in free space, S_{11}, with respect to the lossy dielectric was computed analytically via (5.2), and by applying all three numerical solutions by using the pulse-separation method (see **Appendix C**). **Figures 5.6**, **5.7**, and **5.8** contain plots of the magnitude of the reflection coefficient of several lossy media for frequencies up to 15 *GHz*.† These plots compared the accuracy of the computed coefficient of reflection using the TLM, FDTD, and FVTD methods with the analytical solution. In the majority of cases, the numerical methods computed S_{11} within 1% of the theoretical value for all frequencies; thus, the various curves representing the reflection coefficients are indistinguishable. Hence, in order to further quantify and compare the accuracy of the numerical solutions, each plot is accompanied by a table that contains the "worst case scenario" error for each numerical method. These errors represent the maximum percentage of deviation of the numerical solution with respect to the theoretical value at a given frequency (or

* Recall that the leading and trailing zeros in a transient response will result in a smooth frequency domain transformation especially in the case of lower frequency components.

† This upper limit of frequency was chosen to include most (but not necessarily all) of state-of-the-art applications in computational electromagnetics.

simply *maximum error*). Mathematically, the maximum error is formulated as:

$$\% \ error = \left(\left| \frac{S_{11}^{Ana}(f) - S_{11}^{Num}(f)}{S_{11}^{Ana}(f)} \right| \right) \times 100 \qquad f = 0 \ldots 15 \ GHz. \qquad (5.6)$$

In most cases, the maximum error was found near or at 15 *GHz*, and hence, the maximum error was calculated at that frequency.

Figure 5.6 is a benchmark of the accuracy of the original formulation of the FVTD method (*i.e.* source free formulation) as compared to FDTD and TLM for computing the reflection coefficient of a perfect dielectric. Although, the FVTD technique does not seem to posses the same level of accuracy as do the FDTD and TLM methods,* its error remains within the sub-percent region and from a practical view point is negligible. The new time-averaged FVTD algorithm accurately computed S_{11} since the maximum error of FVTD remained low for low loss dielectrics (see **Figure 5.7**). However, this trend was reversed for the lossy media of **Figure 5.8**, where the maximum error spiked to 2% for $\sigma = 100$ [*S/m*]. Meanwhile, both FDTD and TLM exhibit a consistent yet opposite trend in the accuracy of the computed coefficient of reflection of lossy media. The maximum error indicates that both techniques more accurately model poor conductors ($\sigma > 1$) than they do poor insulators ($\sigma < 1$). However, one must exercise caution with the conclusions drawn in the case of poor insulators. Given that the FDTD and TLM transient response of these cases was diffused, the corresponding coefficient of reflections may not have been accurately computed. Furthermore, although the maximum error calculations were performed at the upper limit of frequency, one might argue that the entire data set is unreliable, and, therefore, no definite conclusions may be dawn regarding their accuracy!

* This is partially due to the artificial dissipation of the LW formulation of the FVTD method and will be addressed in future discussions.

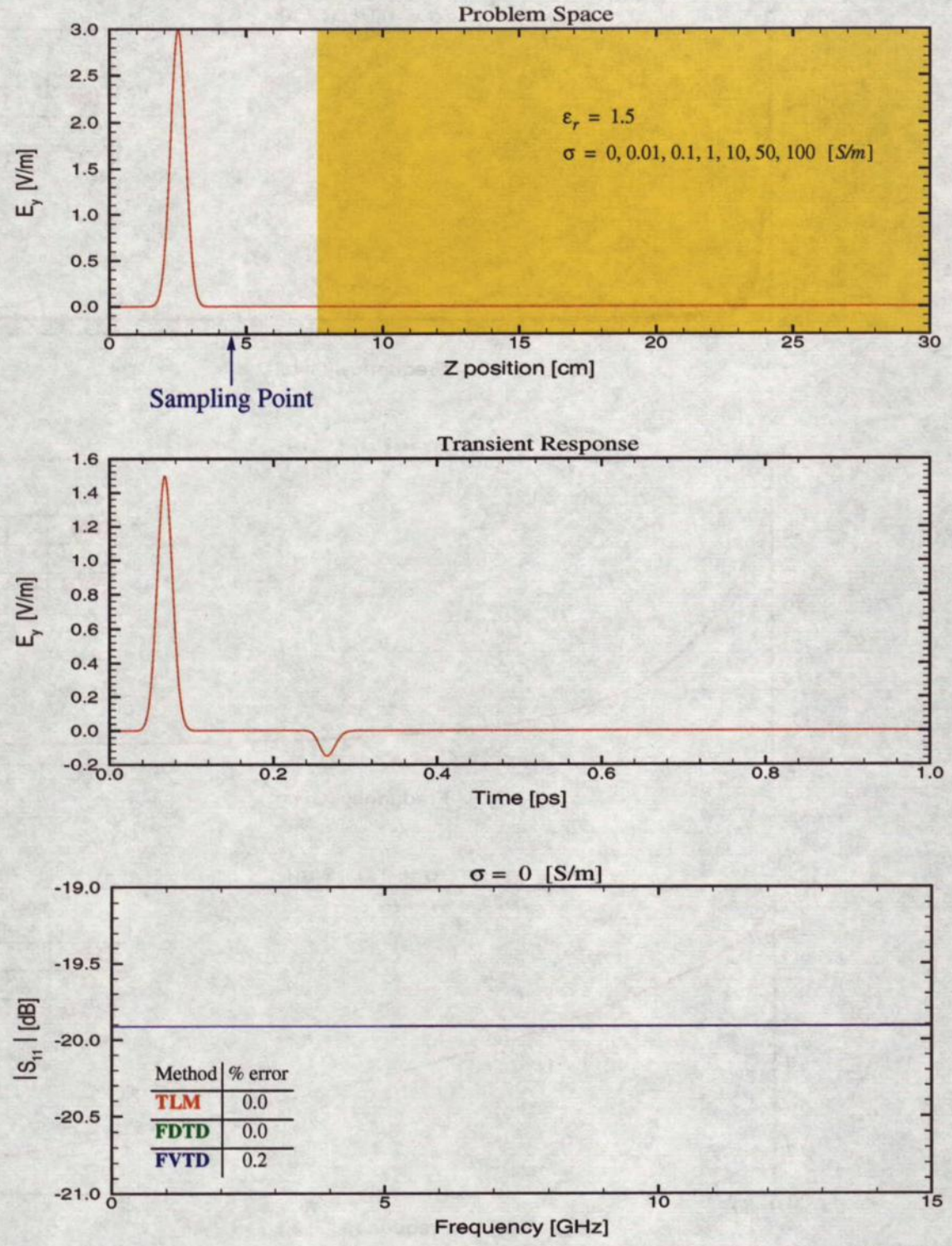

Figure 5.6. Test problem for source term formulation (a): (top) the initial condition at $t = 0$, (middle) the transient response for a perfect dielectric sampled at $z = 4.5\ cm$, and (bottom) its reflection coefficient calculated using **analytical**, TLM, FDTD, and FVTD methods.

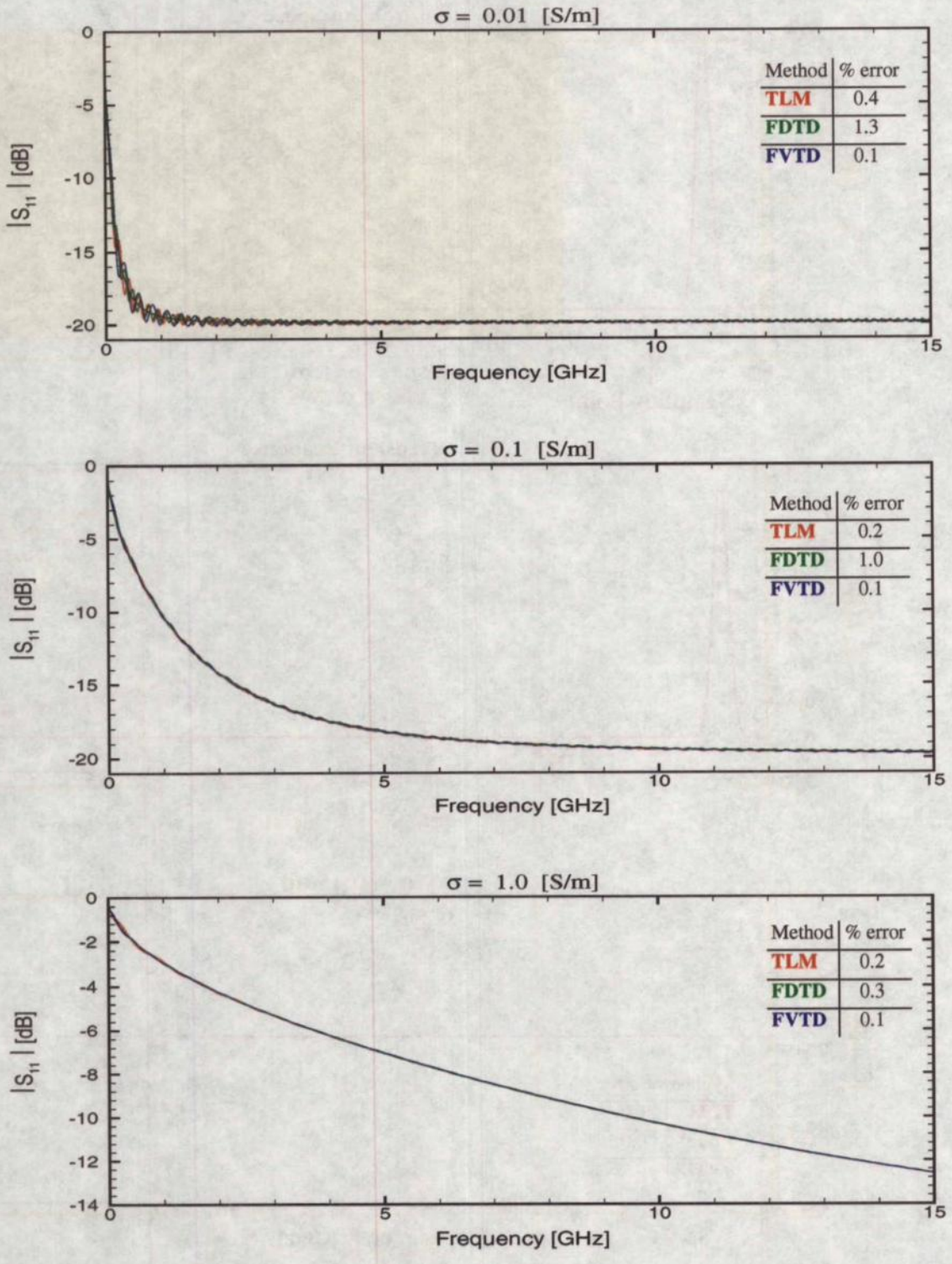

Figure 5.7. Test problem for source term formulation (b): the reflection coefficient for lossy dielectrics of various conductivity was calculated using **analytical**, TLM, FDTD, and FVTD methods.

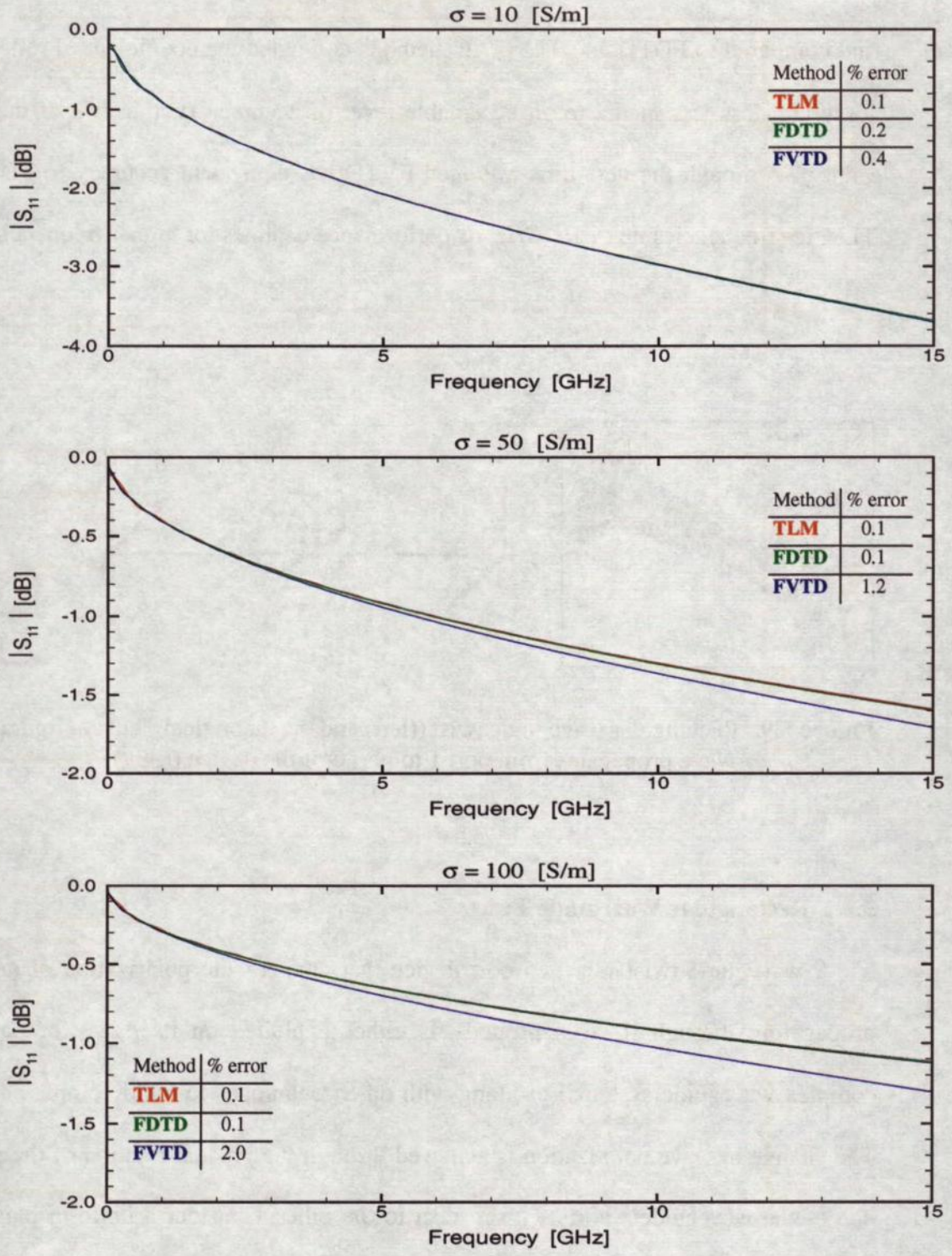

Figure 5.8. Test problem for source term formulation (c): the reflection coefficient for lossy dielectrics of various conductivity was calculated using **analytical**, TLM, FDTD, and FVTD methods.

In general, both the source-free and the new time-averaged FVTD method were tested and compared to FDTD and TLM. All methods computed the coefficient of reflection of lossy and loss-less media to an acceptable level of accuracy (within 2% of theoretical values). Although the new time-averaged FVTD has equivalent accuracy to FDTD and TLM for frequencies up to 10 *GHz*, its performance declines for higher frequencies.

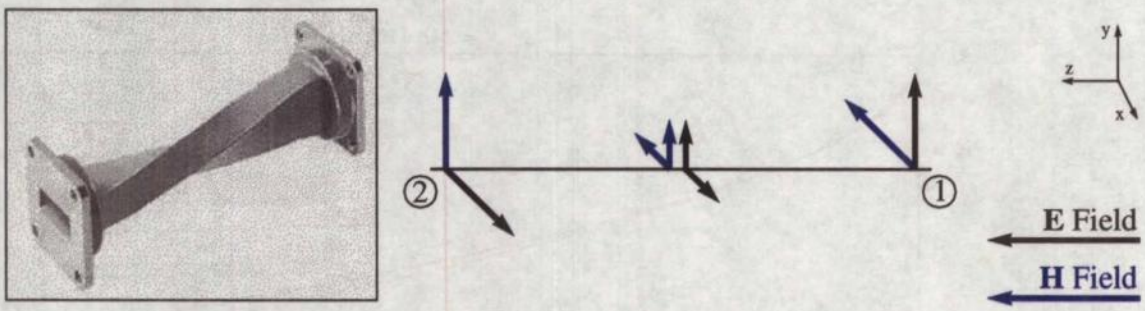

Figure 5.9. Rectangular waveguide twist ((left) and the theoretical field configuration as wave propagates from port 1 to port 2 of the device (right)

5.2.2 Rectangular Waveguide Twists

A waveguide twist is a two port device that changes the polarization of any wave propagating through it. This property is either exploited on its own (for packaging complex waveguide systems) or along with other techniques to build complex devices.* The change in wave polarization is achieved through the gradual rotation of the plane of one of the waveguide's ports with respect to the other. Consider a uniform plane wave propagating from port *one* to port *two* (see **Figure 5.9**). As the wave propagates through

* For example, in a gyrator, the Faraday rotation technique and a 90° twist are used to build a device that has a 180° relative difference in the phase shift for transmission from port 1 to port 2 as compared to the reverse direction [122].

the waveguide twist, the plane of polarization (here defined as the plane perpendicular to the direction of propagation which contains the $\boldsymbol{E}$ and $\boldsymbol{H}$ components of the Poynting vector) progressively rotates, thus merely changing the composition of the components of the Poynting vector.

The mathematical models, propagation characteristics, field configurations, and other parameters of interest for the waveguide twists have been developed and well documented [123]. The main objective of this section is not to characterize, analyse, and extract the various parameters of a specific waveguide twist but rather to verify the application of the general coordinate transformation that was developed in **Section 3.2.2**.

5.2.2.1 Problem Configuration and Excitation

The first step in designing the simulation space is to model the framework of the interior of the waveguide twist. The frame of a twisted guide (aligned with the z-direction) is formulated by the following expressions,

$$\begin{aligned} \xi(x, y, z) &= x\cos\left(\frac{2\pi}{L}z\right) + y\sin\left(\frac{2\pi}{L}z\right) \\ \eta(x, y, z) &= y\cos\left(\frac{2\pi}{L}z\right) - x\sin\left(\frac{2\pi}{L}z\right) \\ \zeta(x, y, z) &= z \end{aligned} \tag{5.7}$$

where (ξ, η, ζ) represent the transformed coordinate system, (x, y, z) are the coordinates of the Cartesian system, and L is the length of the waveguide twist.

The modelled waveguide twist was a "$4''$-$WRT28$-$90°$ E-Field twist" which has a guided area of $(3.556\ mm \times 7.112\ mm)$ and a total length of $L = 101.6\ mm$. For the purpose of this example, the twist was modelled using a simpler (and less mathematical)

approach; the total length of the waveguide twist was divided into 22 equal partitions, and (starting with the second piece) each portion was rotated 4.5° (clockwise) with respect to the previous section. Thus, the final part was rotated 90° with respect to the initial segment. The first and last piece of the model serve as the continuation of the leading or the trailing waveguide circuit. The modelled twisted guide was meshed using a uniform, conformal, and double discretised mesh which assigned 40 cells per wavelength for the lowest cutoff frequency of a waveguide of identical cross-section. Thus, the computational space consisted of $(10 \times 20 \times 386)$ cells. **Table 5.3** presents the properties of the generated mesh in terms of its eigenvalues. The maximum ratio of the eigenvalues in each direction was near unity. The largest eigenvalue necessary for numerical stability was computed to be $|\lambda_{total}| = 2.5193 \times 10^{11}$ $[m/s]$ which corresponds to a time-step of $\Delta t = 4.5835$ ps.

Table 5.3. The ratio of eigenvalues in the twisted waveguide problem

	$\left\|\frac{\lambda_{max}}{\lambda_{min}}\right\|$	$\left\|\frac{\lambda_{total}}{\lambda_{max}}\right\|$	$\left\|\frac{\lambda_{total}}{\lambda_{min}}\right\|$
ξ-direction	1.00	2.98	2.99
η-direction	1.00	2.98	2.98
ξ-direction	1.01	3.02	3.06

5.2.2.2 Simulation Results

In order to test and verify the accuracy and applicability of the derivation (the implementation of the general coordinate system in general, and the mesh generation process and local coordinate transformation in particular), the following test involving the propagation of a uniform plane wave within a twisted guided structure was devised. A Gaussian pulse uniform plane wave was supported using a combination of PEC (on lower

and upper ξ-boundaries) and PMC (on lower and upper η-boundaries) boundary conditions (see **Section 5.2.1.1** for details and formulation).* It was launched in a straight section of space that was added to the source-end of the waveguide twist. This straight section was meshed with cells of comparable size (and eigenvalues) to the twists's computational space. The computational space was terminated with characteristic ABCs at the lower and upper z planes. All electric and magnetic field components were sampled at each time-step at five equal distance locations. These points represented locations within the twisted guide where the change in polarization commenced (***source***) and completed (***end***).

Figure 5.10 contains the plots of these fields at various locations. The successive plotted field values at each observation point are intended to visualize the gradual transformation (*i.e.* change in polarization) of the field components as the wave propagated through the twist. The simulation results of the gradual transformation of the configuration of the propagating pulse are consistent with the theoretical explanation of the operation of a waveguide twist discussed earlier (see **Section 5.2.2**).

---

* As previously discussed, one of the advantages of using the FVTD technique in combination with a general coordinate system is the ease of locating and enforcing various types of boundary conditions. For example, in the case of a twisted guide, the boundary conditions that are defined and applied in the computational space are mapped into the proper locations in the physical space via the coordinate transformation.

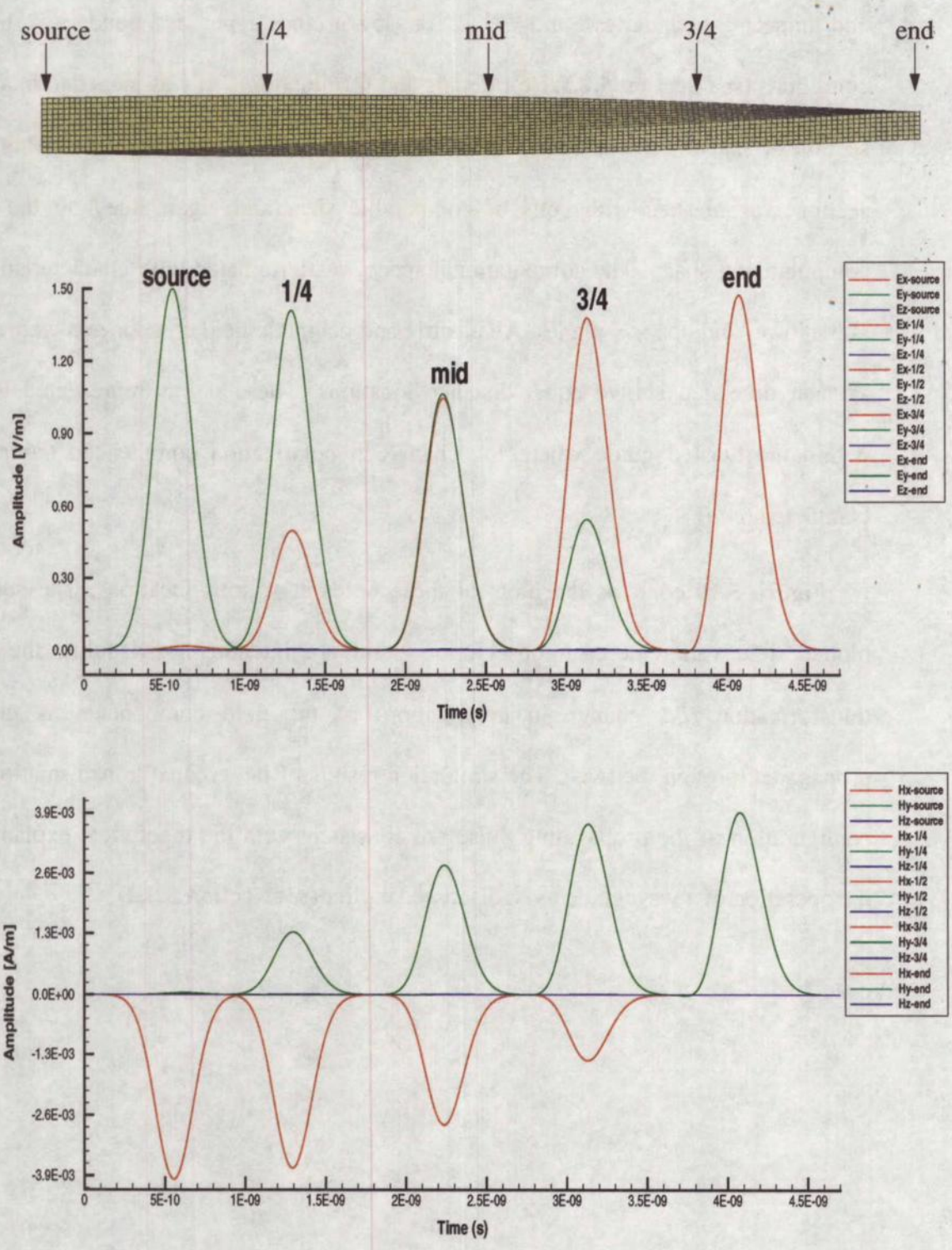

Figure 5.10. Propagation of a uniform plane wave in a twisted rectangular waveguide: meshed simulation space (top) along with the transient response of electric (middle) and magnetic (bottom) fields of a uniform plane wave sampled at various locations.

5.2.3 Characteristic ABCs and Non-Orthogonal Grids

The characteristic ABCs used in the FVTD method are most effective in absorbing normal incident waves. Although conformal meshes can be designed to take advantage of this property (by aligning the direction of the outgoing wave with the normal to the ABC) and maximize the absorbing rate of the ABC, it is not always possible to do so. Hence, it is important to test and document the effectiveness of the characteristic ABCs used in FVTD in several non-uniform conformal meshes.

Three separate tests were conducted using a test case similar to that described in **Section 5.2.1.1**, namely, a Gaussian pulse uniform plane wave propagating in the z-direction supported by a combination of PEC and PMC boundary conditions. The first simulation was conducted on a uniform orthogonal grid which served as a benchmark for future applications. The other two grids consisted of uniform orthogonal portions (where the pulse was launched) and then were gradually deformed using either a skewed or a curved pattern in the same manner as shown in [124]. The largest eigenvalues necessary for the numerical stability of the uniform skewed and curved grids were computed to be $|\lambda_{total}| = 3.5983\times10^{11}$, 9.6174×10^{11}, and 1.2635×10^{12} $[m/s]$, respectively. These correspond to a time-step of $\Delta t = 0.32090$, 1.2006, and 0.91388 ps, respectively. **Table 5.4** and **Table 5.5** contain the properties of the generated skewed and curved meshes in terms of their eigenvalues. In both cases, the maximum ratio of the eigenvalues in each direction was very close to unity which ensured the second order accuracy of the solution.

In all cases using the modal expansion method (described in **Appendix C**), the reflection from the ABC was computed at several grid points adjacent to the ABC. **Figure 5.11** plots the reflection coefficients from the characteristic ABC defined at the end of the

problem space. The reflection from the ABC in the uniform orthogonal space represents the best case scenario and with a reflection of better than -60 *dB*, is more than adequate for analysing most practical problems. Although the reflection coefficient of the ABC for the skewed grid is almost two orders of magnitude larger than is the one computed for the uniform grid, it is still better than -30 *dB* for a wide band of frequencies and can still be used in many applications. In a curved mesh, the characteristic ABC has a reflection coefficient of better than -45 *dB*, which outperforms the skewed mesh case, but is effective for a narrower range of frequencies. The aforementioned reflection coefficient of the characteristic ABCs of the FVTD method was compared with the absorption rate for PML-ABC and FDTD on similar meshes reported in [124]. In all cases, the characteristic ABC of the FVTD method did not perform as well as the PML-ABC in the FDTD technique; however, considering that characteristic ABCs require minimal computation resources (as compared to PML-ABC), its performance is far better than expected.

Table 5.4. The ratio of eigenvalues in the skewed mesh

	$\left\|\frac{\lambda_{max}}{\lambda_{min}}\right\|$	$\left\|\frac{\lambda_{total}}{\lambda_{max}}\right\|$	$\left\|\frac{\lambda_{total}}{\lambda_{min}}\right\|$
ξ-direction	1.00	3.05	3.05
η-direction	1.00	3.05	3.05
ξ-direction	1.07	2.91	3.11

Table 5.5. The ratio of eigenvalues in the curved mesh

	$\left\|\frac{\lambda_{max}}{\lambda_{min}}\right\|$	$\left\|\frac{\lambda_{total}}{\lambda_{max}}\right\|$	$\left\|\frac{\lambda_{total}}{\lambda_{min}}\right\|$
ξ-direction	1.12	3.58	4.26
η-direction	1.19	3.58	4.26
ξ-direction	1.37	2.27	3.10

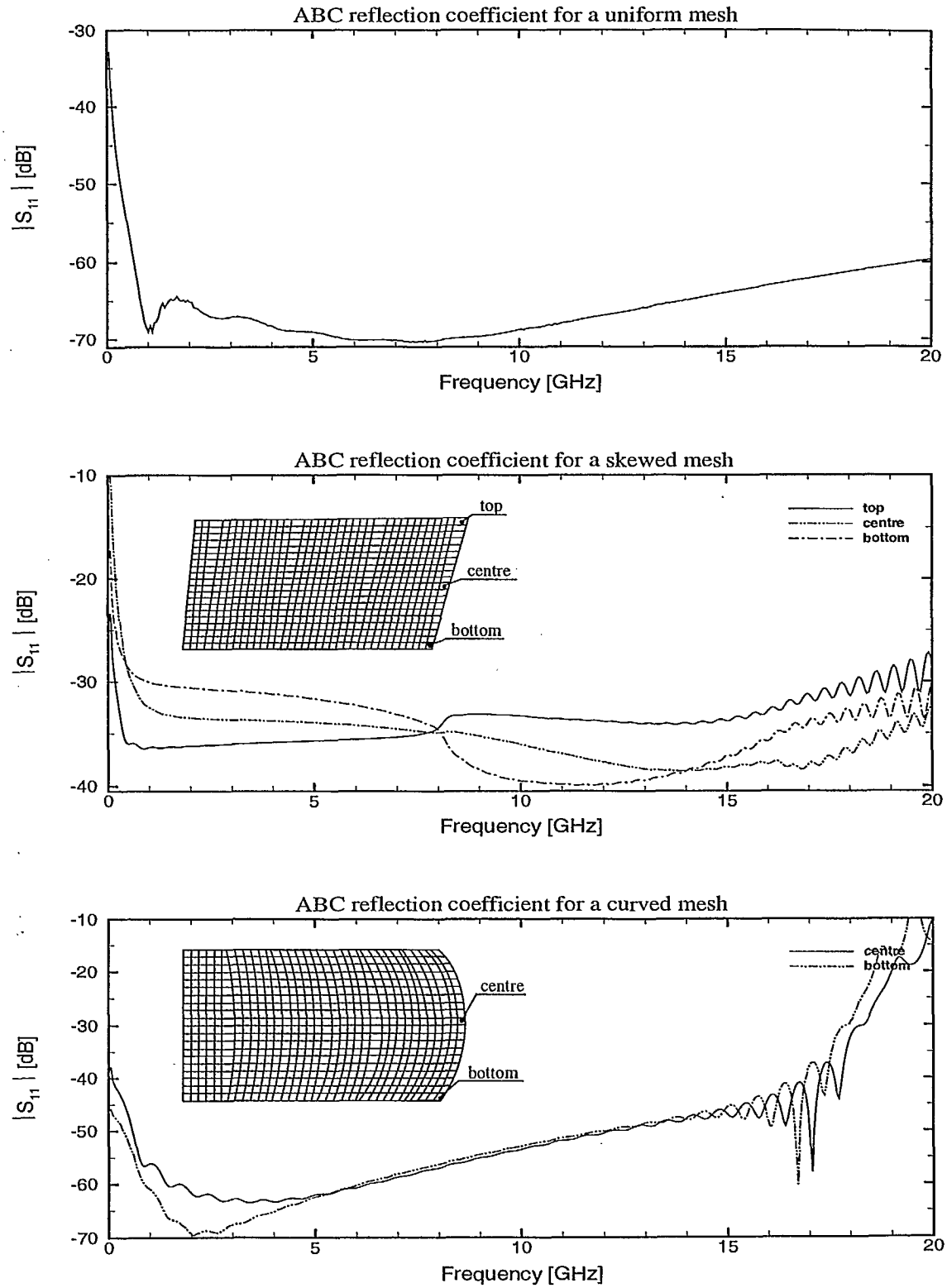

Figure 5.11. Reflection coefficient using characteristic ABCs defined at the ends of uniform, gradually skewed, and gradually curved meshes

5.3 Summary

Since the principal goal of this thesis is to investigate and develop a general purpose EM simulator that is capable of accurately modelling and solving complex EM problems, the testing and implementation of the newly derived time-averaged FVTD algorithm is necessary. In this chapter, the accuracy of the aforementioned algorithm was investigated for both modelling material properties and geometrically complex objects. In addition to these test cases, some key numerical issues, such as the method of discretisation, the computing coordinate transformation metrical coefficient, and the cell size ratio were also discussed. These numerical issues are essential in obtaining solutions of sufficient accuracy. Another crucial issue is the performance of the characteristic ABCs that are used to terminate the problem space. The reflection coefficients from the characteristic ABCs were computed and documented for several uniform and non-uniform grids. Although the characteristic ABCs do not perform as well as the FDTD's PML-ABCs (on similar grid configurations), their performance is well within the acceptable range required for analysing most practical problems.

Chapter 6

Formulation of Lumped Elements in General Coordinate Systems

Recently, the full-wave modelling of (electronic) circuits has been receiving considerable attention from the CEM community [125]. Some of the applications of the EM analysis of circuit structures may include: the study of cross-talk and radiation from circuit elements, EMI/EMC studies, and the broad band analysis of microwave or electronic circuits [126]. However, in order to accurately represent and solve a circuit structure, a model for various lumped elements must be developed. This chapter focuses on extending the Lax-Wendroff version of the 3D-FVTD formulation to include linear passive circuit/lumped elements, such as resistors and capacitors,* and linear independent active elements (*i.e.* voltage and current sources). The modelling and formulation of circuit elements demand an understanding of the basic operation of lumped elements and their relation to Maxwell's equations. Hence, the theory of the operation of these devices is considered first.

* The formulation for inductors was not considered due to the scarcity of applications.

6.1 Introduction to the Formulation of Lumped Elements

The general form of Ampere's Law is given by:

$$\nabla \times \mathcal{E} = \frac{\partial \boldsymbol{D}}{\partial t} + \sigma \mathcal{E} + \boldsymbol{J}_L, \tag{6.1}$$

and after substituting $\boldsymbol{J}_c = \sigma \mathcal{E}$ for the conduction current density term, it becomes:

$$\nabla \times \mathcal{H} - \frac{\partial \boldsymbol{D}}{\partial t} = \boldsymbol{J}_c + \boldsymbol{J}_L, \tag{6.2}$$

where $\frac{\partial \boldsymbol{D}}{\partial t}$ is the displacement current density, and $\boldsymbol{J}_L$ is referred to as the lumped element current density [127]. The lumped element current density is an additional current component due to the presence of the lumped element. Note that this assumption treats lumped elements as imaginary (more specifically size-less) components that are distributed* over a pre-defined region and are connected in parallel to individual cells in the direction of the current flow. This implies that the content (and property) of the cells, for which a lumped element is defined, does not change; that is, the total current density flowing through the cross-section of a cell is the sum of the displacement, conduction, and lumped element current densities. This approach allows for the *independent* modelling of lumped elements as circuit elements (say, the resistance of a resistor) and as an object (say, the physical property of the resistor's casing). Thus, the distributed model of a lumped element may differ from its physical location in a given structure.

6.2 Electric Current and Current Density in Lumped Elements

Electric ***current*** is defined as an ordered motion of electric charges that quantifies the

* The exact method of modelling lumped elements and the rules that apply to the current density distribution of lumped elements are element-type specific and will be clearly stated in later discussions.

magnitude (or intensity) of the flow of charges passing through a reference point in units of magnitude of electric charge per unit time (C/s) [127]. A more rigorous measure of current flow is given by current distribution, a vector field that defines the direction of the flow and the rate of flow of the electric charges through a surface orthogonal to the flow of the charges. Likewise, ***current density***, $\boldsymbol{J}$, is defined as the magnitude of the charges passing through a surface (orthogonal to the current flow) of a unit area in a unit time; hence, an electric current element is defined as:

$$\Delta I = \boldsymbol{J} \cdot \boldsymbol{n} \Delta s \qquad [A], \tag{6.3}$$

where $\boldsymbol{n}$ is the unit normal vector which defines the positive direction of current flow, and Δs is an element of a surface, S, through which the current density flows. The total current flowing through S is determined by [127]:

$$I = \iint_S \boldsymbol{J} \cdot \boldsymbol{n} ds. \tag{6.4}$$

Although the most general formulation of lumped elements in the FVTD method demands the modelling of devices that are arbitrarily shaped and randomly located in the physical space of a given problem, it is realistic to assume that in most practical cases, the lumped element is placed (or can be defined and modelled) in the direction of one of the axes of the computational coordinate system. Hence, the lumped element current density has components that are aligned with the axis of the general coordinate system in the computational space,

$$\boldsymbol{J}_L = J_{L\xi} \boldsymbol{a}_\xi + J_{L\eta} \boldsymbol{a}_\eta + J_{L\zeta} \boldsymbol{a}_\zeta .^{*} \tag{6.5}$$

---

* For most future discussions, the subscript, L, is dropped for brevity.

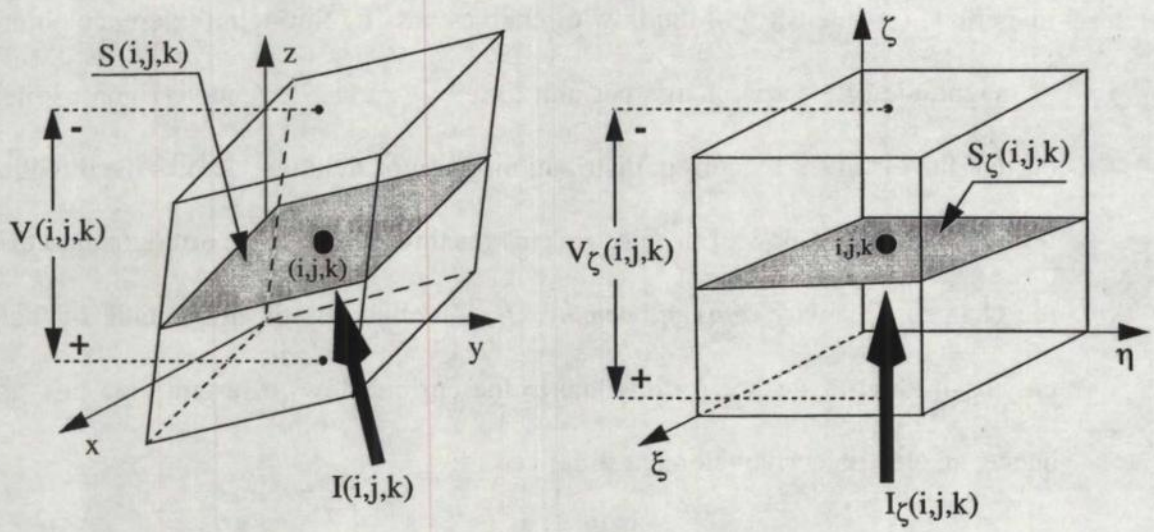

Figure 6.1. The lumped element current in (a) a physical cell and in (b) a computational cell

However, the uniform rectangular grid of the computational space is the transformation of a general (non uniform) coordinate system. This transformation not only affects individual grid points, but also requires that the governing differential equations and differential operators be recast in order to reflect the transformation between the physical and the computational space. Therefore, using the theory of curvilinear coordinates in **Appendix B**, and the corresponding formulation of line and surface elements in general coordinate systems, the current density through (and the potential difference between) the faces of a physical cell is represented in terms of the computational components of the voltage and current of that cell.

Hence, for a given cell centred at (i, j, k), one component of the lumped element current density, J_ζ, is defined to be flowing in the positive ζ direction and is assumed to be uniformly distributed over a surface, S_ζ, orthogonal to the direction of the current flow, and located in the $\xi\eta$ plane (as shown in **Figure 6.1**). The total current flowing through

the computational cell is given by (6.4):

$$(I_\zeta)_{i,j,k} = \iint_S \boldsymbol{J}_{i,j,k} \cdot \boldsymbol{n} ds = \iint_S \boldsymbol{J}_{i,j,k} \cdot \boldsymbol{a}_\zeta ds = (J_\zeta)_{i,j,k}(S_\zeta)_{i,j,k}. \tag{6.6}$$

The current flow through the cell in the physical space is also calculated using (6.4) where the surface integral and its corresponding surface element are evaluated using the expressions derived for curvilinear coordinates (see **Appendix B**).

Consider the total lumped current flowing through a cell in the physical space given by:

$$I_{i,j,k} = \iint_S \boldsymbol{J}_{i,j,k} \cdot \boldsymbol{n} ds. \tag{6.7}$$

The surface integral is then transformed into the computational space via the expression of surface elements in the ζ-surface (B.34):

$$I_\zeta = \iint_S \boldsymbol{J} \cdot \boldsymbol{n} (\sqrt{g_{\xi\xi} g_{\eta\eta} - g_{\xi\eta}^2}) d\xi d\eta, \tag{6.8}$$

where the unit normal vector, $\boldsymbol{n}$, is orthogonal to the ζ-surface and is defined in terms of the reciprocal vector, $\boldsymbol{a}^\zeta$, as well as unitary vectors of the curvilinear coordinates (B.68),

$$\boldsymbol{n} = \frac{\boldsymbol{a}^\zeta}{\sqrt{\boldsymbol{a}^\zeta \cdot \boldsymbol{a}^\zeta}} = \frac{V}{\sqrt{(\boldsymbol{a}_\xi \times \boldsymbol{a}_\eta) \cdot (\boldsymbol{a}_\xi \times \boldsymbol{a}_\eta)}} \boldsymbol{a}^\zeta = \frac{\boldsymbol{a}_\zeta \cdot (\boldsymbol{a}_\xi \times \boldsymbol{a}_\eta)}{\sqrt{(\boldsymbol{a}_\xi \times \boldsymbol{a}_\eta) \cdot (\boldsymbol{a}_\xi \times \boldsymbol{a}_\eta)}} \boldsymbol{a}^\zeta. \tag{6.9}$$

The above expression is then recast in terms of the metrical coefficients of transformation by utilizing equations (B.29) to (B.37). Hence, the scalar product of the current density and unit normal vector of (6.8) becomes:

$$\boldsymbol{J} \cdot \boldsymbol{n} = \frac{\sqrt{g}}{\sqrt{g_{\xi\xi} g_{\eta\eta} - g_{\xi\eta}^2}} (\boldsymbol{J} \cdot \boldsymbol{a}^\zeta). \tag{6.10}$$

Furthermore, it was previously shown (see (B.21)) that

$$\boldsymbol{J}\cdot\boldsymbol{a}^{\zeta}=j^{\zeta}=\frac{J_{\zeta}}{\sqrt{g_{\zeta\zeta}}} \tag{6.11}$$

where J_{ζ} is the unit vector component of the lumped current density in the ζ direction. Next, (6.10) and (6.11) are substituted in (6.8):

$$I_{\zeta}=\iint_{S}\frac{\sqrt{g}}{\sqrt{g_{\xi\xi}g_{\eta\eta}-g_{\xi\eta}^{2}}}\left(\frac{J_{\zeta}}{\sqrt{g_{\zeta\zeta}}}\right)\left(\sqrt{g_{\xi\xi}g_{\eta\eta}-g_{\xi\eta}^{2}}\right)d\xi d\eta\,, \tag{6.12}$$

and then in (6.7). The lumped current flowing through a cell in the ζ direction is given by:

$$I_{\zeta}=\frac{\sqrt{g}}{\sqrt{g_{\zeta\zeta}}}\iint_{S}J_{\zeta}d\xi d\eta\,, \tag{6.13}$$

where, by definition of coordinate transformation, $d\xi$ and $d\eta$ represent the displacement of unit length along the ξ and η axes respectively. The total lumped current flow in a cell in the ζ direction is computed by:

$$(I_{\zeta})_{i,\,j,\,k}=\frac{\sqrt{g_{i,\,j,\,k}}}{\sqrt{(g_{\zeta\zeta})_{i,\,j,\,k}}}(J_{\zeta})_{i,\,j,\,k}\,. \tag{6.14}$$

Similar expressions for the lumped current due to the elements defined in the ξ and η directions can be derived as:

$$(I_{\zeta})_{i,\,j,\,k}=\frac{\sqrt{g_{i,\,j,\,k}}}{\sqrt{(g_{\xi\xi})_{i,\,j,\,k}}}(J_{\xi})_{i,\,j,\,k}\,, \tag{6.15}$$

$$(I_{\eta})_{i,\,j,\,k}=\frac{\sqrt{g_{i,\,j,\,k}}}{\sqrt{(g_{\eta\eta})_{i,\,j,\,k}}}(J_{\eta})_{i,\,j,\,k}\,. \tag{6.16}$$

Therefore, after substituting (6.14) to (6.16) in the expression of the total lumped current density flowing through a cell given in (6.4), this expression is calculated in terms of the components of the lumped element current; that is:

$$(\boldsymbol{J}_L)_{i,j,k} = \frac{\sqrt{(g_{\xi\xi})_{i,j,k}}}{\sqrt{g_{i,j,k}}}(I_{L\xi})_{i,j,k}\boldsymbol{i}_\xi + \frac{\sqrt{(g_{\eta\eta})_{i,j,k}}}{\sqrt{g_{i,j,k}}}(I_{L\eta})_{i,j,k}\boldsymbol{i}_\eta + \frac{\sqrt{(g_{\zeta\zeta})_{i,j,k}}}{\sqrt{g_{i,j,k}}}(I_{L\zeta})_{i,j,k}\boldsymbol{i}_\zeta . \tag{6.17}$$

6.3 Potential Difference and Cell Voltages

Voltage is defined as the negative line integral of the electric field between two points on the path of integration [128]. In a static field, the ***potential difference***, Φ, between points a and b is defined as "*work done on a unit test charge in moving from a to b* [128]"

$$\Phi_{ab} = -\int_b^a \mathcal{E} \cdot d\boldsymbol{l}, \tag{6.18}$$

which would suggest that on a closed path of integration, no net work is done; that is:

$$\oint_C \mathcal{E} \cdot d\boldsymbol{l} = 0, \tag{6.19}$$

and that the value of the potential difference is independent of the path of integration [127]. However, in the case of time-varying electric fields, Faraday's Law,

$$\oint_C \mathcal{E} \cdot d\boldsymbol{l} = -\frac{\partial}{\partial t}\iint_S \boldsymbol{B} \cdot d\boldsymbol{s}, \tag{6.20}$$

indicates that on a closed path of integration, the voltage is not zero because of the contributions of the time varying magnetic flux to the closed path of integration.* Also, due to the contribution of the time-varying magnetic field through the path of integration, the voltage between the two points is path dependent [128]. Therefore, all lumped element voltages (which are due to the flow of lumped element currents in cells) must be defined using an identical path of integration in all cells.

In general, a lumped element voltage between any two cell faces (located on the same

* The voltage on such a closed path is often referred to as the ***electromotive force*** (emf) [3].

coordinate plane) is represented in terms of electric field values located at the centre of the cell. This is accomplished by applying the classical definition of the potential difference between two points:

$$V_{Lab} = -\int_{b}^{a} \mathcal{E} \cdot dl. \tag{6.21}$$

Since the fields located at the centre of each cell are assumed to be constant over the volume of the cell, the potential difference between the two faces of a cell in the ζ direction, for example, is calculated by:*

$$V_{\zeta} = -\int_{b}^{a} \mathcal{E} \cdot a_{\zeta} d\zeta. \tag{6.22}$$

The scalar product of the electric field and the unitary vector is defined by (B.17) to (B.19)

$$\mathcal{E} \cdot a_{\zeta} = e_{\zeta} = \sum_{j=\xi,\eta,\zeta} g_{\zeta j}\, e^{j}. \tag{6.23}$$

In (6.11), $e^{j} = E_j / \sqrt{g_{jj}}$, and hence, (6.23) becomes:

$$\mathcal{E} \cdot a_{\zeta} = \sum_{j=\xi,\eta,\zeta} \left(\frac{g_{\zeta j}}{\sqrt{g_{jj}}} \mathcal{E}_j \right) = \frac{g_{\zeta\xi}}{\sqrt{g_{\xi\xi}}} E_{\xi} + \frac{g_{\zeta\eta}}{\sqrt{g_{\eta\eta}}} E_{\eta} + \frac{g_{\zeta\zeta}}{\sqrt{g_{\zeta\zeta}}} E_{\zeta}. \tag{6.24}$$

Next, the above expression is substituted in (6.22),

$$V_{\zeta} = -\int_{b}^{a} \left(\frac{g_{\zeta\xi}}{\sqrt{g_{\xi\xi}}} E_{\xi} + \frac{g_{\zeta\eta}}{\sqrt{g_{\eta\eta}}} E_{\eta} + \frac{g_{\zeta\zeta}}{\sqrt{g_{\zeta\zeta}}} E_{\zeta} \right) d\zeta \tag{6.25}$$

where in a computational space, a and b are located on two parallel faces of the cell located on the ζ plane, with the path of integration passing through the centre of the cell as well as through a and b. Since in a computational space the differential, $d\zeta$, is of unit

* Once more, the subscript, L, is dropped for brevity.

length, the lumped voltage of a cell (due to the lumped current flow in the ζ direction), with its centre located at (i, j, k), is given by:

$$(V_\zeta)_{i,j,k} = -\left(\frac{(g_{\zeta\xi})_{i,j,k}}{\sqrt{(g_{\xi\xi})_{i,j,k}}}(E_\xi)_{i,j,k} + \frac{(g_{\zeta\eta})_{i,j,k}}{\sqrt{(g_{\eta\eta})_{i,j,k}}}(E_\eta)_{i,j,k} + \frac{(g_{\zeta\zeta})_{i,j,k}}{\sqrt{(g_{\zeta\zeta})_{i,j,k}}}(E_\zeta)_{i,j,k} \right) \quad (6.26)$$

The expressions of the voltages, V_ξ and V_η, which are defined between the other parallel faces of the cell located in the ξ– and η-surface respectively, are:

$$(V_\xi)_{i,j,k} = -\left(\frac{(g_{\xi\xi})_{i,j,k}}{\sqrt{(g_{\xi\xi})_{i,j,k}}}(E_\xi)_{i,j,k} + \frac{(g_{\xi\eta})_{i,j,k}}{\sqrt{(g_{\eta\eta})_{i,j,k}}}(E_\eta)_{i,j,k} + \frac{(g_{\xi\zeta})_{i,j,k}}{\sqrt{(g_{\zeta\zeta})_{i,j,k}}}(E_\zeta)_{i,j,k} \right) \quad (6.27)$$

$$(V_\eta)_{i,j,k} = -\left(\frac{(g_{\eta\xi})_{i,j,k}}{\sqrt{(g_{\xi\xi})_{i,j,k}}}(E_\xi)_{i,j,k} + \frac{(g_{\eta\eta})_{i,j,k}}{\sqrt{(g_{\eta\eta})_{i,j,k}}}(E_\eta)_{i,j,k} + \frac{(g_{\eta\zeta})_{i,j,k}}{\sqrt{(g_{\zeta\zeta})_{i,j,k}}}(E_\zeta)_{i,j,k} \right) \quad (6.28)$$

6.4 Ohm's Law and Lumped Elements

A lumped element refers to any device that is used to construct an electric circuit. However, the following discussion focuses on either ***passive*** (devices without a source of electric energy, such as resistors and capacitors) or ***active*** elements (*i.e.* voltage and current sources). In the case of active devices, the element is assumed to be ***independent***; that is, the terminal voltage or current of the device remains constant regardless of the load connected to the source. In circuit analysis, the relationship between the terminal voltage and the current of a circuit element is determined by Ohm's Law. In all cases, positive current flow is defined in the direction of the voltage rise across the device. Hence, the I-V relationship of various lumped elements, as given by Ohm's Law, is [129]:

resistor: $$I = \frac{V}{R}, \quad (6.29)$$

capacitor: $$I = C\frac{dV}{dt}, \tag{6.30}$$

Thévenin voltage source: $$I = \frac{V + V_{source}}{R}, \tag{6.31}$$

and Norton current source: $$I = \frac{V}{R} + I_{source}. \tag{6.32}$$

Generally, the source term, $\boldsymbol{S}$, of Maxwell's equations (3.25) is the sum of the conduction current and lumped current density. However, the lumped element current is represented as a function of the terminal voltage of a device. Also, the terminal voltage of an element is expressed as a function of the electric field (see (6.26) to (6.28)). Hence, the lumped current density can be written as a function of the electric field; that is [130]:

$$\boldsymbol{J}_c = \mathrm{f}(I) \quad \text{where} \quad I = \mathrm{f}(V) \quad \text{and} \quad V = \mathrm{f}(\mathcal{E}) \quad \text{then} \quad \boldsymbol{J}_c = \mathrm{f}(\mathcal{E}). \tag{6.33}$$

In order to take advantage of the newly formulated Lax-Wendroff FVTD algorithm, (4.108), the source term is expressed as a function of the solution vector, $\boldsymbol{Q}$,

$$\boldsymbol{S} = -\boldsymbol{J}_c - \boldsymbol{J}_L = [\boldsymbol{K}]\boldsymbol{Q} + [\boldsymbol{L}]\mathrm{f}(\boldsymbol{Q}) \tag{6.34}$$

where $[\boldsymbol{K}]$ represents the conductivity of each cell, and $[\boldsymbol{L}]$ contains the coefficients that satisfy the algebraic relationship between the terminal voltage and current of the lumped element as stated by Ohm's Law; *i.e.*:

$$[\boldsymbol{K}] = -\frac{\sigma}{\varepsilon}\begin{bmatrix} 0&0&0&0&0&0 \\ 0&0&0&0&0&0 \\ 0&0&0&0&0&0 \\ 0&0&0&1&0&0 \\ 0&0&0&0&1&0 \\ 0&0&0&0&0&1 \end{bmatrix}, \quad [\boldsymbol{L}] = -\frac{1}{\varepsilon}\begin{bmatrix} 0&0&0&0&0&0 \\ 0&0&0&0&0&0 \\ 0&0&0&0&0&0 \\ 0&0&0&\mathrm{f}(E_\xi)&\mathrm{f}(E_\eta)&\mathrm{f}(E_\zeta) \\ 0&0&0&\mathrm{f}(E_\xi)&\mathrm{f}(E_\eta)&\mathrm{f}(E_\zeta) \\ 0&0&0&\mathrm{f}(E_\xi)&\mathrm{f}(E_\eta)&\mathrm{f}(E_\zeta) \end{bmatrix}. \tag{6.35}$$

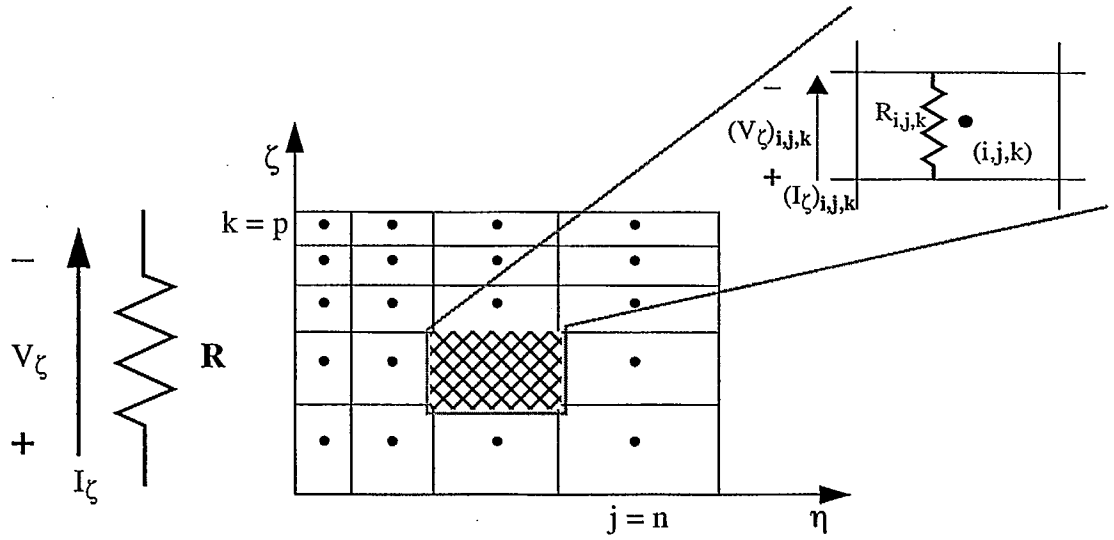

Figure 6.2. Model of a lumped resistor in a general coordinate system

6.5 Formulation of Lumped Resistors

If a resistor (shown in **Figure 6.2**) of resistance, R, is defined (distributed) over a region of $1 \le i \le m$, $1 \le j \le n$, $1 \le k \le p$, aligned with the ζ axis, then according to Ohm's Law, the algebraic relationship between the terminal voltage and current is:

$$I_\zeta^R = \frac{V_\zeta^R}{R_\zeta}, \tag{6.36}$$

where V_ζ^R is the algebraic sum of the individual cell voltages (computed in any column of cells within the lumped model) in the direction of lumped current flow; that is:

$$V_\zeta^R = \sum_{k=1}^{p} (V_\zeta^R)_{i,j,k}. \tag{6.37}$$

The corresponding lumped current, I_ζ^R, is represented in terms of a respective component of the lumped element current density, (6.14). Thus, the total current flowing across any constant plane, say $\xi\eta$-plane, perpendicular to the direction of the current flow is given by:

$$I_\zeta^R = \sum_{i=1}^{m}\sum_{j=1}^{n}(I_\zeta^R)_{i,j,k} = \sum_{i=1}^{m}\sum_{j=1}^{n}\frac{\sqrt{g_{i,j,k}}}{\sqrt{(g_{\zeta\zeta})_{i,j,k}}}(J_\zeta^R)_{i,j,k}. \tag{6.38}$$

It is assumed that the terminal current of the resistor is equally distributed over the entire region of the lumped model; hence, *the current density across any plane surface of the model is constant.* Thus, (6.38) becomes:

$$(J_\zeta^R)_{i,j,k} = \frac{I_\zeta^R}{\sum_{i=1}^{m}\sum_{j=1}^{n}\frac{\sqrt{g_{i,j,k}}}{\sqrt{(g_{\zeta\zeta})_{i,j,k}}}}, \tag{6.39}$$

where the cell current density is replaced by its equivalent expression of (6.14); that is:

$$(I_\zeta^R)_{i,j,k} = \frac{\frac{\sqrt{g_{i,j,k}}}{\sqrt{(g_{\zeta\zeta})_{i,j,k}}}}{\sum_{i=1}^{m}\sum_{j=1}^{n}\frac{\sqrt{g_{i,j,k}}}{\sqrt{(g_{\zeta\zeta})_{i,j,k}}}} I_\zeta^R. \tag{6.40}$$

The above equation represents a cell's lumped current as a function of the total current of the resistor defined along the ζ-direction. Furthermore, using (6.36) and (6.37),

$$(I_\zeta^R)_{i,j,k} = \frac{\frac{\sqrt{g_{i,j,k}}}{\sqrt{(g_{\zeta\zeta})_{i,j,k}}}}{\sum_{i=1}^{m}\sum_{j=1}^{n}\frac{\sqrt{g_{i,j,k}}}{\sqrt{(g_{\zeta\zeta})_{i,j,k}}}}\frac{V_\zeta^R}{R_\zeta} = \frac{\frac{\sqrt{g_{i,j,k}}}{\sqrt{(g_{\zeta\zeta})_{i,j,k}}}\sum_{k=1}^{p}(V_\zeta^R)_{i,j,k}}{R_\zeta\sum_{i=1}^{m}\sum_{j=1}^{n}\frac{\sqrt{g_{i,j,k}}}{\sqrt{(g_{\zeta\zeta})_{i,j,k}}}}. \tag{6.41}$$

Ohm's Law also applies to individual cells of a lumped model; hence:

$$(R_\zeta)_{i,j,k} = \frac{(V_\zeta^R)_{i,j,k}}{(I_\zeta^R)_{i,j,k}}. \tag{6.42}$$

After substituting for $(I_\zeta^R)_{i,j,k}$ from (6.41),

$$(R_\zeta)_{i,j,k} = \frac{\sum_{i=1}^{m}\sum_{j=1}^{n}\frac{\sqrt{g_{i,j,k}}}{\sqrt{(g_{\zeta\zeta})_{i,j,k}}}}{\frac{\sqrt{g_{i,j,k}}}{\sqrt{(g_{\zeta\zeta})_{i,j,k}}}\sum_{k=1}^{p}(V_\zeta)_{i,j,k}} R_\zeta (V_\zeta^R)_{i,j,k}. \tag{6.43}$$

Equation (6.26) supplies the expression for cell voltage; then (6.43) becomes:

$$(R_\zeta)_{i,j,k} = \frac{\sum_{i=1}^{m}\sum_{j=1}^{n}\frac{\sqrt{g_{i,j,k}}}{\sqrt{(g_{\zeta\zeta})_{i,j,k}}}}{\frac{\sqrt{g_{i,j,k}}}{\sqrt{(g_{\zeta\zeta})_{i,j,k}}}} R_\zeta \frac{-\left(\frac{(g_{\zeta\xi})_{i,j,k}}{\sqrt{(g_{\xi\xi})_{i,j,k}}}(E_\xi^R)_{i,j,k} + \frac{(g_{\zeta\eta})_{i,j,k}}{\sqrt{(g_{\eta\eta})_{i,j,k}}}(E_\eta^R)_{i,j,k} + \frac{(g_{\zeta\zeta})_{i,j,k}}{\sqrt{(g_{\zeta\zeta})_{i,j,k}}}(E_\zeta^R)_{i,j,k}\right)}{\sum_{k=1}^{p}-\left(\frac{(g_{\zeta\xi})_{i,j,k}}{\sqrt{(g_{\xi\xi})_{i,j,k}}}(E_\xi^R)_{i,j,k} + \frac{(g_{\zeta\eta})_{i,j,k}}{\sqrt{(g_{\eta\eta})_{i,j,k}}}(E_\eta^R)_{i,j,k} + \frac{(g_{\zeta\zeta})_{i,j,k}}{\sqrt{(g_{\zeta\zeta})_{i,j,k}}}(E_\zeta^R)_{i,j,k}\right)}. \tag{6.44}$$

The current flowing through each cell, $(I_\zeta^R)_{i,j,k}$, and, the current density of the cell, $(J_\zeta^R)_{i,j,k}$, are associated with an electric field component in that direction; that is:

$$(J_\zeta^R)_{i,j,k} = \mathrm{f}((E_\zeta^R)_{i,j,k}). \tag{6.45}$$

Consequently, *the electric fields of the lumped element that are not aligned with the direction of current flow in the resistor are zero*, and (6.44) becomes:

$$(R_\zeta)_{i,j,k} = \frac{\sum_{i=1}^{m}\sum_{j=1}^{n}\frac{\sqrt{g_{i,j,k}}}{\sqrt{(g_{\zeta\zeta})_{i,j,k}}}\frac{(g_{\zeta\zeta})_{i,j,k}}{\sqrt{(g_{\zeta\zeta})_{i,j,k}}}(E_\zeta^R)_{i,j,k}}{\frac{\sqrt{g_{i,j,k}}}{\sqrt{(g_{\zeta\zeta})_{i,j,k}}}\sum_{k=1}^{p}\frac{(g_{\zeta\zeta})_{i,j,k}}{\sqrt{(g_{\zeta\zeta})_{i,j,k}}}(E_\zeta^R)_{i,j,k}} R_\zeta. \tag{6.46}$$

It is also assumed that (*within a lumped element*) *the fields due to the lumped current flow are uniformly distributed along the direction of current flow*. This means that *the* $(E_\zeta^R)_{i,j,k}$ *term is* k *independent*; therefore, upon the cancellation of like terms in (6.46), the value of

the distributed lumped resistance of any cell (within the lumped model defined in the ζ direction) is given in terms of the value of the lumped resistor via:

$$(R_\zeta)_{i,j,k} = \frac{(g_{\zeta\zeta})_{i,j,k} \sum_{i=1}^{m} \sum_{j=1}^{n} \frac{\sqrt{g_{i,j,k}}}{\sqrt{(g_{\zeta\zeta})_{i,j,k}}}}{\sqrt{g_{i,j,k}} \sum_{k=1}^{p} \sqrt{(g_{\zeta\zeta})_{i,j,k}}} R_\zeta . \tag{6.47}$$

Essentially, the aforementioned procedure is repeated to derive expressions for resistors defined in other directions. Thus, the distributed resistance of an ξ-axis aligned resistor is given by:

$$(R_\xi)_{i,j,k} = \frac{(g_{\xi\xi})_{i,j,k} \sum_{j=1}^{n} \sum_{k=1}^{p} \frac{\sqrt{g_{i,j,k}}}{\sqrt{(g_{\xi\xi})_{i,j,k}}}}{\sqrt{g_{i,j,k}} \sum_{i=1}^{m} \sqrt{(g_{\xi\xi})_{i,j,k}}} R_\xi , \tag{6.48}$$

while the distributed resistance of an η-axis aligned resistor becomes:

$$(R_\eta)_{i,j,k} = \frac{(g_{\eta\eta})_{i,j,k} \sum_{i=1}^{m} \sum_{k=1}^{p} \frac{\sqrt{g_{i,j,k}}}{\sqrt{(g_{\eta\eta})_{i,j,k}}}}{\sqrt{g_{i,j,k}} \sum_{j=1}^{n} \sqrt{(g_{\eta\eta})_{i,j,k}}} R_\eta . \tag{6.49}$$

Next, the above expression, along with the I-V relationship of a lumped resistor, (6.29), and the value of various cell voltages, given in (6.26) to (6.28), are substituted in the general expression of the lumped element current density of (6.17);* Thus, the expression for lumped current density (within a lumped element model) becomes:

---

* It must be noted that only the field components along the direction of (lumped) current flow are non-zero.

$$(\boldsymbol{J}_L^R)_{i,j,k} = -\left(\frac{(g_{\xi\xi})_{i,j,k}}{\sqrt{g_{i,j,k}}}\frac{(E_\xi^R)_{i,j,k}}{(R_\xi)_{i,j,k}}\boldsymbol{i}_\xi + \frac{(g_{\eta\eta})_{i,j,k}}{\sqrt{g_{i,j,k}}}\frac{(E_\eta^R)_{i,j,k}}{(R_\eta)_{i,j,k}}\boldsymbol{i}_\eta + \frac{(g_{\zeta\zeta})_{i,j,k}}{\sqrt{g_{i,j,k}}}\frac{(E_\zeta^R)_{i,j,k}}{(R_\zeta)_{i,j,k}}\boldsymbol{i}_\zeta\right). \tag{6.50}$$

However, the general coordinate FVTD formulation requires the field components to be represented in terms of the components in the Cartesian coordinate system. Then using (B.50), the above expression for lumped current density is rewritten as:

$$\begin{aligned}(\boldsymbol{J}_L^R)_{i,j,k} = &-\frac{(g_{\xi\xi})_{i,j,k}^{3/2}}{\sqrt{g_{i,j,k}}}\frac{((\xi_x)_{i,j,k}(E_x^R)_{i,j,k} + (\xi_y)_{i,j,k}(E_y^R)_{i,j,k} + (\xi_z)_{i,j,k}(E_z^R)_{i,j,k})}{(R_\xi)_{i,j,k}}\boldsymbol{i}_\xi \\ &-\frac{(g_{\eta\eta})_{i,j,k}^{3/2}}{\sqrt{g_{i,j,k}}}\frac{((\eta_x)_{i,j,k}(E_x^R)_{i,j,k} + (\eta_y)_{i,j,k}(E_y^R)_{i,j,k} + (\eta_z)_{i,j,k}(E_z^R)_{i,j,k})}{(R_\eta)_{i,j,k}}\boldsymbol{i}_\eta \\ &-\frac{(g_{\zeta\zeta})_{i,j,k}^{3/2}}{\sqrt{g_{i,j,k}}}\frac{((\zeta_x)_{i,j,k}(E_x^R)_{i,j,k} + (\zeta_y)_{i,j,k}(E_y^R)_{i,j,k} + (\zeta_z)_{i,j,k}(E_z^R)_{i,j,k})}{(R_\zeta)_{i,j,k}}\boldsymbol{i}_\zeta\end{aligned} \tag{6.51}$$

The source term in Ampere's law, defined in (6.34), is given by:

$$(\boldsymbol{J}_L^R)_{i,j,k} = [\boldsymbol{L}_R]_{i,j,k}[\boldsymbol{L}_T]_{i,j,k}\boldsymbol{Q}_{i,j,k} \tag{6.52}$$

where $[L_R]$ is the I-V relation matrix of the lumped resistor, and $[\boldsymbol{L}_T]$ is the general-to-. Cartesian coordinate transformation matrix for the electric field components of (6.50). $[L_R]$ is given by:

$$[\boldsymbol{L}_R]_{i,j,k} = \frac{-1}{\varepsilon_{i,j,k}\sqrt{g_{i,j,k}}}\left(\begin{bmatrix} 0 & 0 & 0 & \frac{\xi_x g_{\xi\xi}}{R_\xi} & \frac{\eta_x g_{\eta\eta}}{R_\eta} & \frac{\zeta_x g_{\zeta\zeta}}{R_\zeta}\end{bmatrix}_{i,j,k}\right)_{diag} \tag{6.53}$$

where the cell's discrete lumped resistance, $(R_\xi)_{i,j,k}$, $(R_\eta)_{i,j,k}$, and $(R_\zeta)_{i,j,k}$ are computed via (6.48), (6.49), and (6.47), whereas $[\boldsymbol{L}_T]$ is given by:

$$[L_T]_{i,j,k} = \begin{bmatrix} 0\,0\,0 & 0 & 0 & 0 \\ 0\,0\,0 & 0 & 0 & 0 \\ 0\,0\,0 & 0 & 0 & 0 \\ 0\,0\,0 & \xi_x\sqrt{g_{\xi\xi}} & \xi_y\sqrt{g_{\xi\xi}} & \xi_z\sqrt{g_{\xi\xi}} \\ 0\,0\,0 & \eta_x\sqrt{g_{\eta\eta}} & \eta_y\sqrt{g_{\eta\eta}} & \eta_z\sqrt{g_{\eta\eta}} \\ 0\,0\,0 & \zeta_x\sqrt{g_{\zeta\zeta}} & \zeta_y\sqrt{g_{\zeta\zeta}} & \zeta_z\sqrt{g_{\zeta\zeta}} \end{bmatrix}_{i,j,k} \tag{6.54}$$

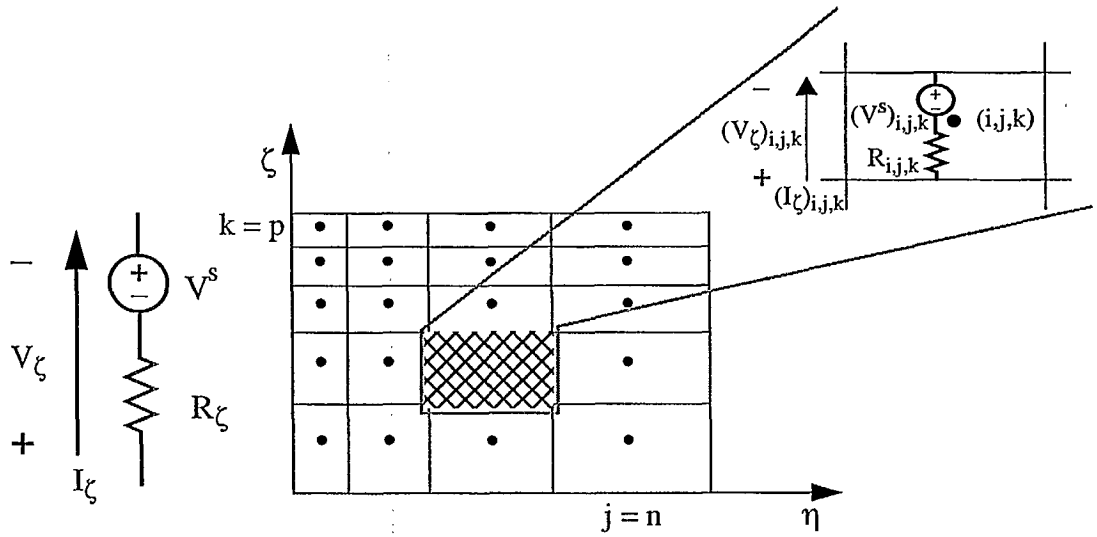

Figure 6.3. Model of a Thévenin source in a general coordinate system

6.6 Formulation of Lumped Resistive Voltage (Thévenin) Sources

In the FDTD method, lumped sources are modelled as (distributed) sources which impose (*i.e.* additional to the existing value of) an electric field density in each cell within the lumped element [130, 131]. A similar approach has been adopted for formulating lumped sources in the FVTD method.

Thus, a lumped voltage source with an internal resistance, R_ζ, and a source voltage of V_ζ^s (aligned with the ζ axis) is modelled as an element distributed over a region of $1 \le i \le m$, $1 \le j \le n$, $1 \le k \le p$, with each cell containing both a distributed resistor, $(R_\zeta)_{i,j,k}$, and a distributed voltage source, $(V_\zeta^s)_{i,j,k}$, as shown in **Figure 6.3**. The

relationship between the terminal voltage and the terminal current of a Thévenin source is given by Ohm's Law as stated in (6.31):

$$I_\zeta = \frac{V_\zeta^R}{R_\zeta} + \frac{V_\zeta^s}{R_\zeta}, \tag{6.55}$$

where the current due to the voltage source, V_ζ^s/R_ζ, is represented as an imposed electric field density in each of the lumped element cells, whereas the term V_ζ^R/R_ζ characterizes the contribution of the source resistance. The latter was examined in the previous section, and appropriate expressions were derived (see (6.47) to (6.53)). Therefore, only the formulation of the current due to the voltage source term is considered here.

The terminal voltage of a lumped element due to the source, V_ζ^s, is the algebraic sum of its (individual cell) counterparts in any column of the lumped model (in the direction of source current flow), and is given by:

$$V_\zeta^s = \sum_{k=1}^{p} (V_\zeta^s)_{i,j,k}, \tag{6.56}$$

and after substituting for the expression of cell voltage from (6.26), it becomes:

$$V_\zeta^s = -\sum_{k=1}^{p} \left(\frac{(g_{\zeta\xi})_{i,j,k}}{\sqrt{(g_{\xi\xi})_{i,j,k}}} (E_\xi^s)_{i,j,k} + \frac{(g_{\zeta\eta})_{i,j,k}}{\sqrt{(g_{\eta\eta})_{i,j,k}}} (E_\eta^s)_{i,j,k} + \frac{(g_{\zeta\zeta})_{i,j,k}}{\sqrt{(g_{\zeta\zeta})_{i,j,k}}} (E_\zeta^s)_{i,j,k} \right), \tag{6.57}$$

where $(E_\xi^s)_{i,j,k}$, *etc.* are the electric field components due to the source voltage and are to be *imposed* in addition to the field components present in each cell within the lumped element model. Since the lumped element current and current density are associated with an electric field oriented in the same direction, *the electric fields of the lumped element not aligned with the direction of current flow in the cells are vanishing*; hence (6.57) becomes:

$$V_\zeta^s = -\sum_{k=1}^{p} \sqrt{(g_{\zeta\zeta})_{i,j,k}}\,(E_\zeta^s)_{i,j,k}. \tag{6.58}$$

As in the case of lumped resistors, *the electric field due to the lumped current is assumed to be uniformly distributed within the lumped element along the direction of lumped current flow. Thus, the* $(E_\zeta^s)_{i,j,k}$ *term becomes* k *independent*; therefore, (6.58) can be rearranged so that the electric field due to the source voltage is given as a function of the lumped element terminal voltage via:

$$(E_\zeta^s)_{i,j,k} = \frac{-V_\zeta^s}{\sum_{k=1}^{p} \sqrt{(g_{\zeta\zeta})_{i,j,k}}}. \tag{6.59}$$

Similar expressions are derived for sources that are aligned in either the ξ- or η-axis respectively:

$$(E_\xi^s)_{i,j,k} = \frac{-V_\xi^s}{\sum_{i=1}^{m} \sqrt{(g_{\xi\xi})_{i,j,k}}}, \tag{6.60}$$

$$(E_\eta^s)_{i,j,k} = \frac{-V_\eta^s}{\sum_{j=1}^{n} \sqrt{(g_{\eta\eta})_{i,j,k}}}. \tag{6.61}$$

Next, the general expression of the lumped element current density of (6.17) is recast for lumped sources,

$$(\boldsymbol{J}_L)_{i,j,k} = (\boldsymbol{J}_L^R)_{i,j,k} + (\boldsymbol{J}_L^s)_{i,j,k}, \tag{6.62}$$

where $(\boldsymbol{J}_L^R)_{i,j,k}$ represents the distributed source resistor's current density, and $(\boldsymbol{J}_L^s)_{i,j,k}$ denotes the current density due to the distributed voltage source. The expression of the former was derived earlier and is given by (6.50) to (6.51). Thus, using the notation of

(6.52), the source term due to a Thévenin source becomes:

$$(J_L)_{i,j,k} = [L_R]_{i,j,k}[L_T]_{i,j,k}(Q_{i,j,k} + V^s_{i,j,k}) \tag{6.63}$$

where $[L_R]$ and $[L_T]$ are given by (6.53) and (6.54) respectively; V^s is a vector containing lumped voltage sources and is computed via:

$$V^s_{i,j,k} = \left[0 \quad 0 \quad 0 \quad \frac{V^s_\xi}{\sum_{i=1}^{m} \sqrt{(g_{\xi\xi})_{i,j,k}}} \quad \frac{V^s_\eta}{\sum_{j=1}^{n} \sqrt{(g_{\eta\eta})_{i,j,k}}} \quad \frac{V^s_\zeta}{\sum_{k=1}^{p} \sqrt{(g_{\zeta\zeta})_{i,j,k}}} \right]^T \tag{6.64}$$

Computationally speaking, the imposed fields due to the lumped source can be imposed any time during the computation of fields at a specific time step; that is, these fields can be added to the total fields within the lumped model at the beginning of each time step and can still correctly represent the I-V relationship of a lumped voltage source! Therefore, in each time step, the following expression is executed before the field update equations:

$$\mathbf{Q}^n_{i,j,k} = \mathbf{Q}^n_{i,j,k} + [L_T]_{i,j,k}(V^s)^n_{i,j,k}. \tag{6.65}$$

Finally, an ideal voltage source, (*i.e.* a Thévenin source whose internal resistance is zero) is considered. In this case, there will be no voltage drop due to internal resistance which will eliminate the need for a lumped resistor current density. This is achieved by setting $[L_R]$ to zero in (6.63) which would effectively remove the lumped element current density term in the update equations; yet the source terms are still added via (6.65).

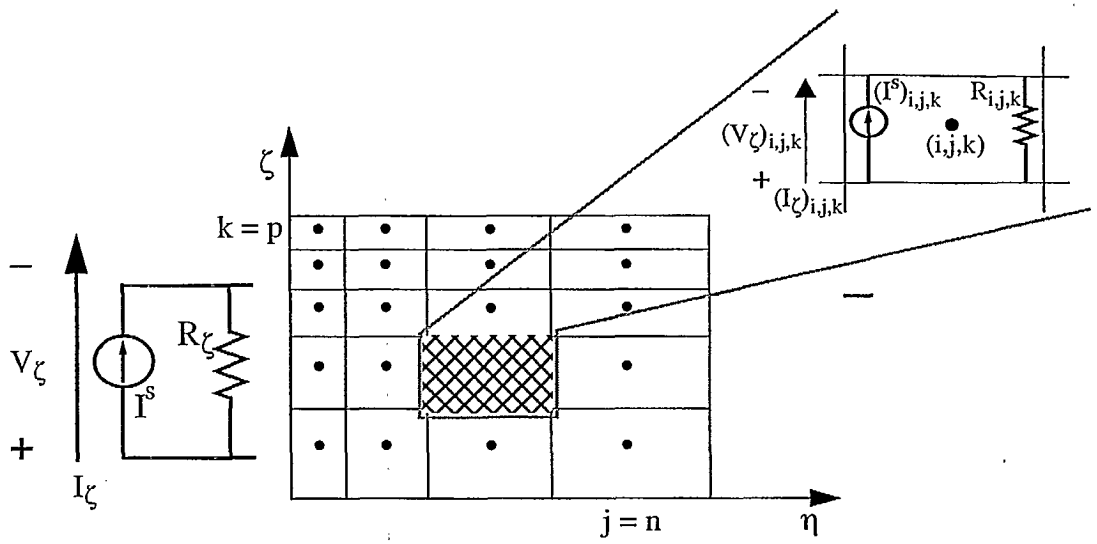

Figure 6.4. Model of a Norton source in a general coordinate system

6.7 Formulation of Lumped Resistive Current (Norton) Sources

Since there is little difference between lumped current (Norton) sources and lumped voltage sources, and in fact one can be easily converted to the other using a source transformation [129], the formulation of lumped current sources can be derived using a procedure very similar to the one described for lumped voltage sources.

A lumped current source with an internal resistance, R_ζ, and source current of I_ζ^s (aligned with the ζ axis) is modelled as an element distributed over a region of $1 \le i \le m$, $1 \le j \le n$, $1 \le k \le p$, with each cell containing both a distributed resistor, $(R_\zeta)_{i,j,k}$, and a distributed current source, $(I_\zeta^s)_{i,j,k}$, as shown in **Figure 6.4**. The relationship between the terminal voltage and the terminal current of a Norton source is given by Ohm's Law as stated in (6.32):

$$I_\zeta = \frac{V_\zeta^R}{R_\zeta} + I_\zeta^s, \tag{6.66}$$

where V_ζ^R/R_ζ represents the contribution of the source resistor, and I_ζ^s is the source current. Appropriate expressions for the former were derived and are given by (6.47) to (6.54). Thus the latter is considered here.

As in case of the lumped resistor, it is assumed that the terminal current of the resistor is equally distributed over the entire region of the lumped model; hence, *the current density across any plane surface of the model (normal to the direction of current flow) is constant*. Thus, the cell current density due to the source current is given by (6.39); that is:

$$(J_\zeta^s)_{i,j,k} = \frac{I_\zeta^s}{\sum_{i=1}^{m}\sum_{j=1}^{n}\frac{\sqrt{g_{i,j,k}}}{\sqrt{(g_{\zeta\zeta})_{i,j,k}}}}, \tag{6.67}$$

Similar expressions are derived for sources that are aligned in either the ξ- or η-axis respectively:

$$(J_\xi^s)_{i,j,k} = \frac{I_\xi^s}{\sum_{j=1}^{n}\sum_{k=1}^{p}\frac{\sqrt{g_{i,j,k}}}{\sqrt{(g_{\xi\xi})_{i,j,k}}}}, \tag{6.68}$$

$$(J_\eta^s)_{i,j,k} = \frac{I_\eta^s}{\sum_{i=1}^{m}\sum_{k=1}^{p}\frac{\sqrt{g_{i,j,k}}}{\sqrt{(g_{\eta\eta})_{i,j,k}}}}. \tag{6.69}$$

The general expression for the lumped element current density,(6.17), is once again re-written to include the current density term for lumped current sources; that is:

$$(\boldsymbol{J}_L)_{i,j,k} = (\boldsymbol{J}_L^R)_{i,j,k} + (\boldsymbol{J}_L^s)_{i,j,k}. \tag{6.70}$$

where $(\boldsymbol{J}_L^s)_{i,j,k}$ denotes the current density due to the distributed current source, and $(\boldsymbol{J}_L^R)_{i,j,k}$ represents the source resistor's current density. The expressions for the source

resistor current density are given by (6.50) to (6.52), and the source current density is computed in a similar manner as in case of the Thévenin source; thus, it is given by:

$$(J_L^s)_{i,j,k} = [L_T]_{i,j,k} I^s_{i,j,k} \tag{6.71}$$

where $[L_T]$ is the transformation matrix defined by (6.54) and $I^s_{i,j,k}$ is the lumped source term given by:

$$I^s_{i,j,k} = \left[0\ 0\ 0\ \frac{I^s_\xi}{\sum_{j=1}^{n}\sum_{k=1}^{p} \frac{\sqrt{g_{i,j,k}}}{\sqrt{(g_{\xi\xi})_{i,j,k}}}} \quad \frac{I^s_\eta}{\sum_{i=1}^{m}\sum_{k=1}^{p} \frac{\sqrt{g_{i,j,k}}}{\sqrt{(g_{\eta\eta})_{i,j,k}}}} \quad \frac{I^s_\zeta}{\sum_{i=1}^{m}\sum_{j=1}^{n} \frac{\sqrt{g_{i,j,k}}}{\sqrt{(g_{\zeta\zeta})_{i,j,k}}}} \right]^T \tag{6.72}$$

Finally, Norton current sources are incorporated into the computational expressions via:

$$\mathbf{Q}^n_{i,j,k} = \mathbf{Q}^n_{i,j,k} + [L_T]_{i,j,k} (I^s)^n_{i,j,k} \tag{6.73}$$

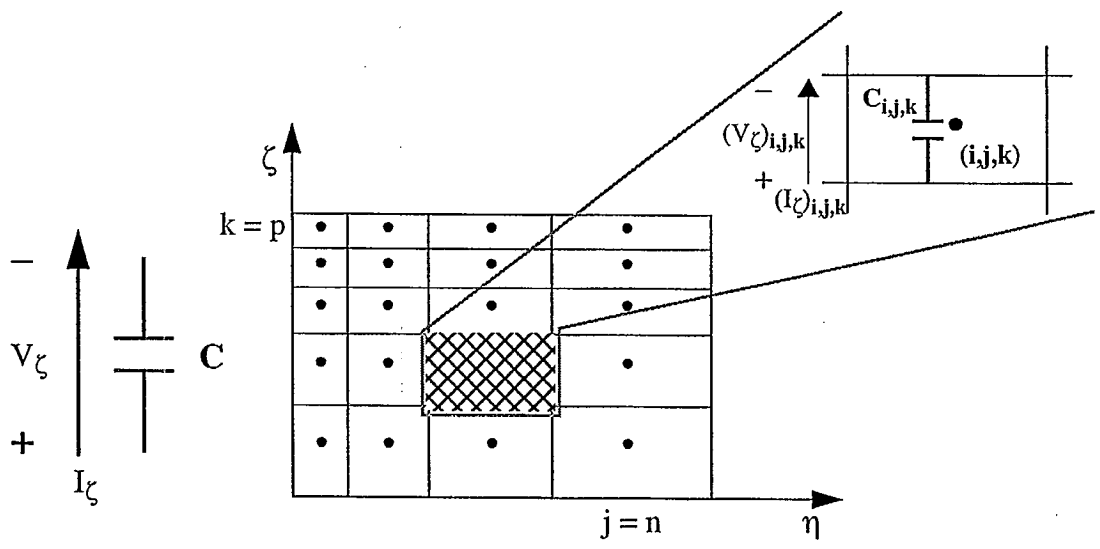

Figure 6.5. Model of a lumped capacitor in a general coordinate system

6.8 Formulation of Lumped Capacitors

A capacitor, C, which is aligned with the ζ axis is shown in **Figure 6.5**. It is modelled as a lumped element distributed over a region of $1 \le i \le m$, $1 \le j \le n$, $1 \le k \le p$. The relationship between its terminal voltage and current is stated in (6.30) as:

$$I_\zeta = C_\zeta \frac{dV_\zeta^c}{dt} = C_\zeta \dot{V}_\zeta^c, \tag{6.74}$$

where I_ζ is the total current flowing across any plane within the lumped model normal to the direction of the current flow, and V_ζ^c is the algebraic sum of the individual cell voltages (in any column of the lumped model) in the direction of the current flow through the element. A procedure (nearly) identical to the one described in the case of lumped resistors (see **Section 6.5**) is used to derive expressions for the distributed capacitance of individual cells. Although in the case of lumped capacitors, the time derivative of the capacitor's terminal voltage, $\dot{V}^c$, and its corresponding electric field, $\dot{E}^c$, replace the terminal voltage and electric fields of the lumped capacitors, this slight alteration does not affect the overall procedure used previously. Hence, the expressions for the distributed capacitance of the ξ, η- and ζ-axis aligned capacitors are given below:

$$(C_\xi)_{i,j,k} = \frac{\sqrt{g_{i,j,k}} \sum_{i=1}^{m} \sqrt{(g_{\xi\xi})_{i,j,k}}}{(g_{\xi\xi})_{i,j,k} \sum_{k=1}^{p} \sum_{j=1}^{n} \frac{\sqrt{g_{i,j,k}}}{\sqrt{(g_{\xi\xi})_{i,j,k}}}} C_\xi, \tag{6.75}$$

$$(C_\eta)_{i,j,k} = \frac{\sqrt{g_{i,j,k}} \sum_{j=1}^{n} \sqrt{(g_{\eta\eta})_{i,j,k}}}{(g_{\eta\eta})_{i,j,k} \sum_{i=1}^{m} \sum_{k=1}^{p} \frac{\sqrt{g_{i,j,k}}}{\sqrt{(g_{\eta\eta})_{i,j,k}}}} C_\eta, \tag{6.76}$$

$$(C_\zeta)_{i,j,k} = \frac{\sqrt{g_{i,j,k}} \sum_{k=1}^{p} \sqrt{(g_{\zeta\zeta})_{i,j,k}}}{(g_{\zeta\zeta})_{i,j,k} \sum_{i=1}^{m} \sum_{j=1}^{n} \frac{\sqrt{g_{i,j,k}}}{\sqrt{(g_{\zeta\zeta})_{i,j,k}}}} C_\zeta . \tag{6.77}$$

Thus, the general expression for a capacitor's lumped density is written as:

$$(\boldsymbol{J}_L^c)_{i,j,k} = [\boldsymbol{L}_C]_{i,j,k}[\boldsymbol{L}_T]_{i,j,k}\dot{\boldsymbol{Q}}_{i,j,k}, \tag{6.78}$$

where $[L_C]$ is the I-V relationship matrix of the lumped capacitor. This matrix is recast in terms of the time derivative of Cartesian electric field components and is given by:

$$[\boldsymbol{L}_C]_{i,j,k} = \frac{-1}{\varepsilon_{i,j,k}\sqrt{g_{i,j,k}}} \left(\begin{bmatrix} 0 & 0 & 0 & \frac{\xi_x g_{\xi\xi}}{C_\xi} & \frac{\eta_x g_{\eta\eta}}{C_\eta} & \frac{\zeta_x g_{\zeta\zeta}}{C_\zeta} \end{bmatrix}_{i,j,k} \right)_{diag} \tag{6.79}$$

However, it must be noted that the treatment (and solution) of the lumped current density of a capacitor is markedly different than that of previously discussed lumped elements. In the case of a lumped capacitor, the source term of Ampere's law, (6.78), contains a time derivative of the solution vector (as opposed to the just the solution vector in the case of other lumped elements). Hence, Maxwell's equations of (3.34) can be written in terms of lumped element current densities as:

$$\boldsymbol{Q}_t + [\boldsymbol{A}]\boldsymbol{Q}_\xi + [\boldsymbol{B}]\boldsymbol{Q}_\eta + [\boldsymbol{C}]\boldsymbol{Q}_\zeta = ([\boldsymbol{K}] + [\boldsymbol{L}_R][\boldsymbol{L}_T])\boldsymbol{Q} + ([\boldsymbol{L}_R][\boldsymbol{L}_T]) \begin{vmatrix} \boldsymbol{V}^s \\ \boldsymbol{I}^s \end{vmatrix} + [\boldsymbol{L}_C][\boldsymbol{L}_T]\boldsymbol{Q}_t, \tag{6.80}$$

where it is simplified into the general form of a system of PDEs that the FVTD method is capable of solving; that is:

$$\boldsymbol{Q}_t + \frac{[\boldsymbol{A}]}{[\boldsymbol{L}_C][\boldsymbol{L}_T]}\boldsymbol{Q}_\xi + \frac{[\boldsymbol{B}]}{[\boldsymbol{L}_C][\boldsymbol{L}_T]}\boldsymbol{Q}_\eta + \frac{[\boldsymbol{C}]}{[\boldsymbol{L}_C][\boldsymbol{L}_T]}\boldsymbol{Q}_\zeta = \left(\frac{[\boldsymbol{K}] + [\boldsymbol{L}_R][\boldsymbol{L}_T]}{[\boldsymbol{L}_C][\boldsymbol{L}_T]}\right)\boldsymbol{Q} + \left(\frac{[\boldsymbol{L}_R][\boldsymbol{L}_T]}{[\boldsymbol{L}_C][\boldsymbol{L}_T]}\right) \begin{vmatrix} \boldsymbol{V}^s \\ \boldsymbol{I}^s \end{vmatrix}. \tag{6.81}$$

6.9 Formulation of Lumped Networks

Thus far, the discussion has concentrated on the modelling of specific types of lumped elements in the FVTD algorithm. Although this is convenient for modelling simple circuits, more complex two terminal networks (that may include several types of lumped elements) cannot be accurately modelled using the characteristics of one type of lumped element. In fact, most lumped networks exhibit a terminal I-V relationship that is a combination of the resistive, capacitive, and inductive elements' I-V characteristics. They are commonly referred to as RLC lumped networks [129]. The I-V relationship of RLC lumped networks is often formulated (and obtained) in the Laplace domain, that is;

$$V_{LN}(s) = Z(s)I_{LN}(s) \tag{6.82}$$

where $V_{LN}(s)$ and $I_{LN}(s)$ are the terminal voltage and the terminal current of the lumped network; $Z(s)$ is the impedance function of the RLC network given by [132]:

$$Z(s) = \left(\sum_{l=0}^{L} b_l(s)^l\right)\left(\sum_{l=0}^{L} a_l(s)^l\right)^{-1} \tag{6.83}$$

with L representing the number of capacitive or inductive elements in the RLC network.

In [132], the lumped network I-V relation of (6.82) was derived for the FDTD method. The resulting equations were discretised and solved using the bilinear transformation method (a standard signal processing technique [133]) and a semi-explicit FDTD scheme). This technique along with other methods capable of modelling nonlinear lumped elements in FDTD [134] can be adopted to model complex electronic circuits using the FVTD method. Additional research on the formulation and modelling of lumped networks using the FVTD technique is required and will be pursued in the future.

6.10 Case Study: Coaxial Transmission Lines

Transmission lines are one of the most common devices of the transportation and the distribution of power* (whether it is microwave or electric power). They are two-(or more) conductor structures that propagate energy via Transverse ElectroMagnetic (TEM) waves (that are characterized by the absence of any components in the axial direction) [135]. The properties and characteristics of various types of transmission lines have been extensively studied, analysed, and documented [14, 15, 135, *etc.*]. The aim of this section is to model a standard coaxial transmission line, excite and propagate a pulse within it (via a lumped voltage source), and verify the general coordinate system formulation of distributed lumped voltage sources, derived in **Section 6.6**, using the FVTD method. In addition, the performance of the characteristic ABCs of the FVTD method are also evaluated in a non-orthogonal grid.

6.10.1 Excitation and Lumped Sources

Although there are various methods of exciting and propagating waves in coaxial transmission lines, a coaxial cable is often connected to an external source (and eventually to a load) via various types of connectors, such as a *Type-N* connector (operation frequency of 11 to 18 *GHz*) or an *SMA* connector (operation frequency of up to 25 *GHz*) [136]. Thus, in numerical simulations, a lumped source must excite the dominant mode of the coaxial guide (*i.e.* TEM-mode). Although the junction of the connector and the cable often forms a discontinuity that could excite higher-order (TE and/or TM) modes, these

* Another popular method of transporting microwave energy is using waveguides. Waveguides are single conductor structures that propagate energy via Transverse Electric (TE) and/or Transverse Magnetic (TM) waves that are characterised by their longitudinal electric or magnetic field components respectively [14].

modes are often cutoff (evanescent) and only exist in very close proximity to the discontinuity or sources where they were excited [1]. Furthermore, one must consider the potential distribution on a given longitudinal plane; that is, the lumped source must correctly represent the solution to the problem: "*when a potential* V_0 *is applied between the inner and the outer conductor of a coaxial guide find the electric field values at any point between the two conductors* [1 page 186]." This problem is solved by the simple application of Laplace's equation in the cylindrical coordinate system (assuming that the line is very long so that $\partial v/\partial z = 0$, and that the space between the inner and outer conductor is filled with a linear homogenous isotropic medium [3]):

$$\nabla^2 V = \frac{1}{r}\frac{\partial}{\partial r}\left(r\frac{\partial V}{\partial r}\right) + \frac{1}{r^2}\frac{\partial^2 V}{\partial \phi^2} + \frac{\partial^2 V}{\partial z^2} = 0, \tag{6.84}$$

where due to the cylindrical symmetry with respect to ϕ, and the assumption of no change in the longitudinal, z, direction, it can be simplified to:

$$\nabla^2 V = \frac{1}{r}\frac{\partial}{\partial r}\left(r\frac{\partial V}{\partial r}\right) = 0. \tag{6.85}$$

The boundary conditions are fairly obvious and are given as: (a) $V = 0$ at $r = b$ and (2) $V = V_0$ at $r = a$. Following two successive integration operations and the application of boundary conditions, the solution to the simplified Laplace's equation of (6.85) is given as:

$$V = V_0 \frac{ln(b/r)}{ln(b/a)}. \tag{6.86}$$

It is important to note that the above solution is applicable to time-varying fields and sources [1].

Hence, the problem space must be excited using a lumped voltage source which not only obeys the above potential distribution, but also excites a TEM-mode. The formulation

of distributed lumped voltage sources developed for general coordinate systems uses directional derivatives that inherently account for the latter; that is, the lumped element formulation resolves the radial and azimuth (circumferential) electric field components into corresponding E_x and E_y components through the use of directional derivatives. By the same token, the axial component, E_z, is negligible since the directional derivatives (metrical coefficients) corresponding to the axial direction are zero. The potential distribution condition is satisfied via (6.86). The effectiveness of both of these formulations is verified next.

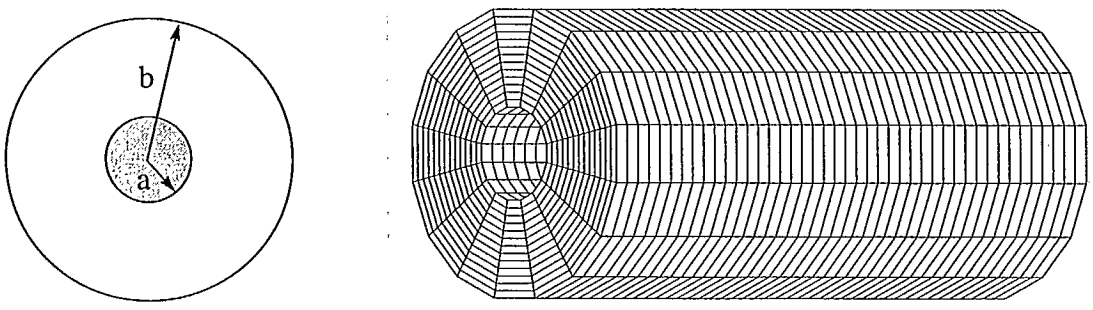

Figure 6.6. Cross section of an RG-9B/U coaxial transmission line with $a = 1.036\ mm$ and $b = 3.612\ mm$ (left) and its meshed model (right).

6.10.2 Problem Configuration

An RG-9B/U standard coaxial cable was selected for modelling. This cable has an overall diameter of 425 *Mils* and a dielectric material (Polyethlene, $\varepsilon_r = 2.25$) diameter of 285 *Mils* (see **Figure 6.6**).* An 8 *cm* long section of the above cable was meshed using **TrueGrid®** for various combinations of discretisation in the radial, circumferential, and

* For an impedance of 50Ω, the coaxial waveguide characteristic impedance is given by:

$$Z_0 = \frac{1}{2\pi}\sqrt{\frac{\mu}{\varepsilon}}\ln\frac{b}{a} = 50.$$

Thus, the radius of the inner conductor can be calculated assuming that the diameter of the dielectric material is $2b$ [136].

axial directions. In all cases, the lower and upper radial limits were terminated using PEC boundary conditions (hence modelling the inner and outer conductors), both limits of the axial direction were terminated with characteristic ABCs, and periodic boundary conditions were used on the lower and upper bounds of the azimuth direction. A double discretised mesh was used to more accurately compute the transformation matrices.

In one such simulation, the above cable was modelled using a $(15 \times 30 \times 150)$ cell space. The value of the largest eigenvalue required for numerical stability was 1.7230×10^{12} $[m/s]$ which corresponded to a time-step of $\Delta t = 0.67016$ ps. The properties of the grid in terms of its eigenvalues are given in **Table 6.1**. Due to the nature of the cylindrical coordinate system, the maximum ratio of the eigenvalues in the azimuth direction could not be unity due to the gradual increase in the perimeters of the concentric circles (as is reflected in the ratio of the eigenvalues). In such problem spaces, every effort was made to maintain the maximum ratio of the eigenvalues near unity.

Table 6.1. The ratio of eigenvalues in a coaxial cable

	$\left\|\frac{\lambda_{max}}{\lambda_{min}}\right\|$	$\left\|\frac{\lambda_{total}}{\lambda_{max}}\right\|$	$\left\|\frac{\lambda_{total}}{\lambda_{min}}\right\|$
ξ-direction	1.00	2.21	2.21
η-direction	3.16	3.02	9.55
ξ-direction	1.00	4.60	4.60

A distributed lumped voltage source was modelled by a one-cell-thick longitudinal plane. It was placed 1.33 mm (3 cells) way from the lower bound of the axial, z, direction. The voltage source generated a Gaussian wave form:

$$V(t) = A_0 e^{\left(\frac{t-t_0}{t_w}\right)^2} \tag{6.87}$$

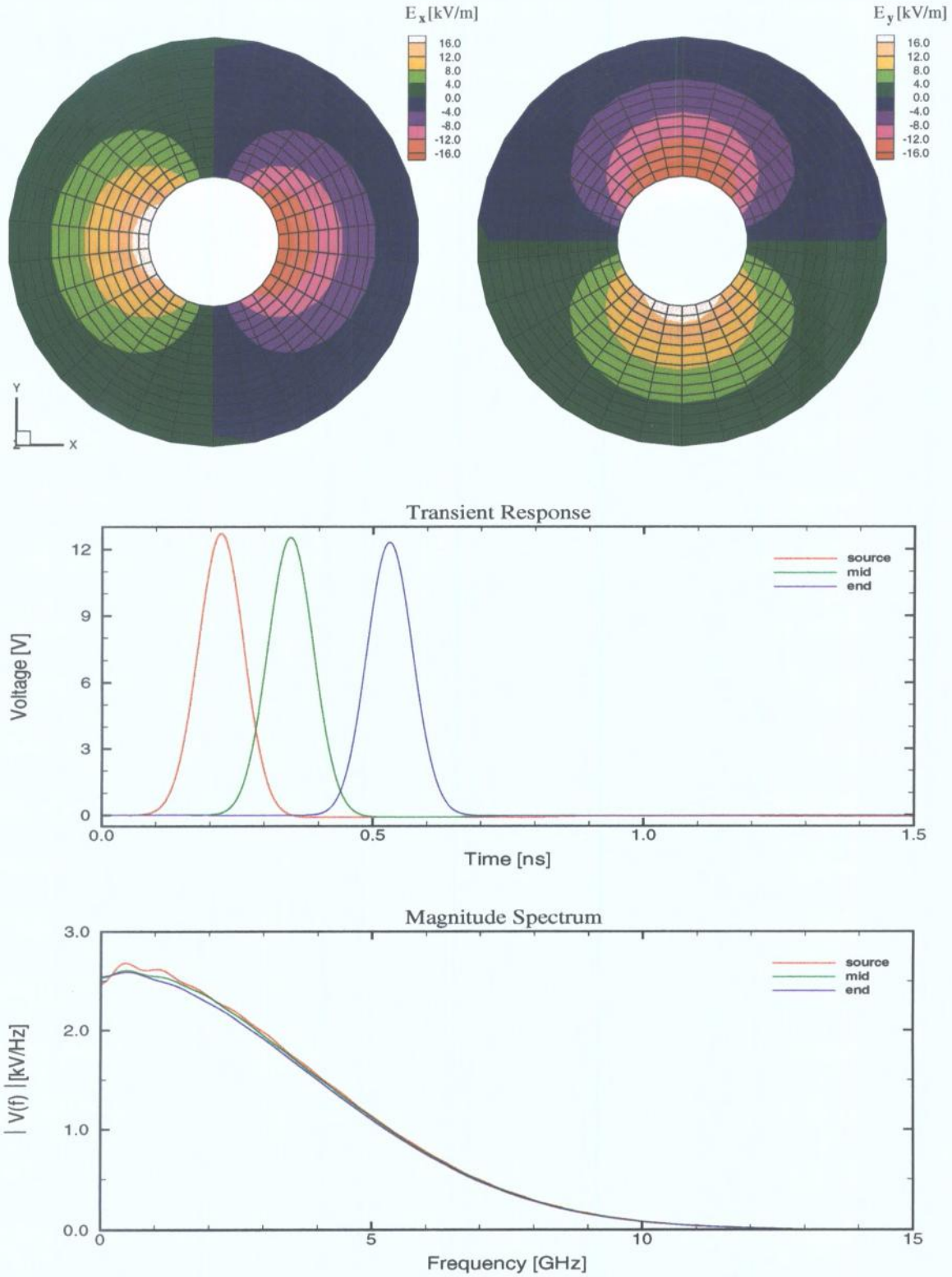

Figure 6.7. (Top) Profile of the transverse electric fields at the distributed lumped voltage source's longitudinal plane, (mid) calculated voltages at various locations along the coaxial line, and (bottom) their respective magnitude spectrum.

of amplitude $A_0 = 30\ V$, pulse width $t_w = 49\ ps$, and $t_0 = 150\ ps$. **Figure 6.7** displays a contour plot of the transverse electric fields at the plane containing the lumped voltage source. The value of the E_z fields in this longitudinal plane was also examined and was determined to be negligible.* At several locations along the coaxial line ($z = 1.7, 3.76, 7.92\ cm$ corresponding to the *source*,† *mid*, and *end* points of **Figure 6.7**), the voltage between the inner and outer conductors was calculated via (6.57) and (B.50). These calculations were repeated at every time step for a total time of 2.1 *ps*. A time domain plot of these voltages and their corresponding magnitude spectrum (calculated using the Discrete Fourier Transform, DFT, method [133]) are also shown in **Figure 6.7**.

The profile of the E_x and E_y fields at the distributed lumped voltage source and the trivial size of the E_z field (in comparison) validate the formulation of the distributed lumped voltage source in general coordinate systems as well as its implementation in the FVTD engine. In addition, the transient response of the line voltages (shown in **Figure 6.7**) has also demonstrated the propagation of a Gaussian voltage pulse within the coaxial cable. The numerical dissipation of the mesh was gauged at 2% of the amplitude of the original pulse (see the transient response plot of **Figure 6.7**). This inherent artificial dissipation of the FVTD algorithm was further studied using a one-sided magnitude spectral plot of the line voltages (see bottom plot of **Figure 6.7**) which demonstrated that the dissipation is uniform across the spectrum. The peculiar behaviour of the magnitude spectrum of the *source* and *mid point* voltages at lower frequencies ($\leq 1.5\ GHz$) is probably due to the effect of evanescent modes and/or the premature termination of the

* It was three orders of magnitude smaller than its corresponding E_x or E_y field strengths.

† Higher-order modes were observed in the vicinity of the lumped source; hence the first observation point, dubbed "source", was located 1.7 *cm* away from the lumped voltage source in order to only capture the contribution of the TEM mode.

transient response.*

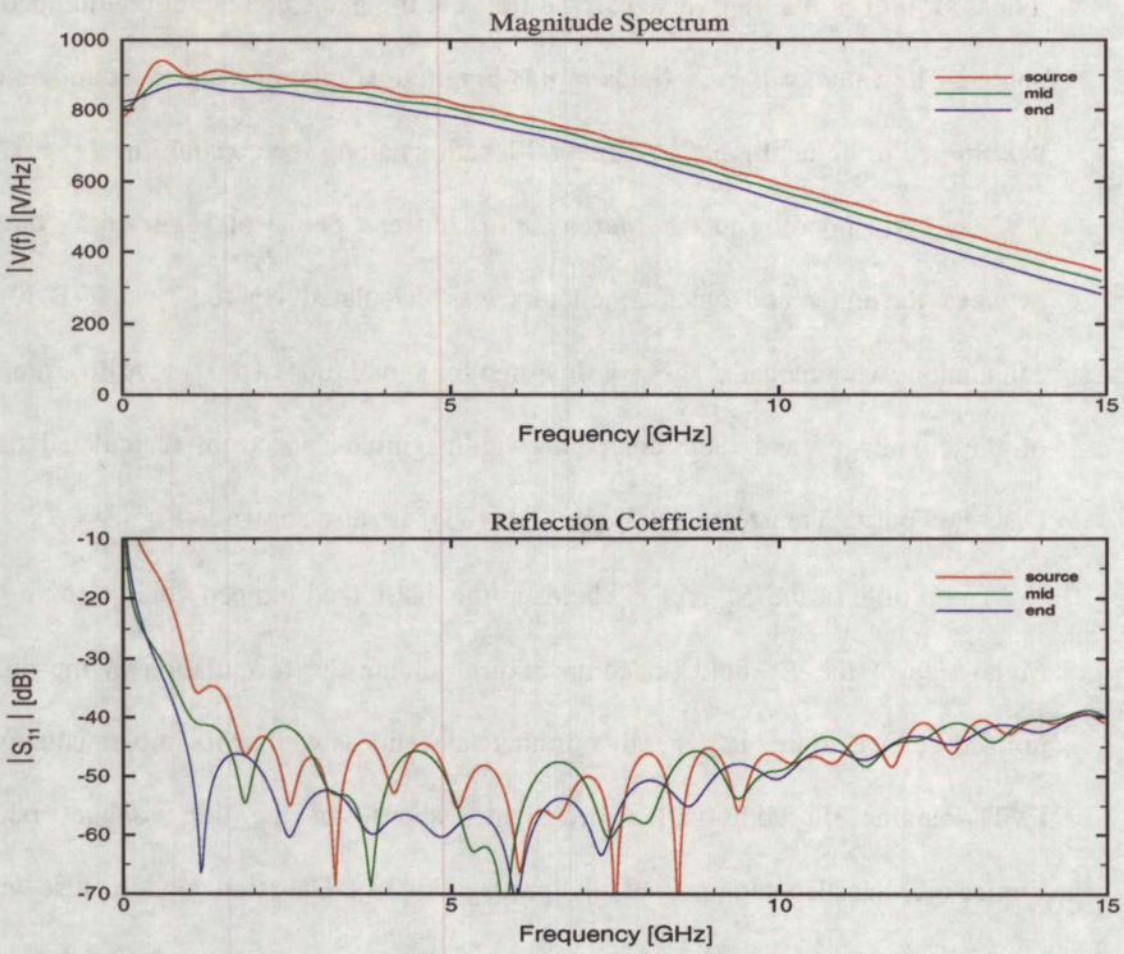

Figure 6.8. (Top) Magnitude spectrum of voltages at various locations along the coaxial line (bottom) and the calculated reflection coefficient from characteristic ABCs.

Finally, in order to evaluate the performance of the characteristic ABCs in a non-rectangular geometry, the coaxial cable was selected as a test case. Thus, the reflection coefficient from the upper z bound was computed by applying the pulse-separation method to the transient voltages at all three observation points. However, in order to achieve better accuracy for higher frequencies, the line was excited with a Gaussian pulse

* Since the cutoff wavelength of the dominant mode of a coaxial guide is infinite (*i.e.* it can support DC [76]), the transient response approaches without becoming zero, which is known to cause inaccuracies in low frequency DFT calculations.

of a higher frequency content (t_w = 24 *ps*) than before. Both the excitation pulse's magnitude spectrum and the reflection coefficient from the characteristic ABCs are shown in **Figure 6.8**. In general, coefficient reflections of better than -40 *dB* were obtained for frequencies above 1 *GHz*.*

6.11 Summary

The general approach in modelling lumped elements is to modify Ampere-Maxwell equations to include a lumped electric current density in addition to the displacement and conduction current of any given cell. This lumped current density is represented as a function of a discrete cell voltage defined by the I-V relations of the lumped element. Finally, these cell voltages are described in terms of the discrete electric field components of Maxwell's equations. In this chapter, this procedure was illustrated by deriving the expressions for distributed lumped voltage and current sources, as well as lumped resistors and capacitors, on a generalised grid. The main advantage of this approach is that the derived expressions were not only coordinate independent but were also independent of the numerical method used for solving Maxwell's equations. The aforementioned formulation of the lumped elements was tested and validated for the case of a coaxial cable.

---

* Once more, due to the premature termination of the transient response, the low frequency calculations are rendered inaccurate.

Chapter 7

Applications of the 3D-FVTD Engine

In previous chapters, the newly derived fully windward, flux split, Lax-Wendroff version of the FVTD algorithm for solving Maxwell's equations with a source term was implemented and validated using several benchmark problems. Some of these cases involved a quantitative study of the FVTD method, which also included a direct comparison with other popular numerical techniques, such as the FDTD and TLM methods (**Section 5.2.1**), while other test cases served as a proof of concept (**Sections 5.2.2** and **6.10**), or as a study of certain characteristics of the FVTD method (**Section 5.2.3**). In general, all of the aforementioned case studies have done little to highlight the strengths and weaknesses of the LW version of the FVTD technique. In this chapter, the 3D-FVTD engine is used to analyse several practical problems that either have appeared in the literature or are currently under study in industry. As is always the case, the proposed LW-FVTD method performs better for a certain class of problems than for others. Hence, the shortcomings of the LW-FVTD are discussed, and possible remedies are considered.

7.1 Case One: TE Cutoff Frequencies of Coaxial Waveguides

Many analytical and semi-analytical methods of calculating TE and TM cutoff frequencies of coaxial and eccentric waveguides (with a variety of combinations of circular and elliptical conductor cross-sections) have been proposed [137, 138, 139]. In order to compare the accuracy of the body fitted coordinate system version of the FVTD method with other rectangular grid based time domain methods (namely TLM) that use stair step lines for curve representation, the TE cutoff frequencies of a circular coaxial metallic waveguide are computed using both the FVTD and TLM methods.* The obtained TE cutoff frequencies of the waveguide using each method are then compared with one of the most widely accepted (semi-analytical) solutions presented by Kuttler in [137].

7.1.1 The Simulation Space and the Results

A coaxial waveguide with an outer-to-inner conductor radius ratio of 4.0, (*i.e.* $r = 1.0\ m$, and $a = 0.25\ m$) was modelled using both TLM and FVTD techniques. The physical space of the TLM simulation was discretised using a uniform mesh with a cell size, Δl, of $1/30\ m$ $(60 \times 60 \times 10)$ (see **Figure 7.1**). The inner and outer conductors were modelled using PEC materials. The FVTD simulation space was modelled using a conformal (double discretised) mesh that was composed of 40 cells radially, 80 cells circumferentially, and 10 cells axially (see **Figure 7.1**). The inner and outer conductors were laid on the lower and upper radial direction and were modelled using PEC boundary conditions, while periodic boundary conditions were used on the lower and upper circumferential direction. In both the TLM and FVTD simulations, the upper and lower

* Although the 3D-FVTD engine is capable of modelling eccentric elliptic-circular waveguides [139], due to the limitations of the TLM engine, only circular coaxial waveguides are considered.

axial direction were terminated using PMC boundary conditions.

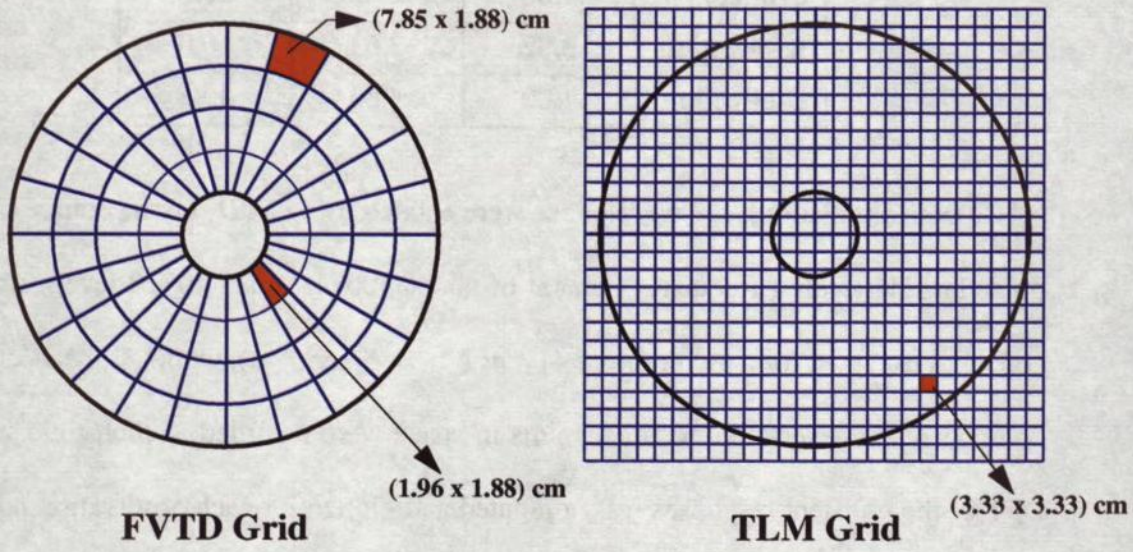

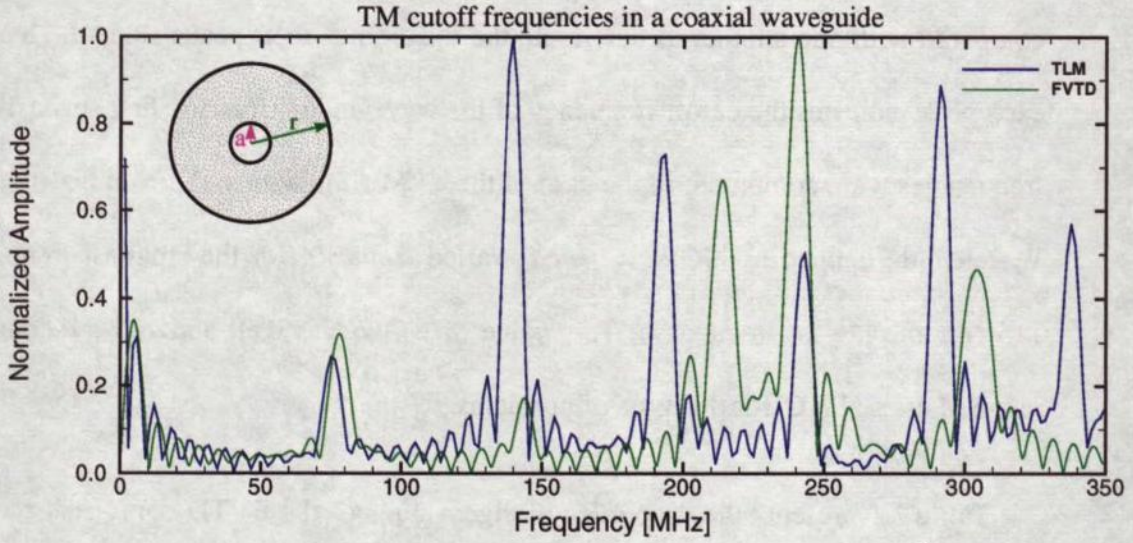

Figure 7.1. (Top) A comparison of an FVTD (body fitted) and a TLM (stair step) simulation space for a circular coaxial waveguide, and (bottom) a comparison of the first seven TE cutoff frequencies for a coaxial waveguide ($r = 1.0\ m$, $a = 0.25\ m$)

Table 7.1. The ratio of eigenvalues in the coaxial waveguide mesh

	$\left\|\frac{\lambda_{max}}{\lambda_{min}}\right\|$	$\left\|\frac{\lambda_{total}}{\lambda_{max}}\right\|$	$\left\|\frac{\lambda_{total}}{\lambda_{min}}\right\|$
ξ-direction	1.00	2.42	2.42
η-direction	3.82	2.63	10.0
ξ-direction	1.00	4.84	4.84

In both simulations, the waveguides were excited using a (D_z) point source Gaussian pulse in time (with a frequency content of about 500 *MHz* at -40 *dB* level). The TLM code was executed for a total time of 417 *ns* (Δt = 55.556 *ps*), while all the electric field components at several observation points in space were recorded at each time step. The DFT of the transient responses was computed and plotted for each observation point (one such DFT plot is provided in **Figure 7.1**). The DFTs of all observation points were compared with one another to determine the location of their peaks since the location of each peak indicates the cutoff frequency of the waveguide. Thus, the first seven TE cutoff frequencies were computed. In the case of the TLM simulations, the Number of Cells per Wavelength, defined as NCW = $\lambda/\Delta l$, varied from 30 (for the smallest frequency) to 115 (for the largest frequency). This value of NCW was well above the recommended range of $10 \leq$ NWC for this type of problems.

Table 7.1 presents the properties of eigenvalues of the FVTD conformal mesh used for modelling the coaxial waveguide. The value of the largest eigenvalue required for numerical stability was 3.87×10^{10} [*m/s*], which corresponded to a time-step of Δt = 29.837 *ps*. The FVTD code was also executed for 417 *ns* during which the previously described procedure was used to extract the first seven TE cutoff frequencies. In this case, the NCW for the smallest wavelength varied from 13 to 53 (due to the

variation of cell sizes of the conformal grid). These NCW values were still larger than were the recommended values.

Table 7.2. TE cutoff frequencies obtained by TLM and FVTD techniques as they compare to the exact solution

Exact	**TLM**			**FVTD**		
$(f_c)^{TE}$ a	$(f_c)^{TE}$	% error	$(\lambda/\Delta l)$	$(f_c)^{TE}$	% error	$(\lambda/\Delta l)$ b
78.465	75.500	3.8	115	78.000	0.6	49-203
143.58	148.25	3.3	63	144.00	0.3	27-111
200.09	183.75	8.2	45	202.50	1.2	19-80
212.21	- - -	- - -	42	213.75	0.7	18-75
238.78	243.00 (?)c	1.8	38	240.50	0.7	16-67
253.66	- - -	- - -	36	251.00	1.0	15-63
303.32	290.75 (?)	4.1	30	304.00	0.2	13-53

a. All cutoff frequencies are in *MHz*

b. Calculated with respect to the "exact" cutoff frequencies.

c. "(?)" indicates that the computed cutoff frequency was located somewhere in between the "exact" solution; hence, it was assumed to be predicting the nearest TE cutoff frequency!

Table 7.2 presents a comparison of the first seven TE cutoff frequencies predicted by the TLM and FVTD methods to the *exact* (semi-analytical) solution given in **Table IX** of [137]. Despite an over discretised computational space, where the NCW ratio was at least three times larger than was the minimum recommended value (10), the TLM method was successful in predicting the cutoff frequencies (with some degree of certainty) in fewer than half of the cases, which is a clear indication of the short-coming of the stair step representation of curved surfaces. However, the stair-step representation of curves is

acceptable for large values of NCW. For example, in the case of the lower cutoff frequencies of **Table 7.2**, where the NCW is about 60 *MHz* or higher, reasonable accuracy (a percentage error of less than 5 percent) was obtained. On the other hand, in all but one case, the FVTD scheme successfully predicted the TE cutoff frequencies of the waveguide within one percentage point of the semi-analytical solution. This was accomplished with the aid of a minimum NCW of 13. Also, the accuracy of the first seven predicted cutoff frequencies appeared to be independent of this ratio, which might indicate that a lower NCW can generate more accurate results.

Table 7.3. Computational requirements for various schemes[a]

Scheme	Multiplication	Addition	Variables
FVTD[b]	$486 \times N$[c]	$504 \times N$	$213 \times N$
FVTD[d]	$1161 \times N$	$1386 \times N$	$105 \times N$
TLM [140]	$12 \times N$	$54 \times N$	$30 \times N$
FDTD [45]	$12 \times N$	$24 \times N$	$18 \times N$

a. In all cases, a free-space formulation is assumed.

b. Fast FVTD method; per-calculation of all coefficients and some fluxes (CPU efficient).

c. Total number of mesh points in the computational space.

d. Memory Efficient FVTD method; recalculation of fluxes at every time step.

7.1.2 Comparison of Computational Resources

Table 7.3 summarizes the computational resources required for several time domain algorithms. In general, the orthogonal-grid-based TLM and FDTD techniques require similar computational resources and yield results with comparable accuracy. Two modes of implementation of the FVTD method are proposed with respect to the computational resources available to the user. The *memory efficient* FVTD method requires that the field

values and the time invariant coefficients be stored in memory while all the numerical fluxes are re-computed for each cell update. Alternatively, the *fast* FVTD scheme stores all time invariant coefficients, the field components, and the numerical fluxes in memory; it only computes numerical fluxes as they are required in the calculation of new time steps.

The memory efficient FVTD scheme is not recommended due to the large number of floating point operations it requires. Although the fast FVTD method is between one to two orders of magnitude slower than is either the TLM or FDTD method, and has seven to twelve times the memory requirement of either method respectively, the fast FVTD scheme's large demand for computational resources is often offset by its use of conformal meshes which results in increased accuracy. For most cases, these results may be obtained using fewer cells, which in turn reduces the required computational resources for an FVTD simulation.

7.2 Case Two: A Cavity Resonance Problem

Sooner or later, one would face the problem of fitting the proverbial square peg in a round hole! The *cavity resonance problem* fits this analogy well. These types of structures are used for a variety of applications, such as tuning the resonant frequency of a cavity or accurately computing the permittivity of sample materials. For a given set of assumptions and size restrictions, these types of problems can be solved using perturbation methods [15]. However, in the majority of cases a numerical solution is more feasible. **Figure 7.2** represents a rectangular PEC cavity partially loaded with a dielectric ring of $\varepsilon_r = 2.06$ [142].

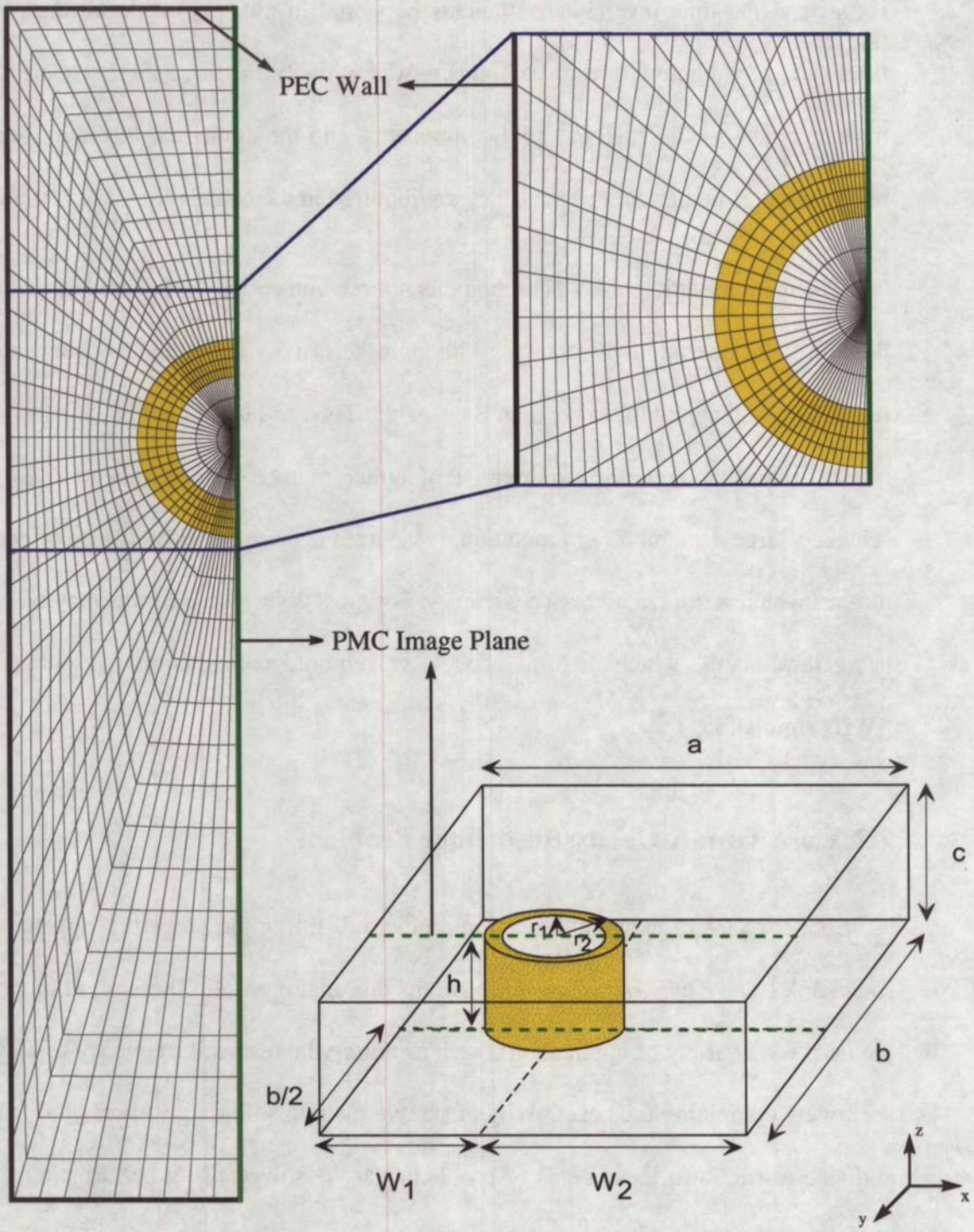

Figure 7.2. (Above) Rectangular PEC cavity (a = 324 *mm*, b = 121 *mm*, c = 43 *mm*) partially loaded with a dielectric ring (r_1 = 16.65 *mm*, r_2 = 26.75 *mm*, h = 39 *mm*) centred at $b/2$, W_1 = 207.25 *mm*, and W_2 = 116.75 *mm*. (Left) the cross- section of its corresponding mesh

Table 7.4. The ratio of eigenvalues in the cavity resonance problem

	$\left\|\frac{\lambda_{max}}{\lambda_{min}}\right\|$	$\left\|\frac{\lambda_{total}}{\lambda_{max}}\right\|$	$\left\|\frac{\lambda_{total}}{\lambda_{min}}\right\|$
ξ-direction	7.07	11.9	79.2
η-direction	117	1.12	131
ξ-direction	1.68	12.6	21.3

Since this structure cannot be meshed using one of the elementary coordinate systems (outlined in [81]), a numerically generated grid is required. The original mesh was based on a circular cylindrical coordinate system where its outer regions were projected onto the walls of the rectangular cavity. Due to the symmetry of the problem, only half of the structure was meshed using **TrueGrid®** (with a magnetic image wall placed at the plane of symmetry) [141]. Three discretised versions of the problem, with resolution of $(14 \times 48 \times 13)$, $(24 \times 48 \times 20)$, and $(24 \times 24 \times 20)$, were tested. The best ratio of eigenvalues was obtained using a $(24 \times 24 \times 20)$ double discretised mesh (see **Figure 7.2**). **Table 7.4** presents the properties of the double discretised $(24 \times 24 \times 20)$ mesh in terms of its eigenvalues. The largest eigenvalue necessary for numerical stability was computed as $|\lambda_{total}| = 1.9174 \times 10^{12}$ $[m/s]$ which corresponded to a time-step of $\Delta t = 0.60222$ ps. Due to the unusual nature of the problem (grid) structure, the maximum ratio of the eigenvalues in all directions (especially in the circumferential direction) far exceeds the ideal value of unity (see **Table 7.4**). Hence, as explained in **Section 5.1.3**, for large eigenvalue ratios, the FVTD algorithm is no longer second order accurate; that is, the obtained solutions are expected to be less accurate. Thus, this problem may serve as a case study where the accuracy of the solutions is examined for grids of large eigenvalue ratios.

The cavity was excited using a (D_z) point source Gaussian pulse in time (with a frequency content of about 5 *GHz* at -40 *dB* level). This point source was located at a non-symmetric position within the cavity. The FVTD code was executed for 30,000 time steps, while at each time step, the D_z field components were recorded at several observation points within the dielectric ring. The DFT of the transient responses of these observation points was computed and analysed in order to extract the resonant frequencies of the partially loaded cavity. The resonant frequencies of the first four cavity modes computed by FVTD are given in **Table 7.5**.

Table 7.5. The resonant frequencies of the first four modes of the partially filled cavity

Mode[a]	Measured	TD-FEM	% error[b]	FVTD	% error[c]
K_{01}	1.258	1.259	0.8	1.283	1.7 (2.0)[b]
K_{02}	---	1.512	---	1.540	1.9
K_{03}	---	1.841	---	1.758	4.5
K_{04}	---	2.175	---	2.117	2.7

a. All resonant frequencies are in *GHz*.

b. Percentage errors are computed with respect to the measured data.

c. Percentage errors are computed with respect to the data obtained via TD-FEM.

A comparison of the first resonant frequency of the partially loaded PEC cavity as obtained via measurements [142], TD-FEM [141], and the FVTD method indicates that although the resonant frequency obtained via the FVTD method is less accurate than is the one computed using TD-FEM, it still predicts the first resonant frequency of the loaded cavity within the range of accuracy of most measuring instruments. The remainder of **Table 7.4** compares the other three resonant frequencies of the cavity modes obtained by

TD-FEM [141]* with the ones computed using the FVTD method. In all cases, the FVTD solutions are within the range of accuracy (of ±5 %) required for most engineering problems. Thus, despite the large eigenvalue ratios of the discretised space, the FVTD method provides reasonably accurate solutions for most engineering applications.

7.3 Case Three: A Wide Band SMA-Air Transformer

In the previous sections, the FVTD technique was successfully used to analyse two (reasonably complex) practical problems that have appeared in the literature. In this section, a complete study of an EM problem (currently under research in industry) is conducted. This study includes theory, design, and FVTD simulations. Unfortunately, measurements are not available at this time.

7.3.1 Background and Theory

Transmission lines are often considered to be simple devices that guide energy from the generator (source) to the load. However, not only must this mode of energy transportation be lossless, but it also must ensure maximum energy/power transfer from the source to the load [3]. Thus, matching networks are often introduced at either or both ends or along the transmission line in order to accomplish impedance matching. In a matched system, most of the generated power is delivered to the load (*i.e.* very little is reflected back to the source), which often results in other improvements in system performance [136].†

---

* Reference [46] also includes resonant frequencies of the PEC cavity obtained by DSI-FDTD and N-FDTD. However, due to the argument put forward in **Chapter 2**, the results obtained via TD-TEM were deemed more accurate, and therefore, are used for comparison.

† For example, impedance matching in some antennas and low-noise amplifiers results in a better signal-to-noise ratio.

As for most circuit parameters, the impedances of the source, the load, and the matching network are frequency dependent. Although the matching network can be designed to have zero or close to zero reflection coefficients at a specific frequency, it is desirable (and often required) to match the impedance over a band of frequencies. Generally, a better than $-10\ dB$ Return Loss, RL, (see **Appendix C** for definition) over the operating bandwidth is the minimum requirement for matching networks in most applications [136]. Many methods of impedance matching have been previously developed where the impedance matching has been achieved using lumped elements, stubs of a variety of configurations, reactive elements, and quarter-wave transformers [3]. However, quarter-wave transformers and specifically, tapered transmission lines, are the main focus of the following discussion.

7.3.2 Quarter-Wave Transformers and Tapered Transmission Lines

The input impedance, Z_{in}, of a quarter-wave transformer of impedance, Z_T, connected to a pure resistive load of impedance, Z_L, can be determined as [136]:

$$Z_{in} = Z_T \frac{Z_L + jZ_T tan\beta l}{Z_T + jZ_L tan\beta l}, \tag{7.1}$$

where $\beta = 2\pi/\lambda$ is the phase constant, and the length of the line is $l = \lambda/4$. Thus, at the tuning frequency, $\beta l \rightarrow \pi/2$, the reflection coefficient of the quarter-wave transformer of impedance,

$$Z_T = \sqrt{Z_{in}Z_L}, \tag{7.2}$$

is zero at the input to the transformer (see **Figure 7.3**). However, the reflection coefficients at adjacent frequencies are non trivial; that is, the matching network is frequency sensitive [136].

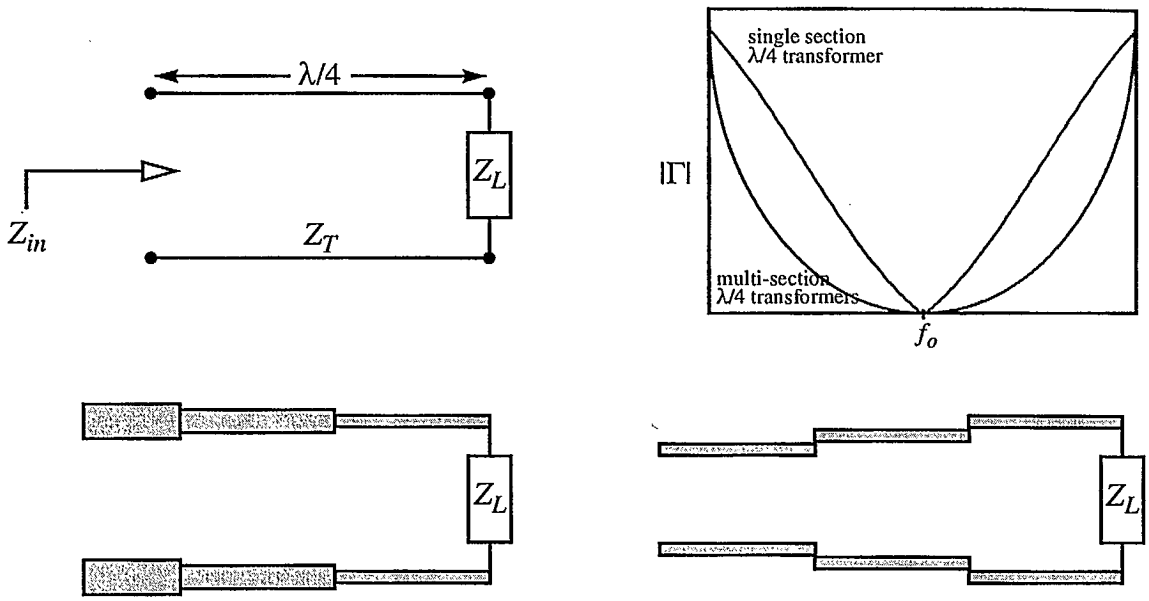

Figure 7.3. The quarter-wave matching transformer (top-left), theoretical response of single and multi-section quarter-wave transformers (top-right), and two possible configurations for three-segment quarter-wave transformers (bottom)

It has been shown that the bandwidth of a matching network may be increased if several quarter-wave transformers of various characteristic impedance are connected in series, where each segment acts as a matching circuit for its neighbouring elements [3].* The resulting matching network will have an overall reflection coefficient which arises from the smaller reflections of each transformer. Thus, for a given tolerance of the maximum value of the reflection coefficient, a broader band of operating frequency may be achieved† (see **Figure 7.3**). Alternatively, the discrete segments of a multi-section quarter-wave transformer can be replaced with a continuously tapered transition matching

* This also represents the standard application of quarter-wave transformers; they are often used as the intermediate matching section of transmission lines with different characteristic impedances, such as connecting transmission lines of different width, height, diameter, *etc.* [3].

† The theory and design of multi-section quarter-wave transformers have been discussed extensively in the literature. Some excellent references include [3, 135, 136].

segment. The impedance matching is accomplished through a continuous but smooth change in the characteristic impedance of the transformer section. Theoretically, a zero return loss over an infinite bandwidth is feasible if an infinitely long and gradually tapered segment of a transmission line is used. However, in most practical circuits, only a finite space is available; thus only a finite bandwidth is matched [3].

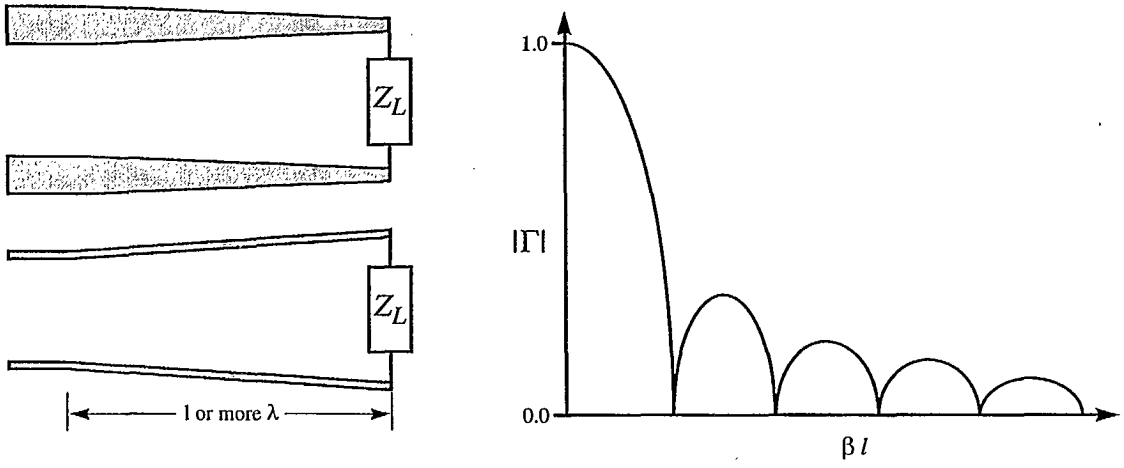

Figure 7.4. Examples of two possible configurations of tapered transformers for wide band applications (Left) and their theoretical input reflection coefficient (Right)

There are a variety of techniques for ensuring a smooth change in a transformer's impedance; two of the more common methods, that is, the gradual changing of the conductors' diameters or the spacing between the conductors, are shown in **Figure 7.4**. **Figure 7.4** also contains a plot of the reflection coefficient response of the tapered line (based on the theory of small reflections) which demonstrates a standard passband characteristic often associated with these types of matching circuits [135, 136]. A detailed study of the theory of small reflections, various design methods, and the evaluation of the performance of tapered transmission lines is beyond the scope of the current discussion and may be found in [136]. However, in the next section, the discussion on SMA-air

transformers will include the theory and design details of the device. The discussion will further concentrate on issues associated with the device's numerical simulations.

7.3.3 SMA-Air Transformer: Theory and Design

As stated earlier, quarter-wave transformers in general, and tapered transmission lines in particular, are often used as an intermediate matching device between two transmission lines of different characteristic impedance. Conversely, a tapered transformer may be utilized to maintain a constant characteristic impedance in transmission lines of changing size and composition [136]. In the case of the SMA-air transition, the input signal to a coaxial transmission line was supplied by means of an SMA connector with an inner conductor radius, r_{inSMA}, of $0.63\,mm$ and an outer conductor of inner radius, $r_{out} = 2.05\ mm$; it was filled with a material with a dielectric constant, $\varepsilon_r = 2.0$. The output was a device surrounded by free space, with an identical outer conductor radius. An input and output impedance of 50 Ω was required. Thus, following the application of the expression of impedance of coaxial lines,

$$Z_o = \frac{1}{2\pi}\sqrt{\frac{\mu}{\varepsilon}}\ln\frac{r_{out}}{r_{inLoad}} = 50, \tag{7.3}$$

the required inner conductor radius, r_{inLoad}, at the load end was $0.89\,mm$. **Figure 7.5** includes both the profile and a 3D view of the SMA-air transition problem.

The SMA-Air transition was designed in two stages [143]. First, the tapered transmission line segment was considered and then, the tapered dielectric region was calculated. The equation for the tapered transmission line segment was easily derived by assuming that at any given cross section of the tapered region, the impedance of an air-filled line was constant, and thus (7.3) was solved in terms of the inner conductor radius

(in the transition region) [143],

$$r_{inTran} = r_{out}\, e^{-\left(2\pi Z_o \sqrt{\frac{\varepsilon_o}{\mu_o}}\right)}. \tag{7.4}$$

The inner radius of the entire coaxial transmission line, r_{inner}, was represented as a linear function of axial distance, z; that is,

$$r_{inner}(z) = \left(\frac{r_{inTran} - r_{inSMA}}{L}\right) z + r_{inSMA}, \tag{7.5}$$

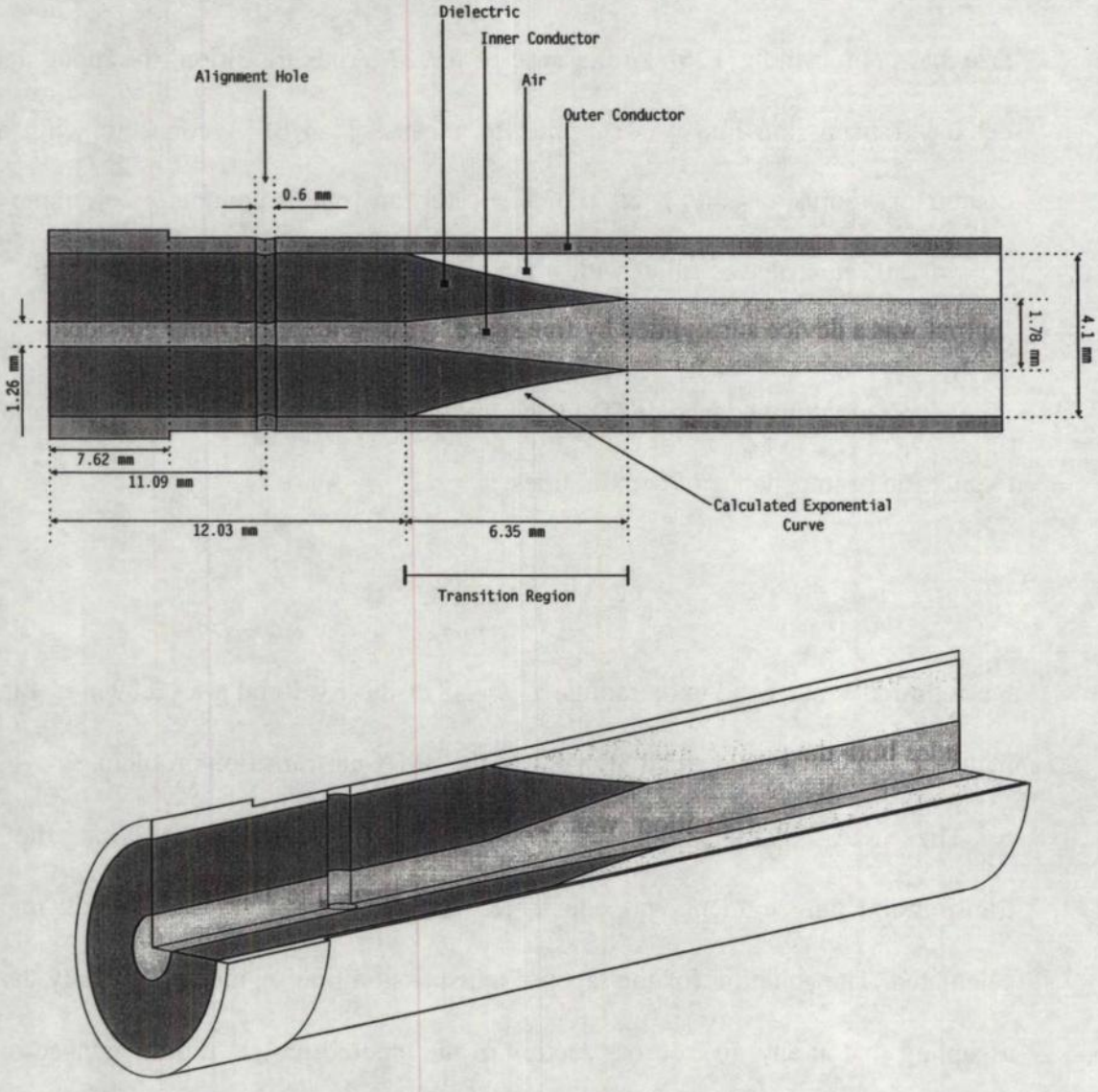

Figure 7.5. Profile and 3D view of the SMA-air transformer problem (not to scale)

where a gradual change in the radius of the tapered line was distributed over the axial length of the transition region, L. This axial length must be at least as long as the wavelength of the maximum frequency of operation (45 *GHz*); it was therefore chosen to be 6.35 *mm* long ($f \approx 47$ *GHz*). The design of an air-filled tapered coaxial line was complete. The tapered dielectric region was considered next.

In order to gradually make the transition from the dielectric material to air in the tapered line region while keeping the characteristic impedance constant, the dielectric region must be slowly phased out. The problem was simplified by equating the series sum of the per-unit-length impedance of two loads (one for air and one for the dielectric region) to the desired characteristic impedance of $Z_o = 50\ \Omega$ and solving for the change of the radius of the tapering dielectric region [143], *i.e.*

$$r_{taper}(z) = e^{\left(\left(\frac{4\pi^2 Z_o^2 \varepsilon_r \varepsilon_o}{\mu_o ln\left(\frac{r_{out}}{r_{inner}(z)}\right)} - \varepsilon_r ln(r_{out}) + ln(r_{inner}(z))\right)/(1-\varepsilon_r)\right)}. \quad (7.6)$$

The expressions for the tapered line and tapered dielectric region of the SMA-air transformer (equations (7.5) and (7.6), respectively) were plotted in an axial plane cross-section of the coaxial transmission line and are shown in **Figure 7.6**. A linear tapered dielectric region was also plotted in order to emphasize the exponential nature of the curvature of the tapered dielectric segment. The SMA-air transformer problem has now been fully defined in terms of mathematical expressions and is ready for modelling/ meshing.

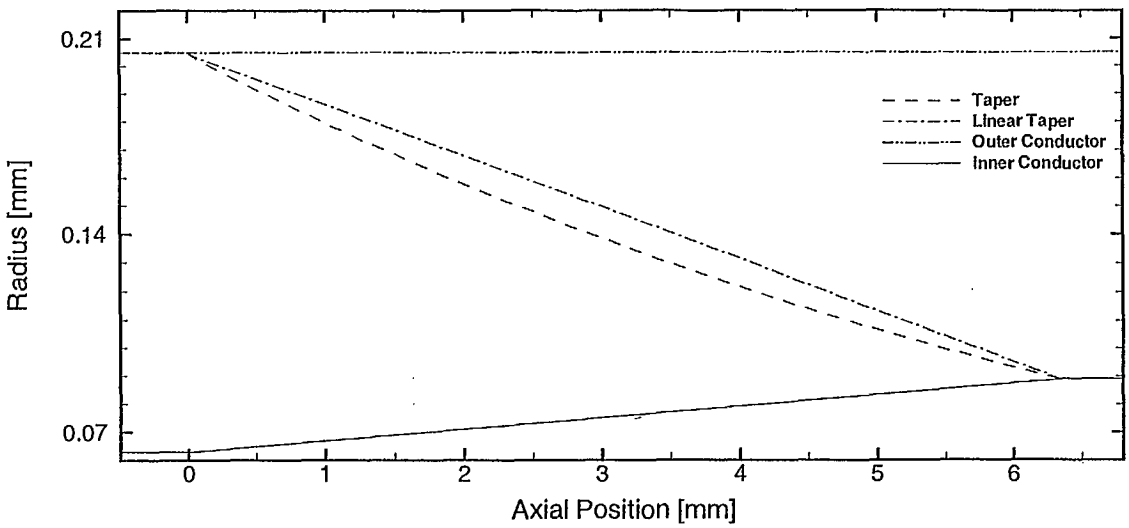

Figure 7.6. Axial plane cross-section of the designed SMA-air transition section

7.3.4 SMA-Air Transformer: Modelling and Discretisation

The SMA-air transformer shown in **Figure 7.5** was modelled using the **TrueGrid®** mesh generation software package. The mathematical expressions derived in **Section 7.3.3** were utilized to define the structure in **TrueGrid®**. The standard cylindrical coordinate system mesh (used for modelling coaxial cables in **Section 6.10**) was then fitted/projected onto the curves and surfaces defining various features of the SMA-air transformer. Many electrically insignificant features, such as the *alignment hole* and the thickness of the inner and outer conductors, were not modelled.

An orientation similar to the coaxial cable example was assumed in which the axial direction was placed along the z-direction. The inner and outer conductors were assumed to be perfect conductors and were modelled using PEC boundary conditions in the lower and upper bounds of the radial direction; periodic boundary conditions were utilized in the lower and upper circumferential directions, while characteristic ABCs terminated the simulation space in the axial direction. The total length of the simulation space in the axial

direction was 44.45 *mm*, which was defined from –25.4 *mm* to 19.05 *mm* in the z-direction of the cylindrical coordinate system. Two uniformly meshed sections of length 12.7 *mm* ($18 \times 50 \times 32$ cells) and 6.35 *mm* ($18 \times 50 \times 16$ cells) were placed at the leading and trailing ends of the simulation space respectively. The uniformly meshed sections provide transition zones in which the outgoing waves at either ends were perpendicular to the ABCs. Thus, the performance of the ABCs was similar to the circular coaxial cables (see **Figure 6.8**).

Although the tapering of the inner conductor and the dielectric region was initiated at the origin and was completed at z = 6.35 *mm*, a gradual deflection of the mesh planes perpendicular to the direction of propagation was launched at z = –12.7 *mm*. The deformed mesh was slowly restored to its original uniform form at z = 12.7 *mm*. This region provided an exact and convenient (structured) fit to both the inner conductor and the dielectric taper without stair-stepping or individual cell assignment.* **Figure 7.7** demonstrates partial profiles of the meshed simulation space; the top frame displays discrete planes that form the dielectric region. The bottom frame is a sketch of the plane of the discretised problem space in the axial direction which clearly outlines the exact form of various mesh points in that direction.

The SMA-air transformer of the aforementioned configuration was meshed using a variety of combinations of discretisation in the radial, circumferential, and axial directions; the ratio of the eigenvalues of all of the meshed cases was computed for the coaxial transformer structures filled with materials of relative dielectric constant ε_r = 1.0

* Recall that in a structured mesh, any object (regardless of its shape) may be defined using only six mesh indices ($i_{start} \rightarrow i_{end}$, $j_{start} \rightarrow j_{end}$, $k_{start} \rightarrow k_{end}$).

(from this point on referred to as an *air-filled SMA-air* transformer) and $\varepsilon_r = 2.0$ (as specified in the original SMA-air transformer design). The best results (*i.e.* lowest ratio of eigenvalues) were obtained using a double discretised mesh of size $(18 \times 50 \times 113)$ cells. For this mesh, the value of the largest eigenvalue was 1.5660×10^{13} $[m/s]$ which corresponded to a time-step of 73.736 *fs* computed at the stability limit. The properties of the meshed space in terms of its eigenvalues for both air-filled and SMA-air transformers are given in **Table 7.6** and **Table 7.7** respectively (The value of the largest eigenvalue remained the same for both meshes.). These tables clearly indicate that due to the unique features of the tapered dielectric region and the nature of the cylindrical coordinate system, various ratios of eigenvalues far exceed unity. Thus, in such cases, the main objective is to reduce this ratio as much as possible.

Table 7.6. The ratio of eigenvalues in the air-filled SMA-air transformer

	$\left\|\frac{\lambda_{max}}{\lambda_{min}}\right\|$	$\left\|\frac{\lambda_{total}}{\lambda_{max}}\right\|$	$\left\|\frac{\lambda_{total}}{\lambda_{min}}\right\|$
ξ-direction	3.75	2.18	8.18
η-direction	3.01	4.40	12.3
ζ-direction	17.5	2.17	37.8

Table 7.7. The ratio of eigenvalues in an SMA-air transformer

	$\left\|\frac{\lambda_{max}}{\lambda_{min}}\right\|$	$\left\|\frac{\lambda_{total}}{\lambda_{max}}\right\|$	$\left\|\frac{\lambda_{total}}{\lambda_{min}}\right\|$
ξ-direction	5.31	2.18	11.6
η-direction	3.14	5.97	18.7
ζ-direction	14.6	2.59	37.8

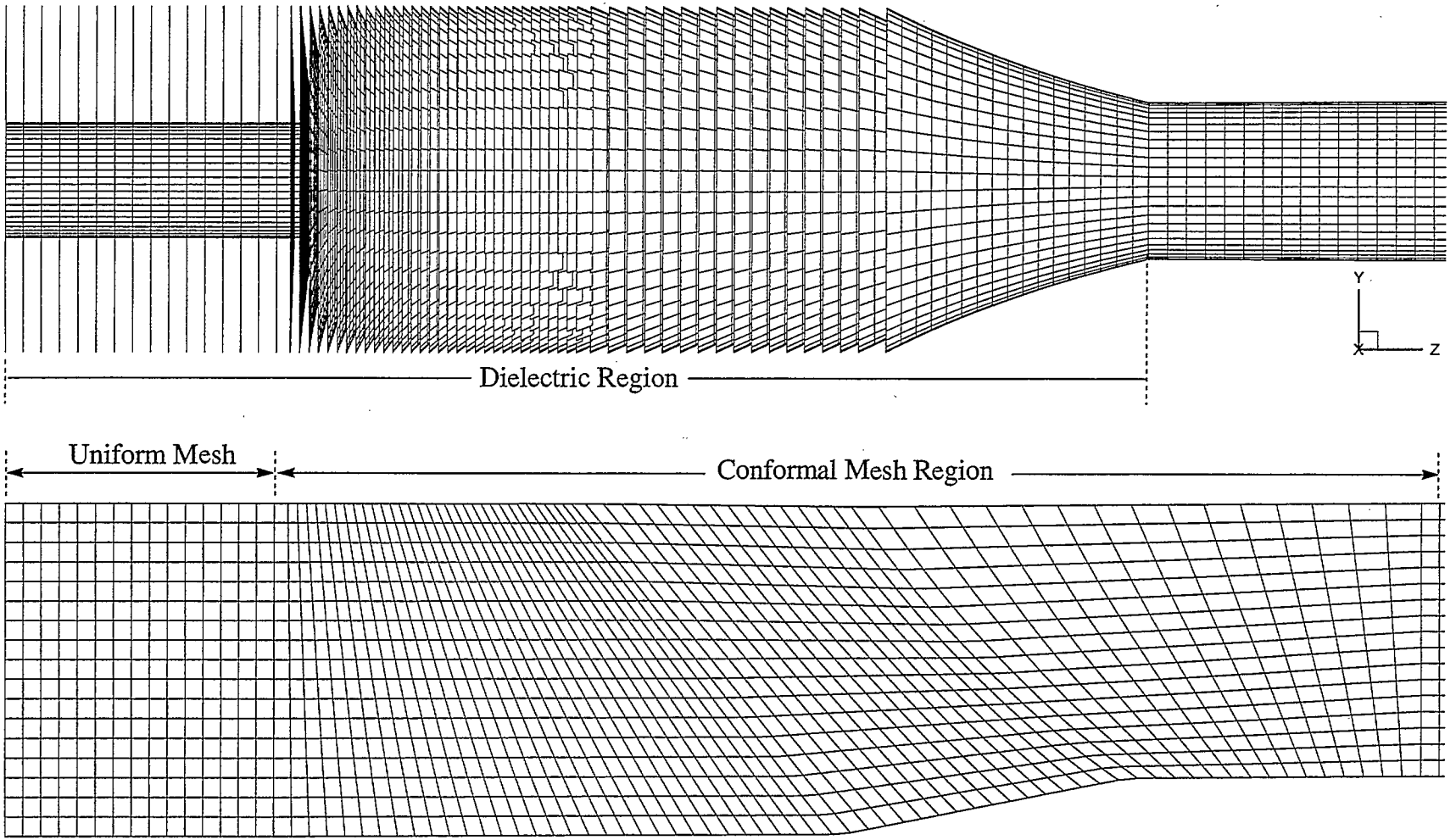

Figure 7.7. Partial profile of the discretised SMA-air transformer problem: (Top) the dielectric region: scale (X, 2Y Z), (Bottom) meshed problem space in the axial direction: scale (X, 6Y Z)

7.3.5 Simulation Results

In both the air-filled and SMA-air transformer case, a one-cell-thick distributed lumped voltage source was placed at $z = -23.6\ mm$ (four cells away from the lower z-bound ABC). The lumped source generated a Gaussian pulse of width $t_w = 6\ ps$ and $t_0 = 18\ mm$ (frequency content of approximately 80 *GHz* at -40 *dB* level). In both cases, the voltage between the inner and outer conductors was computed at several observation points located at $z = -13.3$, -7.42, and $17.62\ mm$ (referred to as V_{source}, V_{mid}, and V_{end} respectively) at every time step for a total of 500 *ps*. The approximate locations of the distributed lumped source and the observation points are marked in a diagram of the cross section of the simulated space in **Figure 7.8** which also contains plots of the transient response of the two simulated cases. The modal decomposition method was applied to the transient responses computed at the *source* and *end* observation points in order to compute the return losses and the reflection coefficient of the ABCs of both structures. The return loss and the reflection coefficient of the ABCs were plotted over a frequency range of 0 to 50 *GHz* and are shown in **Figure 7.9**. One must note that in the case of an air-filled transformer, the tapered transmission line converts (matches) a 70.7 Ω line (on the left) to a 50 Ω line (on the right), whereas in the case of an SMA-air transformer, both ends have a characteristic impedance of 50 Ω. The tapered conductor and dielectric regions are utilized to convert (match) the input physical characteristics to the ones required by the output device.

The simulated transient response of both cases indicates that the frequency components associated with frequencies for which the tapered line and tapered dielectric region were designed ($f \leq 47\ GHz$) are propagating through the transformer, but the

higher frequency components are reflected. This phenomenon is represented by the broadening of the launched pulse, *source*, as it propagates through the transformer section

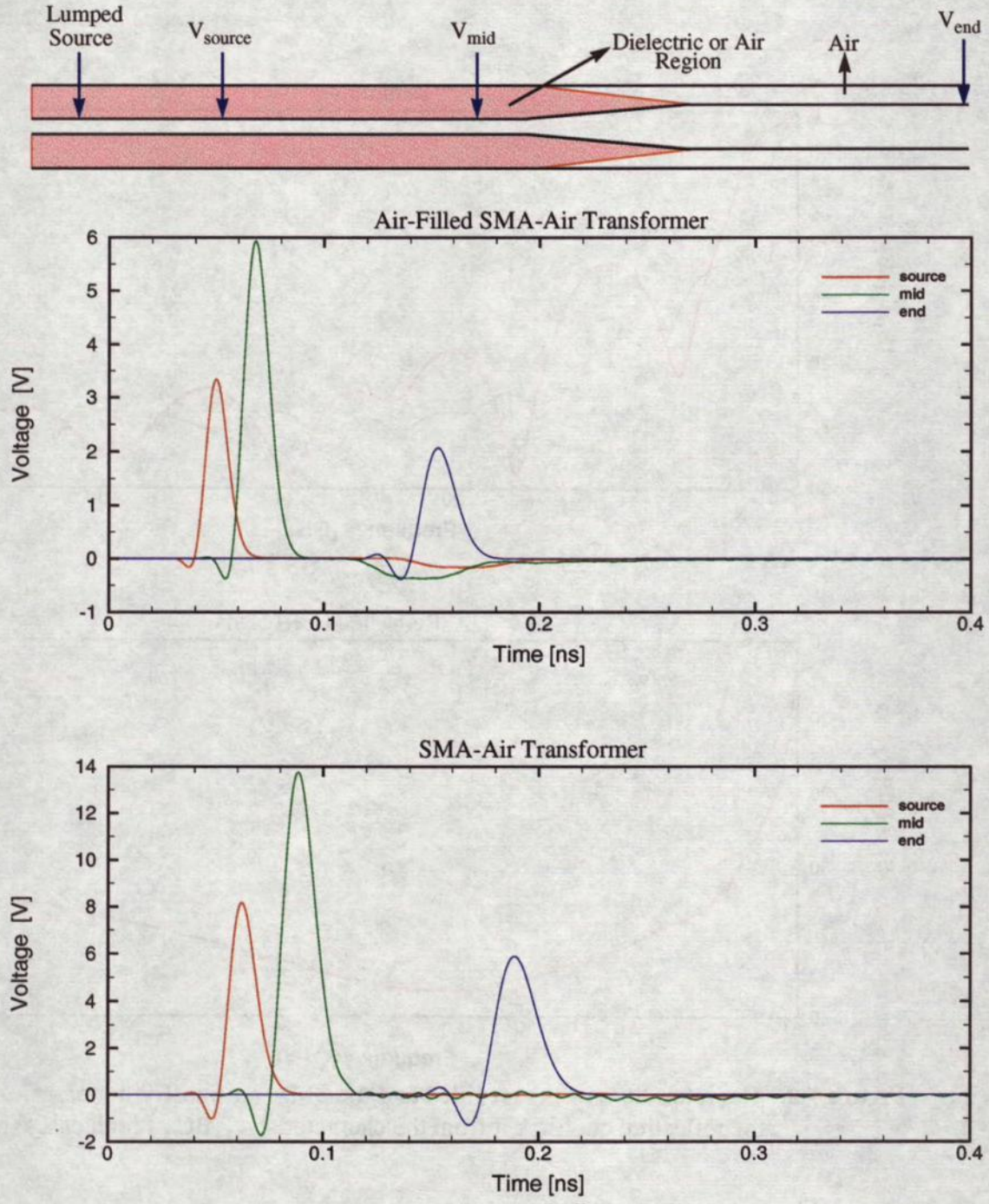

Figure 7.8. Approximate location of the lumped source and observation points (top) and calculated voltages at various locations along the coaxial line for an air-filled (middle) and an SMA-air transformer case (bottom)

(and was recorded at the *end* point). The air-filled configuration also exhibits a larger and more distinct reflection than does the SMA-air transformer structure where the reflections from the transition are limited to small damped oscillations.

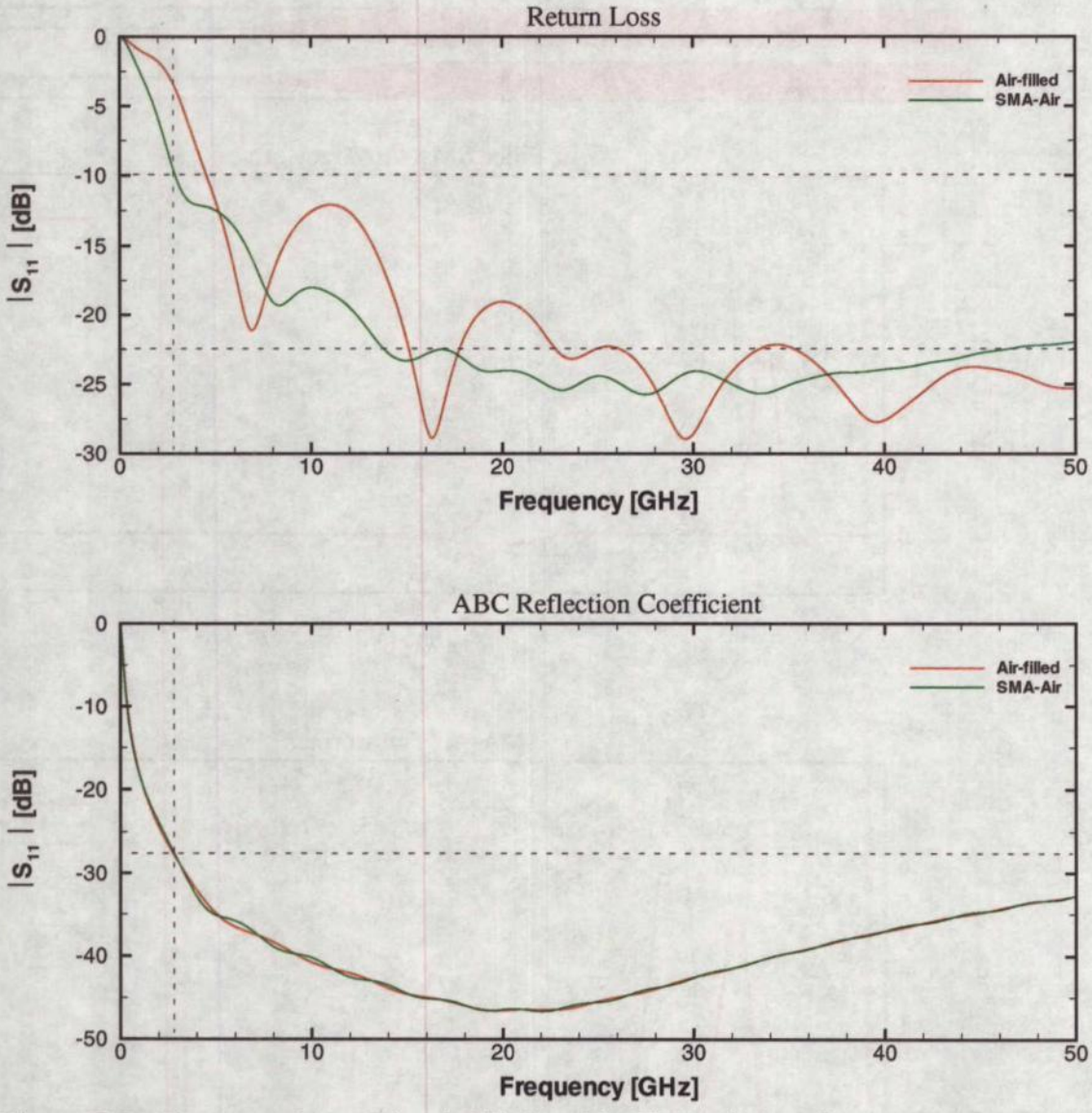

Figure 7.9. The return loss of the air filled and the SMA-air transformer cases (top) and the reflection coefficient from the characteristic ABC of both cases (bottom)

In both cases, the voltages computed in the "transition" region (*mid*) are significantly different in amplitude as compared to the ones at the *source* and *end* locations. This is due

to two independent factors. The first involves the length of the path of integration for which the voltages were computed. The voltages at the *source* and *end* points were calculated in the uniformly meshed region where the path of integration was perpendicular to both the inner and outer conductors. In contrast, the *mid* voltage was calculated in the conformal mesh region where the path of integration was slanted, not perpendicular to either the inner or the outer conductors, and was significantly longer than were the paths of integration utilized in the computation of the *source* and *end* voltages. Secondly, the discontinuity introduced by the tapered region generated reflected waves in the form of higher order (TE and TM) modes. The total effect of these modes will generate a standing TEM mode behind the discontinuity (*i.e.* the transformer). Thus, the position of the observation point in the field of the standing wave could affect the overall amplitude of the computed voltage at that point.

The reflection coefficient of the characteristic ABCs of both structures was better than -28 *dB* for frequencies larger than 3 *GHz* (see **Figure 7.9**). Thus, the results obtained for lower frequency components may not be accurate and hence, are not discussed here. For the case of the air-filled tapered transmission lines, the return losses computed at the *source* point exhibit a behaviour similar to what was predicted by **Figure 7.4** (see top plot of **Figure 7.9**). The addition of the tapered dielectric region dramatically improves the performance of the structure. Not only is the overall matching of the structure now better than -10 dB for the entire operating frequency but also, the frequency dependence of the matching transformer is reduced. A better than -20 dB match was observed for the SMA-air transformer for frequencies of 12 to 50 *GHz*.

7.4 Case Four: The FVTD Method and Sharp Metallic Edges

Heretofore, the problems analysed and solved using the FVTD method have all involved "smooth" and continuous solutions (fields) to Maxwell's equations. However, this is not always the case, since many practical problems, such as microstrip structures and coplanar waveguides, contain sharp metallic edges. As explained in **Section 2.2.2.2**, due to the inherent assumption of the continuity and smoothness of the numerical solution of PDEs, most numerical methods are not capable of accurately modelling the rapid spatial variation of the field distribution in the vicinity of the singularity (of a metallic edge) [147]. Thus, based on the nature and characteristics of a given numerical method, dissipation, dispersion, or both types of errors may appear in the final solution. In reference [10], dissipation and dispersion errors of various numerical techniques for solving PDEs have been rigorously studied and quantified. It is generally known that most finite-difference methods (such as FDTD and TLM) are dispersive [148, 149], while the LW-FVTD method is dissipative [10, 150].

The accuracy of the TLM and FDTD solution of problems containing sharp metallic edges has been the subject of many studies [147-149] in which the dispersive errors are quantified. However, to date, no comprehensive study of dissipation error due to the FVTD modelling of the singularity at sharp metallic edges is available. In the following section, a study of a microstrip structure is conducted using FVTD, FDTD, and TLM methods and the results are compared with measurements.

7.4.1 Multi-Segment Dielectric Resonator Antennas

Multi-Segment Dielectric Resonator Antennas (MSDRAs) offer versatility and design flexibility, making them attractive candidates for numerous applications. MSDRAs can be

designed for narrow band, multi-band, or wideband usage; can be made low-profile or compact; can radiate linear or circular polarization; and can be used as an individual element or in a large planar array [151]. The details of the design and the theory of operation of MSDRAs are outlined in [151, 152]. In general, it is desirable to feed the MSDRAs with microstrip lines, since this facilitates the integration of MSDRAs with printed feed distribution networks. Accurate numerical modelling of these types of structures is of interest, since optimizing the performance (*i.e.* maximizing the amount of energy coupled into the MSDRAs) and various characteristics of MSDRAs via experimental methods is often time consuming and expensive.

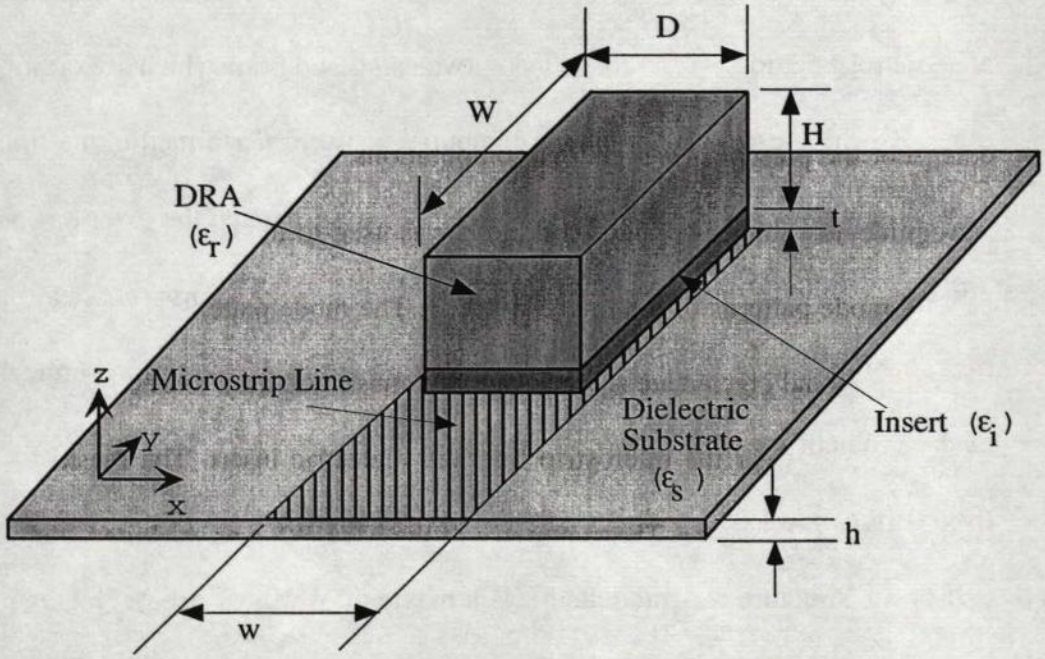

Figure 7.10. The multi-segment dielectric resonator antenna structure

The MSDRA shown in **Figure 7.10** was fabricated from a composite ceramic material with $\varepsilon_r = 10$ and $\varepsilon_i = 40$, with $W = 10.0$ *mm*, $D = 4.0$ *mm*, $H = 6.5$ *mm*, and $t = 1.0$ *mm*. The antenna was placed on a 50 Ω microstrip feed line with substrate

permittivity, ε_s, of 3.0, with w = 1.75 *mm* and h = 0.75 *mm*. The return loss of the aforementioned MSDRA structure was measured over a frequency range of 5 to 15 *GHz*. This structure was also modelled via two types of FDTD-based techniques as well as the TLM method. In all cases, S_{11} data were extracted and were compared to the measured data. A brief description of these methods follows.

7.4.1.1 Computational Methods

The Finite-Integration Technique (FIT), as implemented within the **MAFIA CAE®** tool [153], is based on an integral form of Maxwell's equations where static, time-harmonic, and time-dependent problems can be analysed with this formulation [154]. The analytic formulation is discretised using two staggered grids which are orthogonal to each other. For the present investigation, computations were performed in the time domain. A waveguide absorbing boundary condition was used to match the exterior boundaries that utilized mode patterns of the microstrip line. The mode patterns were determined using a two-dimensional eigenvalue solver. A graded mesh was used to improve the discretisation of the problem near the microstrip line and dielectric insert. The mesh cell size ranged from 0.16 *mm* to 1.0 *mm*. The symmetry of the MSDRA was exploited such that only one half of the structure was modelled (*i.e.* a magnetic wall was used). Details regarding the UWO-FDTD simulation program are given in [155, 156]. To briefly summarize, it is based on Yee's formulation and utilizes first-order Mur ABCs. A Gaussian pulse was launched on the microstrip line using a matched Thévenin equivalent voltage source. The geometry was discretised using a uniform mesh of cell size 0.25 *mm*, within a mesh of $(85 \times 200 \times 70)$ cells.

The TLM simulation tool is based on the SCN-TLM, and is described in [59, 60]. A Gaussian pulse was launched on the microstrip line using an idealized TEM source. The match termination for normal incidence ABCs was applied, which provided a performance that was superior to first-order, but inferior to second-order ABCs. The geometry was discretised using a uniform mesh of cell size 0.25 *mm* within a mesh of $(96 \times 120 \times 71)$ cells.

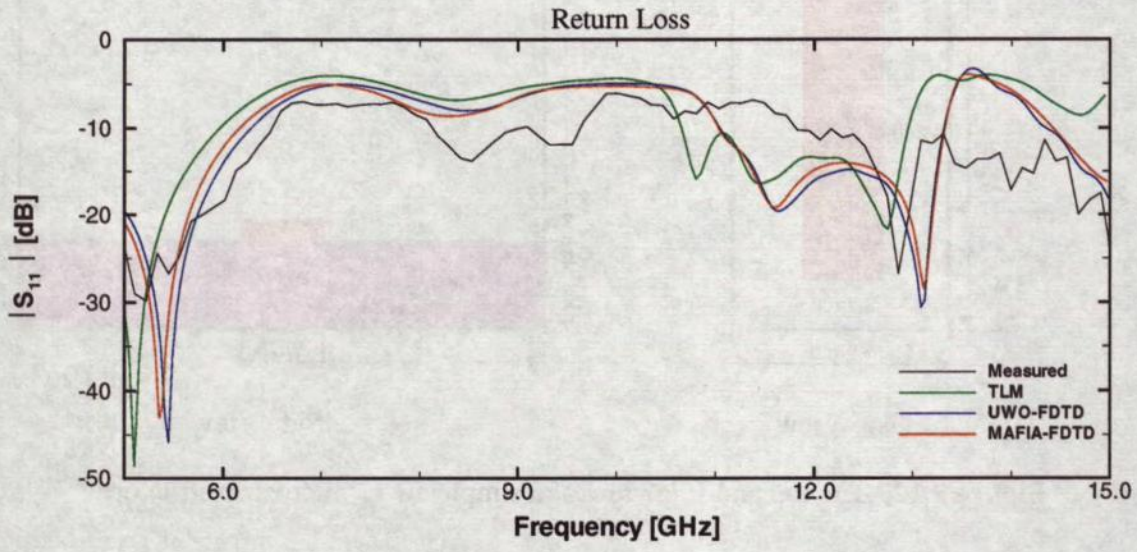

Figure 7.11. The return loss of the MSDRA structure computed via the TLM, FDTD and FIT-FDTD method and compared with measured data.

All simulations were performed for the same amount of physical time which corresponded to approximately 5000 TLM time steps. At each time step, the voltage (with reference to the ground plane) on a specific point of the microstrip line was recorded. In the case of the FDTD and TLM simulations, the pulse separation method was used to compute the return loss of the MSDRA via its transient response. In **Figure 7.11**, the FIT, FDTD, and TLM numerical results for S_{11} are compared to the measured data. Despite the difference in algorithm, mesh size, and ABCs used in the MAFIA-FDTD and the UWO-

FDTD simulator (with the MAFIA code generally being regarded as the more accurate of the two), the numerical results of the two agree well with each other. However, the agreement of the numerical results with the measured data was poor. Further simulations and research have been conducted to improve the agreement between the numerical and measured data. A summary of this ongoing work can be found in [152, 157].

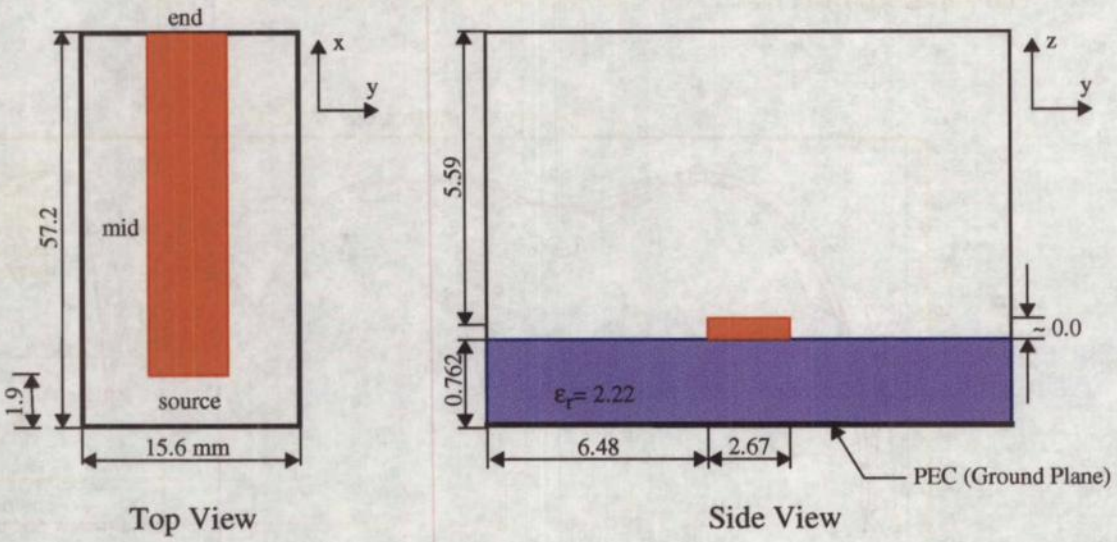

Figure 7.12. The top and side view of a simple 50 Ω microstrip structure

7.4.1.2 FVTD Simulation of Microstrip Structures

An FVTD simulation of the aforementioned MSDRA structure was conducted using a uniform mesh similar to the one utilized for the UWO-FDTD simulation. The computed return loss of the structures exhibited very poor agreement with the previously computed S_{11} data. This prompted a study of the transient response of an FVTD simulation of a 50 Ω microstrip structure which has been extensively studied and documented in [60]. The microstrip structure of **Figure 7.12** was modelled using both the FDTD and FVTD method. The ground plane was modelled using PEC BCs, and the remaining BCs were enforced via Mur's first order ABCs (for the FDTD simulation) or characteristic ABCs (in

case of the FVTD method). In both cases, the microstrip line was excited using a distributed lumped voltage source placed at the *source* end of the line. The Thévenin voltage source ($R = 50\ \Omega$) generated a Gaussian wave form of amplitude 10 V, pulse width $t_w = 12\ ps$, and $t_0 = 50\ ps$. At several locations along the microstrip line (corresponding to the *source*, *mid*, and *end* points of **Figure 7.12**), the voltage between the line and the ground plane was calculated and is plotted in **Figure 7.13**.

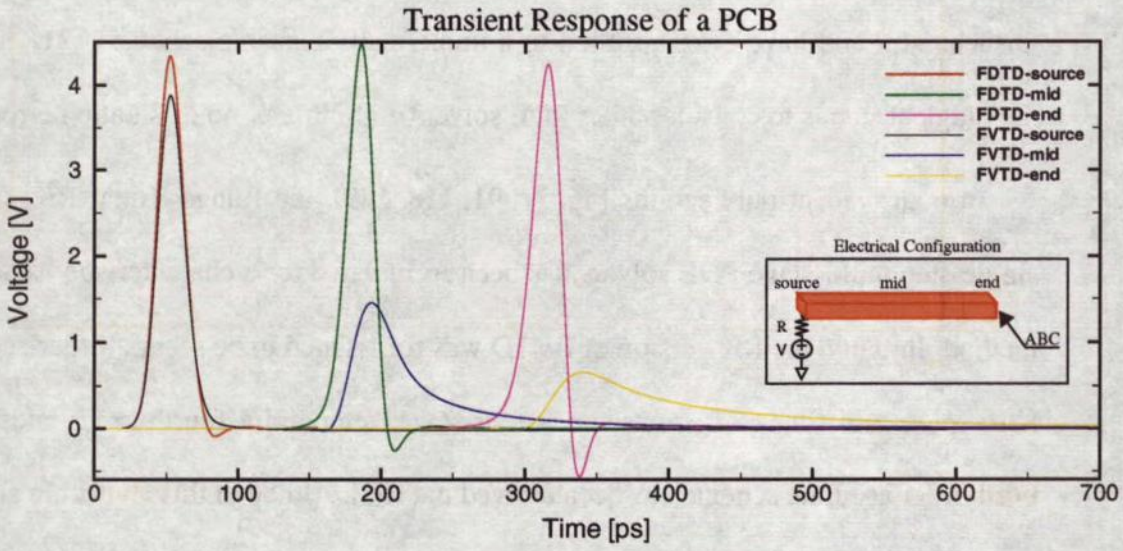

Figure 7.13. A comparison of the FDTD and FVTD simulated transient response of a PCB at several spatial locations

The FDTD simulation displays a dispersive behaviour in the pulse propagation (due to the high frequency content of the excitation pulse). However, the FVTD computed transient response of such a structure bore little resemblance to the typical wave propagation along a microstrip line [60]; rather, it exhibited both diffusion and dissipation behaviour. Upon closer examination of the electric field distribution at the edges of the microstrip line, it was revealed that the FVTD simulation "smooths" the rapid spatial variation of the field distribution in the vicinity of the singularity at the edge of the metal

strip. This numerical property (*i.e.* dissipation error) of the FVTD method changes the behaviour of the pulse propagation along the microstrip line, and hence, affects the scattering parameters of the structure. This example clearly demonstrated that due to the dissipation error associated with the LW version of the FVTD method [10, 150], this technique is incapable of modelling structures that contain sharp metallic edges. The most obvious remedy is to reduce or eliminate the dissipation errors of the LW algorithm. Many attempts at reducing the effect of the dissipation term in the LW algorithm have been unsuccessful and have often resulted in a numerically unstable scheme [121]. Thus, the next logical step is to consider other PDE solvers with little or no dissipation error.

In many recent publications [46, 77, 91, 158, 159], the Runge-Kutta (RK) family of single-step multi-stage PDE solvers has been formulated for a characteristic based FVTD method. Initially, the RK version of FVTD was formulated to be second-order accurate in both space and time [77]; however, a four-stage, temporally fourth-order and spatially third-order accurate scheme has been derived in [158]. Although this algorithm appears to have dissipation and dispersion characteristics superior to LW-FVTD and Yee's FDTD method respectively, the provided examples did not include a case with sharp metallic edges, and, hence, further investigation of this class of PDE solvers is required.

7.5 Case Five: A GTEM Cell

International standards and certifications require radiated emissions and radiated immunity tests of all electronic equipment. Traditionally, full compliance testing has been conducted in Open Area Test Sites (OATS) or anechoic chambers [160]. However, the construction and operation of these facilities are often costly and will have to be added to the final cost of the product [161]. Recently, Gigahertz Transverse Electromagnetic

(GTEM) cells have become a more cost effective alternative to using chambers and OATS for compliance testing [161].

A GTEM cell is a gradually widening rectangular transmission line (with impedance of 50 Ω) [162]. The cell is excited at the narrow end via a coaxial connector and is terminated (at the wide end) via hybrid 50 Ω resistors and absorber materials (see **Figure 7.15** and **Figure 7.16**) [163].* This particular design of the GTEM cell allows the formation of homogenous electromagnetic fields which, in turn, supply the user with an exact knowledge of field distributions within the GTEM cell [164]. This information is used for the calibration of various types of probes as well as for accurately gauging the susceptibility of test results [165].

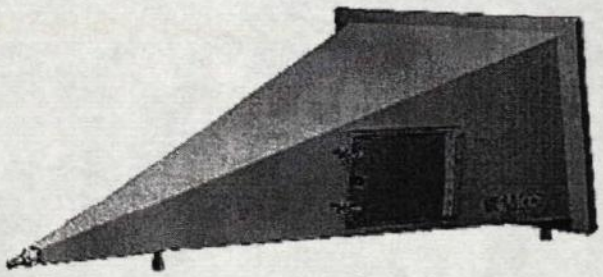

Figure 7.14. A GTEM cell

The matched termination of the GTEM cell over its frequency range of operation is essential. In general, at lower frequencies, the resistors are the main matching circuit, while at the upper frequency range, the absorber materials are the primary matching elements [160]. In the intermediate frequency range, a combination of both is required for a matched termination of the circuit, hence preventing the creation of higher order modes [162]. Therefore, the numerical simulation of various types of septums and termination circuits is of interest in order to optimize the termination circuit without costly and time consuming experimentation [163].

---

* The details of the GTEM cell design and structure, along with its theory of operation, is beyond the scope of the current discussion, but can be found in [160-165].

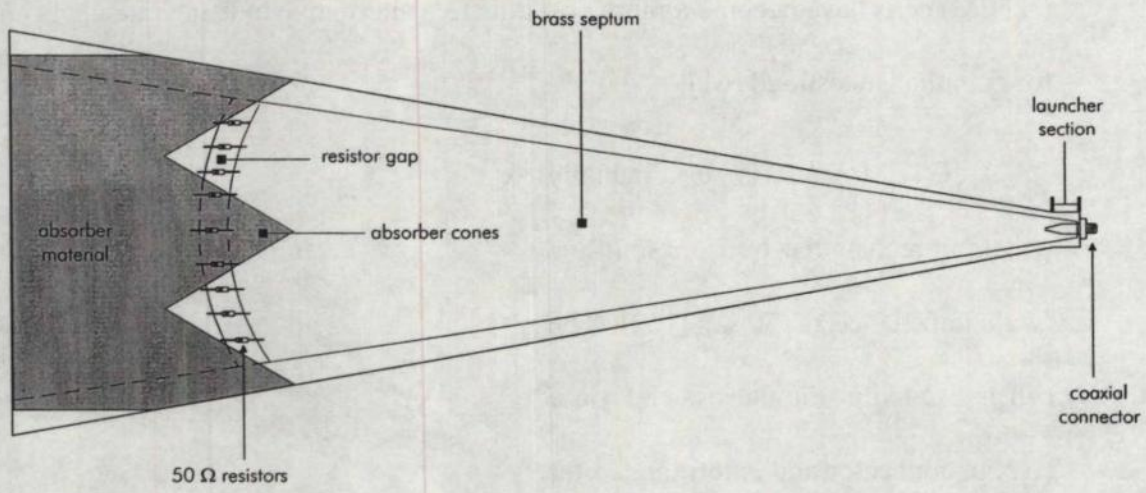

Figure 7.15. Principle schematic of a GTEM cell (side view)

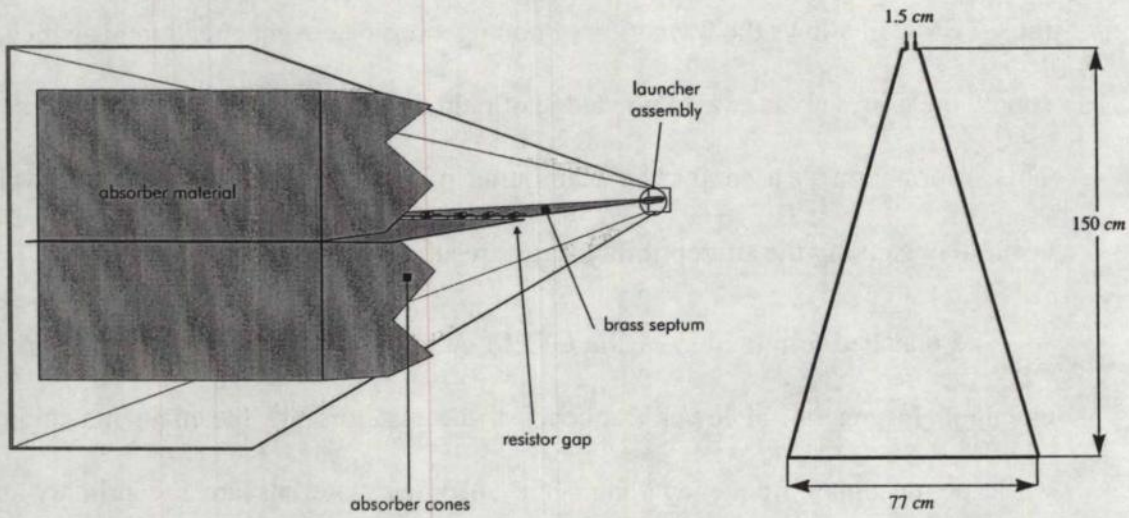

Figure 7.16. Perspective view (left) and approximate dimensions of a GTEM cell (right)

7.5.1 FVTD Modelling of a GTEM Cell

A GTEM cell, as defined in [163], was modelled and meshed using the **TrueGrid®** mesh generation package. The modelling of the GTEM cell began with defining the outer shell of the cell, the septum, and the absorbing materials. Next, a rectangular meshed block was defined and then projected onto the outer shell of the GTEM cell. This

procedure was also repeated with the curved edges of the septum. The most tedious and time consuming part of the mesh generation was projecting the mesh points on the surface of the absorber cones, which was performed one cone at a time (for all 36 cones). Finally, the entire mesh space was inspected for overlapping or triangular cells, and appropriate adjustments to the mesh (where required) were made. Several aspects of the GTEM cell make its modelling and analysis challenging. First, the internal structure of the cell is geometrically complex and is cumbersome to define. Second, the particular geometric features (such as the tip of the absorbing cones), along with the peculiar shape of the GTEM cell, require a highly non-uniform mesh. Third, in the case of the LW version of the FVTD method, numerical dissipation will occur at the septum's sharp metallic edges.

Despite the GTEM cell's geometrically complex structure, most mesh generation packages (including **TrueGrid®**) are capable of defining such an object via mathematical equations and the intersection of surfaces. This process (although very tedious, time consuming, and occasionally frustrating) can be performed for most geometrically complex EM problems. Ideally, the problem structure is defined and supplied in electronic format using one of many available Computer Aided Design (CAD) systems (such as **AutoCAD®**) that can be directly imported into the mesh generator software package and hence shorten the problem structure's definition time. The last short-coming can be easily remedied by using an FVTD engine based on a (temporally fourth-order and spatially third-order accurate) RK-FVTD method which has dissipation and dispersion characteristics superior to the LW-FVTD technique.

Thus, the only remaining challenging aspect of the aforementioned meshed GTEM cell is the highly non-uniform nature of its mesh. Since a structured mesh was utilized to

discretise the problem space, the same number of cells had to be fitted into the narrow end of the GTEM cell as in the wide end which resulted in highly disproportionate cell volumes and hence eigenvalue ratios of 1000 or higher. In addition, similar problems are encountered when modelling the tip of the absorber cones. Such non-uniform grids not only reduce the accuracy of the numerical solution, but also require a very small time step, which in turn increases the computation time of the simulation. For example, the GTEM cell of **Figure 7.16** was modelled using a conformal mesh of $(56 \times 64 \times 186)$ cells with $\Delta t = 43.4\ fs$. The computation time for one time-step was 237 s which means the total computation time required for a complete run (250,000 time steps) was about two years! Obviously, due to this unrealistic computation time, no results were obtained.

Clearly, any structured mesh configuration will experience (similar aforementioned) difficulties in meshing this type of problem. In **Section 5.1.1**, the use of unstructured grids was recommended for modelling very complex geometries. The main advantage of unstructured meshes is their flexibility in terms of controlling mesh density and cell shape (see **Figure 5.1**). For example, in the case of a GTEM cell, a cluster of cells can be allocated near the finer features of the problem space (*i.e.* at the absorber cone tips) or in the areas with a rapidly varying field distribution (such as near the launching assembly or at the edges of the septum) while much larger cells can be fitted into areas with a uniform field distribution, say inside the absorbing material. Hence, an FVTD engine based on an unstructured grid is more suitable for the modelling and analysis of geometrically complex EM problems.

7.6 Summary

The strengths and weaknesses of the LW version of the FVTD technique were examined using five practical case studies. In the first case, the FVTD method computed the TE cutoff frequencies of a coaxial waveguide with much better accuracy than those found using the TLM technique. Next, resonant frequencies of a partially loaded cavity were computed using the FVTD method and were compared with those of measurements and TD-FEM. Once more, the computed resonant frequencies agreed well with those given in literature. The third case involved a complete theory, design, and analysis of a wide band SMA-air coaxial transformer. The air-filled SMA-air transformer exhibited the classical return loss characteristics of such tapered structures. The combination of the tapered conductor and tapered dielectric used in the SMA-air transformer improved the overall return loss characteristics of the structure. A better than –20 dB match was observed for the SMA-air transformer for frequencies of 12 to 50 *GHz*. A better than –10 dB match was observed for frequencies of 3 to 50 *GHz*.

The weaknesses of the developed FVTD engine are mainly due to the properties of the LW algorithm. Due to the dissipative nature of the LW-FVTD method, the FVTD engine is unable to accurately solve problems that contain sharp metallic edges (such as microstrip structures) that generate rapid spatial variations of the field distribution. This was demonstrated in the fourth case study which involved the analysis of an MSDRA and its microstrip feed. It was suggested that these problems are better modelled and solved via less dissipative FVTD algorithms, such as RK-FVTD schemes. The final case study involved another problem of interest to industry, namely modelling a GTEM cell. Although the flexibility and versatility of the structured grid based on the FVTD method

was demonstrated via meshing a complete GTEM cell, due to the particular properties of the structured meshes, it is more practical to use unstructured grids for these types of problems. In general, the current FVTD engine is capable of modelling and solving reasonably complex EM problems but requires further improvements and revisions for more geometrically complex structures.

Chapter 8

Summary and Discussion of Future Work

The purpose of this research was to investigate a class of versatile numerical methods that are capable of providing accurate solutions to general EM field problems without placing restrictions on the composition or geometric configuration of the simulation space. Following a comprehensive literature review, a class of time domain CEM techniques, namely the FVM, was selected as the method of choice. Thus, a time-domain general purpose EM solver was developed, based on a generalised coordinate system and the LW formulation of the FVTD scheme. This EM solver was shown to be capable of modelling a broad range of EM problems defined via rectangular and/or non rectangular geometries in any given simulation environment. In addition, new models for lossy media, lumped elements, and lumped sources were derived and implemented in order to improve and complement the original formulation of the FVTD method. The performance of the 3D-FVTD computational engine was then evaluated and compared to other time domain CEM methods (where possible) for a number of benchmark EM problems involving various

types of geometries. This process was necessary to validate the developed EM engine, as well as to identify the strengths and weaknesses of the developed FVTD EM simulator.

8.1 A Summary of the Presented Work

A brief summary of the contribution of this thesis is as follows:

- A review of some of the more popular differential equation-based numerical methods, such as various types of FDTD, TLM, TD-FEM, and FVTD, was completed where each technique was evaluated for its ability to model complex and curved geometries.

- The governing equations of an EM field problem were expressed in terms of Maxwell's equations in conservative form on a curvilinear frame using a general coordinate system. This multi-dimensional system of PDEs was represented as a succession of flux-split one-dimensional Riemann problems.

- The FVTD method was selected to solve the set of flux-split one-dimensional Riemann problems resulting from Maxwell's equations. The generalised solution to each equation of this set of scalar PDEs is given via the method of characteristics along with the modified Rankine-Hugoniot jump condition.

- A new 3D-FVTD scheme for lossy media was developed using a fully windward algorithm which was derived from a directional-biased upwind LW flux split Riemann solver. The flux difference terms of this algorithm were defined with respect to the numerical fluxes at cell interfaces as well as several types of boundary conditions (*i.e.* PEC, PMC, ABC, and periodic BCs).

- Expressions for distributed lumped elements and lumped sources were derived for a general coordinate system and were validated for the case of a coaxial cable. These expressions are not only coordinate independent, but are also independent of the numerical method used for solving Maxwell's equations.

- The accuracy of the newly derived LW-FVTD algorithm was investigated for both modelling material properties (permittivity and conductivity) and geometrically complex objects (twisted waveguide). The performance of the characteristic ABCs (used in 3D-FVTD engine) for several uniform and non-uniform grids was also evaluated and compared to the FDTD's PML-ABCs.

- The TM cutoff frequencies of a coaxial waveguide and the resonant frequencies of a partially loaded cavity were computed using the 3D-FVTD engine, and the results agreed well with semi-analytical solutions, measurements, or other numerical solutions. In addition, a complete analysis of a wide band SMA-air coaxial transformer was performed and the results agreed well with theory.

8.2 Future Work

During the course of the research, development, implementation, and validation of the LW version of 3D-FVTD EM simulator, two main weaknesses of this CEM tool were identified. The first involved the dissipative nature of the LW-FVTD algorithm, while the second (although not a weakness per se) was due to the original choice of using structured grids which (to a certain degree) limited the level of geometric complexity of the problems that can be solved using the 3D-FVTD engine. Both of these shortcomings can be remedied via the following research plan.

8.2.1 Reducing Dissipative Errors

The dissipative nature of the LW-FVTD method has been well documented [10, 46, 94, 150]. It was shown that the LW version of the FVTD method is unable to accurately solve problems that contain sharp metallic edges which generate rapid spatial variations of the field distribution (see MSDRA example of **Section 7.4**). Recently, several numerical methods with dissipation and dispersion characteristics superior to the LW-FVTD technique have been introduced to supersede the LW version of the FVTD method [46, 77, 91]. One of the most popular methods is the Runge-Kutta family of PDE solvers [26]. Despite the additional memory and computational effort that is associated with this multi-stage technique, its higher order of accuracy (both in space and time) and low and tunable [166] dissipation and dispersion characteristics have made the RK scheme the method of choice for CFD and CEM researchers [158]. Hence, the next step in FVTD research should involve the investigation of the RK family of PDE solvers and their formulation and application to the FVTD method. This research work was recently initiated by the author and is currently under way.

8.2.2 Unstructured Grids

The GTEM cell example of **Section 7.5.1** clearly demonstrated the challenges that one would encounter when modelling a large and very complex EM problem using a structured grid. Although in most cases structured grids are capable of meshing very complex problems, it is more practical (both in terms of the accuracy of modelling and reduced computational resources) to use unstructured grids for griding very complex EM problems. Several formulations of unstructured-grid FVTD methods have been proposed in the literature [46, 159, 167]. These references provide an excellent starting point for the

further investigation and formulation of an unstructured-grid FVTD scheme.

8.3 Fast FVTD Engines

The ever-increasing computational demand of very complex EM scattering and field problems has been partially offset by the advent of massively parallel computer systems. However, most traditional computer programming techniques (*i.e.* vector programming) do not take advantage of the multiple-processing capabilities of these new computers [159]. Thus, any CEM tool must be optimized (distributed) for a specific computer architecture in order to minimize the computation time [46]. Although at first glance this type of research appears to be an exercise in computer programming, one cannot lose sight of its importance; a well optimized CEM simulator may reduce the required computation time from days or weeks to a matter of hours, therefore, removing one of the obstacles in the simulation of practical problems. Hence, further research in the area of code optimization and the development of fast FVTD engines is strongly recommended.

Appendix A

The Finite Difference Method

Over the years, many books and articles have been devoted to the topic of algorithms that could be used in approximating and solving systems of PDEs. The majority of these methods (often referred to as FDMs) are derived from Taylor Series Expansion (TSE). In FDMs, the solution domain is subdivided into discrete points, and information between points is provided using a truncated TSE [4]. The following sections outline the FDM and the terminology and notation associated with it; in addition, some of the commonly used formulations and approximations are also included.

A.1 Taylor Series Expansions

The Taylor series expansion of an analytic function, $\bar{u}(x)$, at the point $x = a$ is [39]:

$$\bar{u}(x) = \sum_{m=0}^{\infty} \frac{(x-a)^m}{m!} \left[\frac{\partial^m \bar{u}}{\partial x^m} \right]_a . \tag{A.1}$$

The first step in developing a finite difference algorithm is to represent a continuous

function, $\bar{u}(x)$, and its variable in terms of a discrete function, $u(i\Delta x) = u_i$, evaluated at discrete grid points, $x = i\Delta x$. Thus, the Taylor expansion of a discrete function at various points is given by:

$$u(i\Delta x + \Delta x) = u_{i+1} = \sum_{m=0}^{\infty} \frac{\Delta x^m}{m!}\left[\frac{\partial^m \bar{u}}{\partial x^m}\right]_i, \tag{A.2}$$

$$u(i\Delta x - \Delta x) = u_{i-1} = \sum_{m=0}^{\infty} \frac{(-\Delta x)^m}{m!}\left[\frac{\partial^m \bar{u}}{\partial x^m}\right]_i, \tag{A.3}$$

where upon expansion, the following infinite series emerge:

$$u_{i+1} = \bar{u}_i + (\Delta x)(\bar{u}_x)_i + \left(\frac{\Delta x^2}{2!}\right)(\bar{u}_{xx})_i + \left(\frac{\Delta x^3}{3!}\right)(\bar{u}_{xxx})_i + \ldots \tag{A.4}$$

$$u_{i-1} = \bar{u}_i - (\Delta x)(\bar{u}_x)_i + \left(\frac{\Delta x^2}{2!}\right)(\bar{u}_{xx})_i - \left(\frac{\Delta x^3}{3!}\right)(\bar{u}_{xxx})_i + \ldots \tag{A.5}$$

The first derivative of a function (denoted as $\bar{u}_x$) is approximated by truncating the higher order terms of the series (*i.e.* terms with Δx^2 or higher) and solving for the derivative term (while substituting for the discrete value of the function); that is,

$$(\bar{u}_x)_i = \frac{u_{i+1} - u_i}{\Delta x} + O(\Delta x), \tag{A.6}$$

$$(\bar{u}_x)_i = \frac{u_i - u_{i-1}}{\Delta x} + O(\Delta x). \tag{A.7}$$

The above expressions are referred to as *forward* (A.6) and *backward* (A.7) difference approximations of the first order derivative of u. They are said to be *first order accurate* ($O(\Delta x)$) since the truncation error is no larger than (Δx). Hence, the accuracy of the estimated solution can be increased by either using algorithms with a higher order of accuracy or by utilizing a finer mesh [40].

A.2 Finite Difference Expressions

There are three classes of finite difference expressions for approximating differential equations. In *central difference* approximation, grid points to both the left and right of the point of differentiation are required. This method has superior accuracy to both backward difference approximation (that requires only points to the left of i) and forward difference approximation (that uses only points to the right of i). The following sections include a summary of some of the three classes of difference approximations that have been used in this thesis. A full derivation of these expressions is presented in [41].

A.2.1 Central Difference Expressions

A.2.1.1 Expressions with Errors $O(\Delta x)^2$

$$(u_x)_i = \frac{u_{i+1} - u_{i-1}}{2\Delta x} \tag{A.8}$$

$$(u_{xx})_i = \frac{u_{i+1} - 2u_i + u_{i-1}}{\Delta x^2} \tag{A.9}$$

A.2.1.2 Expression with Errors $O(\Delta x)^4$

$$(u_x)_i = \frac{-u_{i+2} + 8u_{i+1} - 8u_{i-1} + u_{i-2}}{12\Delta x} \tag{A.10}$$

A.2.2 Forward Difference Expressions

A.2.2.1 Expressions with Errors $O(\Delta x)$

$$(u_x)_i = \frac{u_{i+1} - u_i}{\Delta x} \tag{A.11}$$

$$(u_{xx})_i = \frac{u_{i+2} - 2u_{i+1} + u_i}{\Delta x^2} \tag{A.12}$$

A.2.2.2 Expressions with Errors $O(\Delta x)^2$

$$(u_x)_i = \frac{-u_{i+2} + 4u_{i+1} - 3u_i}{2\Delta x} \tag{A.13}$$

$$(u_{xx})_i = \frac{-u_{i+3} + 4u_{i+2} - 5u_{i+1} + 2u_i}{\Delta x^2} \tag{A.14}$$

A.2.3 Backward Difference Expressions

A.2.3.1 Expressions with Errors $O(\Delta x)$

$$(u_x)_i = \frac{u_i - u_{i-1}}{\Delta x} \tag{A.15}$$

$$(u_{xx})_i = \frac{u_i - 2u_{i-1} + u_{i-2}}{\Delta x^2} \tag{A.16}$$

A.2.3.2 Expressions with Errors $O(\Delta x)^2$

$$(u_x)_i = \frac{3u_i - 4u_{i-1} + u_{i-2}}{2\Delta x} \tag{A.17}$$

$$(u_{xx})_i = \frac{2u_i - 5u_{i-1} + 4u_{i-2} - u_{i-3}}{\Delta x^2} \tag{A.18}$$

A.3 Finite Difference Operators

In order to represent the aforementioned finite difference approximations in a concise format and to avoid lengthy and cumbersome algorithms, a set of difference operators has been developed [10]. **Table A.1** summarizes the standard difference operators that have been used in this thesis.

Table A.1. Standard finite difference operators

Operator	$O(\Delta x)$	Symbol	Operation
Forward Difference	1st	Δ_x	$\Delta_x u_i = u_{i+1} - u_i$
Forward Difference	1st	Δ_x^2	$\Delta_x^2 u_i = u_{i+2} - 2u_{i+1} + u_i$
Forward Difference	2nd	$\bar{\Delta}_x$	$\bar{\Delta}_x u_i = -u_{i+2} + 4u_{i+1} - 3u_i$
Forward Difference	2nd	$\bar{\Delta}_x^2$	$\bar{\Delta}_x^2 u_i = -u_{i+3} + 4u_{i+2} - 5u_{i+1} + 2u_i$
Backward Difference	1st	∇_x	$\nabla_x u_i = u_i - u_{i-1}$
Backward Difference	1st	∇_x^2	$\nabla_x^2 u_i = u_i - 2u_{i-1} + u_{i-2}$
Backward Difference	2nd	$\bar{\nabla}_x$	$\bar{\nabla}_x u_i = 3u_i - 4u_{i-1} + u_{i-2}$
Backward Difference	2nd	$\bar{\nabla}_x^2$	$\bar{\nabla}_x^2 u_i = 2u_i - 5u_{i-1} + 4u_{i-2} - u_{i-3}$
Central Difference	2nd	δ_x	$\delta_x u_i = u_{i+1} - u_{i-1}$
Central Difference	2nd	δ_x^2	$\delta_x^2 u_i = u_{i+1} - 2u_i + u_{i-1}$
Central Difference	4th	$\bar{\delta}_x$	$\bar{\delta}_x u_i = -u_{i+2} + 8u_{i+1} - 8u_{i-1} + u_{i-2}$
Averaging Operation	--	ϑ	$\vartheta u(i+1, i) = (u_{i+1} + u_i)/2$

Appendix B

General Coordinate Systems

The theory of general (curvilinear) coordinate systems is described through the application of differential calculus which is generally known as ***differential geometry***. The purpose of this appendix is to outline some of the general concepts and to introduce some useful terminology and formulae associated with curvilinear coordinate systems. A complete discussion of these topics is included in [80, 81]. The following is a summary of the discussions that appear in these references.

B.1 General Coordinate Systems: Definitions

In a given region, the following functions:

$$u^i = f_i(x^1, x^2, x^3), \qquad i = 1, 2, 3 \tag{B.1}$$

are defined to be independent, continuous, and single-valued in the (x^1, x^2, x^3) coordinate system. There also exist equally independent, continuous, and single-valued functions which represent the solution to (B.1) in terms of the original coordinate system, *i.e.*:

$$x^i = \varphi_i(u^1, u^2, u^3), \qquad i = 1, 2, 3. \tag{B.2}$$

In general, both f_i and φ_i are continuously differentiable functions (within a region that does not contain singular points) that define transformation from one coordinate system to another. For example, point $\boldsymbol{P}(x^1, x^2, x^3)$ is associated with point $\boldsymbol{P'}(u^1, u^2, u^3)$ using the transformation defined in (B.1). The new coordinate system, u^i, is referred to as a ***general*** or ***curvilinear*** coordinate system.

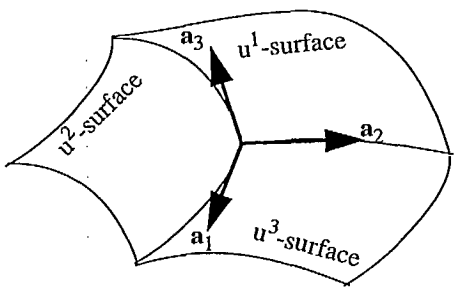

Figure B.1. The parallelepiped defined by base vectors of a curvilinear coordinate system

Consider point $\boldsymbol{P'}$ in a given region where three ***coordinate surfaces*** (see **Figure B.1**)

$$u^i = constant, \qquad i = 1, 2, 3, \tag{B.3}$$

pass through it. Any two of these coordinate surfaces intersect in a curve (commonly known as a ***coordinate curve***). Along any of the three coordinate curves, ***u^i-curve,*** two coordinates are variable, while one is constant. These coordinate curves are labelled by the constant coordinate. If a position vector, $\boldsymbol{r}$, is defined as a function of the curvilinear coordinates, u^1, u^2, u^3,

$$\boldsymbol{r} = \boldsymbol{r}(u^1, u^2, u^3), \tag{B.4}$$

small displacement changes along the coordinate curves (and tangential to the respective coordinate curves) represent differential changes in $\boldsymbol{r}$; that is,

$$d\boldsymbol{r} = \frac{\partial \boldsymbol{r}}{\partial u^1} du^1 + \frac{\partial \boldsymbol{r}}{\partial u^2} du^2 + \frac{\partial \boldsymbol{r}}{\partial u^3} du^3 . \tag{B.5}$$

Hence, ***unitary vectors***, which form the base vectors for a curvilinear coordinated system, are defined as follows:

$$\boldsymbol{a}_1 = \frac{\partial \boldsymbol{r}}{\partial u^1}, \qquad \boldsymbol{a}_2 = \frac{\partial \boldsymbol{r}}{\partial u^2}, \qquad \boldsymbol{a}_3 = \frac{\partial \boldsymbol{r}}{\partial u^3}. \tag{B.6}$$

*

Therefore, the differential changes in the position vector, as given in (B.5), can be re-written in terms of the above base vectors,

$$d\boldsymbol{r} = \boldsymbol{a}_1 du^1 + \boldsymbol{a}_2 du^2 + \boldsymbol{a}_3 du^3 . \tag{B.7}$$

The aforementioned base vectors, $(\boldsymbol{a}_1, \boldsymbol{a}_2, \boldsymbol{a}_3)$, form a parallelepiped in the curvilinear coordinate system, with its volume computed by:

$$V = \boldsymbol{a}_1 \cdot (\boldsymbol{a}_2 \times \boldsymbol{a}_3) = \boldsymbol{a}_2 \cdot (\boldsymbol{a}_3 \times \boldsymbol{a}_1) = \boldsymbol{a}_3 \cdot (\boldsymbol{a}_1 \times \boldsymbol{a}_2) \tag{B.8}$$

After algebraic manipulation of the above expression and the introduction of a new triplet, $(\boldsymbol{a}^1, \boldsymbol{a}^2, \boldsymbol{a}^3)$, a new ***reciprocal*** system is introduced whose ***reciprocal unitary vectors*** are:

$$\boldsymbol{a}^1 = \frac{1}{V}(\boldsymbol{a}_2 \times \boldsymbol{a}_3), \qquad \boldsymbol{a}^2 = \frac{1}{V}(\boldsymbol{a}_3 \times \boldsymbol{a}_1), \qquad \boldsymbol{a}^3 = \frac{1}{V}(\boldsymbol{a}_1 \times \boldsymbol{a}_2). \tag{B.9}$$

The base vectors of this reciprocal system are also perpendicular to the respective coordinate surfaces defined by the pairs $(\boldsymbol{a}_2, \boldsymbol{a}_3)$, $(\boldsymbol{a}_3, \boldsymbol{a}_1)$, and $(\boldsymbol{a}_1, \boldsymbol{a}_2)$, as were their counterparts in the general coordinate system. Conversely, the unitary vectors can be denoted in terms of the reciprocal unitary vectors given in the following expressions:

$$\boldsymbol{a}_1 = \frac{1}{V}(\boldsymbol{a}^2 \times \boldsymbol{a}^3), \qquad \boldsymbol{a}_2 = \frac{1}{V}(\boldsymbol{a}^3 \times \boldsymbol{a}^1), \qquad \boldsymbol{a}_3 = \frac{1}{V}(\boldsymbol{a}^1 \times \boldsymbol{a}^2). \tag{B.10}$$

---

* Although unitary vectors form base vectors for a general coordinate system, their length, as a rule, is not unity! Their length and dimensions will be determined by the nature of the curvilinear coordinate system.

B.2 Differential Vectors and General Coordinate Systems

In the last section, it was shown that any point in a general coordinate system may be represented/associated with either a unitary vector or its corresponding reciprocal unitary vectors. Similarly, a differential change in a position, $d\boldsymbol{r}$, can also be represented in terms of reciprocal unitary vectors:

$$d\boldsymbol{r} = \boldsymbol{a}^1 du_1 + \boldsymbol{a}^2 du_2 + \boldsymbol{a}^3 du_3 \tag{B.11}$$

where du_1, du_2, du_3 are differentials defined in the direction of the base vectors of the reciprocal coordinate system. The two definitions of the differential, $d\boldsymbol{r}$, equations, (B.7) and (B.11), must be equivalent; that is:

$$d\boldsymbol{r} = \sum_{i=1}^{3} \boldsymbol{a}^i du_i = \sum_{j=1}^{3} \boldsymbol{a}^j du_j \tag{B.12}$$

In order to manipulate the above expression to a desirable form, consider the following properties of the scalar product of the unitary and reciprocal vectors. Upon close examination of all of the possible scalar products of a coordinate system with base vectors of its reciprocal system, the following expression is deduced:*

$$\boldsymbol{a}^i \cdot \boldsymbol{a}_j = \delta_{ij} = \begin{cases} 0 & (i = j) \\ 1 & (i \neq j) \end{cases}, \qquad i = 1, 2, 3, \qquad j = 1, 2, 3 \tag{B.13}$$

where δ_{ij} is generally referred to as the ***Kronecker delta***. One of the implications of the above relationship is that the unitary vectors of the base system, $\boldsymbol{a}^i$, and their counterparts in the reciprocal system, $\boldsymbol{a}_i$, are orthogonal. In addition, the differential components of vector, $d\boldsymbol{r}$, can be expressed in terms of unitary vectors through successive scalar multiplications of (B.12) by $\boldsymbol{a}^i$ and $\boldsymbol{a}_j$ application of the condition stated by (B.13):

$$du_j = \sum_{i=1}^{3} a_i \cdot a_j du^i, \qquad du^i = \sum_{j=1}^{3} a^j \cdot a^i du_j, \tag{B.14}$$

The following standard notation is used to replace the scalar product of unitary and reciprocal unitary vectors; that is:

$$g_{ij} = g_{ji} = a_i \cdot a_j, \qquad g^{ij} = g^{ji} = a^j \cdot a^i, \tag{B.15}$$

and the differential components of dr are rewritten as:

$$du_j = \sum_{i=1}^{3} g_{ij} du^i, \qquad du^i = \sum_{j=1}^{3} g^{ij} du_j. \tag{B.16}$$

In addition to differential vectors, fixed vectors can also be represented using the above notations. For example, a fixed vector, $\boldsymbol{F}$, defined at the point, $\boldsymbol{P}$, can be written in terms of components in either a unitary system or a reciprocal system:

$$F = \sum_{i=1}^{3} f^i a_i = \sum_{j=1}^{3} f_j a^j. \tag{B.17}$$

Furthermore, similar methods of the scalar multiplication of unitary vectors and the

---

* **Partial Proof:**

Consider the scalar product: $a^1 \cdot a_1$ where the definition of a_1 is substituted from (B.10):

$$a^1 \cdot a_1 = a^1 \cdot \left[\frac{1}{V}(a^2 \times a^3)\right].$$

After rearranging the above and using the definition of the volume of a parallelepiped formed by base vectors, the above is evaluated as:

$$a^1 \cdot a_1 = \frac{1}{V}[a^1 \cdot (a^2 \times a^3)] = \frac{1}{V}(V) = 1.$$

Next, the following scalar product is evaluated as per the definition of a_3 provided by (B.10):

$$a^1 \cdot a_3 = a^1 \cdot \left[\frac{1}{V}(a^1 \times a^2)\right] = \frac{1}{V}[Va^1 \cdot (a^1 \times a^3)]$$

and by using a vector identity $A \cdot B \times C = A \times B \cdot C$:

$$a^1 \cdot a_3 = \frac{1}{V}[(Va^1 \times a^1) \cdot a^2] = 0.$$

Similar results can be obtained by the evaluation of the remainder of the scalar products of the unitary and reciprocal unitary vectors.

application of condition (B.13) result in:

$$f_j = \sum_{i=1}^{3} g_{ij} f^i, \qquad f^i = \sum_{j=1}^{3} g^{ij} f_j. \tag{B.18}$$

Still, further scalar multiplications of (B.17) provide:

$$f^i = \boldsymbol{F} \cdot \boldsymbol{a}^i, \qquad f_j = \boldsymbol{F} \cdot \boldsymbol{a}_j, \tag{B.19}$$

which can be substituted in (B.17) to express the fixed vector, $\boldsymbol{F}$, in terms of its unitary and reciprocal vectors; that is:

$$\boldsymbol{F} = \sum_{i=1}^{3} (\boldsymbol{F} \cdot \boldsymbol{a}^i)\boldsymbol{a}_i = \sum_{j=1}^{3} (\boldsymbol{F} \cdot \boldsymbol{a}_j)\boldsymbol{a}^j. \tag{B.20}$$

Finally, it is important to recognize the relationship between unitary vectors and ***unit*** vectors with which most readers are more familiar. As was previously stated, the nature of the coordinate system determines the length and dimension of unitary vectors. A unit vector, $\boldsymbol{i}_i$, is defined to be of length, unity, and has the same direction as its respective unitary vector, $\boldsymbol{a}_i$; hence unit vectors can be expressed in terms of unitary vectors:

$$\boldsymbol{i}_1 = \frac{\boldsymbol{a}_1}{\sqrt{\boldsymbol{a}_1 \cdot \boldsymbol{a}_1}} = \frac{\boldsymbol{a}_1}{\sqrt{g_{11}}}, \qquad \boldsymbol{i}_2 = \frac{\boldsymbol{a}_2}{\sqrt{\boldsymbol{a}_2 \cdot \boldsymbol{a}_2}} = \frac{\boldsymbol{a}_2}{\sqrt{g_{22}}}, \qquad \boldsymbol{i}_3 = \frac{\boldsymbol{a}_3}{\sqrt{\boldsymbol{a}_3 \cdot \boldsymbol{a}_3}} = \frac{\boldsymbol{a}_3}{\sqrt{g_{33}}}, \tag{B.21}$$

and vector, $\boldsymbol{F}$, can be resolved into its unit vector components:

$$\boldsymbol{F} = F_1 \boldsymbol{i}_1 + F_2 \boldsymbol{i}_2 + F_3 \boldsymbol{i}_3. \tag{B.22}$$

B.3 Vector Calculus in General Coordinate Systems

A line element, dl, is the magnitude of a displacement vector, $d\boldsymbol{r}$. As was noted earlier, $d\boldsymbol{r}$ expresses an infinitesimal displacement between a pair of points, $\boldsymbol{P}(u^1, u^2, u^3)$ and $\boldsymbol{P}'(u^1 + du^1, u^2 + du^2, u^3 + du^3)$, in terms of differentials, du^1, du^2, du^3. Hence

$$dl^2 = d\boldsymbol{r} \cdot d\boldsymbol{r} = \sum_{i=1}^{3}\sum_{j=1}^{3} \boldsymbol{a}_i \cdot \boldsymbol{a}_j du^i du^j = \sum_{i=1}^{3}\sum_{j=1}^{3} \boldsymbol{a}^i \cdot \boldsymbol{a}^j du_i du_j, \tag{B.23}$$

which can be simplified to:

$$dl^2 = \sum_{i=1}^{3}\sum_{j=1}^{3} g_{ij} du^i du^j = \sum_{i=1}^{3}\sum_{j=1}^{3} g^{ij} du_i du_j. \tag{B.24}$$

In the above definition of the length of a line element, g_{ij} and g^{ij} are coefficients of differential quadratic forms in either a unitary or a reciprocal system. This differential quadratic form is often referred to as ***first fundamental form***, and for a curvilinear coordinate system is given by:

$$\begin{aligned} dl^2 &= \sum_{i=1}^{3}\sum_{j=1}^{3} g_{ij} du^i du^j \\ &= g_{11} du^1 du^1 + g_{12} du^1 du^2 + g_{13} du^1 du^3 \\ &+ g_{21} du^2 du^1 + g_{22} du^2 du^2 + g_{23} du^2 du^3 \\ &+ g_{31} du^3 du^1 + g_{32} du^2 du^3 + g_{33} du^3 du^3 \end{aligned} \tag{B.25}$$

Following the notation of equation (B.15), and after some algebraic manipulation:

$$dl^2 = g_{11}(du^1)^2 + g_{22}(du^2)^2 + g_{33}(du^3)^2 + 2g_{12} du^1 du^2 + 2g_{13} du^1 du^3 + 2g_{23} du^2 du^3. \tag{B.26}$$

Although equation (B.26) provides the most general expression for a line element in a curvilinear system, it is often necessary to compute line, surface, and volume elements from a definition where the differential vector elements represent infinitesimal displacement along a given coordinate curve. Equation (B.12) may be utilized to formulate displacement vectors along the u^1-, u^2-, and u^3-curves, where in each case, there is a differential change in $\boldsymbol{r}$ along the u^i direction, which means the only non-zero

differential is du^i; that is:

$$dr_1 = a_1 du^1, \qquad dr_2 = a_2 du^2, \qquad dr_3 = a_3 du^3. \tag{B.27}$$

The respective line elements are given by the magnitude of the above displacement vectors or by equation (B.24):

$$dl_1 = \sqrt{g_{11}} du^1, \qquad dl_2 = \sqrt{g_{22}} du^2, \qquad dl_3 = \sqrt{g_{33}} du^3. \tag{B.28}$$

A surface element is commonly characterized by the area on an infinitesimal parallelogram on a given surface, say the u^1-surface, defined by two intersecting curves (In this case, the u^2- and u^3-curves.). Mathematically, the surface element of the aforementioned parallelogram is determined by the magnitude of the vector product of its intersecting sides; that is:

$$ds_1 = |dr_2 \times dr_3| = |a_2 \times a_3| du^2 du^3 = \sqrt{(a_2 \times a_3) \cdot (a_2 \times a_3)} du^2 du^3. \tag{B.29}$$

It is evaluated using the vector identity:

$$(A \times B) \cdot (C \times D) = (A \cdot C)(B \cdot D) - (A \cdot D)(B \cdot C) \tag{B.30}$$

where it is rewritten as:

$$ds_1 = \sqrt{(a_2 \cdot a_2)(a_3 \cdot a_3) - (a_2 \cdot a_3)(a_3 \cdot a_2)} du^2 du^3, \tag{B.31}$$

and following the utilization of the notation introduced in (B.16),

$$ds_1 = \sqrt{g_{22}} du^2 du^3. \tag{B.32}$$

An analogous procedure can be employed to compute the surface elements in the u^2-surface as:

$$ds_2 = \sqrt{g_{11} g_{33} - g_{13}^2} du^1 du^3 \tag{B.33}$$

and the surface elements in the u^3-surface as:

$$ds_3 = \sqrt{g_{11}g_{22} - g_{12}^2}\, du^1 du^2. \tag{B.34}$$

A volume element is defined by the three differential vectors of (B.27) which form a parallelepiped whose volume is:

$$dv = dr_1 \cdot dr_2 \times dr_3 = (a_1 \cdot a_2 \times a_3) du^1 du^2 du^3. \tag{B.35}$$

After algebraic and vector manipulation of the above equation,* the expression for a volume element in a curvilinear coordinate system is given by:

$$dv = \sqrt{g}\, du^1 du^2 du^3 \tag{B.36}$$

where g is the determinant of the following matrix:

$$g = \begin{vmatrix} g_{11} & g_{12} & g_{13} \\ g_{21} & g_{22} & g_{23} \\ g_{31} & g_{32} & g_{33} \end{vmatrix}. \tag{B.37}$$

It has already become clear that the coefficients, g_{ij}, play an important role in defining and characterizing the properties of a general coordinate system. In fact these coefficients,

---

* In equation (B.20) set $F = a_2 \times a_3$; hence:

$$a_1 \cdot (a_2 \times a_3) = a_1 \cdot \sum_{i=1}^{3} ((a_2 \times a_3) \cdot a^i) a_i$$
$$= a_1 \cdot [((a_2 \times a_3) \cdot a^1) a_1 + ((a_2 \times a_3) \cdot a^2) a_2 + ((a_2 \times a_3) \cdot a^3) a_3]$$

The definition of the reciprocal unitary vectors of (B.10) allows further development of the former step,

$$a_1 \cdot (a_2 \times a_3) = a_1 \cdot [((a_2 \times a_3) \cdot (a_2 \times a_3)) a_1 + ((a_2 \times a_3) \cdot (a_3 \times a_1)) a_2 + ((a_2 \times a_3) \cdot (a_1 \times a_2)) a_3]$$

where the vector identity of (B.30) is applied to expand and then simplify the previous equation into:

$$a_1 \cdot (a_2 \times a_3) = a_1 \cdot a_1 [(a_2 \cdot a_2)(a_3 \cdot a_3) - (a_2 \cdot a_3)(a_3 \cdot a_2)]$$
$$+ a_1 \cdot a_2 [(a_2 \cdot a_3)(a_3 \cdot a_1) - (a_2 \cdot a_1)(a_3 \cdot a_3)]$$
$$+ a_1 \cdot a_3 [(a_2 \cdot a_1)(a_3 \cdot a_2) - (a_2 \cdot a_2)(a_3 \cdot a_1)]$$

Finally, with the aid of the definition of scalar products of unitary vectors, as noted in(B.16), the above expression is written as:

$$a_1 \cdot (a_2 \times a_3) = g_{11}(g_{22}g_{33} - g_{23}g_{32}) + g_{12}(g_{23}g_{31} - g_{21}g_{33}) + g_{13}(g_{21}g_{32} - g_{22}g_{31})$$

which might be recognized as the determinant of a 3×3 matrix of the respective g_{ij} elements.

generally known as ***metrical coefficients***, contain all the information required to represent the differential of one coordinate system in terms of the differentials in another coordinate system. Hence, determining the values of the metrical coefficients is crucial in computations involving general coordinate systems. Consider a rectangular coordinate system, (x^1, x^2, x^3) which is represented in terms of curvilinear coordinates (u^1, u^2, u^3) and the following functions/transformations:

$$x^1 = x^1(u^1, u^2, u^3), \qquad x^2 = x^2(u^1, u^2, u^3), \qquad x^3 = x^3(u^1, u^2, u^3). \tag{B.38}$$

After differentiating the above equations, the following linear relationships between the differentials of the rectangular coordinate system and the differentials of the general coordinates emerge.

$$\begin{aligned} dx^1 &= \frac{\partial x^1}{\partial u^1}du^1 + \frac{\partial x^1}{\partial u^2}du^2 + \frac{\partial x^1}{\partial u^3}du^3 \\ dx^2 &= \frac{\partial x^2}{\partial u^1}du^1 + \frac{\partial x^2}{\partial u^2}du^2 + \frac{\partial x^2}{\partial u^3}du^3 \\ dx^3 &= \frac{\partial x^3}{\partial u^1}du^1 + \frac{\partial x^3}{\partial u^2}du^2 + \frac{\partial x^3}{\partial u^3}du^3 \end{aligned} \tag{B.39}$$

Next, the first fundamental form of the rectangular coordinates is given by equation (B.25) where, due to the orthogonality of the unitary vectors, it is reduced to:

$$dl^2 = \sum_{i=1}^{3}\sum_{j=1}^{3} g_{ij}dx^i dx^j = g_{11}(dx^1)^2 + g_{22}(dx^2)^2 + g_{33}(dx^3)^2. \tag{B.40}$$

Moreover, by definition, the unitary vectors of the rectangular coordinate system (*i.e.* a_x, a_y, a_z) are of unit length, and, therefore, all the metrical coefficients will have a magnitude of unity as well.

$$dl^2 = \sum_{k=1}^{3} (dx^k)^2 = (dx^1)^2 + (dx^2)^2 + (dx^3)^2 \tag{B.41}$$

A comparison of the first fundamental form of the rectangular coordinate system and the curvilinear coordinate system gives:

$$dl^2 = \sum_{i=1}^{3}\sum_{j=1}^{3} g_{ij} du^i du^j = \sum_{k=1}^{3} (dx^k)^2 \tag{B.42}$$

where the expanded form of the above summation is as follows:

$$\begin{aligned} dl^2 &= g_{11}(du^1)^2 + g_{22}(du^2)^2 + g_{33}(du^3)^2 + 2g_{12}du^1du^2 + 2g_{13}du^1du^3 + 2g_{23}du^2du^3 \\ &= (dx^1)^2 + (dx^2)^2 + (dx^3)^2 \end{aligned} \tag{B.43}$$

Finally, after substituting for the value of the rectangular coordinate system, dx^1, dx^2, dx^3, from (B.39), and solving for the like terms of the above equation, the expression for the metrical coefficients is given by:

$$g_{ij} = \frac{\partial x^1}{\partial u^i}\frac{\partial x^1}{\partial u^j} + \frac{\partial x^2}{\partial u^i}\frac{\partial x^2}{\partial u^j} + \frac{\partial x^3}{\partial u^i}\frac{\partial x^3}{\partial u^j} \qquad i, j = 1, 2, 3. \tag{B.44}$$

In the context of this document, $x^1 = x$, $x^2 = y$, $x^3 = z$; hence:

$$g_{ij} = \frac{\partial x}{\partial u^i}\frac{\partial x}{\partial u^j} + \frac{\partial y}{\partial u^i}\frac{\partial y}{\partial u^j} + \frac{\partial z}{\partial u^i}\frac{\partial z}{\partial u^j} \qquad i, j = 1, 2, 3, \tag{B.45}$$

and after substituting for $u^1 = \xi$, $u^2 = \eta$, and $u^3 = \zeta$, g becomes:

$$g = \left\| \begin{bmatrix} g_{\xi\xi} & g_{\xi\eta} & g_{\xi\zeta} \\ g_{\eta\xi} & g_{\eta\eta} & g_{\eta\zeta} \\ g_{\zeta\xi} & g_{\zeta\eta} & g_{\zeta\zeta} \end{bmatrix} \right\|. \tag{B.46}$$

B.4 Vector Coordinate Transformation

The following procedure outlines the general approach to vector coordinate transformation. Consider the vector field, A, in a general coordinate system where it is represented in terms of the base (Cartesian) coordinate system using the relationship

$$A = \begin{bmatrix} A_\xi a_\xi \\ A_\eta a_\eta \\ A_\zeta a_\zeta \end{bmatrix} = J \begin{bmatrix} A_x a_x \\ A_y a_y \\ A_z a_z \end{bmatrix} = \begin{bmatrix} \xi_x & \xi_y & \xi_z \\ \eta_x & \eta_y & \eta_z \\ \zeta_x & \zeta_y & \zeta_z \end{bmatrix} \begin{bmatrix} A_x a_x \\ A_y a_y \\ A_z a_z \end{bmatrix}. \tag{B.47}$$

However, the length and dimension of unitary vectors, (a_ξ, a_η, a_ζ), of a general coordinate system are determined by the nature of the coordinate system. A set of (curvilinear coordinate) unit vectors derived from unitary vectors was given in (B.21); thus, the unit vectors of a general coordinate system are given by:

$$i_\xi = \frac{a_\xi}{\sqrt{g_{\xi\xi}}}, \qquad i_\eta = \frac{a_\eta}{\sqrt{g_{\eta\eta}}}, \qquad i_\zeta = \frac{a_\zeta}{\sqrt{g_{\zeta\zeta}}}, \tag{B.48}$$

where the above metrical coefficients are evaluated using (B.41):

$$\begin{aligned} g_{\xi\xi} &= x_\xi x_\xi + y_\xi y_\xi + z_\xi z_\xi \\ g_{\eta\eta} &= x_\eta x_\eta + y_\eta y_\eta + z_\eta z_\eta \\ g_{\zeta\zeta} &= x_\zeta x_\zeta + y_\zeta y_\zeta + z_\zeta z_\zeta \end{aligned} \tag{B.49}$$

Hence, the components of A in the general coordinate system are represented in terms of their components in the Cartesian coordinate system; that is:

$$\begin{aligned} A &= A_\xi a_\xi + A_\eta a_\eta + A_\zeta a_\zeta \\ &= \sqrt{g_{\xi\xi}}(\xi_x A_x + \xi_y A_y + \xi_z A_z) i_\xi \\ &+ \sqrt{g_{\eta\eta}}(\eta_x A_x + \eta_y A_y + \eta_z A_z) i_\eta \\ &+ \sqrt{g_{\zeta\zeta}}(\zeta_x A_x + \zeta_y A_y + \zeta_z A_z) i_\zeta \end{aligned} \tag{B.50}$$

In order to demonstrate the applicability of the above theory of vector coordinate transformation, a cylindrical-to-Cartesian coordinate transformation is examined next [81]. Consider a vector field, A, in the cylindrical coordinate system, where the coordinate transformation is given by:

$$x = r\cos\theta, \qquad y = r\sin\theta, \qquad z = z, \tag{B.51}$$

and the inverse Jacobian of transformation is

$$\frac{1}{J} = \begin{bmatrix} x_r & x_\theta & x_z \\ y_r & y_\theta & y_z \\ z_r & z_\theta & z_z \end{bmatrix} = \begin{bmatrix} \cos\theta & -r\sin\theta & 0 \\ \sin\theta & r\cos\theta & 0 \\ 0 & 0 & 1 \end{bmatrix}. \tag{B.52}$$

Thus, the Jacobian of transformation is written as:

$$J = \begin{bmatrix} r_x & r_y & r_z \\ \theta_x & \theta_y & \theta_z \\ z_x & z_y & z_z \end{bmatrix} = \begin{bmatrix} \cos\theta & \sin\theta & 0 \\ \dfrac{\sin\theta}{-r} & \dfrac{\cos\theta}{r} & 0 \\ 0 & 0 & 1 \end{bmatrix} \text{ with } |J| = \frac{1}{r}. \tag{B.53}$$

The unitary vectors of the cylindrical coordinate system are represented in terms of the Cartesian coordinate system using the relation:

$$\begin{bmatrix} a_r \\ a_\theta \\ a_z \end{bmatrix} = \begin{bmatrix} \cos\theta & \sin\theta & 0 \\ \dfrac{\sin\theta}{-r} & \dfrac{\cos\theta}{r} & 0 \\ 0 & 0 & 1 \end{bmatrix} \begin{bmatrix} a_x \\ a_y \\ a_z \end{bmatrix}. \tag{B.54}$$

However, as discussed earlier, the length and dimension of the unitary vectors of a general coordinate system are determined by the nature of the coordinate system. Therefore, the unit vectors of a cylindrical coordinate system are given by:

$$i_r = \frac{a_r}{\sqrt{g_{rr}}}, \qquad i_\theta = \frac{a_\theta}{\sqrt{g_{\theta\theta}}}, \qquad i_z = \frac{a_z}{\sqrt{g_{zz}}}, \tag{B.55}$$

where the above metrical coefficients are evaluated by (B.49):

$$\begin{aligned} g_{rr} &= x_r x_r + y_r y_r + z_r z_r = 1 \\ g_{\theta\theta} &= x_\theta x_\theta + y_\theta y_\theta + z_\theta z_\theta = r^2 \\ g_{zz} &= x_z x_z + y_z y_z + z_z z_z = 1 \end{aligned} \tag{B.56}$$

Hence, vector A in the cylindrical system is represented in terms of its components in the Cartesian system by:

$$A(r, \theta, z) = J \begin{bmatrix} A_x \\ A_y \\ A_z \end{bmatrix} = \begin{bmatrix} cos\theta & sin\theta & 0 \\ \frac{sin\theta}{-r} & \frac{cos\theta}{r} & 0 \\ 0 & 0 & 1 \end{bmatrix} \begin{bmatrix} A_x \\ A_y \\ A_z \end{bmatrix}. \tag{B.57}$$

$$A(r, \theta, z) = (A_x cos\theta + A_y sin\theta)a_r + \left(\frac{sin\theta}{-r}A_x + \frac{cos\theta}{r}A_y\right)a_\theta + (A_z)a_z, \tag{B.58}$$

and following the substitution of unit vectors, (i_r, i_θ, i_z), for unitary vectors, (a_r, a_θ, a_z), from (B.55) and (B.56), the final expression of vector A in the cylindrical system in terms of its rectangular coordinate components becomes:

$$A(r, \theta, z) = (A_x cos\theta + A_y sin\theta)i_r + (A_y cos\theta - A_x sin\theta)i_\theta + (A_z)i_z, \tag{B.59}$$

which is identical to the one derived via geometric methods [81].

B.5 Operators in a General Coordinate System

Although any general discussion of vector calculus must include a general review of various differential operators (*i.e.* gradient, $\nabla\Phi$, divergence, $\nabla \cdot \boldsymbol{F}$, curl, $\nabla \times \boldsymbol{F}$, and Laplacian, $\nabla^2\Phi$), only the curl operator is utilized in this thesis. Thus, in the interest of

brevity, only the formulation of the curl of a vector in the curvilinear coordinate system is examined here. Excellent discussions and derivations of other operators are given in [80, 81].

The definition of the curl of a vector is often derived from the second fundamental theorem of vector analysis, *i.e.* ***Stoke's theorem***. Stoke's theorem states that ([81] page 5): "*the line integral of the vector* $\boldsymbol{F}(u^1, u^2, u^3)$ *along a closed path* C *is equal to the integral of the dot product of the curl of the vector* (function) $\boldsymbol{F}$ *with the normal to the surface* S *that has the contour* C *as its boundary.*" That is,

$$\oint_C \boldsymbol{F} \cdot d\boldsymbol{l} = \iint_S (\nabla \times \boldsymbol{F}) \cdot \boldsymbol{n} ds \tag{B.60}$$

where $d\boldsymbol{l}$ is the line element along the integral path, C, and $\boldsymbol{n}$ is a unit vector normal to the positive side of the plane containing the surface element, ds. Therefore, the curl of the vector function, $\boldsymbol{F}$, written as $\nabla \times \boldsymbol{F}$, is evaluated at the point, $\boldsymbol{P}$, using Stoke's theorem where the contour, C, is allowed to shrink to the point, P, which requires the area it encloses, *i.e.* S, to become infinitesimally small,* or

$$(\nabla \times \boldsymbol{F}) \cdot \boldsymbol{n} = \lim_{C \to 0} \frac{1}{S} \oint_C \boldsymbol{F} \cdot d\boldsymbol{l}. \tag{B.61}$$

The scalar product of the curl of $\boldsymbol{F}$ and unit normal vector, $\boldsymbol{n}$, indicates the direction of the component of the curl. Consider the surface element enclosed by C located on the u^1-surface where the path of integration is represented by a parallelogram and is also located on the u^1-surface. The path of integration is determined by the direction of an outward unit vector normal to the positive side of the plane containing the surface, S, and the right hand

* The inherent assumption of this argument is that all first derivatives of $\boldsymbol{F}$ are continuous at P, and all other points are enclosed by C.

rule, as shown in **Figure B.2.** The contribution of each side of the parallelogram to the contour integral is computed by evaluating the components of the original function, parallel to each side, at the appropriate spatial location. These components are determined using the scalar product of the vector function with infinitesimally small displacement along the coordinate curve where the respective sides are located. Hence, the components of the original function representing the sides of the parallelogram are given by $\boldsymbol{F} \cdot \boldsymbol{a}_2 du^2$ and $\boldsymbol{F} \cdot \boldsymbol{a}_3 du^3$ respectively. Therefore, the contour integral of (B.61) is written as:

$$\oint_C \boldsymbol{F} \cdot d\boldsymbol{l} = (\boldsymbol{F} \cdot \boldsymbol{a}_2 du^2)\Big|_{u^3} + (\boldsymbol{F} \cdot \boldsymbol{a}_3 du^3)\Big|_{u^2+du^2} - (\boldsymbol{F} \cdot \boldsymbol{a}_2 du^2)\Big|_{u^3+du^3} - (\boldsymbol{F} \cdot \boldsymbol{a}_3 du^3)\Big|_{u^2} \quad \text{(B.62)}$$

and then it is re-arranged to highlight the contributions of the sides along the coordinate curves, or:

$$\oint_C \boldsymbol{F} \cdot d\boldsymbol{l} = \left\{(\boldsymbol{F} \cdot \boldsymbol{a}_3 du^3)\Big|_{u^2+du^2} - (\boldsymbol{F} \cdot \boldsymbol{a}_3 du^3)\Big|_{u^2}\right\} - \left\{(\boldsymbol{F} \cdot \boldsymbol{a}_2 du^2)\Big|_{u^3+du^3} - (\boldsymbol{F} \cdot \boldsymbol{a}_2 du^2)\Big|_{u^3}\right\} \quad \text{(B.63)}$$

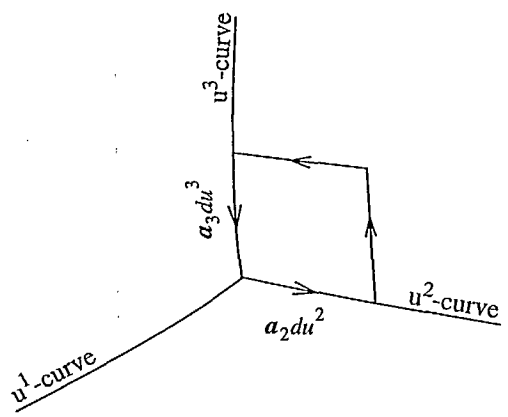

Figure B.2. Contour integral and surface element of a function located in the u^1-surface

The bracketed terms of (B.63) resemble the first two terms of the linear Taylor expansion* of the derivative of a function centred at u^2 and u^3 respectively. These terms are then

replaced with their corresponding definition from Taylor's expansion; *i.e.*

$$\oint_C \boldsymbol{F}\cdot d\boldsymbol{l} = \frac{\partial}{\partial u^2}(\boldsymbol{F}\cdot \boldsymbol{a}_3 du^3)du^2 - \frac{\partial}{\partial u^3}(\boldsymbol{F}\cdot \boldsymbol{a}_2 du^2)du^3, \tag{B.64}$$

and the final expression for a line integral taken about the contour, C, enclosing a surface element, S, located on the u^1-surface is:

$$\oint_C \boldsymbol{F}\cdot d\boldsymbol{l} = \left[\frac{\partial}{\partial u^2}(\boldsymbol{F}\cdot \boldsymbol{a}_3) - \frac{\partial}{\partial u^3}(\boldsymbol{F}\cdot \boldsymbol{a}_2)\right]du^2 du^3. \tag{B.65}$$

Similarly, the expression of the contour integral on the u^2-surface is:

$$\oint_C \boldsymbol{F}\cdot d\boldsymbol{l} = \left[\frac{\partial}{\partial u^3}(\boldsymbol{F}\cdot \boldsymbol{a}_1) - \frac{\partial}{\partial u^1}(\boldsymbol{F}\cdot \boldsymbol{a}_3)\right]du^1 du^3 \tag{B.66}$$

and for the u^3-surface, it is given by:

$$\oint_C \boldsymbol{F}\cdot d\boldsymbol{l} = \left[\frac{\partial}{\partial u^1}(\boldsymbol{F}\cdot \boldsymbol{a}_2) - \frac{\partial}{\partial u^2}(\boldsymbol{F}\cdot \boldsymbol{a}_1)\right]du^1 du^2. \tag{B.67}$$

In addition, one must consider the unit normal vector of the left hand side of (B.61). According to the original definition of surface, unitary, and reciprocal vectors, the reciprocal vector, $\boldsymbol{a}^1$, is normal to the plane containing the vector product of unitary vectors $\boldsymbol{a}_2$ and $\boldsymbol{a}_3$ (*i.e.* the u^1-surface). In general, the unit normal vector, $\boldsymbol{n}$, is defined in terms of the appropriate reciprocal vectors, $\boldsymbol{a}^i$, for a given surface element located in the u^i-surface; that is:

$$\boldsymbol{n} = \frac{\boldsymbol{a}^i}{\sqrt{\boldsymbol{a}^i\cdot\boldsymbol{a}^i}}. \tag{B.68}$$

---

* The Taylor expansion of a function, $f(x)$, centred at a is given by:

$$f(x) = f(a) + f'(a)(x-a) + O(x^2)$$

where the first derivative of the function is approximated as:

$$f'(a)(x-a) = f(x) - f(a).$$

In the case of a unit vector normal to the u^1-surface, the above expression is modified using the definition of the reciprocal vectors of equation (B.9) and the volume of a parallelepiped of (B.8):

$$\boldsymbol{n} = \frac{\boldsymbol{a}^1}{\sqrt{\boldsymbol{a}^1 \cdot \boldsymbol{a}^1}} = \frac{V}{\sqrt{(\boldsymbol{a}_2 \times \boldsymbol{a}_3) \cdot (\boldsymbol{a}_2 \times \boldsymbol{a}_3)}} \boldsymbol{a}^1 = \frac{\boldsymbol{a}_1 \cdot (\boldsymbol{a}_2 \times \boldsymbol{a}_3)}{\sqrt{(\boldsymbol{a}_2 \times \boldsymbol{a}_3) \cdot (\boldsymbol{a}_2 \times \boldsymbol{a}_3)}} \boldsymbol{a}^1 . \qquad \text{(B.69)}$$

The above definition of unit normal, along with the expression of the contour integral of (B.67), and the area of the surface element on the u^1-surface given by (B.29), are substituted into (B.61), and following some simplification:

$$(\nabla \times \boldsymbol{F}) \cdot [\boldsymbol{a}_1 \cdot (\boldsymbol{a}_2 \times \boldsymbol{a}_3)] \boldsymbol{a}^1 = \left[\frac{\partial}{\partial u^2} (\boldsymbol{F} \cdot \boldsymbol{a}_3) - \frac{\partial}{\partial u^3} (\boldsymbol{F} \cdot \boldsymbol{a}_2) \right]. \qquad \text{(B.70)}$$

As was demonstrated in the derivation of the expression for volume elements, $\boldsymbol{a}_1 \cdot (\boldsymbol{a}_2 \times \boldsymbol{a}_3) = \sqrt{g}$, the component of the curl of $\boldsymbol{F}$ perpendicular to the u^1-surface is written as:

$$(\nabla \times \boldsymbol{F}) \cdot \boldsymbol{a}^1 = \frac{1}{\sqrt{g}} \left[\frac{\partial}{\partial u^2} (\boldsymbol{F} \cdot \boldsymbol{a}_3) - \frac{\partial}{\partial u^3} (\boldsymbol{F} \cdot \boldsymbol{a}_2) \right]. \qquad \text{(B.71)}$$

Thus, the curl of $\boldsymbol{F}$ is given by:

$$(\nabla \times \boldsymbol{F}) \cdot \boldsymbol{a}^1 = \frac{1}{\sqrt{g}} \left[\left(\frac{\partial}{\partial u^2} (\boldsymbol{F} \cdot \boldsymbol{a}_3) - \frac{\partial}{\partial u^3} (\boldsymbol{F} \cdot \boldsymbol{a}_2) \right) \right]. \qquad \text{(B.72)}$$

Appendix C

Calculation of Scattering Parameters

The scattering matrix, $[S]$, represents the reflected voltages (waves), V_{1out} and V_{2out}, in terms of the input voltages (incident waves), V_{1in} and V_{2in}; that is:

$$\begin{bmatrix} V_{1out} \\ V_{2out} \end{bmatrix} = \begin{bmatrix} S_{11} & S_{12} \\ S_{21} & S_{22} \end{bmatrix} \begin{bmatrix} V_{1in} \\ V_{2in} \end{bmatrix} \qquad \text{(C.1)}$$

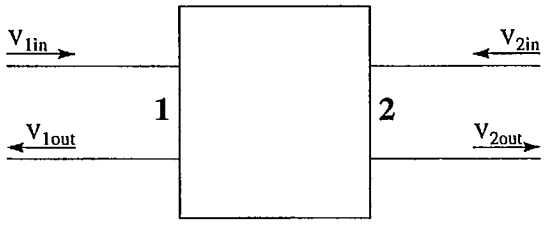

Figure C.1. Waves (voltages) at ports of a microwaves circuit

where S_{11} is the reflection coefficient from port (medium) **1**, S_{22} is the reflection coefficient from port (medium) **2**, and S_{12}, S_{21} are transmission coefficients from port (medium) **2** to port (medium) **1** or vice versa [3]. Hence, the reflection and transmission coefficients can be written as:

$$S_{11} = \left.\frac{V_{1out}}{V_{1in}}\right|_{V_{2in}=0} \text{ and } S_{12} = \left.\frac{V_{1out}}{V_{2in}}\right|_{V_{1in}=0} \qquad \text{(C.2)}$$

respectively [3]. In general, the scattering matrix elements are complex; however in the majority of cases, only the magnitude of the elements is of interest [136].

One of the most common methods of assessing the efficiency of the impedance-matching of a circuit is by utilizing scattering parameters, and in particular, the magnitude of the reflection coefficient, $|S_{11}|$ (also known as *return loss*, RL) where [136]:

$$RL = -20log|\Gamma| = 20log|S_{11}|. \qquad \text{(C.3)}$$

The following is a brief description of two methods that can be used to calculate the RL of various circuits and circuit structures.

C.1 Pulse Separation Method

The *pulse separation method* is one of the simplest methods of computing the scattering parameters of a circuit (or structure). It only requires the voltage (or field) response of the corresponding port (or medium) that contains both the incident voltage and the reflected voltage response of the circuit. The exact procedure of this method is illustrated in the following example.

In the case of the MSDRA test example (see **Figure 7.10** and **Section 7.4.1**), the microstrip line was excited using a time domain Gaussian pulse voltage source (with a frequency content of approximately 60 *GHz*). A voltage observation point was placed at an equal distance from both the source and the MSDRA. The total transient response observed at this point is plotted in **Figure C.2**. This transient response includes both the incident voltage response, V_i, as well as the reflected voltage response, V_r, of the MSDRA. However, due to the temporal distance between the incident and reflected *pulses*, the two voltage responses can be easily identified and *separated* (thus the term

pulse separation method). Next, the frequency domain voltage response of the circuit is obtained via the application of the DFT method. Finally, the return loss of the MSDRA is computed by:

$$RL = 20log|S_{11}| = 20log\left|\frac{V_r(f)}{V_i(f)}\right|. \quad \text{(C.4)}$$

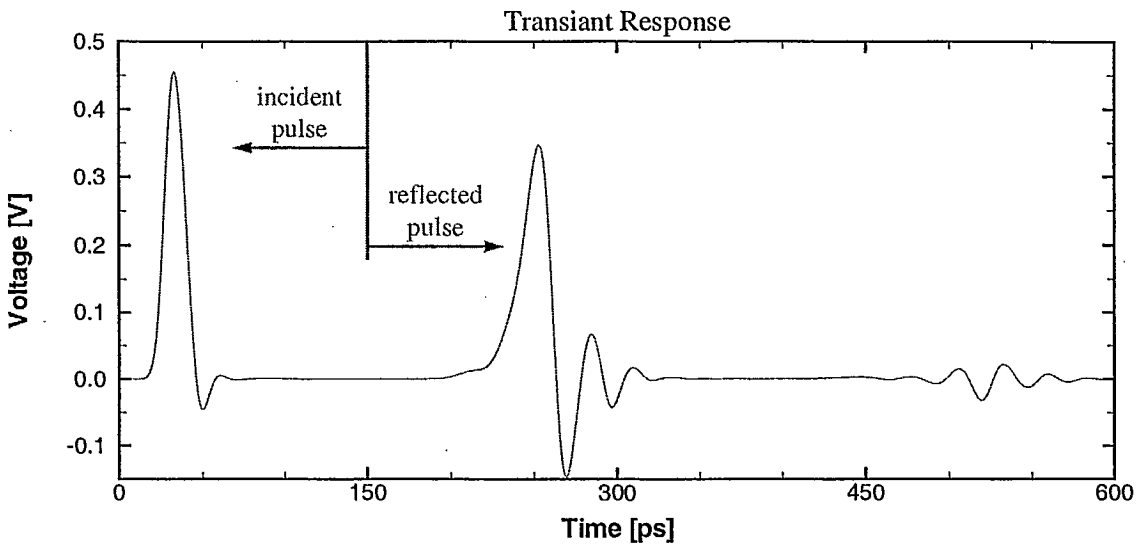

Figure C.2. Transient response of an MSDRA structure computed via the FDTD method.

C.2 Modal Expansion Method

In the pulse separation method, an adequate physical distance between the source (or the scatterer) and the observation point is required in order to provide a temporal separation between the incident and reflected wave. This requirement often demands either a narrow (in time) excitation pulse (hence a very small time step) or a very large distance between the source (or the scatterer) and the observation point; both of these requirements are computationally expensive if not prohibitive. In the method presented below, the scattering parameters are evaluated by using a *modal expansion* of the fields in

the frequency domain. With very little computational effort, this simple and rigorous method is capable of computing scattering parameters using the circuit's transient response observed at any two consecutive observation points (planes) on the circuit [144]. A detailed description of this method can be found in [146]; however, for completeness, the main steps taken in computing the scattering matrix parameters using the modal expansion method are presented below.

The modal expansion method is based on the orthogonal decomposition of fields on two neighbouring planes on a transmission line [145]. The field distribution on the observation points is expressed as linearly independent modal fields that can be represented via the following potential functions [145]:

$$F_1(\omega) = A_1\psi_1 e^{-j\beta_1 z} + B_1\psi_1 e^{j\beta_1 z} + \sum_{n=2}^{\infty} C_n\psi_n e^{j\beta_n z}, \tag{C.5}$$

$$F_2(\omega) = A_1\psi_1 e^{-j\beta_1 (z+\Delta z)} + B_1\psi_1 e^{j\beta_1 (z+\Delta z)} + \sum_{n=2}^{\infty} C_n\psi_n e^{j\beta_n (z+\Delta z)}, \tag{C.6}$$

where $F_1(\omega)$ and $F_2(\omega)$ are frequency domain field distribution values at the observation points (planes); ψ_1 and ψ_n are the potential functions of the dominant and the higher order modes (on the observation planes) respectively; β_1 and β_n are the propagation constants of the dominant and the higher order modes respectively; A_1 and B_1 are the amplitudes of the dominant mode's incident and reflected waves respectively; and C_n is the amplitude of the higher order modes' reflected waves. Finally, z and Δz are the location of the first observation point and the separation of the observation points respectively. Since the amplitude of the higher order modes attenuates exponentially as a function of the distance from the discontinuity (or scatterer) where they originated, the summation terms of (C.5)

and (C.6) can be neglected if the observation points are located sufficiently away from the discontinuity. Hence, (C.5) and (C.6) can be simplified to:

$$F_1(\omega) = A_1\psi_1 e^{-j\beta_1 z} + B_1\psi_1 e^{j\beta_1 z}, \tag{C.7}$$

$$F_2(\omega) = A_1\psi_1 e^{-j\beta_1 (z+\Delta z)} + B_1\psi_1 e^{j\beta_1 (z+\Delta z)}. \tag{C.8}$$

The above equation can be solved for unknown incident and reflected wave amplitudes (*i.e.* A_1 and B_1), and the reflection coefficient is computed by:

$$S_{11} = \frac{B_1}{A_1}. \tag{C.9}$$

References

[1] D. T. Paris and F. K. Hurd, *Basic Electromagnetic Theory*, McGraw-Hill, Inc., New York, 1969.

[2] C. T. Tai, "Teaching Electromagnetics Without Magnetism," *IEEE Transactions on Antennas and Propagation Magazine*, v. 41, n. 5, pp. 60-65, 1999.

[3] J. D. Kraus, *Electromagnetics*, 3rd. ed., McGraw-Hill, Inc., New York, 1984.

[4] M. N. O. Sadiku, *Numerical Techniques in Electromagnetic*, CRC press, Inc., New York, 1969.

[5] K. S. Yee, "Numerical Solution of Initial Boundary Value Problems Involving Maxwell's Equations in Isotropic Media," *IEEE Transactions on Antennas and Propagation*, v. 14, n. 5, pp. 302-307, 1966.

[6] R. F. Harrington, "Matrix Methods for Field Problems," *Proceedings of the IEEE*, v. 55, n. 2, pp. 136-149, 1967.

[7] R. Mittra, Editor, *Numerical and Asymptotic Techniques in Electromagnetics*, Springer-Verlag, Inc., New York, 1975.

[8] K. S. Kunz and R. J. Luebbers, *The Finite Difference Time Domain for Electromagnetics*, CRC Press, Inc., Boca Raton, 1992.

[9] J. M. Johnson and Y. Rahmat-Samii, "Genetic Algorithms in Engineering Electromagnetics," *IEEE Transactions on Antennas and Propagation Magazine*, v. 39, n. 4, pp. 7-21, 1997.

[10] L. Lapidus and G. F. Pinder, *Numerical Solution of Partial Differential Equations in Science and Engineering*, John Wiley & Sons, Inc., New York, 1982.

[11] K. W. Morton and D. Mayers, *Numerical Solutions of Partial Differential Equations: An Introduction*, Cambridge University Press, Cambridge, 1994.

[12] C. A. Balanis, *Advance Engineering Electromagnetics*, John Wiley & Sons, Inc., New York, 1989.

[13] E. K. Miller, "A Selective Survey of Computational Electromagnetics," *IEEE Transactions on Antennas and Propagation*, v. 36, n. 9, pp. 1281-1305, 1988.

[14] C. A. Balanis, *Antenna Theory: Analysis and Design*, 2nd ed., John Wiley & Sons, Inc., New York, 1997.

[15] R. F. Harrington, *Time-Harmonic Electromagnetic Fields*, McGraw-Hill, Inc., New York, 1961.

[16] V. Shankar, A. H. Mohammadian, and W. F. Hall, "A Time-Domain Finite-Volume Treatment for the Maxwell Equations," *Electromagnetics*, v. 10, n. 1-2, pp. 127-145, 1990.

[17] A. H. Mohammadian, V. Shankar, and W. F. Hall, "Computation of Electromagnetic Scattering and Radiation Using a Time-Domain Finite-Volume Discretisation Procedure," *Computer Physics Communications*, v. 68, n. 1, pp. 175-196, 1991.

[18] C. Hirsch, *Numerical Computation of Internal and External Flows, Volume 1: Fundamentals of Numerical Discretisation*, John Wiley & Sons, Inc., Chichester, 1988.

[19] R. F. Warming and R. M. Beam, "On the Construction and Application of Implicit Factored Schemes for Conservation Laws," *SIAM-AMS Proceedings*, v. 11, n. 1, pp. 85-129, 1978.

[20] D. Zwillinger, *Handbook of Differential Equations*, Academic Press, Inc., Boston, 1989.

[21] C. A. J. Fletcher, *Computational Techniques for Fluid Dynamics 1: Fundamental and General Techniques*, 2nd ed., Springer-Verlag, Inc., Berlin, 1991.

[22] C. Hirsch, *Numerical Computation of Internal and External Flows, Volume 2: Computational Methods for Inviscid and Viscous Flows*, John Wiley & Sons, Inc., Chichester, 1988.

[23] J. D. Anderson, J. C. Tannehill, and R. H. Pletcher, *Computational Fluid Mechanics and Heat Transfer*, McGraw-Hill, Inc., New York, 1984.

[24] C. A. J. Fletcher, *Computational Techniques for Fluid Dynamics 2: Specific Techniques for Different Flow Categories*, 2nd ed., Springer-Verlag, Inc., Berlin, 1991.

[25] J. D. Anderson, *Computational Fluid Dynamics: The Basics with Applications*, McGraw-Hill, Inc., New York, 1995.

[26] J. S. Shang, "Characteristic-Based Algorithms for Solving the Maxwell's Equations in the Time Domain," *IEEE Transactions on Antennas and Propagation Magazine*, v. 37, n. 3, pp. 15-25, June 1995.

[27] E. Kreyszig, *Advanced Engineering Mathematics*, 6th ed., John Wiley & Sons, Inc., Toronto, 1988.

[28] F. John, *Applied Mathematical Sciences Volume 1: Partial Differential Equations*, 4nd ed., Springer-Verlag Inc., New York, 1982.

[29] G. A. Sod, *Numerical Methods in Fluid Dynamics: Initial and Initial Boundary-Value Problems*, Cambridge University Press, Cambridge, 1985.

[30] J. Noye, Editor, *Numerical Solution of Differential Equations*, North-Holland, Inc., Amsterdam, 1984.

[31] J. W. Thomas, *Numerical Partial Differential Equations: Finite Difference Method*, Springer-Verlag, Inc., New York, 1995.

[32] R. D. Richtmyer and K. W. Morton, *Differential Methods for Initial-Value Problems*, Interscience, Inc., New York, 1967.

[33] J. C. Strikwerda, *Finite Difference Schemes and Partial Differential Equations*, Wadsworth & Brooks, Inc., Belmont, CA, 1989.

[34] R. Siushansian, "A New Time Domain Numerical Technique for Modelling Electromagnetic Dispersive Media," M.E.Sc. dissertation, The University of Western Ontario, 1995.

[35] A. H. Mohammadian, V. Shankar, and W. F. Hall, "Application of the Time-Domain Differential Solver to 2D Electromagnetic Penetration Problems," *IEEE Transactions on Magnetics*, v. 25, n. 4, pp. 2875-2877, 1989.

[36] SunPro, *Numerical Computation Guide: SPARCompiler™ C 2.0,* Sun Microsystems, Inc., Mountain View, CA, 1992.

[37] R. Siushansian, N. R. S. Simons, and J. LoVetri, "A Comparative Study of the FDTD and FVTD Schemes," *IEEE Antennas and Propagation Society International Symposium and URSI Radio Science Meeting*, Symposium Digest, Montreal, Canada, July 13-18, p. 132, 1997.

[38] A. Thom and C. J. Apelt, *Field Computations in Engineering and Physics*, Van Nostrand, Inc., London, 1961.

[39] H. P. Greenspan, D. J. Benney, and J. E. Turner, *Calculus: An Introduction to Applied Mathematics*, 2nd ed., McGraw-Hill Ryerson, Ltd., Toronto, 1986.

[40] M. L. James, G. M. Smith, and J. Wolford, *Applied Numerical Methods for Digital Computation*, 4th ed., Harper Collins, Inc., New York, 1993.

[41] M. G. Salvadori and M. L. Baron, *Numerical Methods in Engineering*, Prentice-Hall, Inc., Englewood Cliffs, N.J., 1961.

[42] K. L. Shlager and J. B. Schneider, "A Selective Survey of the Finite-Difference Time-Domain Literature" *IEEE Antennas and Propagation Magazine*, v. 37, n. 4, pp. 39-56, 1995.

[43] A. F. Peterson, S. Ray, and R. Mittra, *Computational Methods for Electromagnetics*, IEEE Press, New York, 1998.

[44] D. Mardare, R. Siushansian, and J. LoVetri, *3D Dispersive EMFDTD Manual: Version 1.3,* The University of Western Ontario, London, ON, 1995.

[45] A. Taflove, *Computational Electrodynamics: The Finite-Difference Time-Domain Method,* Artech House, Inc., Norwood, MA, 1995.

[46] A. Taflove, Editor, *Advances in Computational Electrodynamics: The Finite-Difference Time-Domain Method,* Artech House, Inc., Norwood, MA, 1998.

[47] R. Holland, "Finite Difference Solution of Maxwell's Equations in Generalizes Nonorthogonal Coordinates," *IEEE Transactions on Nuclear Science*, v. 30, n. 6, pp. 4589-4591, 1983.

[48] J. F. Lee, R. R. Palandech, and R. Mittra, "Modelling Three-dimensional Discontinues in Waveguides Using Nonorthogonal FDTD Algorithm," *IEEE Transactions on Microwave Theory and Techniques*, v. 40, n. 2, pp. 346-353, 1992.

[49] K. S. Yee and J. S. Chen, "Conformal Hybrid Finite Difference Time Domain and Finite Volume Time Domain," *IEEE Transactions on Antennas and Propagation*, v. 42, n. 10, pp. 1450-1455, 1994.

[50] T. G. Jurgens and A. Taflove, "Three-dimensional contour FDTD Modelling of Scattering from Single and Multiple Bodies," *IEEE Transactions on Antennas and Propagation*, v. 41, n. 12, pp. 1703-1708, 1993.

[51] C. J. Railton and R. J. Craddock, "Analysis of General 3D PEC Structure Using Improved CPFDTD Algorithm," *Electronic Letters*, v. 31, n. 20, pp. 1753-1754, 1995.

[52] M. Madsen, "Divergence Preserving Discrete Surface Integral Method for Maxwell's Equations Using Nonorthogonal Unstructured Grids," *Journal of Computational Physics*, v. 119, n. 1, pp. 34-45, 1995.

[53] S. D. Geddey, F. S. Lansing, and D. L. Rascoe, "A Full-Wave Analysis of Passive monolithic Integrated Circuit Devices Using a Generalized Yee Algorithm," *IEEE Transactions on Microwave Theory and Techniques*, v. 44, n. 8, pp. 1393-1400, 1996.

[54] S. Dey, and R. Mittra, "A Conformal Finite-Difference Time-Domain Technique for Modelling Cylindrical Dielectric Resonators," *IEEE Transactions on Microwave Theory and Techniques*, v. 47, n. 9, pp. 1737-1739, 1999.

[55] W. J. R. Hoefer, "The Transmission-Line Matrix Method: Theory and Applications," *IEEE Transactions on Microwave Theory and Techniques*, v. 33, n. 10, pp. 882-893, 1985.

[56] P. B. Johns and R. L. Beurle, "Numerical Solution of Two-Dimensional Scattering Problems using a Transmission-Line Matrix," *Proceedings of IEEE*, v. 118, n. 9, pp. 1203-1208, 1971.

[57] P. B. Johns, "The Solution of Inhomogeneous Waveguide Problems Using a Transmission-Line Matrix," *IEEE Transactions on Microwave Theory and Techniques*, v. 22, n. 3, pp. 209-215, 1974.

[58] C. Christopoulos, *The Transmission-Line Modelling Method: TLM*, IEEE Press, Inc., New York, 1995.

[59] N. R. S. Simons, A. Sebak, and A. Ittipiboon, "Analysis of Aperture-Coupled Microstrip-Antenna and Circuit Structures Using the Transmission-Line Matrix Method," *IEEE Antennas and Propagation Magazine*, v. 37, n. 4, pp. 27-37, 1995.

[60] N. R. S. Simons, "Development and Application of Differential-Equation Based Numerical Techniques to Electromagnetic Scattering and Radiation Problems," Ph. D. dissertation, University of Manitoba, Winnipeg, Manitoba, 1994.

[61] N. R. S. Simons and E. Bridges, "Equivalence of Propagation Characteristics for the Transmission-Line Matrix and Finite-Difference Time-Domain Methods in Two Dimensions," *IEEE Transactions on Microwave Theory and Techniques*, v. 39, n. 2, pp. 354-357, 1991.

[62] P. B. Johns, "On the Relationship Between TLM and Finite-Difference method for Maxwell's Equations," *IEEE Transactions on Microwave Theory and Techniques*, v. 35, n. 1, pp. 60-61, 1987.

[63] S. Hein, "Finite-Difference Time-Domain Approximation of Maxwell's Equations with Non-Orthogonal Condensed TLM Mesh," *International Journal of Numerical Modelling: Electronic Networks, Devices and Fields*, v. 7, n. 3, pp. 179-188, 1994.

[64] M. Celuch-Marcysiak and W. K Gwarek, "Generalized TLM Algorithm with Controlled Stability Margin and Their Equivalence with Finite-Difference Formulations for Modified Grids," *IEEE Transactions on Microwave Theory and Techniques*, v. 43, n. 9, pp. 2081-2089, 1995.

[65] J. Paul, C. Christopoulos, and D. P Thomas, "Generalized Material Models in TLM Part I and II," *IEEE Transactions on Antennas and Propagation*, v. 47, n. 10, pp. 1528-1542, 1999.

[66] P. P. Silvester and R. L. Ferrari, *Finite Element for Electrical Engineers*, Cambridge University Press, Cambridge, 1983.

[67] D. R. Lynch and K. D. Paulsen, "Time-Domain Integration of Maxwell Equations on Finite Elements," *IEEE Transactions on Antennas and Propagation*, v. 38, n. 12, pp. 1933-1942, 1990.

[68] S. D. Gedney and U. Navsariwala, "An Unconditional Stable Finite Element Time-Domain Solution of the Vector Wave Equations," *IEEE Microwave and Guided Wave Letters,* v. 5, n. 10, pp. 332-334, 1995.

[69] A. C. Cangellaris, C. Lin, and K. K. Mei, "Point-matched Time Domain Finite Element Methods for Electromagnetic Radiation And Scattering," *IEEE Transactions on Antennas and Propagation*, v. 35, n. 10, pp. 1160-1173, 1987.

[70] D. Koh, H. Lee, and T. Itoh, "A Hybrid Full-Wave Analysis of Via-Holes Grounds Using Finite-Difference and Finite-Element Time-Domain Methods," *IEEE Transactions on Microwave Theory and Techniques*, v. 45, n. 12, pp. 2217-2222, 1997.

[71] A. Monorchio, and R Mittra, "A Novel Subgridding Scheme Based on Combination of the Finite-Element and Finite-Difference Time-Domain Methods," *IEEE Transactions on Antennas and Propagation*, v. 46, n. 9, pp. 1391-1393, 1998.

[72] C. Hwang, and R. Wu, "Treating Late-Time Instability of Hybrid Finite-Element/ Finite-Difference Time-Domain Method," *IEEE Transactions on Antennas and Propagation*, v. 47, n. 2, pp. 227-232, 1999.

[73] A. C. Cangellaris, "Time-Domain Finite Methods for Electromagnetic Wave Propagation and Scattering," *IEEE Transactions on Magnetics*, v. 27, n. 5, pp. 3780-3785, 1991.

[74] J. Lee, R. Lee, and A. C. Cangellaris, "Time-Domain Finite-Element Methods," *IEEE Transactions on Antennas and Propagation*, v. 45, n. 3, pp. 430-441, 1997.

[75] K. S. Komisarek, N. N. Wang, A. K. Dominek, and R. Hann, "An Investigation of New FETD/ABC Methods of Computation of Scattering from Three-Dimensional Material Objects," *IEEE Transactions on Antennas and Propagation*, v. 47, n. 10, pp. 1579-1585, 1999.

[76] J. A. Kong, *Electromagnetic Wave Theory*, John Wiley & Sons, Inc., New York, 1986.

[77] J. .S. Shang and R. M. Fithen, "A Comparative Study of Characteristic-Based Algorithms for the Maxwell Equations," *Journal of Computational Physics*, v. 125, pp. 378-394, 1996.

[78] V. Shankar, W. F. Hall, A. H. Mohammadian and S. Chakravarthy, "Application of Computational Fluid Dynamics-Based Methods to Problems in Computational Science," *Computing Systems in Engineering*, v. 1, n. 1, pp. 7-22, 1990.

[79] J. .S. Shang, "Time-Domain Electromagnetic Scattering Simulations on Multi computers," *Journal of Computational Physics*, v. 128, pp. 381-390, 1996.

[80] E. Kreyszig, *Introduction to Differential Geometry and Reimannian Geometry*, University of Toronto Press, Toronto, 1968.

[81] J. A. Stratton, *Electromagnetic Theory*, McGraw-Hill, Inc., New York, 1941.

[82] T. Liu, *Admissible Solutions of Hyperbolic Conservation Laws*, Memoirs of the American Mathematical society, v. 30, n. 240, 1981.

[83] P. D. Lax, "Hyperbolic Systems of Conservation Laws and the Mathematical Theory of Shock Waves," *CBMS Regional Conference Series in Applied Mathematics v. 11, Society for Industrial and Applied Mathematics*, Philadelphia, 1973.

[84] S. Osher and S. Chakravarthy, "High Resolution Schemes and the Entropy Condition," *SIMA Journal of Numerical Analysis*, v. 21, pp. 797-838, 1979.

[85] A. Majda and S. Osher, "Numerical Viscosity and the Entropy Condition," *Communications on Pure and Applied Mathematics*, v. 32, n. 5, pp. 955-983, 1984.

[86] P. D. Lax and B. Wendroff, "Systems of Conservation Laws," *Communications in Pure. Applied Mathematics*, v. 13, pp. 217-237, 1960.

[87] J. L. Steger and R. F. Warming, "Flux Vector Splitting of the Inviscid Gasdynamic Equations with Application to Finite-Difference Methods," *Journal of Computational Physics Magazine*, v. 40, pp. 263-293, 1981.

[88] W. K. Anderson, J. L. Thomas, and B. Van Leer, "Comparison of Finite Volume Flux Vector Splittings for the Euler Equations," *AIAA Journal*, v. 24, n. 9, pp. 1453-1460, 1986.

[89] J. S. Shang and D. Gaitonde, "Characteristic-Based, Time-Dependent Maxwell Equation Solver on a general curvilinear Frame," *AIAA Journal*, v. 33, n. 3, pp. 491-498, 1995.

[90] P. L. Roe, "Approximate Riemann Solvers, Parameter Vectors, and Difference Schemes," *Journal of Computational Physics Magazine*, v. 43, pp. 357-372, 1981.

[91] J. .S. Shang, "A Fractional-Step Method for Solving 3D, Time-Domain Maxwell Equations," *Journal of Computational Physics*, v. 118, pp. 119-109, 1995.

[92] R. F. Warming and R. M. Beam, "Upwind Second-Order Difference Schemes and Applications in Aerodynamic Flows," *AAIA Journal*, v. 14, n. 9, pp. 1241-1249, 1976.

[93] V. Shankar, W. F. Hall, and A. H. Mohammadian, "A Time Domain Differential Solver for Electromagnetic Scattering Problems," *Proceedings of the IEEE*, v. 77, n. 5, pp. 709-721, 1989.

[94] S. Palaniswamy, W. F. Hall, and V. Shankar, "Numerical Solution to Maxwell's Equations in the Time Domain on Nonuniform Grids," *Radio science*, v. 31, n. 4, pp. 905-912, 1996.

[95] R. F. Warming, P. Kutler, and H. Lomax, "Second- and Third-Order Noncentred Difference Schemes for Nonlinear Hyperbolic Equations," *AAIA Journal*, v. 11, n. 2, pp. 189-204, 1973.

[96] P. Glaister, "Second Order Accurate Upwind Difference Schemes for Scalar Conservation Laws with Source Term," *Computers and Mathematics with Applications*, v. 25, n. 4, pp. 65-73, 1993.

[97] P. Glaister, "Flux Difference Splitting for Hyperbolic Systems of Conservation Laws with Source Term," *Computers and Mathematics with Applications*, v. 26, n. 7, pp. 79-96, 1993.

[98] J. LoVetri and T. Lapohos, "Explicit Upwind Schemes for Lossy MTLs with Linear Terminations," *IEEE Transactions on Electromagnetic Compatibility*, v. 39, n. 3, pp. 189-200, 1997.

[99] A. Harten, P. D. Lax, and B. Van Leer, "On Upstream Differencing and Godunov-Type Schemes for Hyperbolic Conservation Laws," *SIAM Review*, v. 25, n. 1, pp. 35-61, 1983.

[100] D. Gaitonde and J. S. Shang, "Accuracy of Flux-Split Algorithms in High-Speed Viscous Flows," *AIAA Journal*, v. 31, n. 7, pp. 1215-1221, 1993.

[101] P. K. Sweby, "High Resolution Schemes Using Flux Limiters for Hyperbolic Conservation Laws," *SIMA Journal of Numerical Analysis*, v. 21, n. 5, pp. 995-1011, 1984.

[102] B. Van Leer, "On the Relation Between the Upwind-Differencing Schemes of Godunov, Engquist-Osher, and Roe," *SIAM Journal on Scientific and Statistical Computing*, v. 5, n. 1, pp. 1-20, 1984.

[103] S. Osher, "Riemann Solvers, the Entropy Condition, and Difference Approximations" *SIMA Journal of Numerical Analysis*, v. 21, n. 2, pp. 217-235, 1984.

[104] M. Mrozowski, "Stability Condition for the Explicit Algorithms of the Time Domain Analysis of Maxwell's Equations," *IEEE Microwave Guided Wave Letters*, v. 4, n. 8, pp. 279-281, 1994.

[105] D. E. Merewether, "Transient Currents on a Body of Revolution by an Electromagnetic Pulse," *IEEE Transactions on Electromagnetic Compatibility*, v. 13, n. 1, pp. 41-44, 1971.

[106] G. Mur, "Absorbing Boundary Conditions for the Finite Difference Approximation of the Time Domain Electromagnetic Field Equations," *IEEE Transactions on Electromagnetic Compatibility*, v. 23, n. 4, pp. 377-382, 1981.

[107] R. L. Higdon, "Numerical Absorbing Boundary Conditions for the Wave Equation," *Mathematics of Computation*, v. 49, n. 1, pp. 65-90, 1987.

[108] J. Fang, "Absorbing Boundary Conditions Applied to Model Wave Propagation in Microwave Integrated Circuits," *IEEE Transactions on Microwave Theory and Techniques*, v. 42, n. 8, pp. 1506-1513, 1994.

[109] J. P. Berenger, "A Perfectly Matched Layer for the Absorbing of Electromagnetic Waves," *Journal of Computational Physics*, v. 114, n. 1, pp. 185-200, 1994.

[110] S. D. Gedney, "An Anisotropic Perfectly Matched Layer Absorbing Medium of the Truncation of FDTD Lattices," *IEEE Transactions on Antennas and Propagation*, v. 44, n. 12, pp. 1630-1649, 1996.

[111] R. W. Ziolkowski, "The Design of Maxwellian Absorbers for Numerical Boundary Conditions and for Practical Applications Using Engineering Artificial Materials," *IEEE Transactions on Antennas and Propagation*, v. 45, n. 4, pp. 656-671, 1997.

[112] J. P. Berenger, "Improved PML for the FDTD Solution of Wave-structure interaction Problems," *IEEE Transactions on Antennas and Propagation*, v. 45, n. 3, pp. 466-473, 1997.

[113] R. Schneiders, "Mesh Generation: Software," www-users.informatik.rwthaachen.de/~roberts/software.html.

[114] A. Petersson, "Chalmesh," www.na.chalmers.se/~andersp/chalmesh/chalmesh.html.

[115] B. K. Soni, "Genie++ Title Page," www.erc.msstate.edu/research/thrusts/grid/genie.

[116] "NGP Title Page," www.erc.msstate.edu/research/thrusts/grid/ngp.

[117] Pointwise, Inc., "Pointwise Inc. - The GRIDGENeration Experts (tm)," www.pointwise.com.

[118] XYZ Scientific Applications, Inc., "TrueGrid (R) Mesh Generator Home Page," truegrid.com/xyz.html.

[119] *Gridgen® Version 12: User's Manual,* Pointwise, Inc., Fort Worth, Texas, 1997.

[120] *TrueGrid® Manual Version 1.4.0,* XYZ Scientific Applications, Inc., Livermore, CA, 1997.

[121] R. Siushansian, *The 3D Finite Volume Time Domain Engine, Reports 1-6*, Communications Research Centre Canada (CRC Contract No. U6800-9-1124/00), Ottawa, Canada, 1999.

[122] R. E. Collin, *Foundation for Microwave Engineering*, McGraw-Hill Book Company, Inc., New York, 1966.

[123] L. Lewin, D. C. Chang, and E. F. Kuester, *Electromagnetic waves and curved structures*, IEE, ISBS, Inc., Forest Grove, Or., 1977.

[124] E. A. Navarro, C. Wu, P. Y. Chung, and J. Litva, "Application of PML Superabsorbing Boundary Condition to Non-orthogonal FDTD Method," *Electronic Letters*, v. 30, n. 20, pp. 1654-1655, 1994.

[125] C. Kuo, B. Houshmand, and T. Itch, "Full-wave Analysis of Packaged Microwave Circuits with Active and Nonlinear Devices: An FDTD Approach," *IEEE Transactions on Microwave Theory and Techniques*, v. 45, n. 5, pp. 819-826, 1997.

[126] W. Sui, D. A. Chistensen, and C. H. Durney, "Extending the Two Dimensional FDTD Method to Hybrid Electromagnetic Systems with Active and Passive Lumped Elements," *IEEE Transactions on Microwave Theory and Techniques*, v. 40, n. 8, pp. 724-730, 1992.

[127] P. Lorrain and D. R. Corson, *Electromagnetism: Principles and Applications*, 2nd. ed., W. H. Freeman and Company Inc., San Francisco, 1978

[128] S. Ramo, J. R. Whinnery, and T. Van Duzer, *Fields and Waves in Communication Electronics*, 3rd. ed., John Wiley & Sons, Inc., New York, 1993.

[129] J. W. Nilsson, *Electric Circuits*, 3rd. ed., Addison-Wesley Publishing Company, Inc., Don Mills, ON, 1990.

[130] M. Piket-May, A. Taflove, and J. Baron, "FDTD Modelling of Digital Signal Propagation in 3D Circuits with Passive and Active Loads," *IEEE Transactions on Microwave Theory and Techniques*, v. 42, n. 8, pp. 1514-1532, 1994.

[131] A. Christ and H. L. Hartnagel, "Three-Dimensional Finite Difference Method for the Analysis of Microwave-Devices Embedding," *IEEE Transactions on Microwave Theory and Techniques*, v. 35, n. 8, pp. 688-695, 1987.

[132] J. A. Pereda, F. Alimenti, P. Mezzanotte, L. Roselli, and R. Sorrentino, "A New Algorithm for Incorporation of Arbitrary Linear Lumped Networks into FDTD Simulator," *IEEE Transactions on Microwave Theory and Techniques*, v. 47, n. 6, pp. 943-948, 1999.

[133] J. G. Proakis and D. G. Manolakis, *Digital Signal Processing: Principles Algorithms and Applications*, Macmillan Inc., New York, 1992.

[134] P. Ciampolini, P. Mezzanotte, L. Roselli, and R. Sorrentino, "Accurate and Efficient Circuit Simulation with Lumped-element FDTD Technique," *IEEE Transactions on Microwave Theory and Techniques*, v. 44, n. 12, pp. 2207-2215, 1996.

[135] R. E. Collin, *Field Theory of Guided Waves*, 2nd. ed., IEEE Press, Inc., New York, 1991.

[136] D. M. Pozar, *Microwave Engineering*, Addison-Wesley Publishing Company, Inc., Reading, MA, 1990.

[137] J. R. Kuttler, "A New Method for Calculating TE and TM Cutoff Frequencies of Uniform Waveguides with Lunar or Eccentric Annular Cross Section," *IEEE Transactions on Microwave Theory and Techniques*, v. 32, n. 4, pp. 348-354, 1984.

[138] L. Zhang, J. Zhang, and W. Wang, "Correct Determination of TE and TM Cutoff Wave Numbers in Transmission Lines with Circular Outer Conductors and Eccentric Circular Inner Conductors," *IEEE Transactions on Microwave Theory and Techniques*, v. 39, n. 8, pp. 1416-1419, 1991.

[139] J. A. Roumeliotis and S. P. Savaidis, "Cutoff Frequencies of Eccentric Circular-Elliptic Metallic Waveguides," *IEEE Transactions on Microwave Theory and Techniques*, v. 42, n. 11, pp. 2128-2138, 1994.

[140] V. Trenkic, C. Christopoulos, and T. M. Benson, "Efficient Computation Algorithms for TLM,", *First International Workshop on Transmission Line Matrix (TLM) Modelling Theory and Applications*, pp. 77-80, Victoria, Canada, August 1-3, 1995.

[141] I. Bardi, O. Biro, K. Preis, G. Vrisk, and K. R. Richter, "Nodal and Edge Element Analysis of Inhomogeneously Loaded 3D Cavity," *IEEE Transactions on Magnetics*, v. 28, n. 2, pp. 1142-1145, 1992.

[142] T. Weiland, "On the Unique Numerical Solution of Maxwellian Eigenvalue Problems in Three Dimensions," *Particle Accelerators*, v. 17, n. 2, pp. 227-242, 1985.

[143] T. Lapohos, "*SMA-Air Transition*," personal correspondence, 1999.

[144] S. Haffa, D. Hollmann, and W. Wiesbeck, "The Finite Difference Method for *S*-Parameter Calculation of Arbitrary Three-Dimensional Structures," *IEEE Transactions on Microwave Theory and Techniques*, v. 40, n. 8, pp. 1602-1609, 1992.

[145] B. Ghosh, N. R. S. Simons, L. Shafai, A. Ittipiboon, A. Petosa, and M. Cuhaci, "Extraction of Generalized Scattering Matrix Coefficients of Waveguide Discontinuities Using the TLM Method," *Symposium on Antenna Technology and Applied Electromagnetics (ANTEM'96)*, Ottawa, Canada, pp. 535-538, August 9-12, 1999.

[146] A. Christ and H. L. Hartnagel, "Three-Dimensional Finite-Difference Method for the analysis of Microwave-Devices Embedding," *IEEE Transactions on Microwave Theory and Techniques*, v. 35, n. 8, pp. 688-696, 1987.

[147] N. R. S. Simons, R. Siushansian, J. LoVetri, and M. Cuhaci, "Comparison of the Transmission-Line Matrix and Finite-Difference Time-Domain Methods for a Problem Containing a Sharp Metallic Edge," *IEEE Transactions on Microwave Theory and Techniques*, v. 47, n. 10, pp. 2042-2045, 1999.

[148] J. L. Herring and W. J. R. Hoefer, "Improved Correction for 3-D TLM Coarseness Error," *Electronic Letters*, v. 30, n. 14, pp. 1149-1150, 1994.

[149] K. L. Shlager, J. G. Maloney, S. L. Ray, and A. F. Peterson, "Relative Accuracy of Several Finite-Difference Time-Domain Methods in Two and Three Dimensions," *IEEE Transactions on Antennas and Propagation*, v. 41, n. 12, pp. 1732-1737, 1993.

[150] J. LoVetri, "Algorithmic Techniques," Ph. D. dissertation, University of Ottawa, Ottawa, Ontario, 1991.

[151] A. Petosa, A. Ittipiboon, Y. M. M. Antar, D. Roscoe, and M. Cuhaci, "Recent Advances in Dielectric Resonator Antenna Technology," *IEEE Antennas and Propagation Magazine,* v. 40, n. 3, pp. 35-48, 1998.

[152] A. Petosa, N. R. S. Simons, R. Siushansian, A. Ittipiboon, and M. Cuhaci, "Design and Analysis of Multi-Segment Dielectric Resonator Antennas," to appear in *IEEE Transactions on Antennas and Propagation,* v. 48, n. 5, 2000.

[153] Computer Simulation Technology, Inc., "MAFIA," www.cst.de.

[154] T. Weiland, "Time-Domain Electromagnetic Field Computation with Finite Difference Methods," *International Journal of Numerical Modelling: Electronic Networks, Devices and Fields*, v. 9, n. 2, pp. 295-319, 1996.

[155] M. Rizvi and J. LoVetri, "Modelling and Reduction of Crosstalk on Coupled Microstrip Line Structures and Multichip Modules: An FDTD Approach," *International Journal on Microwave and Millimetre-Wave Computer-Aided Engineering*, v. 6, n. 1 pp. 58-68, 1996.

[156] D. Mardare, R. Siushansian, and J. LoVetri, "3D Dispersive EM-FDTD Electromagnetic Simulation Tool Version 1.3: User's Manual," The University of Western Ontario, London, Ontario, Canada, December 1995.

[157] N. R. S. Simons, R. Siushansian, A. Petosa, M. Cuhaci, A. Ittipiboon, J. LoVetri, and S. Gutschling, "Validation of Transmission Line Matrix, Finite-Integration Technique, and Finite-Difference Time-Domain Simulations of a Multi-Segment Dielectric Resonator Antenna," *13th Annual Review of Progress in Applied Computational Symposium (ACES-97)*, Monterey, CA, pp. 1425-1430, March 17-21, 1997.

[158] J. S. Shang, "High Resolution Schemes for Maxwell's Equations in the Time Domain," *13th Annual Review of Progress in Applied Computational Symposium (ACES-97)*, Monterey, CA, pp. 74-81, March 17-21, 1997.

[159] D. C. Blake and J. S. Shang, "An Analysis of Programming Models for Time-Domain CEM Codes on RISC-Based Computers," *14th Annual Review of Progress in Applied Computational Symposium (ACES-98)*, Monterey, CA, pp. 808-815, March 16-20, 1998.

[160] K. Huang and Y. Liu, "A Simple Method for Calculating Electric and Magnetic FIelds in GTEM Cell," *IEEE Transactions on Electromagnetic Compatibility*, v. 36, n. 4, pp. 355-358, 1994.

[161] EMC Test Systems, Inc., "GTEM Cell Page," www.emctest.com.

[162] R. De Leo, L. Pierantoni, T. Rozzi, and L. Zappelli, "Accurate Analysis of the GTEM Cell Wide-Band Termination," *IEEE Transactions on Electromagnetic Compatibility*, v. 38, n. 2, pp. 188-197, 1998.

[163] J. Seregelyi, "*GTEM Cell Design*," DREO technical memorandum, 1999.

[164] L. Turnbull and A. C. Marvin, "A Treatment of the Phase Properties of GTEM to Open-Area Test-Site Correlation Technique," *IEEE Transactions on Electromagnetic Compatibility*, v. 40, n. 1, pp. 62-69, 1998.

[165] M. D. Judd and O. Farish, "A Pulse GTEM System for UHF Sensor Calibration," *IEEE Transactions on Instrumentation and Measurement*, v. 47, n. 4, pp. 875-880, 1998.

[166] F. Q. Hu, M. Hussaini, and J. Manthey, "Low-Dissipation and -Dispersion Runge-Kutta Schemes for Computational Acoustics," NASA technical report, NAS1-19480, NASA Langley Research Centre, Hampton, VA 23665, USA, 1997.

[167] P. Bonnet, X. Perrieres, F. Issac, F. Paladian, J. Grando, J. C. Alliot, and J. Fontaine, "Numerical Modelling of Scattering Problems Using a Time Domain Finite Volume Method," *Journal of Electromagnetic Waves and Applications*, v. 11, pp. 1165-1169, 1997.